Micro-Structural Evolution and Size-Effects in Plastically Deformed Single Crystals: Strain Gradient Continuum Modeling

El-Naaman, Salim Abdallah

Publication date:
2016

Document Version
Publisher's PDF, also known as Version of record

Micro-Structural Evolution and Size-Effects in Plastically Deformed Single Crystals

Strain Gradient Continuum Modeling

PhD Thesis

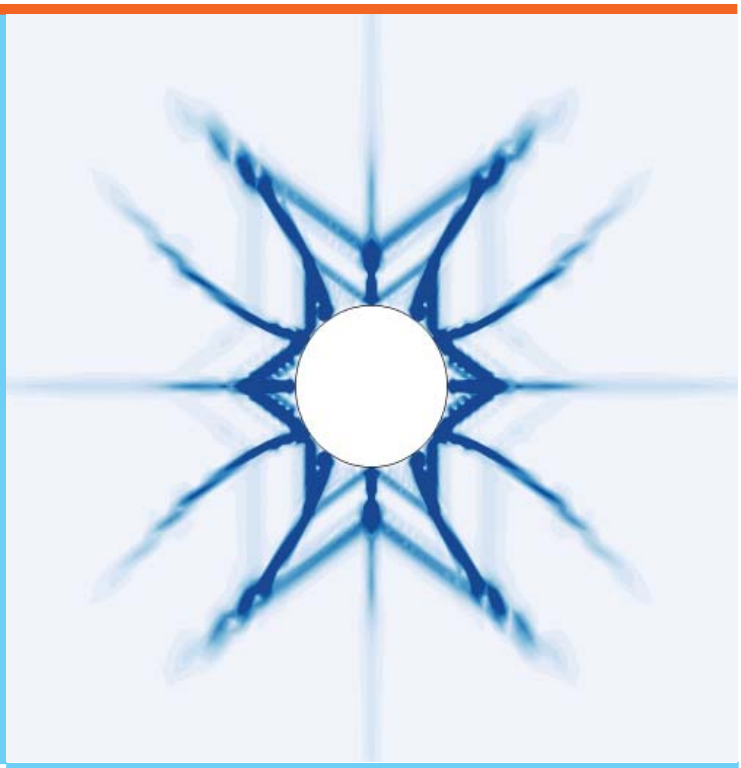

Salim Abdallah El-Naaman
DCAMM Special Report No. S213
July 2016

DTU Mechanical Engineering
Department of Mechanical Engineering

Micro-Structural Evolution and Size-Effects in Plastically Deformed Single Crystals

Ph.D. Thesis

Strain Gradient Continuum Modeling

Salim Abdallah El-Naaman

Department of Mechanical Engineering
Technical University of Denmark

The figure on the cover page is a smooth contour showing a numerical prediction of the distribution of geometrically necessary dislocations around a cylindrical void in the (110) crystallographic plane of a face centered cubic single crystal subject to equi-biaxial tension.

Title of the thesis:
Micro-Structural Evolution and Size-Effects in Plastically Deformed Single Crystals

Ph.D. student:
Salim Abdallah El-Naaman
E-mail: saeln@mek.dtu.dk

Main supervisor:
Professor, PhD Christian Frithiof Niordson
Technical University of Denmark
E-mail: cfn@mek.dtu.dk

Co-supervisor:
Associate Professor, PhD Kim Lau Nielsen
Technical University of Denmark
E-mail: kln@mek.dtu.dk

Published in 2016 by
DTU Mechanical Engineering & Danish Center for Applied Mathematics and Mechanics

Technical University of Denmark
Department of Mechanical Engineering
Nils Koppels Allé, Building 404, DK-2800 Kgs. Lyngby, Denmark
DK-2800 Kgs. Lyngby, Denmark
Phone: (+45) 45 25 42 50, Fax: (+45) 45 93 14 75
E-mail: info@mek.dtu.dk

DCAMM Special Report no. S213
ISSN: 0903-1685
ISBN: 978-87-7475-465-7

DTU Mechanical Engineering
Section of Solid Mechanics
www.mek.dtu.dk

Danish Center for Applied
Mathematics and Mechanics
www.dcamm.dk

To Luise and Zacharias

Resumé (in Danish)

Der er udført megen forskning i forbindelse med udviklingen af mikromekanisk baserede gradientplasticitets-kontinuumteorier, som er nødvendige for at kunne modellere plasticitet på mikroskala ved høje plastiske tøjningsgradienter. Mens mange modeller har vist sig at være i stand til at fange de makroskopiske effekter relateret til tøjningsgradienter, forudses oftest glatte mikrostrukturer. Udviklingen af dislokationsmikrostrukturer, ved plastisk deformation i duktile krystallinske materialer, er meget kompleks og uensartet. Publicerede eksperimentelle målinger udført på deformerede metalliske krystaller viser tydelige mønsterdannelser, hvor geometrisk nødvendige dislokationer danner væg- og cellestrukturer. Denne særlige delmængde af retningsbestemte dislokationer, som har en samlet Burgers vektor, er den vigtigste kilde til de observerede størrelseseffekter og er direkte knyttet til de plastiske tøjningsgradienter. Der er naturligvis mange udfordringer forbundet med modellering af dislokationsstrukturer inden for teorier baseret på kontinuumstørrelser, men da disse gradienteffekter tilskrives dislokationsmikrostrukturen, er det et naturligt skridt i den videre udvikling af gradient teorier, at fokusere på deres evne til at beskrive en realistisk udvikling af mikrostruktur. Denne udfordring er hovedfokus i nærværende afhandling, hvor der tages udgangspunkt i en ikke-arbejdskonjugeret "back stress"-baseret højereordens-krystalplasticitetsteori. "Back stress" er et udtryk for langtrækkende indre spændinger, som opstår på grund af ophobning af dislokationer. Inden for denne teoris rammer, udledes flere alternativer til en "back stress"-relation, baseret på en postuleret gradientenergi, men også baseret på en mere fænomenologisk tilgang. Gennem en omfattende numerisk undersøgelse vises det, at de foreslåede "back stress"-formuleringer tilbyder nye modelleringskapaciteter både med hensyn til mikrostrukturelle forudsigelser, men også i forhold til at fange kompleks makroskopisk materialeopførsel forbundet med tilstedeværelsen af langtrækkende indre spændinger. En formulering baseret på en næsten lineær gradientenergi, afslører slående ligheder med formuleringer baseret på diskret dislokationsteori og viser perspektivrige kapaciteter i forbindelse med den anvendte højereordensteori. Det foreliggende arbejde giver ydermere ny indsigt i modellering af plan tøjningstilstand i fladecentreret kubiske krystaller.

Abstract

An extensive amount of research has been devoted to the development of micro-mechanics based gradient plasticity continuum theories, which are necessary for modeling micron-scale plasticity when large spatial gradients of plastic strain appear. While many models have proven successful in capturing the macroscopic effects related to strain gradients, most predict smooth micro-structures. The evolution of dislocation micro-structures, during plastic straining of ductile crystalline materials, is highly complex and nonuniform. Published experimental measurements on deformed metal crystals show distinct pattern formation, in which dislocations, of the geometrically necessary kind, are arranged in wall and cell structures. This particular subset of signed dislocations, which have a net Burgers vector, are the main source for the observed size-effects and are directly linked to the gradients in plastic strain. It is clear that many challenges are associated with modeling dislocation structures, within a framework based on continuum fields, however, since the strain gradient effects are attributed to the dislocation micro-structure, it is a natural step, in the further development of gradient theories, to focus on their ability to capture realistic micro-structural evolution. This challenge is the main focus of the present thesis, which takes as starting point a non-work conjugate type back stress based higher order crystal plasticity theory. Within this framework, several possibilities for the back stress relation are formulated, based on a postulate of a gradient energy as well as by engaging in a phenomenological approach. Through an extensive numerical investigation, the proposed back stress formulations are shown to offer novel modeling capabilities both in terms of micro-structural predictions but also in terms of capturing complex macroscopic behavior tied to the presence of long range internal stresses. A formulation based on a near linear gradient energy reveals striking similarities to formulations based on discrete dislocation theory, and shows promising capabilities within the adopted higher order theory. Moreover, the present work offers new insight into plane strain modeling of face centered cubic crystals.

Preface

This thesis is submitted in partial fulfillment of the requirements for obtaining the degree of Ph.D. in Mechanical Engineering. The work is financially supported by The Danish Council for Independent Research, under the research career programme Sapere Aude, as part of the project "Higher Order Theories in Solid Mechanics" (grant 11-105098/FTP). The work was carried out at the Department of Mechanical Engineering, Solid Mechanics, Technical University of Denmark, in the period September 2012 to July 2016.

I sincerely wish to thank my main supervisor, Professor Christian Frithiof Niordson and co-supervisor Assoc. Professor Kim Lau Nielsen, for their valuable input and guidance, and for supporting me in my choices throughout the project. It has been enriching to collaborate with them in this work and I am grateful for having been given the opportunity to go through this unique academic and professional development. Moreover, I would like to thank my colleagues and fellow students at the department for contributing to a pleasant and inspiring atmosphere.

Part of this work was carried out during an eight months research stay at Columbia University in the City of New York, USA, with Professor Jeffrey W. Kysar. I am very grateful to Professor Kysar for making the stay possible. For financial support of this research stay, I would especially like to thank The Denmark-America Foundation in collaboration with the FLSmidth Group.

Last but not least, I wish to thank my family for their love and support. In particular, I must thank my wife Luise and my son Zacharias, whom I have neglected lately. Without their support I would not have been able to carry through. The time away from them has, without a doubt, been the toughest part of this project.

Salim Abdallah El-Naaman
Kgs. Lyngby, July 2016

List of Publications

The present Ph.D. thesis is based upon the following publications:

[P1] El-Naaman, S.A., Nielsen, K.L., Niordson, C.F. (2015). "Strain gradient crystal plasticity: A continuum mechanics approach to modeling micro-structural evolution". *Plastic Behavior of Conventional and Advanced Materials: Theory, Experiment, and Modeling*, pp. 7-9

[P2] El-Naaman, S.A., Nielsen, K.L., Niordson, C.F. (2016). "On modeling micro-structural evolution using a higher order strain gradient continuum theory". *International Journal of Plasticity 76*, pp. 285-298

[P3] El-Naaman, S.A., Nielsen, K.L., Niordson, C.F. (2016). "An investigation of back stress formulations under cyclic loading". *Mechanics of Materials*, *Submitted*

[P4] El-Naaman, S.A., Nielsen, K.L., Niordson, C.F. (2016). "Attaining the rate-independent limit of a rate-dependent strain gradient plasticity theory". *Extreme Mechanics Letters*, *In Press*

[P5] El-Naaman, S.A., Nielsen, K.L., Niordson, C.F., J.W. Kysar (2016). "Micron scale analysis of deformation around a cylindrical void in a face centered cubic crystal". *In Preparation*

The following work was conducted and published during the course of the Ph.D. program, but does not constitute part of the thesis:

[P6] El-Naaman, S.A., Nielsen, K.L. (2013). "Observations on Mode I ductile tearing in sheet metals ". *European Journal of Mechanics A/Solids 42*, pp. 54-62

[P7] Juul, K.J., El-Naaman, S.A., Nielsen, K.L., Niordson, C.F. (2016). "Size-effects in steady-state crack growth in rate-sensitive single crystals". *In preparation*

Contents

Resumé (in Danish) **iv**

Abstract **v**

Preface **vi**

List of Publications **vii**

1 Introduction **1**
1.1 Plasticity at small scales . . . 2
1.2 Micro-structure and motivation of the thesis . . . 4
1.3 Structure of the thesis . . . 6

2 Strain gradient plasticity **9**
2.1 The Kuroda & Tvergaard gradient plasticity theoretical framework . . . 10
2.2 Higher order boundary conditions . . . 12
2.3 Numerical implementation . . . 13

3 Back stress **15**
3.1 Gradient energy approach . . . 15
3.2 Phenomenological approach . . . 18
3.3 Effective framework for plane strain deformation in FCC crystals . . . 19

4 Summary of numerical results **23**
4.1 Monotonic loading . . . 23
4.2 Cyclic loading . . . 28
4.2.1 Macroscopic response under cyclic loading . . . 30
4.2.2 Micro-structure evolution predictions . . . 39
4.3 Rate-independent results . . . 40
4.4 Plane strain deformation around a cylindrical void in an FCC crystal . . . 43

5 Experimental considerations **51**
5.1 Experimental design . . . 51
5.2 Preparation and crystallographic orientation of the aluminum crystal . . . 52
5.3 Analyzing the dimensions of the notch and void specimen . . . 52
5.4 The Nye tensor . . . 55

6 Concluding remarks **59**

Appendices **61**
A Generalized back stress model accounting for edge and screw dislocations . 61
B Nano-indentation curves 62
C Engineering drawing of the single crystal specimen 63
D Errata [P2] 64

References **65**

Publications **71**
[P1] Strain gradient crystal plasticity: A continuum mechanics approach to modeling micro-structural evolution 73
[P2] On modeling micro-structural evolution using a higher order strain gradient continuum theory 79
[P3] An investigation of back stress formulations under cyclic loading 95
[P4] Attaining the rate-independent limit of a rate-dependent strain gradient plasticity theory 122
[P5] Micron scale analysis of deformation around a cylindrical void in a face centered cubic crystal 129

Chapter 1

Introduction

Metal plasticity has been studied since the mid nineteenth century (Tresca, 1864), however, in 1900 Ewing and Rosenhain discovered that the crystalline structure of metals is preserved during plastic deformation. This discovery led them to conclude that the observed plasticity occurred by crystallographic slip (Ewing and Rosenhain, 1900). However, it was not until 1934, when Taylor proposed that plastic deformation was due to the individual movement of defects in the atomic lattice on crystallographic slip systems, that we began to understand the true nature of plastic deformation[1]. These defects, which Taylor then referred to as "dislocations", offered an explanation as to why the theoretical strength of metals was several orders of magnitude higher than what scientists had measured in experiments at the time. Apart from these earlier discoveries, plasticity theory has been extensively studied over the years, and has enabled us to understand and predict complex permanent deformation phenomena. It has played a significant role in the design of metal structures, forming processes, and other technological advances, crucial to our modern-day society. During the past few decades an increasing interest in plasticity at small scales has emerged, where namely metals have been observed to behave in a size-dependent manner during plastic deformation.

There are many circumstances which can induce size-dependent behavior in metals, e.g. artificially introduced boundaries and other material inhomogeneities. Whenever a material sample is prepared, machined, treated, or processed in any other way, boundary layers are created. Often these boundary layers are insignificant, however, a small sample or component, e.g. produced from a larger processed bulk of material, can be entirely controlled by what was done to the original surfaces. Apart from artificially introduced scale dependence, a vast amount of experimental studies, reported during the recent years, also point to a more intrinsic size-dependent behavior in ductile crystalline materials, which occurs in the presence of spatial gradients of plastic strain. More specifically, an increase in hardening and/or an apparent increase in yield point (also referred to as strengthening) is observed for diminishing size. The phenomena may be explained in terms of the so-called geometrically necessary dislocations (GNDs), and statistically stored dislocations (SSDs), of which the former play a key role in micron and sub-micron scale plasticity problems.

Our understanding of plasticity at the micron scale and below, where the effects of GNDs become significant, is less profound. This is partially due to the challenges involved

[1] *"Plastic strain must be due to stability interchanges in which atoms jump, owing to thermal or other agitation and to the applied stress, from one position of equilibrium to another."* (Taylor, 1934)

in conducting experimental studies at these scales, however, the ability to accurately predict the response and performance of ductile crystalline materials, on the micron scale and below, may become an important factor for the advance of micron and nano technologies, involving metal structures, in the future. At these scales, conventional theories are simply inadequate for capturing the plastic response of metal structures, since they do not incorporate a material length scale into the constitutive framework. Moreover, they do not allow so-called micro-structural boundary conditions to be imposed, which are needed to capture boundary effects on the plastic flow. This realization has lead to a vast amount of research on strain gradient theories of plasticity and, due to the increasing interest in micron and nano scale plasticity, these have become an established part of contemporary solid mechanics. Most theories, however, contain a rather high degree of phenomenology and build on mathematical concepts and parameters which do not necessarily have a physical interpretation. Thus, much tuning is needed against experimental data which is scarce at this stage. The present thesis treats a so-called back stress based type of theory, proposed by Kuroda and Tvergaard (2006), and focuses on modeling of the complex material behavior of metals at small scales and the associated micro-structural evolution.

This Chapter gives an introduction to plasticity at small scales and to the micromechanics involved in the observed size effects. Moreover, the existing experimental data is reviewed and the dislocation micro-structure associated with the material behavior is discussed. Finally, the details of the thesis structure and format are given.

1.1 Plasticity at small scales

In 1994 Norman Fleck and his coworkers published a paper where they clearly demonstrated the effect of strain gradients on plastic deformation (Fleck et al., 1994). In that study they conducted tension and torsion tests on polycrystalline copper wires with diameters ranging from 12 to 170 microns. In the tension tests, where the strain is uniform, little dependence of the flow stress on wire diameter was observed, as would be predicted by conventional plasticity theory, where there is no internal length scale. However, for the torsion tests, where the wire cross section experiences a large strain gradient which increases with diminishing wire diameter for a given surface shear strain, a clear dependence on wire diameter was observed, where *smaller is stronger* seems to be the rule that applies. A few years later Stölken and Evans (1998) showed that, for pure bending of annealed high purity poly crystal nickel films with thicknesses ranging from 12.5 to 50 microns, decreasing film thicknesses led to an increased bending moment at a given surface strain. The effect of penetration depth on nano-hardness of metals is another example often referred to in the literature (Doener and Nix, 1986; Atkinson, 1995; Poole et al., 1996; Begley and Hutchinson, 1998), where materials appear harder at smaller indentation depths. During this period, the general notion that "*smaller is stronger*" was established and a vast research field emerged. One of the most recent additions to the experimental evidence of scale dependent plasticity, is the work of Mu et al. (2014). For this study, micro-pillar samples were produced, by focused ion beam milling, from material containing a thin copper film (with thicknesses ranging between 150 nm to 1180 nm) confined between Si and CrN. The compression samples were produced with the pillar axis either normal to or tilted 45° relative to the Cu film. In this manner, they conducted tests where the copper

films were subject to combined compression and shear or constrained shear, respectively, with significant size effects observed. In these experiments, not only does the height of the copper film have an effect, also the interfaces, Cu/Si and Cu/CrN, micro-structurally passivate the surfaces of the copper film, by constraining plastic flow with dislocation pile-up as a consequence.

In crystalline materials plasticity occurs when defects in the atomic lattice, also known as dislocations, move through the material in the slip systems. The slip systems are combinations of slip planes (the close packed atomic planes) and slip directions (plus and minus the close packed directions). In terms of dislocation densities, we may distinguish between two types; the statistically stored dislocations (SSDs) and the geometrically necessary dislocations (GNDs). The SSDs are the dislocations which are statistically present and evenly distributed in crystalline materials, thus, they have a zero net Burgers vector density, whereas the GNDs are the dislocations which arise in order to accommodate plastic strain gradients. Let us look at an example which illustrates this concept: Consider a single crystal beam, with its axis parallel to the x_1-direction. The beam is subject to the displacement field

$$u_1 = 0, \quad u_2 = \frac{1}{2}\kappa x_1^2, \quad u_3 = 0, \tag{1.1}$$

which results in a constant curvature, κ, as shown in Fig. 1.1a for a sample domain on the beam. The material is assumed to deform by crystallographic slip on a single slip system, with slip direction parallel to the x_1-direction, given by

$$\gamma = \kappa x_1. \tag{1.2}$$

Therefore, the only way the curvature can be accommodated is by having a gradient in slip in the x_1-direction. Say that the crystal contains a population of SSDs and Frank-Read sources. In the loaded material, the dislocations move and dislocation loops expand out from the Frank-Read sources, due to the resolved shear stress on the slip system. This is schematically illustrated in Fig. 1.1b, as edge dislocations of opposite sign emitted in each direction, where the gradient is shown by dividing the crystal domain into cells of length δx_1. The slip gradient, resulting from the prescribed displacement field, corresponds to the uniform GND density field,

$$\rho_{GND} = -\frac{1}{b}\frac{\partial \gamma}{\partial x_1} = \frac{\kappa}{b}, \tag{1.3}$$

associated with a lattice rotation of $\phi = \kappa x_1$, where b is the magnitude of the Burgers vector. By rejoining the cells in Fig. 1.1c, we see that the dislocations of opposite sign annihilate at the interfaces (or combine to form densities with a zero net Burgers vector and become essentially SSDs), leaving only the dislocations necessary in order to accommodate the slip gradient—the *geometrically necessary dislocations*.

GNDs are often referred to as signed dislocations, in that they essentially represent a population of dislocations which have the same sign and produce a net Burgers vector. In reality SSDs and GNDs are one and the same, however, this distinguishing is useful in the context of small scale plasticity. In the general sense, the SSDs are the main carriers of plastic deformation and their immobilization, due to entanglement or pile-up e.g. at grain boundaries or around second phase particle and precipitates, is the main cause of work

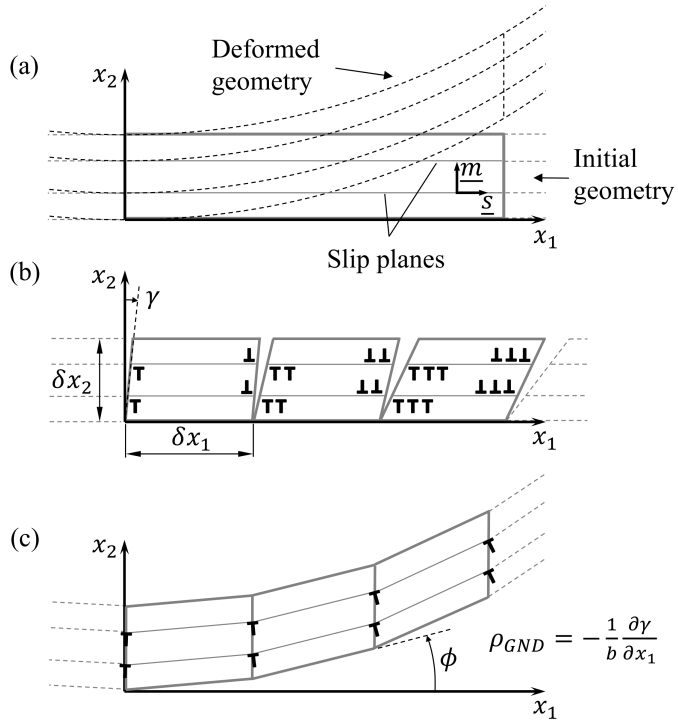

Figure 1.1: Schematic illustration demonstrating the concept of geometrically necessary dislocations (GNDs).

hardening. On a macroscopic level, this behavior is adequately captured by conventional theories. However, when plasticity occurs in geometries at the micron scale and below, strain gradients can entail that GNDs account for a significant portion of the overall lattice defect population and may even far exceed the number of SSDs. Thereby, depending on size, the GNDs can significantly affect the material plastic properties. If a structure or system is dominated by such conditions it is expected that it will behave stronger than a conventional theory would predict and thus it is necessary to incorporate additional gradient terms in the material model to obtain accurate results. This will be discussed in further detail in Chapter 2.

1.2 Micro-structure and motivation of the thesis

It is well known that dislocations arrange themselves in wall and cell structures, within the grains of crystalline materials, during plastic deformation. Bands of high dislocation density (dislocation walls) typically form webs enclosing regions of relatively low dislocation content (cell interiors). Many examples of this behavior can be found in the literature (see e.g. Ananthan et al., 1991; Huang and Winther, 2007; Hong et al., 2013). The movement of dislocations into cell structures or subgrains during plastic deformation is often associated with *dynamic recovery*. The effect of this becomes stronger at elevated temperatures due to the increasing mobility of the dislocations with increasing temperature, and therefore dislocation patterning is especially significant in the deformation of metals

under hot working conditions (Abbaschian et al., 2010). However, it is also seen in metals deformed at very low temperatures, especially in pure metals of high stacking-fault energy. Cell-structures lower the average strain energy associated with the dislocations, and thus the effective rate of work hardening, and are driven by the interaction stresses between the dislocations.

The behavior of dislocations is well documented in the literature, however, recent developments in experimental techniques enables researchers to specifically measure the density of GNDs using electron microscopy, and resolve these measurements to a degree where GND patterning can be observed. The most clear example of this is found in Öztop (2011). In this study, high resolution electron backscatter diffraction (HR-EBSD) measurements were performed on a nickel single crystal, subject to wedge indentation in an approximate two-dimensional plane strain deformation state. Figure 1.2 shows a sample of results from Öztop (2011), exploiting methods of identifying components of the lattice curvature tensor (e.g. Pantleon, 2008). These measurements show highly nonuniform and discontinuous lattice rotations, which are linked directly to the existence of geometrically necessary dislocations (GNDs) through the Nye (1953) tensor, and reveal distinct dislocation wall and cell pattern formation. Details on the experimental techniques employed by Öztop (2011) can also be found in Kysar et al. (2010) and Dahlberg et al. (2014), where similar highly localized GND structures are shown. See also the results of Ruggles et al. (2016), where a different technique is employed to identify the types of dislocations. Some of the theory employed in these studies is treated in Chapter 5 of the thesis.

The observations reported on GND micro-structures are highly relevant in the context of strain gradient plasticity models, since these are all directly or indirectly based on the presence of GNDs. A vast number of numerical studies on the evolution of dislocation structure exist in the literature. Apart form studies based on continuum mechanics (e.g. Yefimov et al., 2004; Klusemann and Yalçinkaya, 2013; van Beers et al., 2013), other studies employ theories of discrete dislocations and molecular dynamics (e.g. Deshpande et al., 2003, 2005; Yaghoobi and Voyiadjis, 2014; Tarleton et al., 2015). The continuum theories have, for many cases, been proven to adequately capture the macroscopic size-

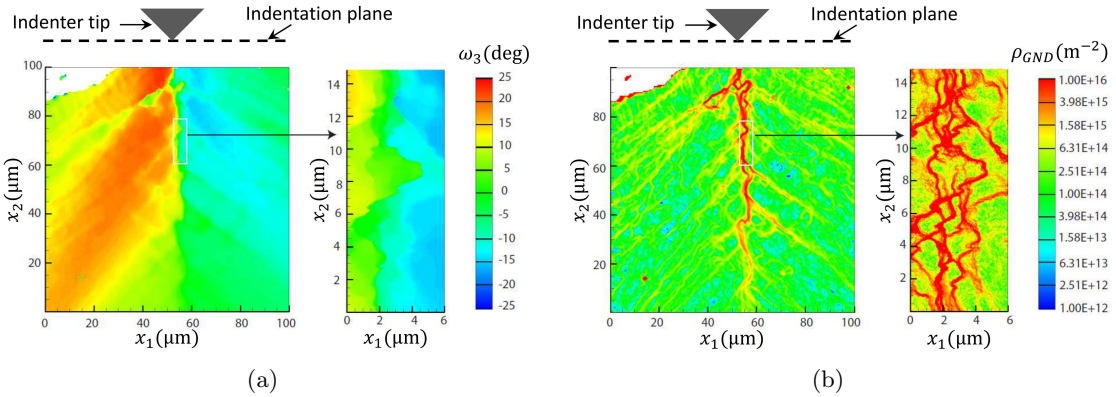

Figure 1.2: Experimental results of Öztop (2011) showing, for a wedge indented nickel single crystal, (a) HR-EBSD measurements of the lattice rotation about the [110] crystallographic direction, and (b) the inferred GND density. Figure courtesy of Prof. J.W. Kysar.

effects discussed in the previous section, however, common for these theories is the tendency to predict a uniform micro-structure, which is not consistent with the experimental observations. Recently, van Beers et al. (2013) studied the grain boundary interface mechanics using a micro-structurally based formulation within the gradient crystal plasticity framework developed by Evers et al. (2004) and Bayley et al. (2006). Here, wall formation type behavior was predicted at the grain boundaries. However, the micro-structural development was characterized by a rather smooth distribution of GNDs, which clearly demonstrates the challenge of representing the highly nonuniform response associated with dislocation wall and cell structures. Traditionally, in strain gradient plasticity models, one can adjust a material length scale parameter to capture size-effects, however, the same single material length parameter also governs the micro-structural behavior of the model. Obviously, this does not necessarily lead to a realistic distribution of GNDs, and since the size-dependence in the macroscopic behavior in real materials is directly tied to the evolution of GND micro-structure, it seems only natural to focus attention on this capability within the models.

Generally, the clustering of dislocations is characterized by sharp and abrupt transitions between cell walls and cell interiors, which, in a continuum context, translates into high spatial gradients of GND density. In the present thesis the numerical predictions of micro-structure will be discussed and from a qualitative point of view, a dislocation cell, is defined by the following two characteristics, within a phenomenological continuum mechanics representation:

i. Dislocation wall: The minor portion of the cell structure, dominated by high GND density and high GND density gradients.

ii. Cell interior: The major portion of the cell structure, dominated by low (several orders of magnitude lower than the walls) to zero GND density and low (approaching zero) GND density gradients.

A theory for predicting realistic micro-structural evolution in plastically deformed crystalline materials, suitable for large scale continuum modeling, has yet to be established. It is clear that many challenges are associated with modeling the discrete and discontinuous nature of dislocation structures, within a framework based on continuum fields, and although the strain gradient plasticity theories are highly motivated by micro-structural considerations, there are clear deficiencies in this regard. However, the challenges of the existing models has been a motivational factor for the studies behind the present thesis, exploring the possibilities of phenomenologically bridging the gap between the macroscopic and microscopic scales. To this end, the formulation of back stress constitutive equations has been the main focus of the present thesis, which is key to expanding the model capabilities in terms of capturing complex material behavior and micro-structural development within the adopted framework.

1.3 Structure of the thesis

The present thesis uses Cartesian tensor notation with Einstein's summation convention, such that recurring indices symbolize summation over the index. Furthermore, spatial derivatives with respect to the Cartesian coordinates are indicated by a subscript comma

preceding the index. Moreover, Greek letter superscripts in parentheses indicate slip systems and subscripts in parentheses indicate dislocation type (edge or screw).

The thesis is structured as follows: Chapter 2 gives a short introduction to strain gradient plasticity and dives into the details of the higher order strain gradient crystal plasticity theory proposed by Kuroda and Tvergaard (2006, 2008), after which the formulation of back stress relations is treated in Chapter 3. In Chapter 4 a series of numerical results are presented and discussed in relation to physical arguments and experimental observations. Chapter 5 describes the experimental considerations of the present work, and finally the thesis is concluded in Chapter 6.

The publications upon which the present thesis is based can be found in the final section appended under Publications for further reading.

Chapter 2

Strain gradient plasticity

Since the first gradient dependent theory appeared some 30 years ago, micro-mechanically based crystal plasticity models have been studied extensively and numerous theories have been proposed to model the experimentally observed size effects. Among the significant contributions are Fleck et al. (1994), Gurtin (2000, 2002), Fleck and Hutchinson (2001),Yefimov et al. (2004), Evers et al. (2004), Bayley et al. (2006), and Fleck and Willis (2009a,b). The theories have been applied to study many plasticity phenomena at small scales. One example, often referred to in the literature, is crack tip plasticity and its influence on the fracture toughness (e.g. Wei and Hutchinson, 1997, 1999; Nielsen et al., 2012; Martínez-Pañeda and Niordson, 2015). The field remains highly active and some of the more recent contributions include Hutchinson (2012); van Beers et al. (2013); Klusemann and Yalçinkaya (2013); Niordson and Kysar (2014); Fleck et al. (2015). Within the class of continuum models both so-called lower order theories (e.g Bassani, 2001; Huang et al., 2004), for which unexpected strain localization behavior was pointed out by Niordson and Hutchinson (2003), and higher order theories have emerged. Nowadays it is generally accepted that higher order theories offer important modeling capabilities. Unlike the lower order theories, the higher order theories incorporate micro-structural boundary conditions, which enter either through an extended virtual work principle or through additional partial differential equations.

The importance of this capability was illustrated experimentally by Kraft et al. (2000) in uniaxial testing of polycrystalline copper films (0.4 μm to 1.5 μm thickness) deposited onto polymer substrates. The substrates functioned as micro-structural passivation layers, obstructing the dislocations from exiting the material, which in turn results in dislocation pile up at the boundary causing long range internal stresses. The samples with passivation layers were significantly stronger than regular free-standing samples. Similar results were found by Xiang and Vlassak (2016) for bulge testing of 0.6 μm Cu and 1 μm Al films deposited onto silicon wafers. Again, when compared to the load curves of free-standing film samples, the flow stress was found to be significantly higher for the samples with passivated surfaces. Higher order theories can model this particular type of material behavior through the application of micro-structural boundary conditions, enforcing constraints on plastic strain, or enforcing so-called microscopic hard boundaries, whereas the conventional theories predict uniform strain for such a structure.

Different families of higher order strain gradient plasticity theories have evolved, and these can be categorized into two branches: Work conjugate theories and Non-work con-

jugate theories. The work conjugate formulations (e.g. Gurtin, 2002) make use of higher-order stress concepts as work conjugates to the strain/slip gradients in higher order power balance equations, whereas the non-work conjugate theories often employ a coupling between the conventional governing equations and additional equations of higher order nature. The present study employs the non-work conjugate type theory proposed by Kuroda and Tvergaard (2006, 2008), which is a higher order extension of conventional crystal plasticity theory. In this type of theory the virtual work principle remains the conventional one, while the evolution of GND densities is accounted for through additional differential equations. Here, a back stress, representing the long range internal stresses due to pile-up of GNDs, affects the plastic slip rate as kinematic hardening.

2.1 The Kuroda & Tvergaard gradient plasticity theoretical framework

The present study employs a small strain formulation, with the total strain rate given by; $\dot{\varepsilon}_{ij} = \left(\dot{u}_{i,j} + \dot{u}_{j,i}\right)/2$, which decomposes into an elastic part, $\dot{\varepsilon}^e_{ij}$, and a plastic part, $\dot{\varepsilon}^p_{ij}$, so that; $\dot{\varepsilon}_{ij} = \dot{\varepsilon}^e_{ij} + \dot{\varepsilon}^p_{ij}$. The formulation builds on the framework of conventional crystal visco-plasticity theory, where plastic deformation occurs by means of crystallographic slip on the individual slip systems. Thus, the plastic strain rate is given in terms of the slip rate, $\dot{\gamma}$, on the α'th slip system, as

$$\dot{\varepsilon}^p_{ij} = \sum_\alpha \dot{\gamma}^{(\alpha)} P^{(\alpha)}_{ij}, \quad P^{(\alpha)}_{ij} = \frac{1}{2}\left(s^{(\alpha)}_i m^{(\alpha)}_j + m^{(\alpha)}_i s^{(\alpha)}_j\right), \tag{2.1}$$

where the superposed dot denotes material time derivative, $P^{(\alpha)}_{ij}$ is the Schmid orientation tensor, and $s^{(\alpha)}_i$ and $m^{(\alpha)}_i$ are unit vectors specifying the slip direction and slip plane normal, respectively (see Fig. 2.1). The slip rate is given by

$$\dot{\gamma}^{(\alpha)} = \dot{\gamma}_0 \mathrm{sgn}\left(\tau^{(\alpha)} - \tau^{(\alpha)}_b\right)\left(\frac{|\tau^{(\alpha)} - \tau^{(\alpha)}_b|}{g^{(\alpha)}}\right)^{1/m}, \tag{2.2}$$

where $\dot{\gamma}_0$ is a reference slip rate, $\tau^{(\alpha)}$ is the Schmid stress (taken as the macroscopic Cauchy stress tensor resolved onto the slip plane), $\tau^{(\alpha)}_b$ is a back stress, m is the rate sensitivity exponent, and $g^{(\alpha)}$ is the slip resistance, taken to follow the hardening law

$$\dot{g}^{(\alpha)} = \sum_\beta h^{(\alpha\beta)} |\dot{\gamma}^{(\beta)}|, \quad g^{(\alpha)}|_{t=0} = \tau_0, \tag{2.3}$$

where the initial value of $g^{(\alpha)}$ is set to the initial critical resolved shear stress τ_0. Here, t is time and $h^{(\alpha\beta)}$ are slip hardening moduli, in which the trace accounts for self hardening, and the off-diagonal parts for latent hardening. Equation (2.2) is a gradient-enhanced version of the widely used conventional visco-plastic power law slip rate relation (Hutchinson, 1976; Peirce et al., 1983), in that $\tau^{(\alpha)} - \tau^{(\alpha)}_b$ replaces $\tau^{(\alpha)}$ as an effective resolved shear stress[1]. The back stress, $\tau^{(\alpha)}_b$, is related directly to the GND micro-structure (see Chapter

[1] Note that for $\tau^{(\alpha)}_b$ equal to zero, Eq. (2.2) reduces to the conventional theory.

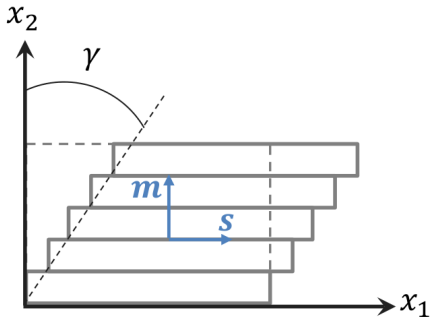

Figure 2.1: Schematic of the concept of crystallographic slip (Deck of cards analogy).

3), and impedes (or aids, depending on load path) slip at nonuniform pile-ups of GNDs. Thereby, the effective resolved shear stress becomes the driving force behind dislocation glide (Harder, 1999; Groma et al., 2003; Yefimov et al., 2004; Evers et al., 2004).

The theory, formulated by Kuroda and Tvergaard (2006, 2008), is of a higher order nature but does not directly employ higher order stresses as work conjugates to plastic strains and their spatial derivatives, and thus, there is no direct incentive for higher order power balance equations. Instead, the governing equations of the non-work conjugate formulation, are given by the conventional stress equilibrium equation; $\sigma_{ij,j} + f_i = 0$, where f_i are body forces and the Cauchy stress rate tensor is given by the Linear elastic relationship; $\dot{\sigma}_{ij} = \mathscr{L}_{ijkl}\left(\dot{\varepsilon}_{kl} - \dot{\varepsilon}^p_{kl}\right)$, in which $\mathscr{L}_{ijkl}$ is the fourth order elastic stiffness tensor. Thereby, the conventional rate-dependent incremental principle of virtual work yields the weak form of the velocity field equation:

$$\int_V \dot{\sigma}_{ij}\delta\dot{\varepsilon}_{ij}\mathrm{d}V = \int_V \dot{f}_i\delta\dot{u}_i\mathrm{d}V + \int_S \dot{T}_i\delta\dot{u}_i\mathrm{d}S, \quad \dot{T}_i \equiv \dot{\sigma}_{ij}n_j, \tag{2.4}$$

where $\dot{T}_i$ is the traction rate, n_i is the outward unit normal to the surface S bounding the volume V. Equation (2.4) is rewritten according to the above stress relation and strain decomposition as

$$\int_V \mathscr{L}_{ijkl}\dot{\varepsilon}_{kl}\delta\dot{\varepsilon}_{ij}\mathrm{d}V = \int_V \mathscr{L}_{ijkl}\dot{\varepsilon}^p_{kl}\delta\dot{\varepsilon}_{ij}\mathrm{d}V + \int_V \dot{f}_i\delta\dot{u}_i\mathrm{d}V + \int_S \dot{T}_i\delta\dot{u}_i\mathrm{d}S, \tag{2.5}$$

The evolution of GND density, in balance with the slip gradients, is accounted for by an additional set of partial differential equations:

$$\frac{1}{b}\gamma^{(\alpha)}_{,i}s^{(\alpha)}_i + \rho^{(\alpha)}_{G(e)} = 0 \tag{2.6a}$$

$$\frac{1}{b}\gamma^{(\alpha)}_{,i}p^{(\alpha)}_i + \rho^{(\alpha)}_{G(s)} = 0, \tag{2.6b}$$

where $\mathbf{p}^{(\alpha)} = \mathbf{s}^{(\alpha)} \times \mathbf{m}^{(\alpha)}$, b is the magnitude of the Burgers vector, and $\rho^{(\alpha)}_G$ are GND densities on slip system α (Ashby, 1970). Subscripts (e) and (s) denote edge and screw components, respectively. The GND densities appear directly as free field variables in Eqs. (2.6a) and (2.6b), and their weak form are obtained by integrating over the volume and

applying the divergence theorem, so that

$$\frac{1}{b}\int_V \delta\rho_{,i} s_i^{(\alpha)} \gamma^{(\alpha)} \mathrm{d}V = \frac{1}{b}\int_S \delta\rho \zeta^{(\alpha)} \mathrm{d}S + \int_V \delta\rho \rho_{G(e)}^{(\alpha)} \mathrm{d}V, \qquad \zeta^{(\alpha)} \equiv \gamma^{(\alpha)} n_i s_i^{(\alpha)}, \tag{2.7a}$$

$$\frac{1}{b}\int_V \delta\rho_{,i} p_i^{(\alpha)} \gamma^{(\alpha)} \mathrm{d}V = \frac{1}{b}\int_S \delta\rho \eta^{(\alpha)} \mathrm{d}S + \int_V \delta\rho \rho_{G(s)}^{(\alpha)} \mathrm{d}V, \qquad \eta^{(\alpha)} \equiv \gamma^{(\alpha)} n_i p_i^{(\alpha)}, \tag{2.7b}$$

where $\delta\rho$ is a virtual GND density. Thereby, the higher order crystal plasticity framework is completed, once an appropriate constitutive relation for the back stress, $\tau_b^{(\alpha)}$, has been formulated. There are several approaches to formulating the back stress, some are physics based, while others are more phenomenological in nature. The present higher order theory is a sound platform for an investigation, where back stress constitutive relations may even be formulated in a direct phenomenological manner, and at first glance, without restrictions from thermodynamics. The formulation of back stress equations is covered in Chapter3.

2.2 Higher order boundary conditions

The higher order boundary conditions are central to scale dependent theories. In the Kuroda and Tvergaard (2006, 2008) framework, there are essentially two types of higher order boundary conditions which can be applied: (i) enforcing zero plastic flow (microscopic hard boundary) or (ii) enforcing zero GND density (microscopic free boundary). However, it is also possible to model an intermediate higher order boundary condition (a so-called micro-flexible boundary), which may be more realistic for some applications (see e.g. Ekh et al., 2011), but the present thesis does not go into further detail about this approach. Boundary conditions of type (i) models the case where the dislocations are unable to penetrate to the surface and relieve the internal stresses, resulting in dislocation pile-up. In the GND density equations (2.7), a hard interface impenetrable for dislocations is enforced by

$$\zeta^{(\alpha)} \equiv \gamma^{(\alpha)} n_i s_i^{(\alpha)} = 0 \tag{2.8a}$$

$$\eta^{(\alpha)} \equiv \gamma^{(\alpha)} n_i p_i^{(\alpha)} = 0. \tag{2.8b}$$

The possibilities for type (i) conditions are as follows:

- In the case of $n_i s_i^{(\alpha)} = 0$ and $n_i p_i^{(\alpha)} = 0$, slip can occur without constraints.
- In the case of $n_i s_i^{(\alpha)} = 0$ and $n_i p_i^{(\alpha)} \neq 0$, a constraint on plastic flow at the boundary is imposed, with $\rho_{G(e)}^{(\alpha)} = 0$ automatically.
- In the case of $n_i s_i^{(\alpha)} \neq 0$ and $n_i p_i^{(\alpha)} = 0$, a constraint on plastic flow at the boundary is imposed, with $\rho_{G(s)}^{(\alpha)} = 0$ automatically.
- $n_i s_i^{(\alpha)} \neq 0$ and $n_i p_i^{(\alpha)} \neq 0$, results in a constraint on plastic flow at the boundary, and pile-up of both edge and screw dislocations can occur.

Boundary condition of type (ii) models the case of a surface where dislocations can exit the material body and vanish. This condition corresponds to enforcing

$$\rho^{(\alpha)}_{G(e)} = \rho^{(\alpha)}_{G(s)} = 0, \tag{2.9}$$

in Eqs. 2.7a and 2.7b, respectively. From a physical point of view, this boundary condition is only valid for edge dislocations when $n_i s_i^{(\alpha)} \neq 0$ and for screw dislocations when $n_i p_i^{(\alpha)} \neq 0$. For a further discussion on the micro-structural boundary conditions see Kuroda and Tvergaard (2008).

2.3 Numerical implementation

The results presented in Chapter 4 of the present thesis, are based on a numerical implementation employing the finite element method (FEM). The finite element equations and details of the solution scheme are provided in the following. As discussed in Section 2.1, the Kuroda and Tvergaard (2006, 2008) framework builds on classical crystal visco-plasticity, while additional GND density evolution equations account for the higher order contributions. These two sets of equation systems are solved separately in a staggered solution scheme, where back stresses are evaluated based on the solved GND density fields, which in turn affect the slip rates as kinematic hardening. Employing a small strain formulation, the finite element equation corresponding to the weak form velocity field equation (2.5) reads

$$\int_V [B]^T [\mathscr{C}] [B] \{\dot{u}\} \mathrm{d}V = \int_V [B]^T [\mathscr{C}] [\dot{\varepsilon}^p] \, \mathrm{d}V + \int_V [N]^T \{\dot{f}\} \mathrm{d}V + \int_S [N]^T \{\dot{T}\} \mathrm{d}S. \tag{2.10}$$

where $[N]$ are standard finite element shape functions and $[B]$ contains the spatial derivatives of each component of $[N]$ and $[\mathscr{C}]$ is the stiffness matrix. For the finite element solution, the GND densities are chosen as nodal degrees of freedom, so that

$$\rho^{(\alpha)}_{G(e)} = [N] \, \rho^{(\alpha)}_{G(e)} \tag{2.11a}$$

$$\rho^{(\alpha)}_{G(s)} = [N] \, \rho^{(\alpha)}_{G(s)}. \tag{2.11b}$$

Finite element equations are derived by substituting these into Eqs. (2.7a) and (2.7b), such that

$$\int_V [N]^T [N] \, \mathrm{d}V \{\rho^{(\alpha)}_{G(e)}\} = \int_V [B]^T \{s^{(\alpha)}\} \gamma^{(\alpha)} \mathrm{d}V + \int_S [N]^T \zeta^{(\alpha)} \mathrm{d}S \tag{2.12a}$$

$$\int_V [N]^T [N] \, \mathrm{d}V \{\rho^{(\alpha)}_{G(s)}\} = \int_V [B]^T \{p^{(\alpha)}\} \gamma^{(\alpha)} \mathrm{d}V + \int_S [N]^T \eta^{(\alpha)} \mathrm{d}S, \tag{2.12b}$$

where $\{s^{(\alpha)}\}$ and $\{p^{(\alpha)}\}$ contain Cartesian components of $s_i^{(\alpha)}$ and $p_i^{(\beta)}$, respectively.

For all numerical computations, presented in the present thesis, Eight-node isoparametric quadrilateral elements with reduced Gauss integration are used for the displacement field analysis, whereas equivalent four-node elements with full Gauss integration are used for the GND density field analysis and time integration is performed by the forward Euler method.

Chapter 3

Back stress

The micro-structural behavior is of particular interest in the present study, where the non-work conjugate type formulation, proposed by Kuroda and Tvergaard (2006, 2008), is adopted. In this continuum theory, a back stress, related to the micro-structure, accounts for the gradient effects in the plastic behavior, and the mathematical form of such a back stress is still a rather open matter. However, back stress models can, for the most part, be classified into two types: (i) The physically based models, which build on considerations of the stress field of a single dislocation (e.g. Groma et al., 2003; Yefimov et al., 2004), and (ii) the more phenomenologically based models, which either build on a postulated strain gradient energy relation (e.g. Kuroda and Tvergaard, 2008; Öztop et al., 2012; Bargmann et al., 2016) or may be formulated directly to possess certain constitutive properties as in (El-Naaman et al., 2016c, [P2]).

3.1 Gradient energy approach

In the gradient visco-plasticity theory proposed by Kuroda and Tvergaard (2006, 2008), which is adopted in the present study, the back stress, τ_b, was originally assumed to be proportional to the first gradients of the GND densities. One possible framework that can be applied to this higher order theory builds on the theory of Gurtin (2000, 2002), in which an extended virtual power principle is introduced, asserting additional work contributions associated with slip and slip gradients, given by

$$\begin{aligned} &\int_V \left[\sigma_{ij} \delta \dot{\varepsilon}^e_{ij} + \sum_\alpha \left(\tau^{(\alpha)}_{eff} \delta \dot{\gamma}^{(\alpha)} + \xi^{(\alpha)}_i \delta \dot{\gamma}^{(\alpha)}_{,i} \right) \right] \mathrm{d}V \\ &= \int_V f_i \delta \dot{u}_i \mathrm{d}V + \int_S T_i \delta \dot{u}_i \mathrm{d}S + \sum_\alpha \int_S \Theta^{(\alpha)} \tilde{\nu}^{(\alpha)} \mathrm{d}S, \end{aligned} \tag{3.1}$$

where $\tau^{(\alpha)}_{eff} = \tau^{(\alpha)} - \tau^{(\alpha)}_b$ is the effective resolved shear stress, $\xi^{(\alpha)}_i$ is a higher order stress quantity, and $\Theta^{(\alpha)}$ is a micro-traction. For $\delta \dot{u}_i = 0$, i.e. no macroscopic work done and $\delta \dot{\varepsilon}^e_{ij} = -\sum_\alpha \delta \dot{\gamma}^{(\alpha)} P^{(\alpha)}_{ij}$, Eq. (3.1) reduces to the microscopic power balance equation

$$\sum_\alpha \int_V \left[\left(\tau^{(\alpha)}_{eff} - \tau^{(\alpha)} \right) \delta \dot{\gamma}^{(\alpha)} + \xi^{(\alpha)}_i \delta \dot{\gamma}^{(\alpha)}_{,i} \right] \mathrm{d}V = \sum_\alpha \int_S \Theta^{(\alpha)} \delta \dot{\gamma}^{(\alpha)} \mathrm{d}S. \tag{3.2}$$

Variational arguments and application of Gauss's divergence theorem yield the micro-traction condition, $\Theta^{(\alpha)} = \xi_i^{(\alpha)} n_i$, and the micro-force balance equation

$$\xi_{i,i}^{(\alpha)} + \tau^{(\alpha)} - \tau_{eff}^{(\alpha)} = 0. \tag{3.3}$$

Thereby, within the framework of Gurtin, we can write the back stress as the divergence of the vector-valued higher order stress

$$\tau_b^{(\alpha)} \equiv -\xi_{i,i}^{(\alpha)}. \tag{3.4}$$

Through thermodynamic restrictions on the free energy, assumed to be given by the elastic strain energy augmented by a gradient energy, $\psi_G^{(\alpha)}$, as

$$\Psi = \frac{1}{2}\mathscr{L}_{ijkl}\varepsilon_{kl}^e\varepsilon_{ij}^e + \sum_\alpha \psi_G^{(\alpha)}, \tag{3.5}$$

the framework of Gurtin provides the constitutive equation for the higher order stress, which reads

$$\xi_i^{(\alpha)} = \frac{\partial \psi_G^{(\alpha)}}{\partial \gamma_{,i}^{(\alpha)}}. \tag{3.6}$$

$\psi_G^{(\alpha)}$ may also be referred to as the defect energy. It was shown by Kuroda and Tvergaard (2008), that by adopting this interpretation of the relation between defect energy, higher order stress, and back stress, their theory corresponds to the work conjugate theory of Gurtin (2000, 2002), and it is effectively recast in a work conjugate form. Consequently, upon assuming a continuous differentiable relation for the gradient energy, the framework is completed in a thermodynamically consistent manner.

The gradient energy is often assumed to have the quadratic form (see e.g. Kuroda and Tvergaard, 2006, 2008; Anand et al., 2012; Klusemann and Yalçinkaya, 2013; Niordson and Kysar, 2014)

$$\psi_G^{(\alpha)} = \frac{1}{2}\tau_0 L^2 \left(\gamma_{,i}^{(\alpha)} s_i^{(\alpha)}\right)^2, \tag{3.7}$$

where L is a material length scale parameter, entering for dimensional consistency. This length parameter has no direct physical interpretation, but it is clear that many intrinsic length scales are present in materials, e.g. the mean free path of moving dislocations, and L may be related to such length scales. However, these physical length scales may evolve with plastic deformation, while L is often assumed to be a constant for simplicity. The above form of the gradient energy is chosen primarily for mathematical convenience rather than based on physical arguments and, through Eqs. (3.4) and (3.6), it leads to the following back stress relation, depending on the second order gradients of slip

$$\tau_b^{(\alpha)} = -\tau_0 L^2 \gamma_{,ij}^{(\alpha)} s_i^{(\alpha)} s_j^{(\alpha)}, \tag{3.8}$$

which, expressed in terms of GND densities, becomes

$$\tau_b^{(\alpha)} = b\tau_0 L^2 \rho_{G(e),i}^{(\alpha)} s_i^{(\alpha)}. \tag{3.9}$$

While this theory captures size effects in strain gradient hardening well, it cannot realistically capture the highly non-uniform dislocation structures observed in experimental

studies of e.g. wedge indentation (Kysar et al., 2010; Öztop, 2011; Dahlberg et al., 2014). Numerical results obtained using Eq. (3.9) are presented in Chapter 4.

It is possible to achieve increasingly non-uniform GND density distributions, by decreasing L to suppress the back stress effect, however, decreasing L until a satisfactory micro-structure is achieved clearly does not guarantee the proper size-dependence in the hardening behavior and vice versa. Thus, in general one must assume that more than one constitutive parameter is needed for a model describing both size-effects and evolution of micro-structure.

In the following, alternative options for the back stress formulation will be explored in order to pursue a GND field response closer to experimental observations. There are arguments pointing toward a gradient energy which is closer to linear rather than quadratic (Evans and Hutchinson, 2009). A free energy potential linear in the slip gradients was investigated by Ohno and Okumara (2007) and Forest and Guéninchault (2013). Here, a generalization from the quadratic form of the gradient energy in Eq. (3.7), shall serve as basis for the following analysis. Assuming power law dependence on the slip gradients, one could write the gradient energy as

$$\psi_G^{(\alpha)} = \frac{1}{\mu+1}\tau_0 L^{\mu+1}\left|\gamma_{,i}^{(\alpha)} s_i^{(\alpha)}\right|^{\mu+1}. \tag{3.10}$$

A similar energy relation was proposed by Fredriksson and Gudmundson (2007) for interface modeling, where a near linear to quadratic dependence on the plastic strain was investigated. For a linear dependence on the plastic strain, their theory conforms with the dislocation based theory of Read and Shockley (1950) for low angle tilt boundaries. Recently, Bardella (2010), Bardella and Panteghini (2015), and Fleck et al. (2015) also proposed expressions for the free energy similar to Eq. (3.10). The generalized energy expression (Eq. (3.10)) leads to a back stress which is still a linear function of the second order gradients of slip (as Eq. (3.9)), but in turn reveals a dependence on the first order gradients of slip (or the GND densities), to the power of $\mu - 1$ (El-Naaman et al., 2016c, [P2]):

$$\tau_b^{(\alpha)} = -\mu\tau_0 L^{\mu+1}\left|\gamma_{,j}^{(\alpha)} s_j^{(\alpha)}\right|^{\mu-1}\gamma_{,ki}^{(\alpha)} s_i^{(\alpha)} s_k^{(\alpha)}, \tag{3.11}$$

which, expressed in terms of GND densities, becomes

$$\tau_b^{(\alpha)} = \mu\tau_0 b^{\mu} L^{\mu+1}\left|\rho_{G(e)}^{(\alpha)}\right|^{\mu-1}\rho_{G(e),i}^{(\alpha)} s_i^{(\alpha)}. \tag{3.12}$$

For $\mu = 1$, Eq. (3.10) is quadratic and Eqs. (3.11) and (3.12) reduce to Eqs. (3.8) and (3.9), respectively. The effect of μ is schematically illustrated in Fig. 3.1. In the studies by Groma et al. (2003) and Yefimov et al. (2004) on a single slip continuum description of dislocation dynamics, a back stress relation similar to Eq. (3.12) for $\mu \to 0$ was found, based on the shear stress field of a single dislocation. In fact, the functional dependence on dislocation densities in Yefimov et al. (2004) is identical to Eq. (3.12), if no distinction is made between the so-called total and signed dislocation densities (see Yefimov et al. (2004) Eq. 13). Equations (3.11) and (3.12) maintain thermodynamic consistency through Eq. (3.4), while, in the wording of Kuroda and Tvergaard (2006), they have a non-constant back stress coefficient, which evolves with the GND density for $\mu \neq 1$.

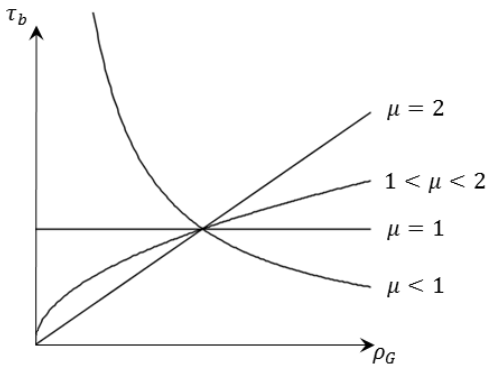

Figure 3.1: Schematic illustration of the generalized gradient energy based back stress law (Eq. (3.12)).

For $\mu < 1$, the back stress in Eq. (3.12) is singular when the GND density goes to zero, and thus, an "effective" GND density is employed, such that $\rho^{(\alpha)}_{G(e),eff} = |\rho^{(\alpha)}_{G(e)}| + \rho_0$ replaces $|\rho^{(\alpha)}_{G(e)}|$ in Eq. (3.12), for values of μ below one. This is a numerical trick which is necessary, in order to facilitate a numerical solution at low GND densities, but it resembles the presence of SSDs in the back stress relations of e.g. Groma et al. (2003) and Yefimov et al. (2004).

Evers et al. (2004) argue that the GND density itself does not contribute to the long range internal stresses (i.e. the back stress). However, this is not the case in Eq. (3.12), where a strong dependence on the GND density is seen. The present thesis does not attempt to advocate any physical advantages of the dependence on GND density, however, it is noted that a uniform GND field yields zero back stress in accordance with the arguments put forth by Evers et al. (2004).

The proposed back stress formulation is investigated numerically in Chapter 4.

3.2 Phenomenological approach

When $\mu \to 0$ or $\mu \to 2$ in the back stress relation in Eqs. (3.11) and (3.12), slip localization is promoted through its relationship with the GND density, enabling GND wall formation at the hard boundaries (see numerical results in Chapter 4). This type of behavior can also be obtained through the relationship between the back stress and the GND density gradients, since a GND wall is also tied to high levels of GND density gradients (El-Naaman et al., 2015, 2016c, [P1],[P2]). In the framework proposed by Kuroda and Tvergaard (2006, 2008) any function $\tau_b^{(\alpha)}(\rho^{(\alpha)}_{G(e),i} s_i^{(\alpha)})$ may be considered. Thus, one could assume the following power law proportionality for the back stress relation:

$$\tau_b^{(\alpha)} \propto \left| \rho^{(\alpha)}_{G(e),i} s_i^{(\alpha)} \right|^{\kappa}, \quad 0 \leq \kappa \leq 1. \tag{3.13}$$

For values of κ below one, this type of relation allows the slip to build up more severely with less restriction imposed by the back stress as the GND density gradients evolve. In order to investigate the influence of $|\rho^{(\alpha)}_{G(e),i} s_i^{(\alpha)}|^{\kappa}$ in the back stress formulation, the quadratic

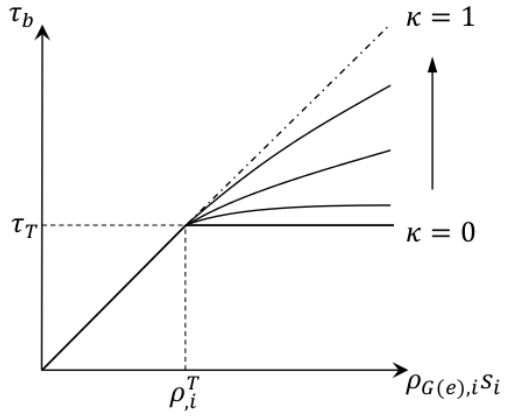

Figure 3.2: Schematic illustration of the back stress power law (Eq. 3.14).

gradient energy based back stress is taken as starting point in a piece-wise function such that

$$\tau_b^{(\alpha)} = \begin{cases} b\tau_0 L^2 \rho_{G(e),i}^{(\alpha)} s_i^{(\alpha)} & , \text{ for } |\tau_b^{(\alpha)}| \leq \tau_T \\ \text{sgn}\left(\rho_{G(e),i}^{(\alpha)} s_i^{(\alpha)}\right) b^\kappa \tau_T^{1-\kappa} \tau_0^\kappa L^{2\kappa} \left|\rho_{G(e),i}^{(\alpha)} s_i^{(\alpha)}\right|^\kappa & , \text{ for } |\tau_b^{(\alpha)}| > \tau_T \end{cases}. \tag{3.14}$$

with τ_T being a transition back stress parameter. When κ is equal to one, Eq. (3.14) reduces to the expression in Eq. (3.9), i.e., corresponding to a quadratic gradient energy. With κ equal to zero, Eq. (3.14) corresponds to a blunt cut-off of the back stress at $\tau_b^{(\alpha)} = \tau_T$. A schematic representation of this back stress relation can be found in Fig. 3.2. This set-up allows for the back stress to build up linearly with the gradients of GND density, corresponding to a quadratic free energy, until a preassigned level ($|\tau_b^{(\alpha)}| = \tau_T$), after which it subsides according to the power law (for $0 \leq \kappa \leq 1$). The two formulations (Eqs. (3.12) and (3.14)) coincide for μ and κ equal to one (quadratic gradient energy), for which the back stress in Eq. (3.14) naturally provides a thermodynamically consistent theory. However, since a gradient energy relation that leads to Eq. (3.14) is not readily available, this back stress formulation must be considered a non-thermodynamically consistent formulation. However, for the majority of the numerical solutions which will be presented in Chapter 4 of the present thesis, it was checked that positive dissipation was satisfied throughout the load history, such that

$$\sigma_{ij}\dot{\varepsilon}_{ij}^p = \sum_\alpha \tau^{(\alpha)}\dot{\gamma}^{(\alpha)} \geq 0. \tag{3.15}$$

3.3 Effective framework for plane strain deformation in FCC crystals

In face centered cubic (FCC) crystals, a total of twelve individual slip systems exist, and plastic deformation occurs by slip on a combination of these slip systems. Here, we consider plane strain deformation in the (110) plane in an FCC crystal, which is assumed infinite in the [110] direction. This implies that equal amounts of slip occurs on three pairs of slip

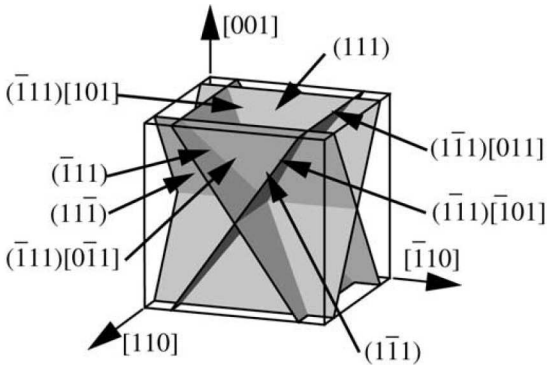

Figure 3.3: The {111} crystallographic planes in a FCC crystal. The wire frame illustrates the outer surface of the crystal which is rotated 45° about the [001] direction relative to the FCC unit cell. The figure is copied from Kysar et al. (2005).

systems which are symmetric about the (110) plane and that together each pair combine to form one effective in-plane slip system (Rice, 1987; Kysar et al., 2005). In Fig. 3.3 (from Kysar et al. (2005)) the family of (111) planes can be seen shaded in gray, and the wire frame can be viewed as a representation of the considered crystal which is rotated 45° about the [001] axis relative to the FCC unit cell. Here it is seen that the in-plane slip system (1) is formed by pairing slip systems $(1\bar{1}1)[\bar{1}01]$ and $(1\bar{1}1)[011]$, resulting in the effective slip system $(1\bar{1}1)[\bar{1}12]$, in-plane slip system (3) is formed by pairing slip systems $(\bar{1}11)[101]$ and $(\bar{1}11)[0\bar{1}1]$, resulting in the effective slip system $(\bar{1}11)[1\bar{1}2]$, and in-plane slip system (2) is formed by pairing slip systems $(111)[\bar{1}10]$ and $(11\bar{1})[\bar{1}10]$, resulting in the effective slip system $(001)[\bar{1}10]$. In order for the effective 2D FCC crystal to correspond to plane strain deformation in the true FCC crystal structure, the plastic properties which enter into the slip rate relation (Eq. (2.2)) and back stress relations (Eqs. (3.12) and (3.14)), must be scaled in an appropriate manner, assuming that these quantities refer to the true FCC crystal. This is done by the following relations for the reference slip rate and critical resolved shear stress (Niordson and Kysar, 2014; Rice, 1987):

$$\dot{\gamma}_0^{(\alpha)} = \beta^{(\alpha)}\dot{\gamma}_0, \tag{3.16}$$

$$\tau_0^{(\alpha)} = \lambda^{(\alpha)}\tau_0, \tag{3.17}$$

with $\lambda^{(\alpha)} = 2/\beta^{(\alpha)}$. Moreover, since dislocations of both edge and screw type may exist on the three dimensional crystallographic slip systems, these can both contribute to the gradient energy. Thus, assuming a unified material length scale parameter, L, for both edge and screw components, we rewrite Eq. (3.10) as a function of the Euclidean norm of the edge and screw densities (e.g. Gurtin et al., 2007) so that

$$\psi_G^{(\alpha a)} = \frac{1}{\mu+1}\tau_0 L^{\mu+1}\left\{\sqrt{\left(\gamma_{,i}^{(\alpha a)}s_i^{(\alpha a)}\right)^2 + \left(\gamma_{,i}^{(\alpha a)}p_i^{(\alpha a)}\right)^2}\right\}^{\mu+1}. \tag{3.18}$$

The back stress relation that results from this choice of gradient energy can be found in Appendix A. For simplicity, Eq. (3.18) is not based on an invariant of the Nye tensor, and thus, the interaction between slip systems is omitted, except for screw dislocations on the

pair of slip systems that constitute the second effective slip system, as will be discussed in the following. Equation (3.18) can be written in terms of effective quantities as

$$\psi_G^{(\alpha a)} = \frac{1}{\mu+1}\tau_0 L^{\mu+1}\frac{1}{(\beta^{(\alpha)})^{\mu+1}}\left\{\sqrt{\left(\omega^{(\alpha)}\gamma_{,i}^{(\alpha)}s_i^{(\alpha)}\right)^2+\left(\chi^{(\alpha)}\gamma_{,i}^{(\alpha)}\mathscr{P}_i^{(\alpha)}\right)^2}\right\}^{\mu+1}, \tag{3.19}$$

with

$$\mathscr{P}_i^{(\alpha)} = \begin{cases} s_i^{(\alpha)} & , \text{ for } \alpha = 1 \text{ or } 3 \\ m_i^{(\alpha)} & , \text{ for } \alpha = 2 \end{cases}, \tag{3.20}$$

given that $\gamma_{,3}^{(\alpha)} = 0$. $\mathscr{P}_i^{(\alpha)}$ is the unit vector that represents the direction of $p_i^{(\alpha a)}$ and $p_i^{(\alpha b)}$ projected onto the (110) plane. The scaling coefficients, $\omega^{(\alpha)}$ and $\chi^{(\alpha)}$, are the lengths of the projections of the vectors $s_i^{(\alpha a)}$ and $p_i^{(\alpha a)}$, respectively, onto the plane (110). Their values can be found in Table 3.1. However, for plane strain deformation of FCC crystals in the (110) plane, the symmetric activity of screw dislocations on each of the crystallographic slip systems of the pair that forms effective slip system 2, cancel each other out or annihilate (the projections of $p_i^{(\alpha a)}$ and $p_i^{(\alpha b)}$ are opposite). These can therefore be considered as effective SSDs, which do not contribute to the long range internal stresses. This can be seen through the Nye (1953) tensor. The only nonzero components of the Nye tensor for plane strain deformation in this crystal configuration are $\mathscr{G}_{12}$ and $\mathscr{G}_{13}$ (Kysar et al., 2007), which do not include contributions from screw density (the Nye tensor is discussed in detail in Section 5.4). Therefore, it is chosen that $\chi^{(2)} = 0$. From a physical point of view, this "annihilation" can be facilitated by cross-slip of the screw dislocations. Moreover, since $\omega^{(2)} = 1$ and $\sqrt{(\omega^{(1)})^2+(\chi^{(1)})^2} = \sqrt{(\omega^{(3)})^2+(\chi^{(3)})^2} = 1$, Eq. (3.19), written in terms of GND density, reduces to

$$\psi_G^{(\alpha a)} = \frac{1}{\mu+1}\tau_0 L^{\mu+1}\frac{1}{(\beta^{(\alpha)})^{\mu+1}}\left|\rho_{G(e),i}^{(\alpha)}\right|^{\mu+1}, \tag{3.21}$$

which gives the following back stress on the (αa)'th crystallographic slip system:

$$\tau_b^{(\alpha a)} = \mu\tau_0 b^\mu L^{\mu+1}\frac{1}{(\beta^{(\alpha)})^{\mu+1}}\left|\rho_{G(e)}^{(\alpha)}\right|^{\mu-1}\rho_{G(e),i}^{(\alpha)}s_i^{(\alpha)}. \tag{3.22}$$

The total back stress on the (α)'th effective slip system is then given by

$$\tau_b^{(\alpha)} = \lambda^{(\alpha)}\tau_b^{(\alpha a)} = \lambda^{(\alpha)}\tau_b^{(\alpha b)} = \mu\tau_0 b^\mu L^{\mu+1}\frac{\lambda^{(\alpha)}}{(\beta^{(\alpha)})^{\mu+1}}\left|\rho_{G(e)}^{(\alpha)}\right|^{\mu-1}\rho_{G(e),i}^{(\alpha)}s_i^{(\alpha)}. \tag{3.23}$$

Similarly, we can write Eq. (3.14) for the effective FCC crystal as

$$\tau_b^{(\alpha)} = \begin{cases} \tau_0 b L^2\dfrac{\lambda^{(\alpha)}}{(\beta^{(\alpha)})^2}\rho_{G(e),i}^{(\alpha)}s_i^{(\alpha)} & , \text{ for } |\tau_b^{(\alpha)}| \le \tau_T^{(\alpha)} \\ \operatorname{sgn}\left(\rho_{G(e),i}^{(\alpha)}s_i^{(\alpha)}\right)\tau_0^\kappa b^\kappa\left(\tau_T^{(\alpha)}\right)^{1-\kappa}L^{2\kappa}\dfrac{(\lambda^{(\alpha)})^\kappa}{(\beta^{(\alpha)})^{2\kappa}}\left|\rho_{G(e),i}^{(\alpha)}s_i^{(\alpha)}\right|^\kappa & , \text{ for } |\tau_b^{(\alpha)}| > \tau_T^{(\alpha)} \end{cases}, \tag{3.24}$$

where $\tau_T^{(\alpha)} = \lambda^{(\alpha)}\tau_T$. Thus, in the present case, the material length parameter for the effective slip systems corresponds exactly to the crystallographic length parameter. This result differs from the findings of Niordson and Kysar (2014), where the contribution from screw dislocations was neglected leading to a scaling of the material length parameters.

Table 3.1: Scaling coefficients between crystallographic and effective quantities

Effective slip system no., α	(1)	(2)	(3)
Angle to $[\bar{1}10]$ in (110) plane, θ	54.7°	0°	125.3°
$\beta^{(\alpha)} = \dfrac{\dot{\gamma}_0^{(\alpha)}}{\dot{\gamma}_0} = \dfrac{s_i^{(\alpha a)} m_j^{(\alpha a)} + s_i^{(\alpha b)} m_j^{(\alpha b)}}{s_i^{(\alpha)} m_j^{(\alpha)}}$	$\sqrt{3}$	$\dfrac{2}{\sqrt{3}}$	$\sqrt{3}$
$\lambda^{(\alpha)} = \dfrac{\tau_0^{(\alpha)}}{\tau_0} = \dfrac{2}{\beta^{(\alpha)}}$	$\dfrac{2}{\sqrt{3}}$	$\sqrt{3}$	$\dfrac{2}{\sqrt{3}}$
$\omega^{(\alpha)} = s_i^{(\alpha)} s_i^{(\alpha a)} = s_i^{(\alpha)} s_i^{(\alpha b)}$	$\dfrac{\sqrt{3}}{2}$	1	$\dfrac{\sqrt{3}}{2}$
$\chi^{(\alpha)} = \begin{cases} s_i^{(\alpha)} p_i^{(\alpha a)} = s_i^{(\alpha)} p_i^{(\alpha b)} & \text{, for } \alpha = 1 \text{ or } 3 \\ m_i^{(\alpha)} p_i^{(\alpha a)} = m_i^{(\alpha)} p_i^{(\alpha b)} & \text{, for } \alpha = 2 \end{cases}$	$\dfrac{1}{2}$	$\dfrac{\sqrt{3}}{\sqrt{2}}$	$\dfrac{1}{2}$

Chapter 4

Summary of numerical results

In the present chapter, a series of numerical results are presented to evaluate the proposed theory and its applications to solve a sample of small scale plasticity problems. Emphasis is placed on the micro-structural model predictions and how these relate to the associated macroscopic behavior.

4.1 Monotonic loading

The present results are confined to plane strain single slip, i.e., all terms associated with screw dislocations vanish. The single slip simple shear problem, illustrated in Fig. 4.1, is considered in order to demonstrate the influence of the back stress formulations derived in Section 3. This analysis shall serve as a lucid benchmark for the performance of the proposed models. In order to allow comparison with the results of Kuroda and Tvergaard (2008), the following model parameters are used throughout: Slip angle $\theta = 90°$, Young's modulus $E = 130$ GPa, Poisson's ratio $\nu = 0.3$, $\tau_0 = 50$ MPa, $b = 0.286$ nm, $h^{(\alpha\beta)} = h = 250$ MPa, and $m = 0.02$. On the semi-infinite material slab, of height H and width W, the following boundary conditions are imposed on the displacement field

$$u_1 = u_2 = 0 \ \text{ at } \ x_2 = 0 \tag{4.1a}$$

$$u_1 = U(t) = H\dot{\gamma}_0 t \ \text{ and } \ u_2 = 0 \ \text{ at } \ x_2 = H, \tag{4.1b}$$

where the overall macroscopic shear strain applied is $\Gamma = 0.03$ at a rate of $\dot{\Gamma} = \dot{\gamma}_0$. Microscopic hard conditions are enforced at the top and bottom horizontal boundaries for the GND evolution, such that

$$\zeta^{(\alpha)} \equiv \gamma^{(\alpha)} n_i s_i^{(\alpha)} = 0 \ \text{ at } \ x_2 = 0 \ \text{ and } \ x_2 = H, \tag{4.2}$$

and periodicity in the x_1-direction requires that

$$u_i(0, x_2) \quad = u_i(W, x_2) \tag{4.3a}$$

$$\rho^{(\alpha)}_{G(e)}(0, x_2) = \rho^{(\alpha)}_{G(e)}(W, x_2). \tag{4.3b}$$

The above boundary conditions entail a one dimensional field analysis. Typical finite element meshes employed here consist of 50 elements in the x_2-direction and mesh refinements is used when steep gradients appear in the solution.

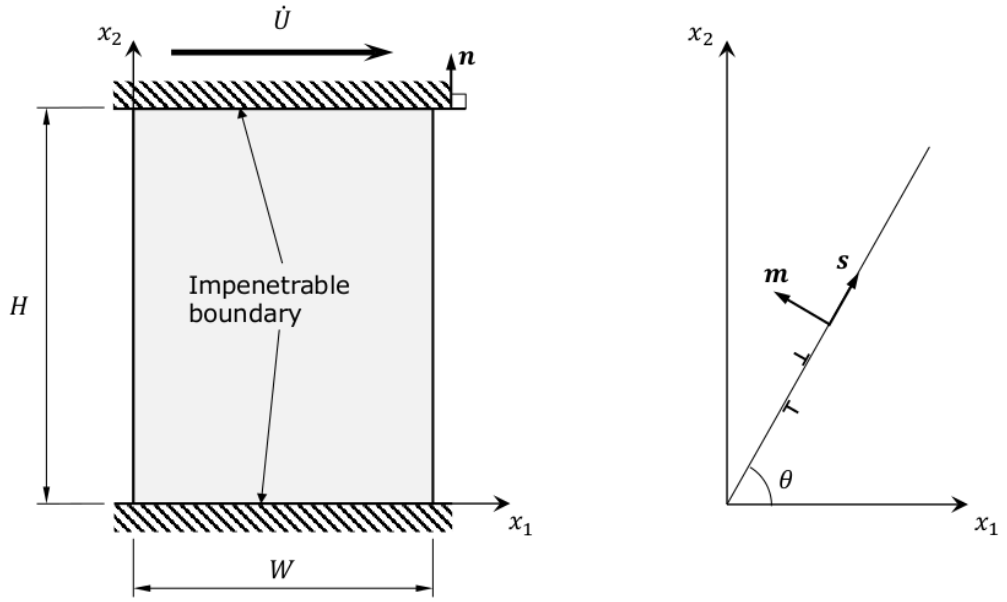

(a) (b)

Figure 4.1: Schematic of the simple shear problem: (a) the material domain, which is modeled as infinite in the x_2-direction, is constrained by two rigid impenetrable boundaries and subject to a prescribed displacement rate $\dot{U}$. (b) definition of the slip system.

First, the single slip simple shear problem is solved to demonstrate the behavior of the model assuming the classical back stress given by Eqs. (3.8) and (3.9), which corresponds to a quadratic defect energy. Results for different values of the material length scale parameter, L, are shown in Fig. 4.2, where the slip profile across the material slab is shown in Fig. 4.2a and the GND profile is shown in Fig. 4.2b. The slip profile indicates an increasing flattening of the central part of the domain for decreasing L, while a rather smooth distribution of GNDs is obtained. It is noticed, however, that increased localization of GNDs takes place at the boundaries for decreasing values of L. The shear stress vs. macroscopic shear strain response is shown in Fig. 4.2c. Hardening clearly increases with L, as the back stress effect becomes increasingly significant, whereas for very low values of L, the size-effect diminishes. Similar results can be found in Anand et al. (2005). Although no experimental results exist for direct comparison with the plane strain simple shear case, this boundary value problem outlines the model's ability to represent the highly localized GND structures observed experimentally[1].

Next, we will consider the implications of deviating from the commonly assumed quadratic defect energy by employing the back stress formulation proposed in El-Naaman et al. (2016c) (see [P2]), which is given in Eq. (3.12). The behavior is demonstrated in Figs. 4.3 through 4.6. In the computations presented here, a value of $\rho_0 = 10^5$ mm^{-2} is used. In El-Naaman et al. (2016c), it was shown that ρ_0 has negligible effect on the

[1]Moreover, in the wedge indentation case studied by Kysar et al. (2010), Öztop (2011), and Dahlberg et al. (2014), there are regions beneath the indentation which are dominated by approximate simple shear, of which Fig. 4.1 can be considered a simple model.

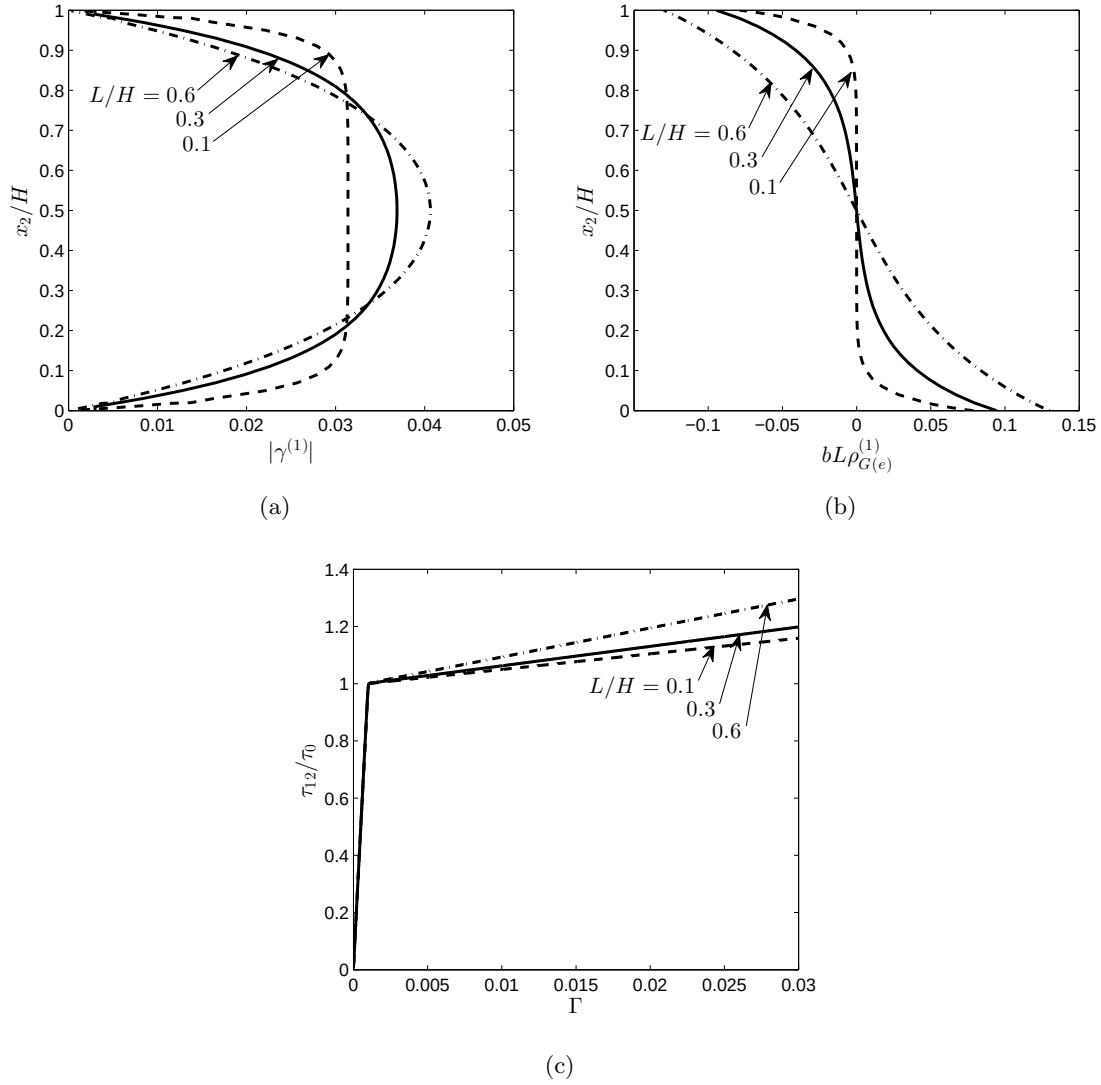

Figure 4.2: Numerical results for the single slip simple shear problem (Fig. 4.1) with $\theta = 90°$, for different values of the material length scale parameter L. The figure shows (a) slip profile, (b) normalized GND density, and (c) shear stress vs. macroscopic shear strain.

qualitative results for low values of L, however, for approximately $L/H > 1$, ρ_0 has a strong influence on the macroscopic behavior (El-Naaman et al., 2016b, [P3]), which will be elaborated in Section 4.2.

First, the nearly linear to quadratic regime of the gradient energy ($0 < \mu \leq 1$) is considered (Fig. 4.3). Figure 4.3a shows the slip profile with a flattening evident for low values of μ. As μ goes to one, the effect of the back stress singularity extends toward ρ_0 and instabilities arising in the numerical solution begin to have an effect on the back stress behavior. This is seen, in Fig. 4.3a, as a small notch on the slip profile in the center region of the material domain, that diminishes as μ goes to zero. Figure 4.3b shows the GND density profile, where the density is found to intensify at the boundaries for very low values

of μ, however, the opposite effect occurs at intermediate values, e.g. at $\mu = 0.4$. The GND density profile is normalized with its boundary value (the maximum GND density in the material domain, $\rho^{(1)}_{G(e),B}$ at $\Gamma = 0.03$) in order to qualitatively demonstrate the effect of μ. The normalization value, $\rho^{(1)}_{G(e),B}$, is plotted in Fig. 4.5 as function of μ for different values of the material length scale parameter. The general trend of the dependence on μ has a turning point, which appears as a local minimum in Fig. 4.5, when plotting $\rho^{(1)}_{G(e),B}$ as function of μ. The local minimum shifts upward for increasing L and is found, e.g., at approximately $\mu = 0.5$ for $L/H = 0.3$. Figure 4.3c shows the shear stress vs. macroscopic shear strain, where a non-linear response is observed for lower values of μ. Here, as well, a non-trivial effect of μ is predicted, which is evident from Fig. 4.6. It is seen that the flow stress level at $\Gamma = 0.03$ has a local maximum, which shifts upward for increasing L. This maximum is found, e.g., at approximately $\mu = 0.3$ for $L/H = 0.3$ (see Fig. 4.6).

The quadratic to cubic regime of the gradient energy ($1 \leq \mu \leq 2$) is considered next. Although, a postulate of a defect energy within this regime has no physical basis, the results are interesting from a phenomenological point of view. A flattening of the slip profile is seen in Fig. 4.4a for increasing values of μ, associated with an intense build-up of GND density at the boundaries (Fig. 4.4b). In the case of $\mu = 2$ (cubic energy), the GND density gradients are practically eliminated in the interior region of approximately 70 percent of the slab height, whereas a steep increase takes place at the boundaries. In the shear stress vs. macroscopic shear strain response (Fig. 4.4c), the linear hardening decreases with increasing μ. This is further demonstrated in Fig. 4.6 for different values of the material length scale parameter. The results show that the proposed back stress formulation provides an additional degree of freedom in the model in terms of capturing both macroscopic and microscopic material behavior.

Figure 4.7 shows results using the phenomenological piece-wise back stress formulation in Eq. (3.14) for different values of κ with $\tau_T/\tau_0 = 0.12$ and $L/H = 0.3$ (The effect of τ_T is investigated in Section 4.2). Figure 4.7a shows the slip profile with increased localized slip at the boundaries for decreasing values of κ and Fig. 4.7b shows the GND density profile normalized with the value at the boundary, $\rho^{(1)}_{G(e),B}$, in order to qualitatively demonstrate the effect of κ. Here, the transition point, $\tau_b = \tau_T$, is marked with a small circle on the individual curves near the lower boundary for the values $0 < \kappa < 1$. This point appears exactly on the boundary for κ equal to zero, since $|\tau_b| \leq \tau_T$ is enforced in this case (hence, not marked on the figure). The normalization value is presented in Fig. 4.8 as function of κ, showing also the effect of the material length scale parameter L. Here, it is noticed that the effect of L, on the level of GND density at the boundaries, changes character in the low regime of κ. As κ approaches zero, the GND density evolves more locally, whereby more pronounced dislocation "walls" form. The results demonstrate that a highly non-uniform micro-structure, with high GND density at the boundaries and low GND density and GND density gradients in the interior region, can be achieved through the dependence of the back stress on the GND density gradient. Figure 4.7c shows the shear stress vs. macroscopic shear strain response with little effect of the κ parameter—though with a slight non-linear hardening effect appearing as κ decreases. The effect of κ on the flow stress is further demonstrated in Fig. 4.9 for different values of the material length scale. Thus, through the value of κ, it is possible to control the kinematic hardening behavior and also achieve a cell-like GND distribution, which provides a better basis for modeling

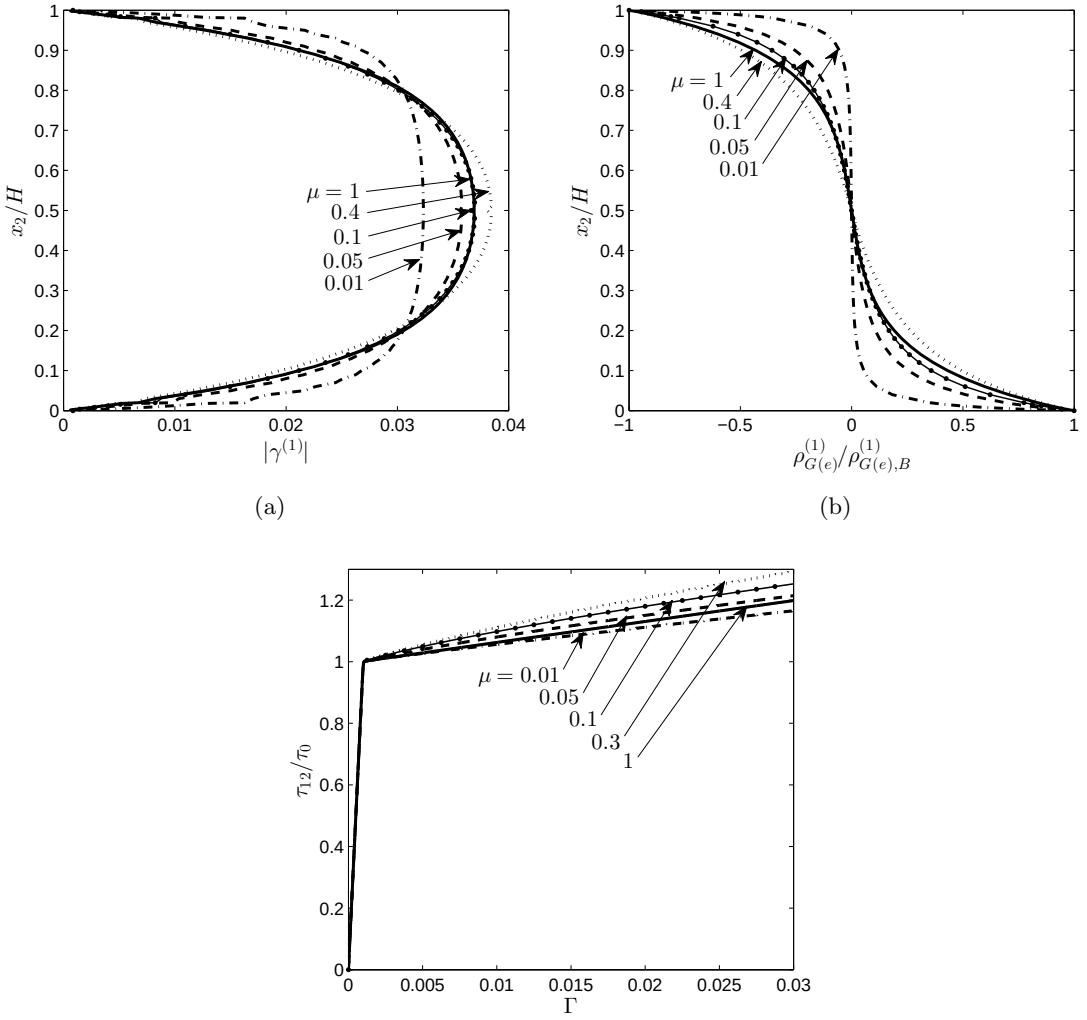

Figure 4.3: Numerical results for the single slip simple shear problem (Fig. 4.1), using the generalized gradient energy based back stress (Eqs. (3.11) and (3.12)), with $\theta = 90°$, $L/H = 0.3$, and $\rho_{G(e),0} = 10^5$ m^{-2}, illustrating the effect of the μ parameter in the linear to quadratic regime ($0 < \mu \leq 1$). The figure shows (a) Slip profile, (b) normalized GND density, and (c) shear stress vs. macroscopic shear strain.

the micro-structures observed in experimental studies. The effect of the rate exponent, m, on the GND density distribution, using back stress relation (3.14), was studied in El-Naaman et al. (2015) (see [P1]), where increasing values of m was shown to increase the effect of κ.

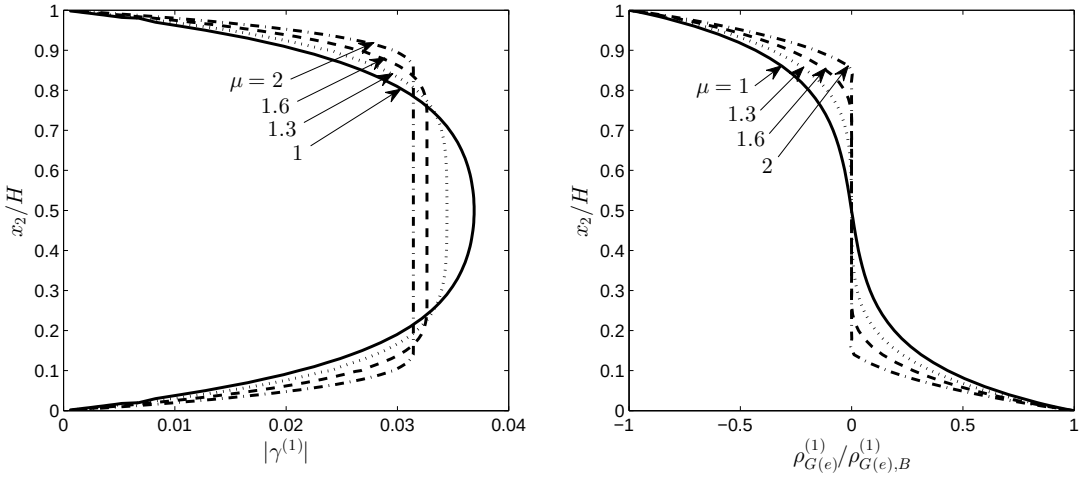

(a) (b)

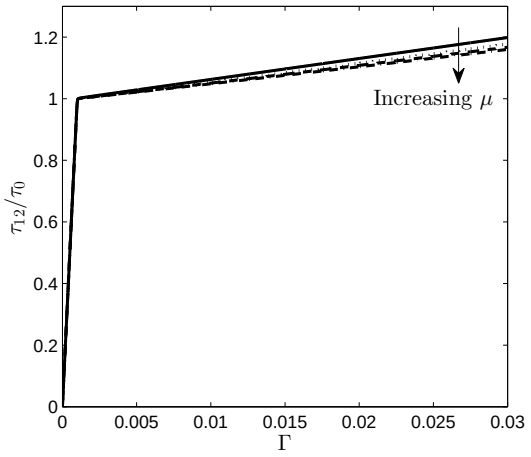

(c)

Figure 4.4: Numerical results for the single slip simple shear problem (Fig. 4.1), using the generalized gradient energy based back stress (Eqs. (3.11) and (3.12)), with $\theta = 90°$ and $L/H = 0.3$, illustrating the effect of the μ parameter in the quadratic to cubic regime ($1 \leq \mu \leq 2$). The figure shows (a) slip profile, (b) normalized GND density, (c) shear stress vs. macroscopic shear strain.

4.2 Cyclic loading

The following numerical study focuses on the macroscopic response under cyclic loading, when employing the back stress formulations derived in Chapter 3. Moreover, the predicted evolution in micro-structure is discussed in relation to the macroscopic behavior demonstrating novel modeling capabilities provided by the proposed back stress formulations (El-Naaman et al., 2016b, [P3]).

As in Section 4.1, the single slip simple shear problem, illustrated in Fig. 4.1, is

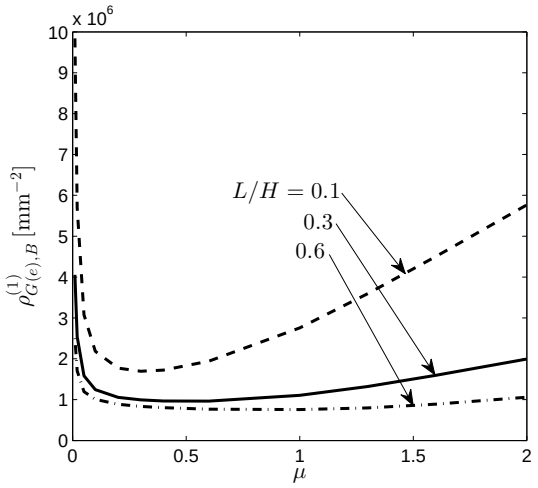

Figure 4.5: Magnitude (normalization values in Figs. 4.3b and 4.4b) of GND density as function of μ (Eqs. (3.11) and (3.12)) at a macroscopic shear strain of $\Gamma = 0.03$. Results are shown for different values of the material length scale parameter L.

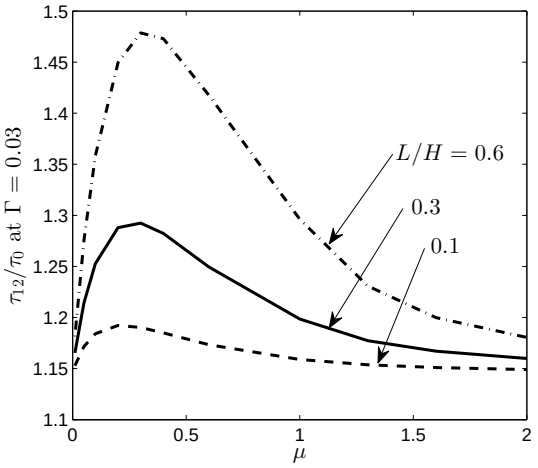

Figure 4.6: Shear flow stress at macroscopic shear strain $\Gamma = 0.03$ as function of μ, illustrating the effect of μ (Eqs. (3.11) and (3.12)) on the stress/strain response in Figs. 4.4c and 4.3c. Results are shown for different values of the material length scale parameter L

considered in order to demonstrate the behavior of the back stress formulations under cyclic loading. To compare results to those found for monotonic loading in Kuroda and Tvergaard (2008) and to those presented in Section 4.1, the same model parameters are used here: Slip angle $\theta = 90°$, Young's modulus $E = 130$ GPa, Poisson's ratio $\nu = 0.3$, $\tau_0 = 50$ MPa, and $b = 0.286$ nm.

The finite element mesh, employed for the following numerical analysis, consists of 58 elements in the x_2-direction including a refined mesh at the microscopically passivated

boundaries to resolve the steep gradients.

4.2.1 Macroscopic response under cyclic loading

At first, the boundary value problem described in Section 4.1 is solved with conventional hardening ($h^{(\alpha\beta)} = h = 250$ MPa), at a rate sensitivity $m = 0.02$. With $\dot{U} = H\dot{\gamma}_0$, the material domain is sheared to a macroscopic shear strain $\Gamma = 0.03$, after which, one complete load cycle is performed, such that the macroscopic shear strain goes once to -0.03 and back to 0.03. Figure 4.10 shows results obtained when adopting the thermodynamically

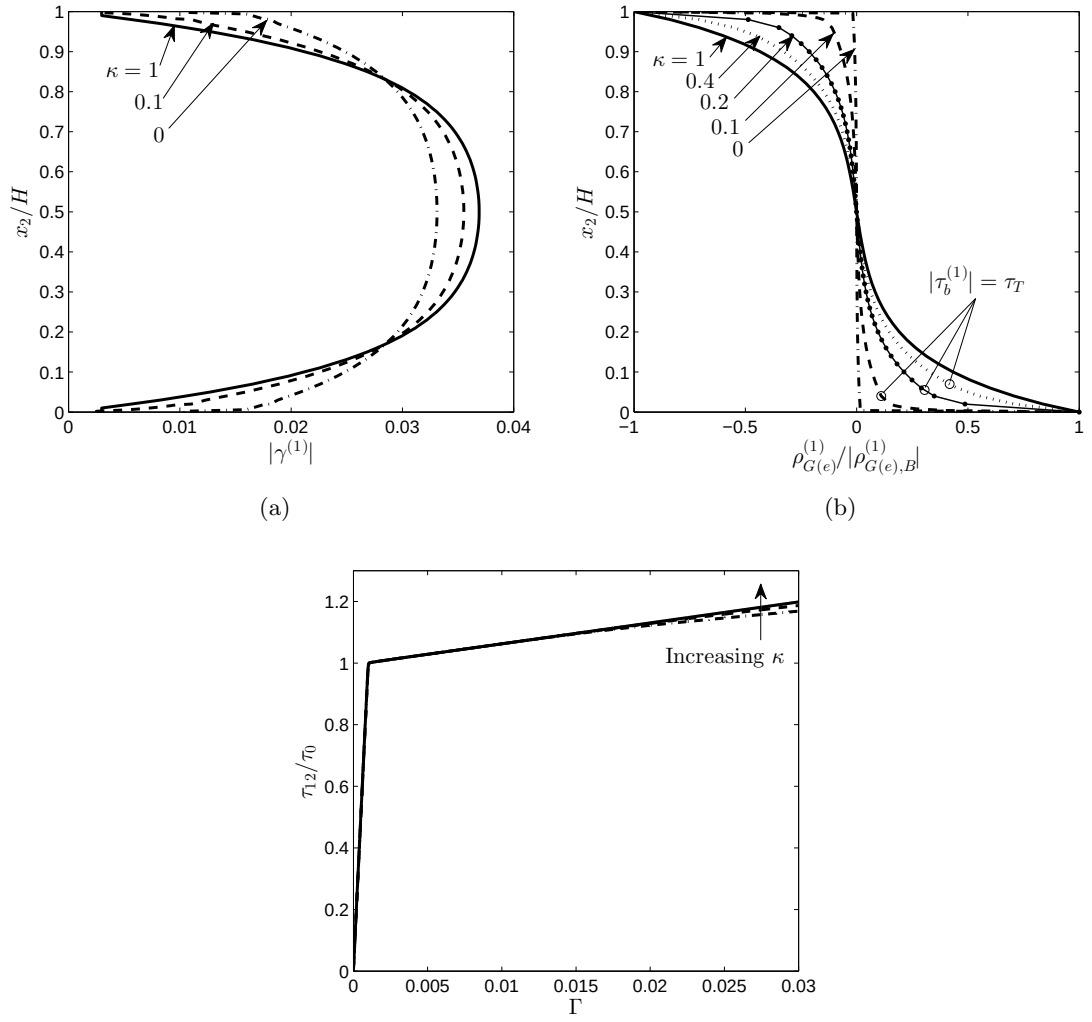

Figure 4.7: Numerical results for the single slip simple shear problem (Fig. 4.1), using the back stress power law (Eq. (3.14)), with $\theta = 90°$, $L/H = 0.3$, and $\tau_T/\tau_0 = 0.12$, illustrating the effect of the κ parameter. The figure shows (a) Slip profile, (b) normalized GND density, with circles marking the transition point $\tau_b = \tau_T$, and (c) shear stress vs. macroscopic shear strain.

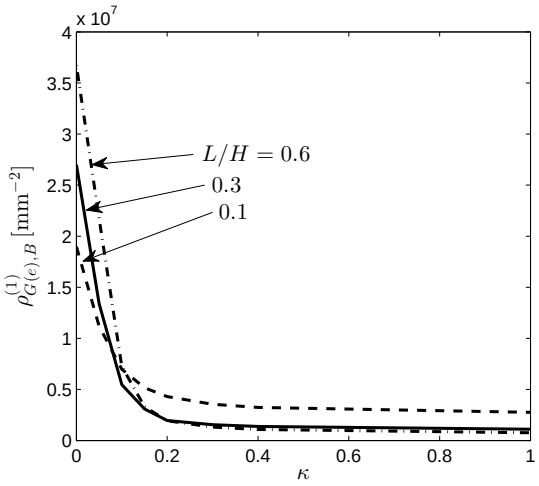

Figure 4.8: Magnitude (normalization values in Fig. 4.4b) of GND density as function of κ (Eq. 3.14) at a macroscopic shear strain of $\Gamma = 0.03$. Results are shown for different values of the material length scale parameter L

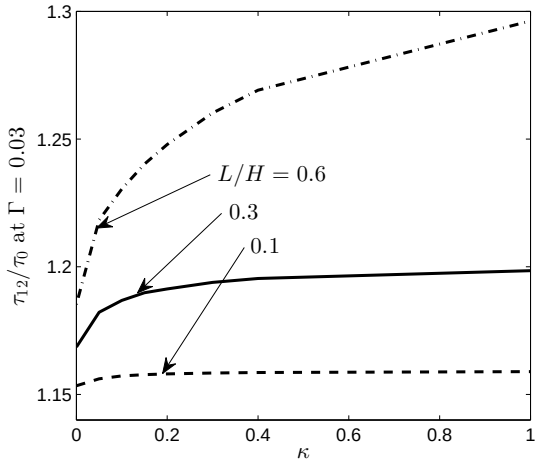

Figure 4.9: Shear flow stress at 0.03 macroscopic shear strain as function of κ (Eq. 3.14), to illustrate the effect of κ on the stress/strain response in Fig. 4.7c. Results are shown for different values of the material length scale parameter L

consistent back stress formulation in Eq. (3.12) for different values of μ. The complete shear stress vs. macroscopic shear strain curve is shown in Fig. 4.10a. For the final load step, the slip profile can be seen in Fig. 4.10b and the distribution of GNDs can be seen in Fig. 4.10c. The GND density distributions in Fig. 4.10c are normalized with the values found at the boundary, denoted $\rho^{(1)}_{G(e),B}$, to enable qualitative comparison. Going from $\mu = 1$ (quadratic free energy) to $\mu = 0.4$ the spatial gradient of slip decreases, corresponding to a smoother distribution of GNDs (Fig. 4.10c), while a low value of μ (close to linear free

energy) results in a steep gradient in slip, and thereby more localized pile-up of GNDs. It is also noticed that for $\mu = 0.4$, the smooth slip profile is maintained, while for all other values additional waves in the profile are developed. Along the same line, using the purely phenomenological back stress formulation in Eq. (3.14), similar localized GND structures are predicted. For different values of κ and with $\tau_T/\tau_0 = 0.12$, Fig. 4.11a shows the shear stress vs. macroscopic shear strain over the entire modeling history. Figures 4.11b and

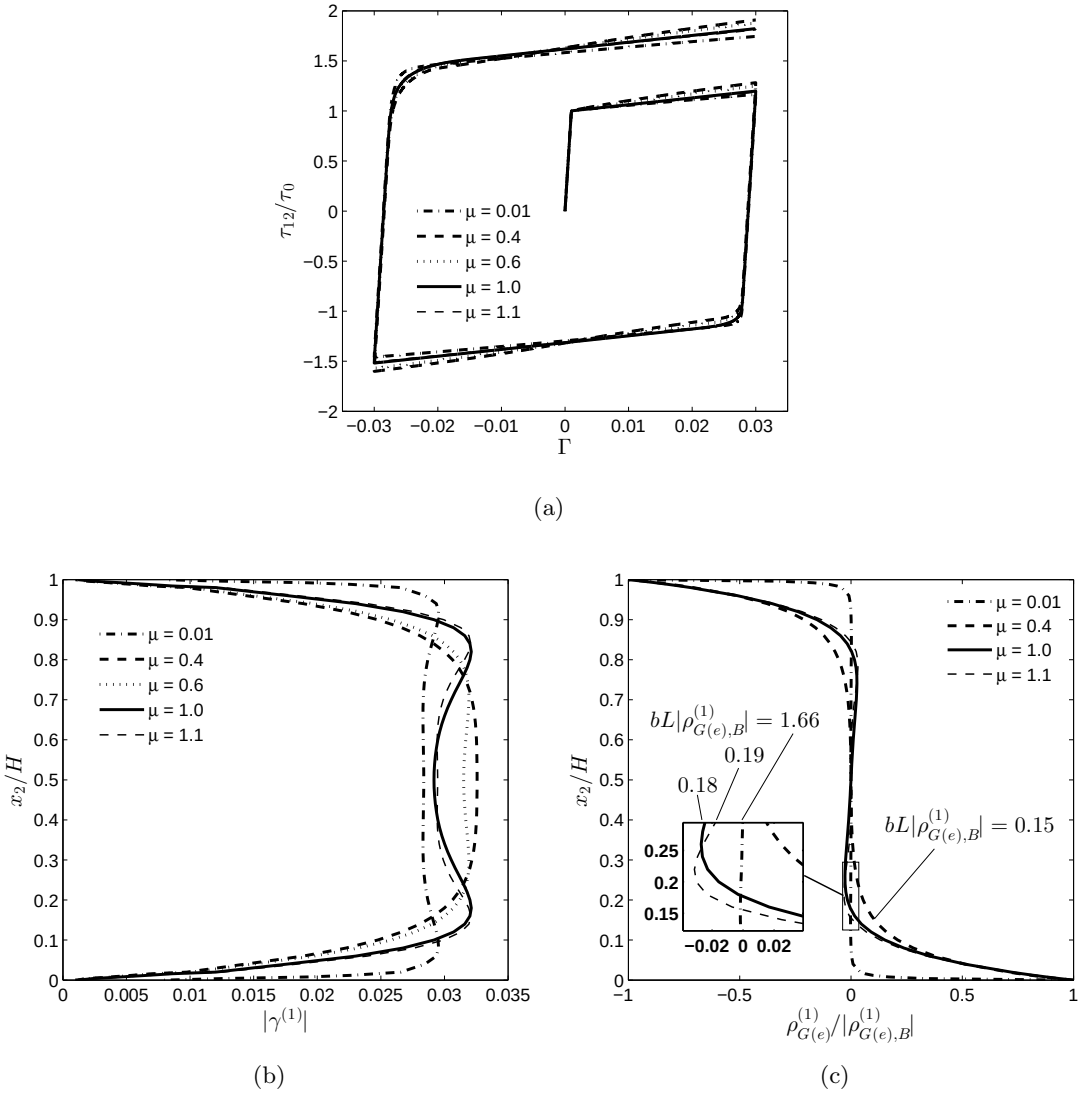

Figure 4.10: Numerical results for the single slip simple shear problem (Fig. 4.1) subject to one load cycle, using the generalized gradient energy based back stress (Eqs. (3.11) and (3.12)), with $\theta = 90°$, $h^{(\alpha\beta)} = h = 250$ MPa, $L/H = 0.3$, $m = 0.02$, $\rho_0 = 10^5$ mm^{-2}, and $\dot{U} = H\dot{\gamma}_0$, illustrating the effect of the μ parameter, on the cyclic behavior, in the linear to quadratic regime ($0 < \mu \leq 1$). The figure shows (a) shear stress vs. macroscopic shear strain, (b) slip profile, and (c) normalized GND density. Slip profile (b) and GND density (c) are shown for $\Gamma = 0.03$ after the final load step.

4.11c show the slip profile and the GND density, respectively, after the final load step. When letting κ go to zero, large slip gradients occur locally at the hard boundaries (Fig. 4.11b), resulting in increasingly localized GND structures (Fig. 4.11c), in contrast to the more smooth development seen for $\kappa = 1$ (quadratic gradient energy). It is noticed that an additional wave appears in the central part of the slip profile for the low values of κ (Fig. 4.11b).

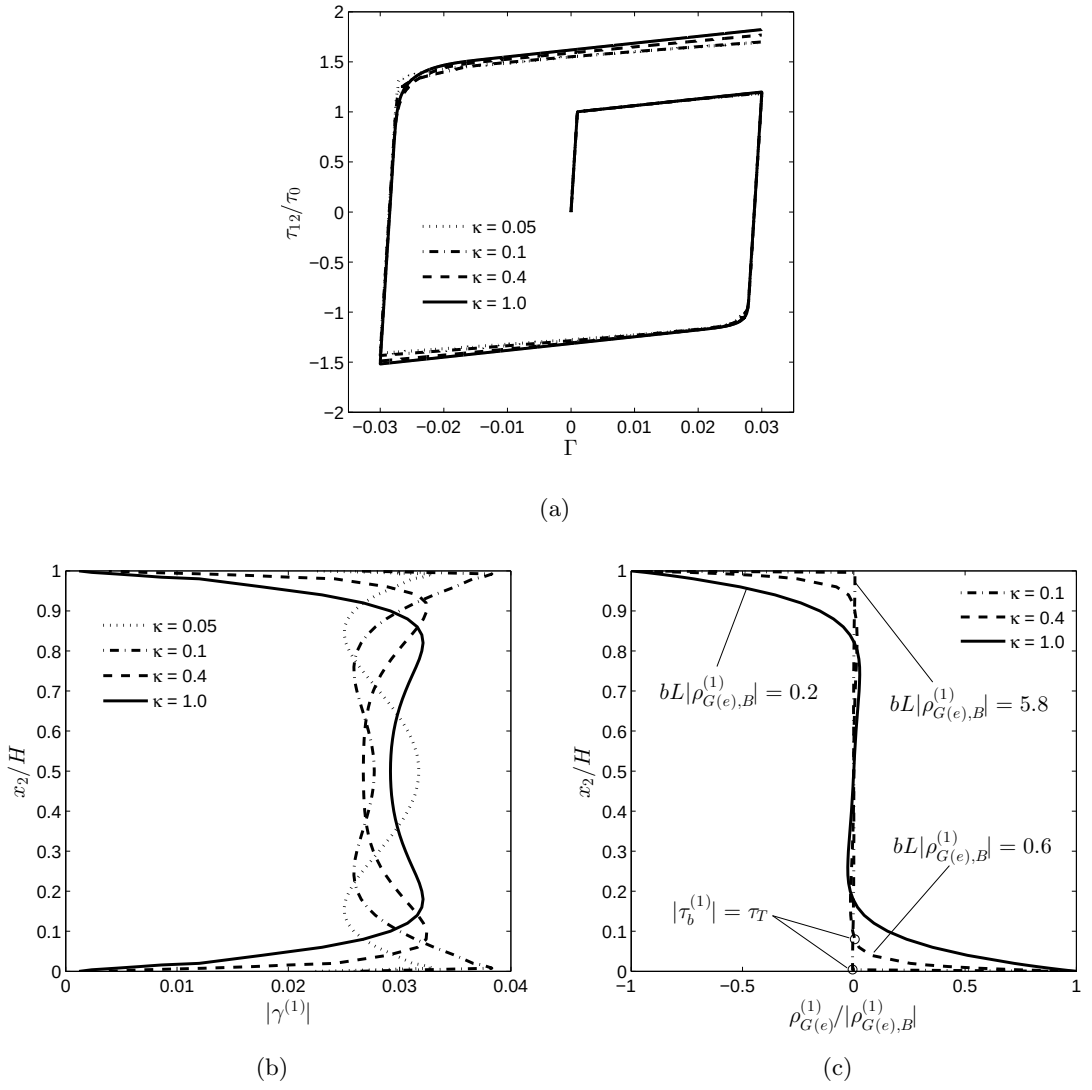

Figure 4.11: Shear stress vs. macroscopic shear strain for the single slip simple shear problem (Fig. 4.1) subject to one load cycle, using the back stress power law (Eq. (3.14)), with $\theta = 90°$, $h^{(\alpha\beta)} = h = 250$ MPa, $L/H = 0.3$, $m = 0.02$, $\tau_T/\tau_0 = 0.12$, and $\dot{U} = H\dot{\gamma}_0$, illustrating the effect of the κ parameter on the cyclic behavior. The figure shows (a) shear stress vs. macroscopic shear strain, (b) Slip profile, and (c) normalized GND density, with circles marking the back stress transition point ($|\tau_b^{(1)}| = \tau_T$) near the lower horizontal boundary. Slip profile (b) and GND density (c) are shown for $\Gamma = 0.03$ after the final load step.

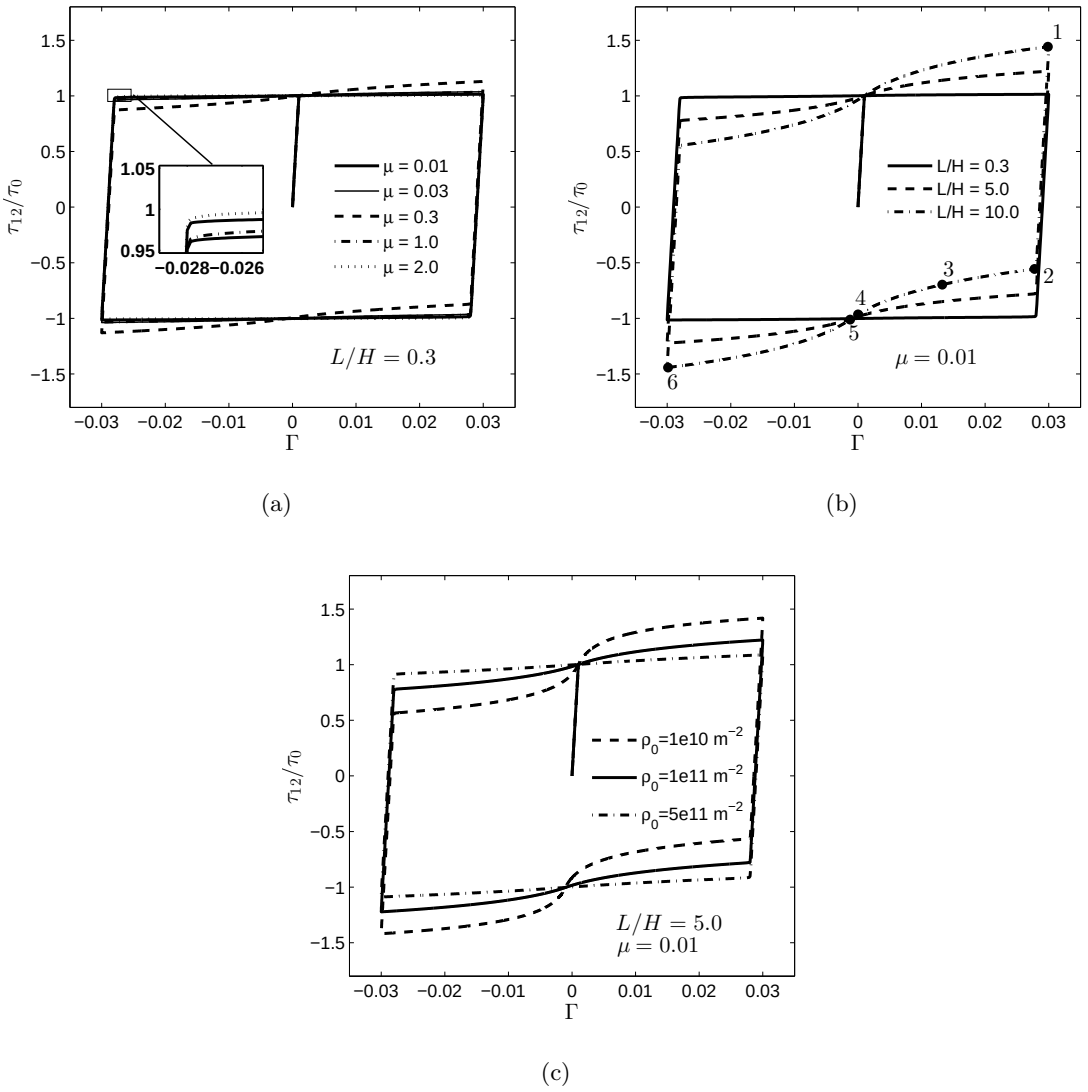

Figure 4.12: Numerical results for the single slip simple shear problem (Fig. 4.1), using the generalized gradient energy based back stress (Eqs. (3.11) and (3.12)), with $\theta = 90°$, $h^{(\alpha\beta)} = h = 0$, $m = 0.02$, and $\dot{U} = H\dot{\gamma}_0$. The figure shows normalized shear stress vs. macroscopic shear strain: (a) for different values of μ, (b) for different values of L, and (c) for different values of ρ_0. In (a) and (b), $\rho_0 = 1.0\text{e}11$ m^{-2} for $\mu < 1$, and otherwise zero. In (b) the numbered dots mark the load stages at which the slip and back stress are plotted in the subsequent figures.

In the following, a parametric study, for the case of zero conventional hardening ($h^{(\alpha\beta)} = h = 0$), is performed in order to bring out additional details on how the micro-structural predictions relate to the macroscopic response, considering the two different back stress formulations. In these computations it was checked that a steady state cyclic response was achieved by running multiple load cycles about the zero strain axis. Figure 4.12 shows the shear stress vs. macroscopic shear strain using the thermodynamically consistent back stress formulation (3.12). Results are shown for different values of the back stress exponent,

μ (Fig. 4.12a), for different values of the material length parameter, L (Fig. 4.12b), and for different values of the additional micro-structural parameter, ρ_0 (Fig. 4.12c). For the low material length parameter value ($L/H = 0.3$) there is no considerable difference in the macroscopic response for $\mu = 0.01$, 1.0, and 2.0. This observation is significant in relation to the predicted micro-structural development, which will be discussed in Section 4.2.2. When going to higher values of the material length parameter, a seemingly anomalous local change in slope on the response curves is predicted during plastic flow, so that these exhibit inflection points close to zero strain (Fig. 4.12b). In Fig. 4.12c, showing results for the intermediate material length scale ($L/H = 5$), it is evident that this behavior is largely controlled by the micro-structural parameter, ρ_0.

Figure 4.13 shows the shear stress vs. macroscopic shear strain using the purely phenomenologically constructed back stress formulation (3.12). Results are shown for different values of the back stress exponent, κ (Fig. 4.13a), for different material length scales, L (Fig. 4.13b), and for different values of the transition parameter, τ_T (Fig. 4.13c). Similar to the predictions resulting from the former back stress formulation, Fig. 4.13a shows no significant difference in the macroscopic response, for the low value of the material length parameter ($L/H = 0.3$), when varying the value of κ (see also Section 4.2.2). When employing higher material length scales, inflection points are formed on the response curves close to zero strain during plastic flow (Fig. 4.13b). Figure 4.13c shows that this behavior is largely controlled by the transition parameter, τ_T. For the thermodynamically consistent formulation this local slope change takes place rather smoothly, whereas the purely phenomenological formulation displays a much more rapid change in slope. This is due to the particular choice of constitutive parameters, which will be elaborated in the following.

To understand what controls this seemingly anomalous cyclic behavior observed for both back stress formulations, the plastic slip and back stress distribution are plotted across the material slab height at different stages of the load cycle (Figs. 4.14 through 4.17). The different load stages are marked and numbered on one representative curve in each of Figs. 4.12b and 4.13b. Figure 4.14 shows results for a back stress based on quadratic free energy ($\mu = \kappa = 1$), while Figs. 4.15 and 4.16 show results using back stress relation (3.12) with $\mu = 0.01$ and back stress relation (3.14) with $\kappa = 0.1$, respectively. In these computations a low value of the material length parameter ($L/H = 0.3$) is used. For the phenomenological back stress formulation (Eq. (3.14)), the value $\tau_T/\tau_0 = 0.06$ will be used henceforth. In these results, it is generally observed that, when the load is reversed, the back stress changes direction over a gradually increasing domain (illustrated by stages 1 through 6), and that the change initiates locally at the micro-structurally passivated boundaries. A large central portion of the slab height experiences relatively little change in back stress (see Figs. 4.14-4.16). This is especially true when assuming a cubic energy potential ($\mu = 2.0$), where the central part remains basically unchanged with zero back stress throughout the deformation (see El-Naaman et al., 2016b, [P3]). Furthermore, it is noticed that for the purely phenomenological formulation, the majority of the material is dominated by a quadratic free energy, which is illustrated by the $|\tau_b^{(1)}| = \tau_T$ lines plotted in Fig. 4.16b. Thus, the power law part of Eq. (3.14) controls only the outermost regions of the material domain close to the passivated boundaries. For both back stress formulations, when a high value of the material length scale is employed ($L = 10$), it is observed that a high level of back stress develops in the entire material domain (this is shown for the phenomenological back stress relation (3.14) in Fig. 4.17b). Thus, the behavior of

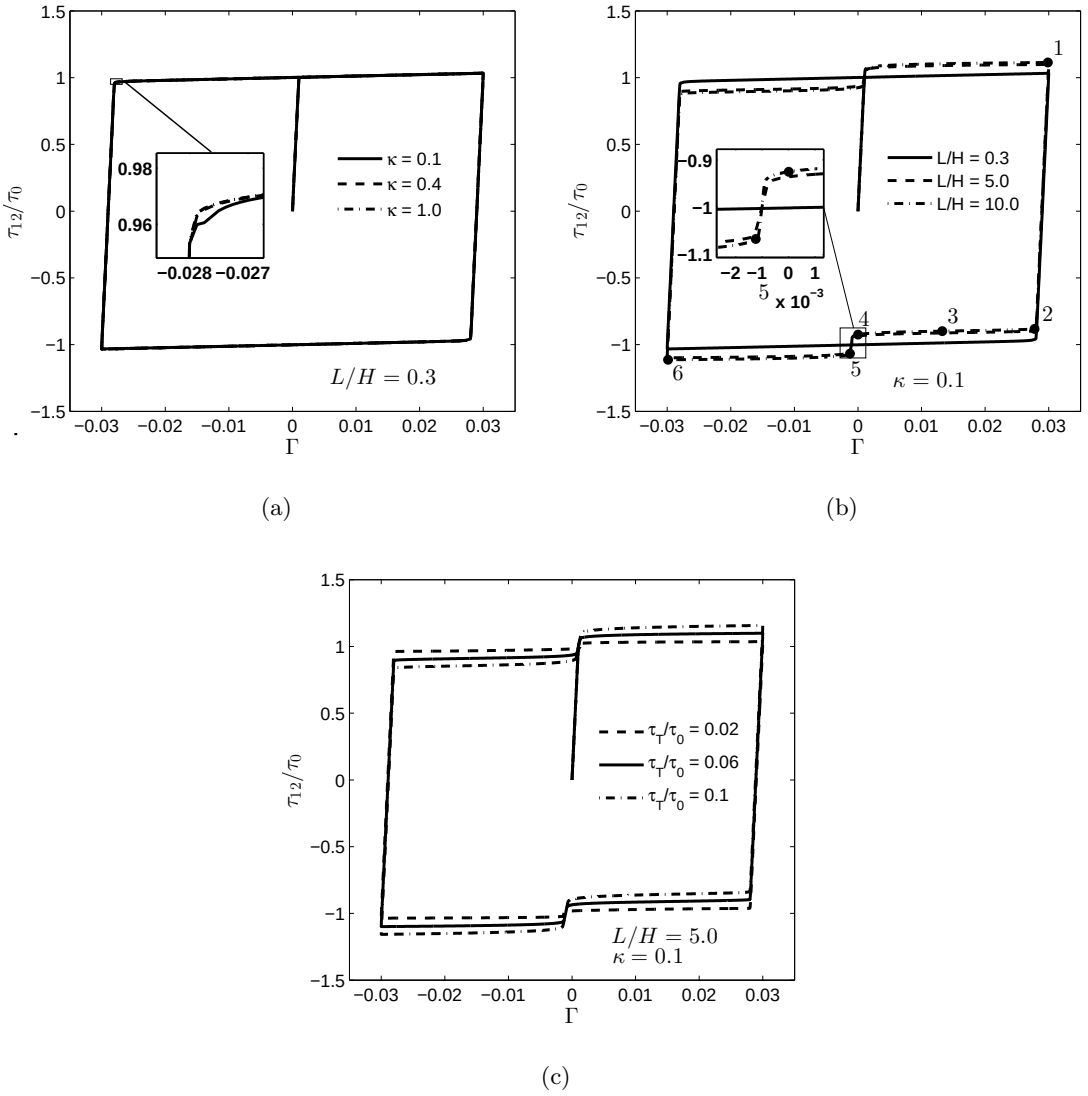

Figure 4.13: Numerical results for the single slip simple shear problem (Fig. 4.1), using the purely phenomenological back stress formulation (Eq. (3.14)), with $\theta = 90°$, $h^{(\alpha\beta)} = h = 0$, $m = 0.02$, and $\dot{U} = H\dot{\gamma}_0$. The figure shows normalized shear stress vs. macroscopic shear strain: (a) for different values of κ, (b) for different values of L, and (c) for different values of τ_T. In (a) and (b), $\tau_T/\tau_0 = 0.06$. In (b) the numbered dots mark the load stages at which the slip and back stress are plotted in the subsequent figures.

the back stress controls, quite directly, the macroscopic response throughout, resulting in the pronounced unconventional Bauschinger effect, in terms of inflection points. The change in back stress initiates at the boundaries here as well, but subsequently the shift from aiding slip to impeding slip, takes place in the entire domain upon reversed loading. Moreover, it is noticed in Fig. 4.17b, that the power law part of Eq. (3.14) dominates the material completely in stages 1, 2, 5, and 6. More details can be found in El-Naaman et al. (2016b) (see [P3]).

Cyclic plastic deformation of ductile crystalline materials gives rise to the Bauschinger

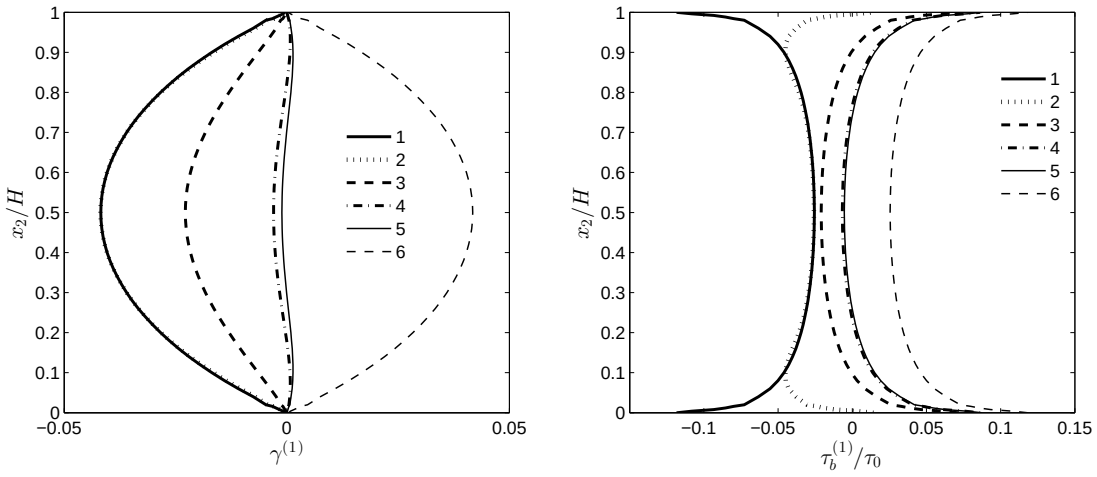

(a) (b)

Figure 4.14: Numerical results for the single slip simple shear problem (Fig. 4.1), using the classical quadratic gradient energy based back stress (corresponding to $\mu = \kappa = 1$), with $\theta = 90°$, $h^{(\alpha\beta)} = h = 0$, $m = 0.02$, and $\dot{U} = H\dot{\gamma}_0$, The figure shows (a) slip profiles and (b) back stress distribution at six different stages during cyclic loading corresponding to the points marked on the curve in Fig. 4.12.

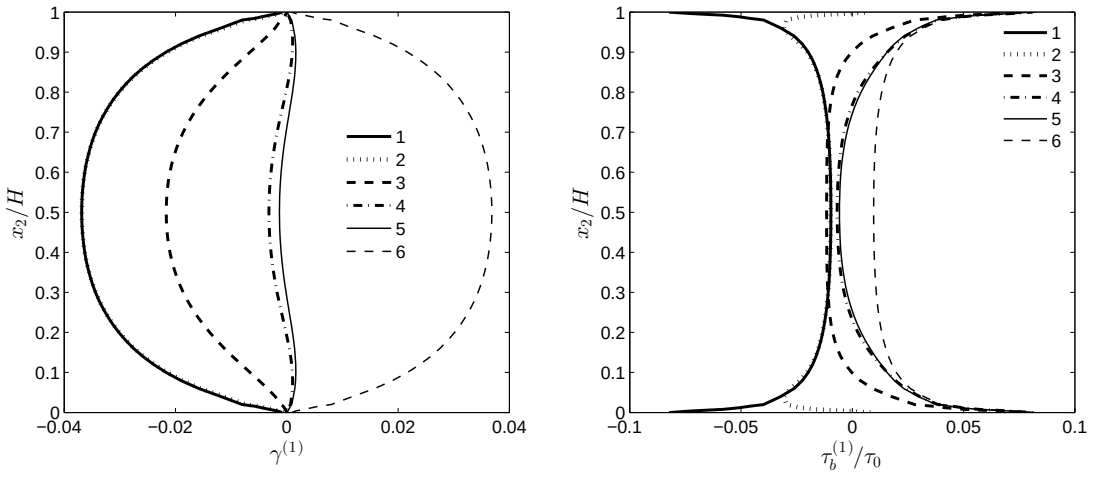

(a) (b)

Figure 4.15: Numerical results for the single slip simple shear problem (Fig. 4.1), assuming a nearly linear gradient energy based back stress $\mu = 0.01$ (Eqs. (3.11) and (3.12)), with $\theta = 90°$, $h^{(\alpha\beta)} = h = 0$, $m = 0.02$, $L/H = 0.3$, and $\dot{U} = H\dot{\gamma}_0$. The figure shows slip profile (a) and back stress distribution (b) at six different stages during cyclic loading corresponding to the points marked on the curve in Fig. 4.12.

effect, which reflects micro-structural mechanisms related to the pile up of dislocations. The inflection points on the flow curves express a sudden increase and subsequent de-

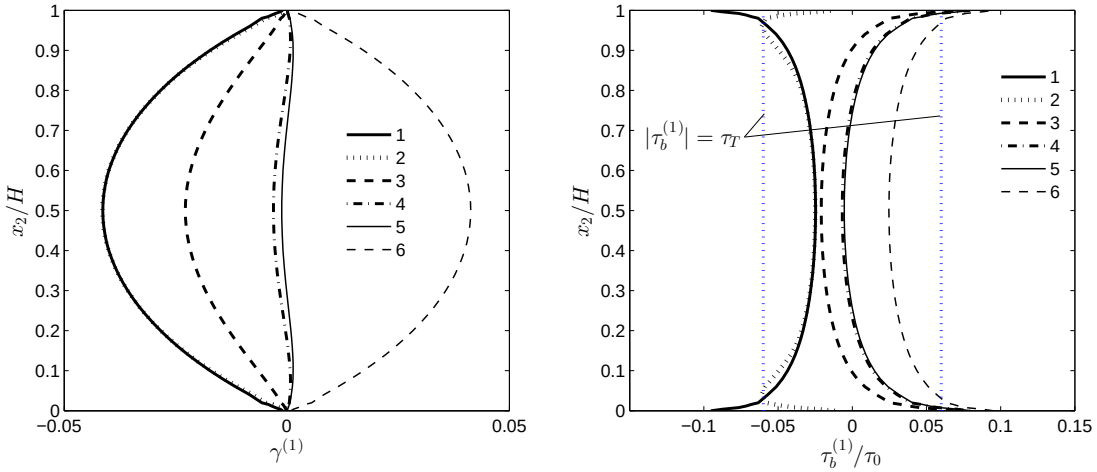

(a) (b)

Figure 4.16: Numerical results for the single slip simple shear problem (Fig. 4.1), using the back stress power law (Eq. (3.14)), with $\theta = 90°$, $h^{(\alpha\beta)} = h = 0$, $L/H = 0.3$, $m = 0.02$, $L/H = 0.3$, $\kappa = 0.1$, $\tau_T/\tau_0 = 0.06$, and $\dot{U} = H\dot{\gamma}_0$. The figure shows (a) slip profiles and (b) back stress distribution at six different stages during cyclic loading corresponding to the points marked on the curve in Fig. 4.13.

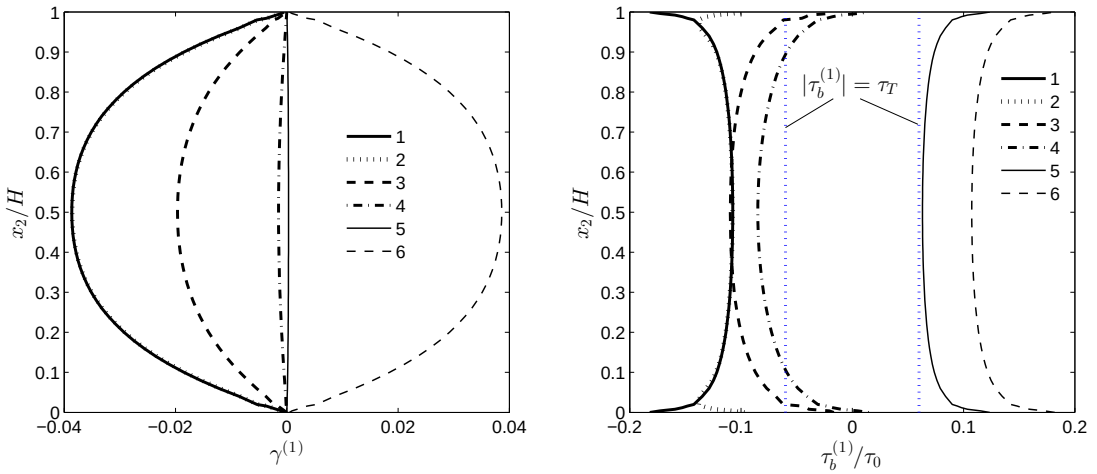

(a) (b)

Figure 4.17: Numerical results for the single slip simple shear problem (Fig. 4.1), using the back stress power law (Eq. (3.14)), with $\theta = 90°$, $h^{(\alpha\beta)} = h = 0$, $m = 0.02$, $L/H = 10.0$, $\kappa = 0.1$, $\tau_T/\tau_0 = 0.06$, and $\dot{U} = H\dot{\gamma}_0$. The figure shows (a) slip profiles and (b) back stress distribution at six different stages during cyclic loading corresponding to the points marked on the curve in Fig. 4.13.

crease in growth rate of the back stress close to the zero strain point. In terms of the thermodynamically consistent formulation (Eqs. (3.11) and (3.12)), the inflection points are essentially caused by the back stress approaching its singularity as the GND density goes to zero (in competition with the GND density gradient going to zero). How close the back stress can come to singular behavior is controlled by ρ_0, and thus, also the characteristics of the flow curve surrounding the inflection point is controlled by ρ_0 (see Fig. 4.12c). The very differently devised purely phenomenological back stress formulation (Eq. (3.14)) exhibits a behavior similar to that of the thermodynamically consistent back stress, showing a temporary change in slope of the flow curve, which initiates immediately after stage 4 (see Fig. 4.13) and persists approximately until stage 5. Approximately at stage 4, the back stress in the majority of the material domain has changed sign and is now impeding slip. Moreover, at this point and until stage 5, the quadratic free energy dominates (see Fig. 4.17b). The characteristics of the jump in the flow curve, in terms of strain interval and slope of the inflection tangent, is controlled by an interplay between τ_T and L (see Figs. 4.13b and 4.13c).

Asaro (1975) showed that this behavior is a natural outcome of theories that incorporate hardening due to long range internal stresses, and the inflected type of Bauschinger effect has been reported recently in other numerical strain gradient plasticity studies (Bardella and Panteghini, 2015; Wulfinghoff et al., 2015). Moreover, substantial experimental evidence of such cyclic behavior, observed for poly-crystals, exists in the literature (Asaro, 1975; Stoltz and Pelloux, 1976; Taillard and Pineau, 1982; Proudhon et al., 2008), and the observed behavior is attributed to long range internal stresses due to dislocation pile-up around precipitates and at grain boundaries. The governing mechanisms involved in these experimental studies, are analogous to the pile-up of dislocations at the passivated boundaries imposed in the present computations. The experimental results of Kiener et al. (2010) have been incorrectly referred to in the literature as a single crystal example of an anomalous Bauschinger effect, however, this particular result is tied to the test setup and has no connection with the material behavior. At present, due to the lack of experimental data, it is unknown whether this type of macroscopic behavior is acceptable, from a physical point of view, in a single crystal theory. However, since the inflected hysteretic behavior is believed to be tied to the influence of long range internal stresses due to pile-up of dislocations, it is most likely equally relevant for single crystal plasticity, especially in the presence of micro-structurally passivated boundaries.

4.2.2 Micro-structure evolution predictions

In general, dislocations tend to form cell structures in metals under plastic deformation and the same behavior has been reported for the evolution of GNDs as discussed in Section 1.2. The following results confirm the fact that the approaches in El-Naaman et al. (2016c) to a back stress formulation offer additional control of the micro-structural predictions mainly through one additional model parameter (μ or κ in the two models). The results presented below should be seen in contrast to the fact that the shear stress vs. macroscopic shear strain curves in Fig. 4.12a, representing the assumption of quadratic free energy (μ = 1), near linear free energy (μ = 0.01, 0.03), and cubic free energy (μ = 2), can be considered as macroscopically equivalent. The same observation is made for the response curves in Fig. 4.13a, representing the two choices of exponent (κ = 0.1 and 0.4) for the

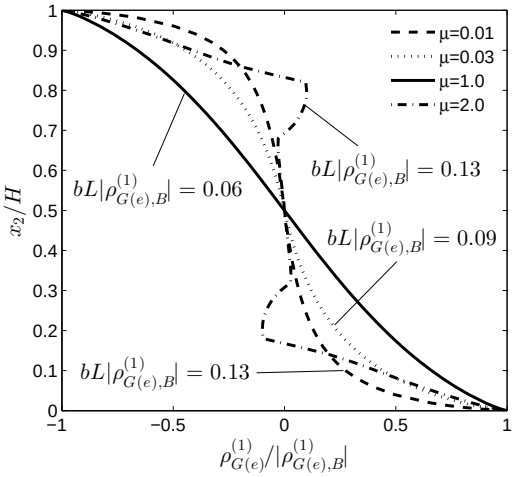

Figure 4.18: Predicted GND micro-structure, at $\Gamma = 0.03$ after two load cycles, assuming a nearly linear (dashed line, $\mu = 0.01$ and dotted line, $\mu = 0.03$), quadratic (solid line, $\mu = 1.0$), and cubic (dashed-dotted line, $\mu = 2.0$) gradient energy based back stress (Eqs. (3.11) and (3.12)), with $\theta = 90°$, $h^{(\alpha\beta)} = h = 0$, $m = 0.02$, $L/H = 0.3$, and $\dot{U} = H\dot{\gamma}_0$.

purely phenomenological back stress, including the assumption of quadratic free energy throughout ($\kappa = 1.0$). Figures 4.18 and 4.19, on the other hand, show that there is a significant difference in the micro-structure predicted when deviating from the classical back stress formulation based on quadratic free energy ($\mu = \kappa = 1$). The figures show the GND density normalized with the value at the boundary, $\rho^{(1)}_{G(e),B}$, at $\Gamma = 0.03$ after the final load step. Results are shown for different values of μ and κ, respectively. Figure 4.18 shows that, compared to a quadratic free energy, a more localized pile up of GNDs is predicted near the micro-structurally passivated boundaries, when approaching a linear gradient energy ($\mu = 0.01, 0.03$). Similarly, when assuming a cubic free energy ($\mu = 2$), localization of GNDs is achieved at the boundaries. However, clear qualitative differences are observed here, in that dislocations of opposite sign appear to pile up adjacent to the dislocation walls at the passivated boundaries. For the purely phenomenological formulation a clearly localized micro-structure is achieved with a low power law dependence ($\kappa = 0.1$) compared to the traditional quadratic free energy assumption.

As evident from Figs. 4.18 and 4.19, this additional modeling capability is useful when seeking realistic micro-structures, and cannot be achieved in the classical type of back stress formulation (corresponding to $\mu = \kappa = 1$), where the material length scale parameter, L, alone governs the micro-structural behavior.

4.3 Rate-independent results

The following numerical study demonstrates the existence of characteristic slip rates, at which specific macroscopic quantities becomes independent of the rate sensitivity exponent (see also El-Naaman et al., 2016a, [P4]). To this end, once again, the idealized simple shear case for a single crystal is considered and the model parameters used are given in Section

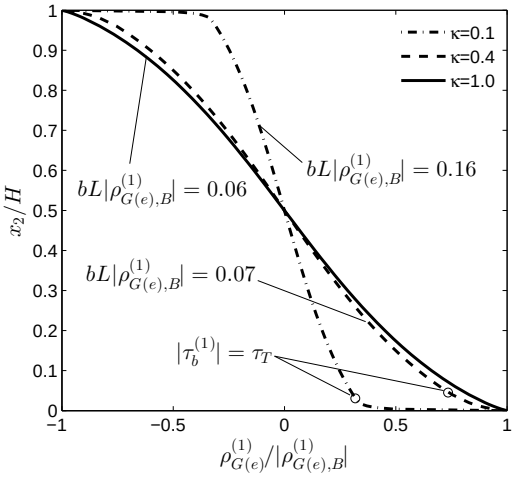

Figure 4.19: Predicted GND micro-structure, at $\Gamma = 0.03$ after two load cycles, using the back stress power law (Eq. (3.14)) with $\kappa = 0.1$ and $\kappa = 0.4$, and $\tau_T/\tau_0 = 0.06$, compared with the the classical quadratic gradient energy based back stress formulation ($\kappa = 1.0$), with $\theta = 90°$, $h^{(\alpha\beta)} = h = 0$, $m = 0.02$, $L/H = 0.3$, and $\dot{U} = H\dot{\gamma}_0$. Circles mark the back stress transition point ($|\tau^{(1)}_b| = \tau_T$) near the lower horizontal boundary.

4.2. The phenomenon was first discussed in detail by Nielsen and Niordson (2012) and later exploited in Nielsen et al. (2012) to extract rate-independent results from a rate-dependent framework. Nielsen (2015) also found similar results for steady-state sheet rolling. Characteristic rates may exist for a wide range of other structural problems, and a broader sense of the phenomenon is demonstrated, here focusing on the macroscopic response of the adopted gradient crystal plasticity model. The model rate sensitivity is investigated, and a problem dependent characteristic rate is identified for constrained simple shear. As in Section 4.2, the material domain is sheared to a macroscopic shear strain $\Gamma = 0.03$, after which, one complete load cycle is performed, so that the macroscopic shear strain goes once to -0.03 and back to 0.03. Care was taken to ensure that a steady state cyclic response is obtained by running multiple load cycles about the zero strain axis.

In order to identify the characteristic rate for a given specific quantity, a simple procedure is carried out. This procedure implies running a series of calculations for different values of the rate exponent, m, so that the quantity of interest can be plotted as function of the applied rate for each value of m. The convergent intersection between the curves then reveals the quantity specific rate-independent point. The existence of a well defined intersection is contingent upon the quantity investigated being monotonically increasing or decreasing with the rate sensitivity in an interval above and below the characteristic rate, respectively. Note that in order to identify the rate-independent point it is not necessary to employ low values of m, since the intersection may be obtained for curves at any given rate sensitivity. Indirectly introduced through the reference slip rate, $\dot{\gamma}_0$, in Eq. (2.2), the rate-independent point, tied to the characteristic rate, may open the door for a parameter space, which is otherwise inaccessible due to the numerical difficulties associated with the limit $m \to 0$ (see also Nielsen et al., 2012). The Kuroda and Tvergaard (2006, 2008) theory is not formulated in a rate-independent framework, however, rate-independent results

may readily be extracted by identifying the characteristic rate through the aforementioned procedure. In the following, this will be demonstrated for the maximum attained shear stress on the hysteresis curve, $|\tau_{12}|_{max}$.

Figures 4.20 and 4.21 show $|\tau_{12}|_{max}$ as function of the applied shear rate. Figure 4.20 shows results obtained using the thermodynamically consistent back stress formulation (Eq. (3.12)) for different values of μ and L, and Fig. 4.21 shows results obtained using the purely phenomenological back stress formulation (Eq. (3.14)) for different values of κ and L. Clearly convergent intersections are observed for both back stress models, which occur at a higher shear stress when L is increased, due to the increased strain gradient hardening. Furthermore, the intersection translates slightly toward lower rates for increasing L. The peak in strain gradient hardening at intermediate values of μ discussed in Section 4.1 is evident in Fig. 4.20a for $\mu = 0.3$.

Analogous to the results obtained for the maximum shear stress, $|\tau_{12}|_{max}$, rate-independent points also exist for the dissipated hysteresis energy, which is defined as the area inside the hysteresis loop. However, the results are omitted, since a high level of coincidence between the curves impair a graphical representation. This is due to the fact that, while the shape of the hysteresis loop changes significantly, the area remains approximately the same for all computations. The uncertainty in the intersections for the hysteresis energy were found to be on the order of 0.5 percent (or below).

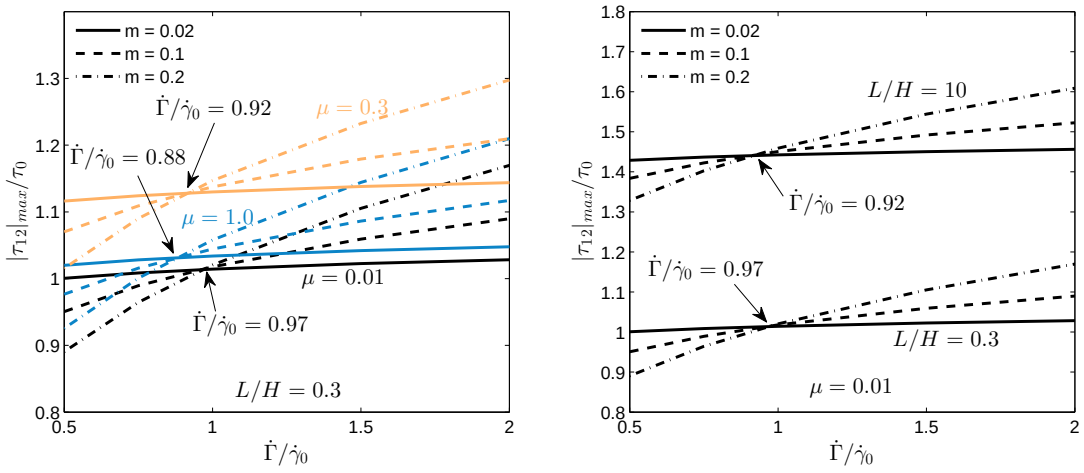

Figure 4.20: Maximum shear stress vs. macroscopic shear strain rate for three different values of the rate sensitivity exponent m. The figure shows (a) results for three different values of μ with $L/H = 0.3$, and (b) results for two different values of L with $\mu = 0.01$. The characteristic rates corresponding to the intersections are given in the figures.

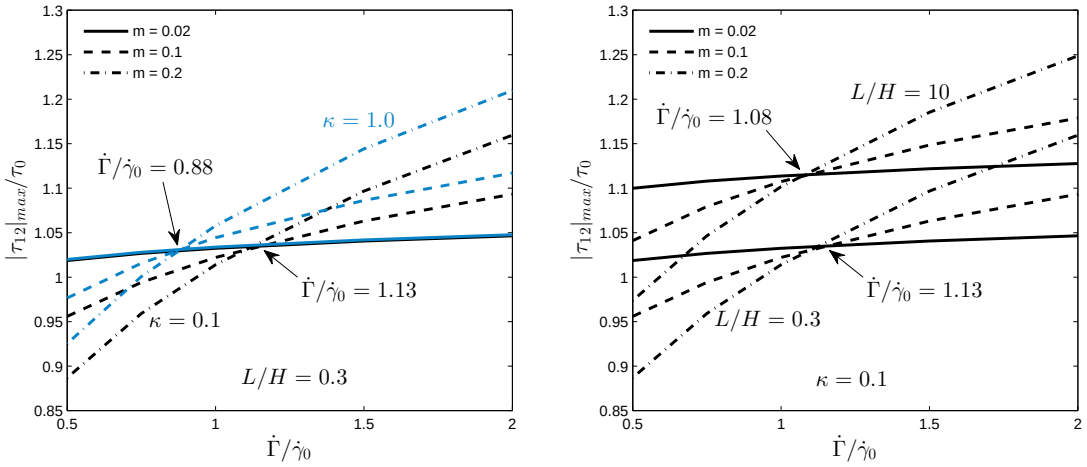

(a) (b)

Figure 4.21: Maximum shear stress vs. macroscopic shear strain rate using the back stress power law (Eq. (3.14)) for three different values of the rate sensitivity exponent m. The figure shows (a) results with $\kappa = 0.1$ and $\tau_T/\tau_0 = 0.06$, compared with the the classical quadratic gradient energy based back stress, both with $L/H = 0.3$, and (b) shows results for two different values of L with $\kappa = 0.1$. The characteristic rates corresponding to the intersections are given in the figures.

4.4 Plane strain deformation around a cylindrical void in an FCC crystal

In the following a two dimensional multi-slip numerical analysis is carried out employing the framework developed in Section 3.3. Here, plane strain deformation in the (110) plane of an FCC single crystal is considered. The crystal contains a cylindrical void and is loaded in far-field equi-biaxial tension. The boundary value problem is illustrated in Fig. 4.22a, with the definition of slip systems shown in Fig. 4.22b. Throughout, the following model parameters are used: Young's modulus $E = 63{,}9$ GPa, Poisson's ratio $\nu = 0.36$, $\tau_0 = 10$ MPa, $\dot{\gamma}_0 = 10^{-3}$, $b = 0.286$ nm, and $m = 0.02$. Zero conventional hardening is assumed, so that , $h^{(\alpha\beta)} = h = 0$. The crystal is subjected to the equi-biaxial macroscopic strain $\Gamma_{biaxial} = \delta_{biaxial}/R = 3.75\text{x}10^{-4}$. Figure 4.23 shows the finite element mesh used for the numerical analysis.

The evolution of the void area with respect to macroscopic biaxial straining is shown in Fig. 4.24 for different values of L and the exponents μ and κ. The void area is numerically integrated by the trapezoid rule.

Figure 4.25 shows the slip on each of the effective slip systems for zero material length scale parameter ($L = 0$) normalized with a reference slip, while Fig. 4.26 shows the total slip, defined as the sum of the absolute value of slip on each effective slip system. The reference slip is defined as $\gamma_{ref} = \tau_0/G$, where G is the shear modulus. Figure 4.27 shows the GND density on each of the effective slip systems for zero material length scale parameter ($L = 0$) normalized with a reference density, while Fig. 4.28 shows the total GND density, defined as the sum of the absolute value of GND density on each

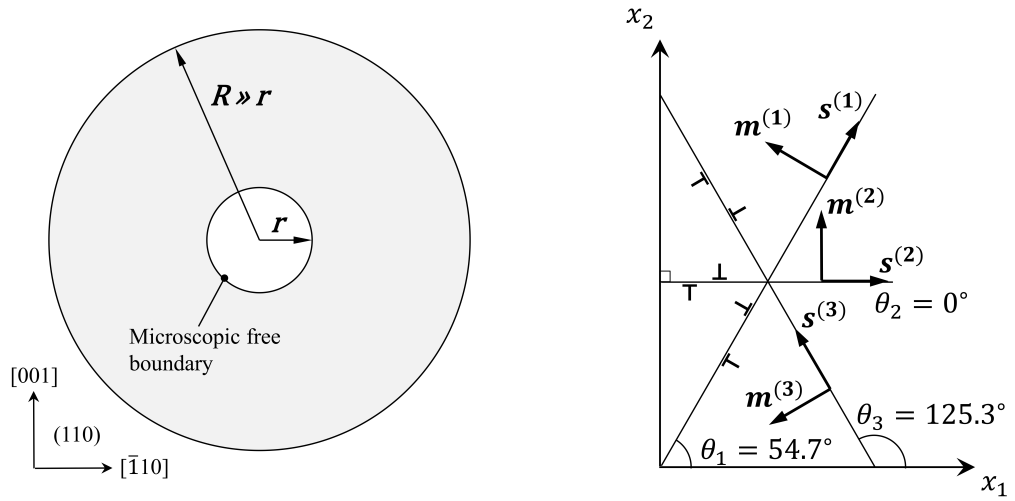

(a) (b)

Figure 4.22: Illustraion of the boundary value problem: (a) the (110) crystallographic plane material domain with a cylindrical void, which is modeled with a microscopic free boundary along the inner perimeter and subject to equi-biaxial tension in the (110) plane. (b) definition of the effective in-plane slip systems for the FCC crystal.

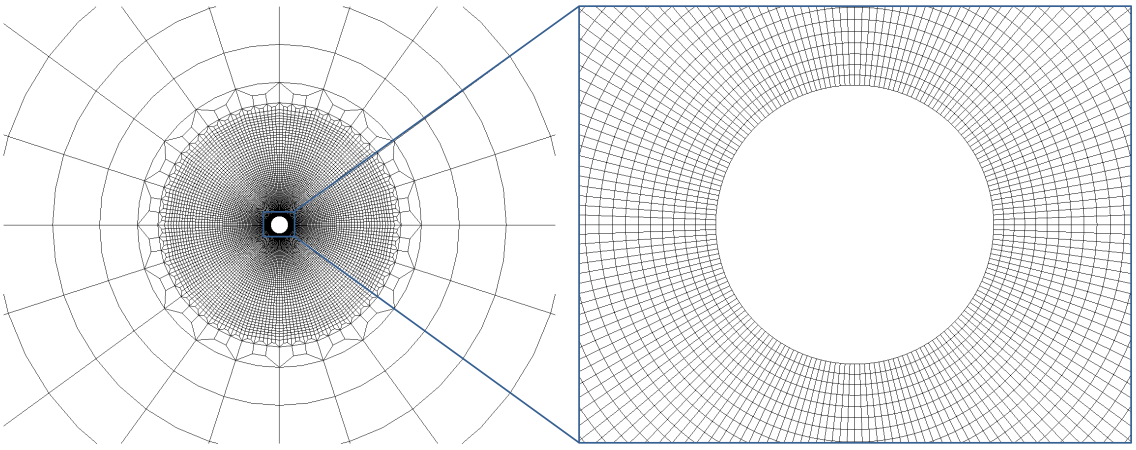

Figure 4.23: The finite element mesh employed for the analysis on the left with a zoom of the void region on the right.

effective slip system. The reference GND density is defined as $\rho_{ref} = \gamma_{ref}/(br)$. The scaling provided through $\beta^{(\alpha)}$ and $\lambda^{(\alpha)}$ results in more curved slip lines and GND density contours. The results show consistency with the lattice rotation measurements performed on a compression tested single crystal with a cylindrical void by Gan et al. (2006). In these measurements the curved lines, seen in the slip and GND contours predicted with the numerical model, are visible. The density on slip systems (1) and (3), may be considered as a combination of edge and screw density, while the density on slip system (2) is of pure

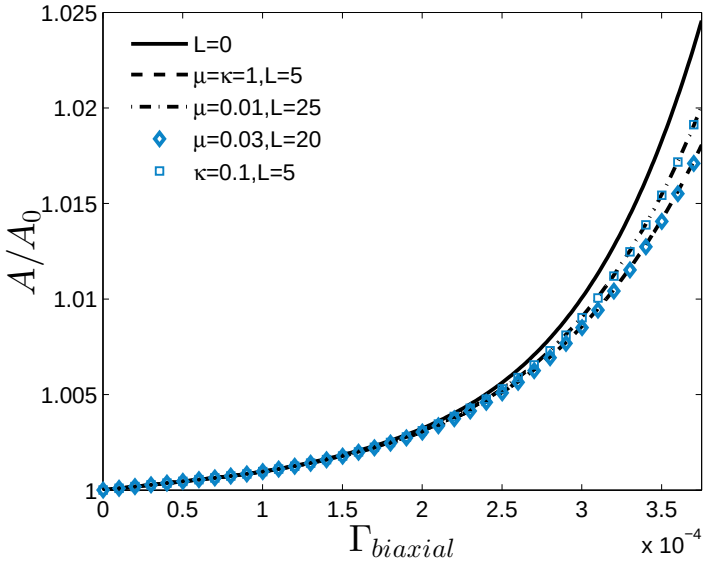

Figure 4.24: Predicted macroscopic response for different material parameters showing void area as function of macroscopic biaxial straining.

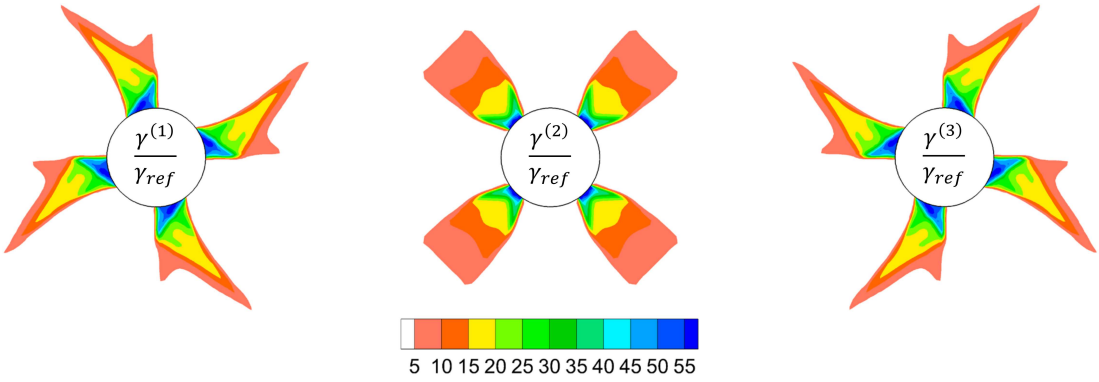

Figure 4.25: Predicted crystallographic slip on each of the slip systems for $L = 0$.

edge character. Neglecting the cancellation of the screw density on slip system (2) in the analysis, and evaluating the screw density based on the slip gradient in the direction of $\mathscr{P}_i^{(2)} = m_i^{(2)}$, would be equivalent to the edge density shown in Fig. 4.27, however, it would be rotated 90° clockwise about the void axis ([110] direction).

The size-effects on void growth and micro-structure are now analyzed by employing a material length scale parameter of $L/r = 5$ and assuming a quadratic gradient energy based back stress. This corresponds to having $\mu = \kappa = 1$ in Eqs. (3.23) and (3.24). Figure 4.29 shows the total accumulated slip, which is suppressed by the effect of strain gradients. Moreover, a more widely spread development of slip, creates more overlap between the single slip sectors compared to the conventional solution. Figure 4.30 shows the total predicted GND density, which reflects the smaller size of the plastically deforming region

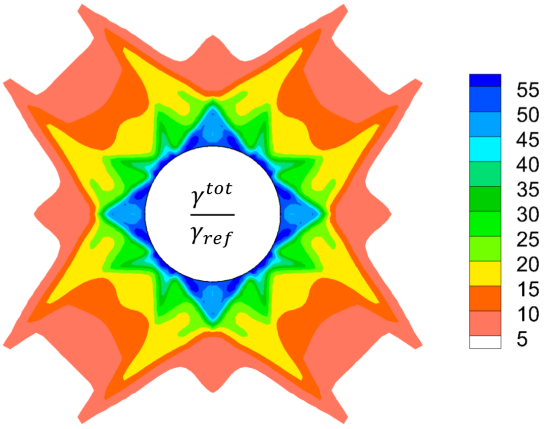

Figure 4.26: Total slip for $L = 0$.

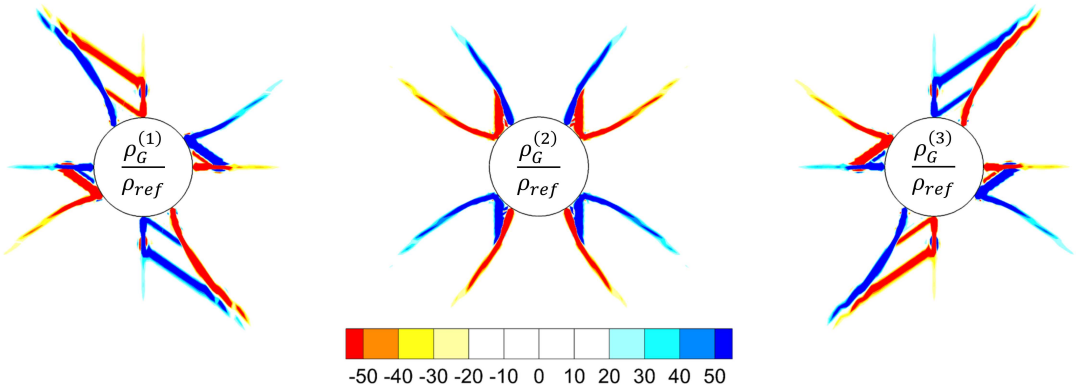

Figure 4.27: GND density on each of the slip systems for $L = 0$.

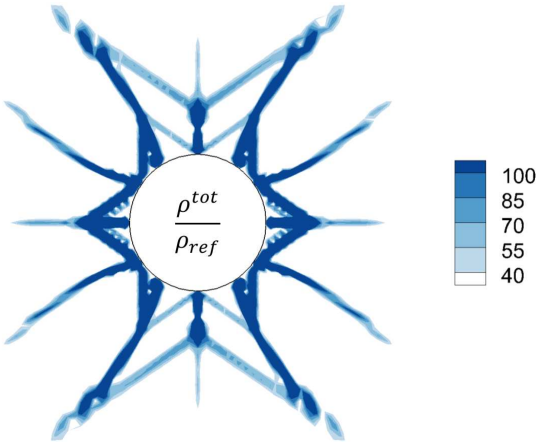

Figure 4.28: Total GND density for $L = 0$.

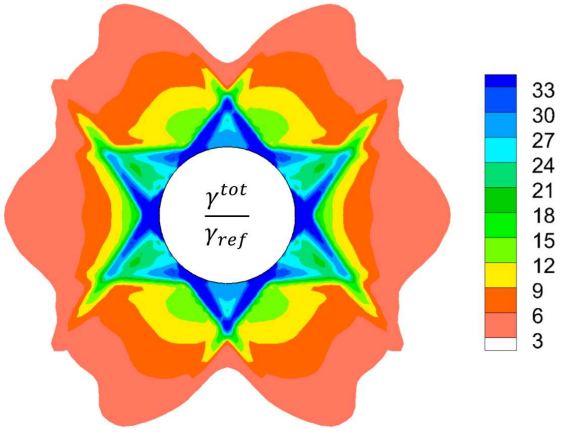

Figure 4.29: Total slip for $L/r = 5$ assuming quadratic gradient energy.

by less localized GND structures. Structures along the effective slip planes appear together with secondary orthogonal structures (see also El-Naaman et al., 2016d, [P5]). The length scale effect is based on the internal back stress field, $\tau_b^{(\alpha)}$, which is shown for each effective slip system in Fig. 4.31 normalized with the effective critical resolved shear stress. The back stress on each slip system develops in directions perpendicular to the slip planes, with features that run along the slip directions of the two other effective slip systems. Furthermore, it is observed that a spatially larger stress field develops on slip system (2) compared to systems (1) and (3). In comparison to the assumption of quadratic gradient energy, no immediate effect of the parameters μ and ρ_0 were found independent of L, when employing the back stress (3.23) resulting from the generalized gradient energy potential (3.21). This contradicts the findings in El-Naaman et al. (2016c) and El-Naaman et al. (2016b). However, a more elaborate parametric study for the current type of boundary value problem may reveal other capabilities. As an example of the findings of the present study, the computation for $\mu = 0.03$ with $L = 20$ has a macroscopic response very close to the one for quadratic gradient energy with $L = 5$. Despite the different setup of the back stress in the two computations, there is no significant difference in the predicted micro-structure. On the other hand, when comparing the micro-structures predicted using back stress (3.23) with $L/r = 25$, $\mu = 0.01$, and $\rho_0 = 10^5$ mm^{-2} (Fig. 4.32a), with those obtained using back stress (3.24) with $L/r = 5$, $\kappa = 0.1$, and $\tau_T/\tau_0 = 0.2$ (Fig. 4.32b), these show significant differences despite the fact that the void growth vs. biaxial straining curves are virtually identical (see Fig. 4.24). The GND density in Fig. 4.32a extends farther out from the void, while a tendency toward developing structures parallel to effective slip system (2) is observed in Fig. 4.32b. The different behaviors resulting from the two different back stress formulations is clearly reflected in their very different stress fields shown in Figs. 4.33 and 4.34. The field obtained for effective slip system (2), using the phenomenological back stress (3.24), develops more contour lines parallel to the slip system, which also extend farther out from the void. For all three slip systems in Fig. 4.34, additional features are developed compared to Fig. 4.33. The power law part of the piece-wise back stress function (3.24) governs only a very minor part of the back stress field shown in Fig. 4.34. More details can be found in El-Naaman et al. (2016d) (see [P5]).

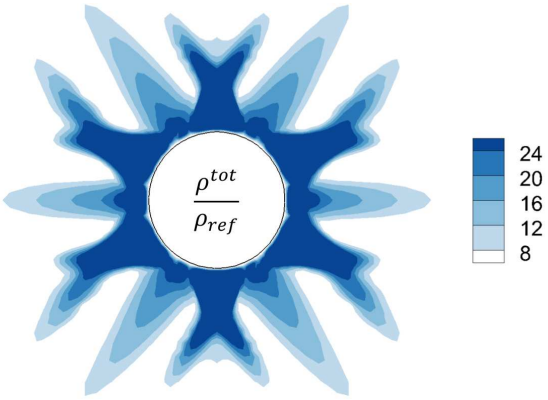

Figure 4.30: Total GND density for $L/r = 5$ assuming quadratic gradient energy.

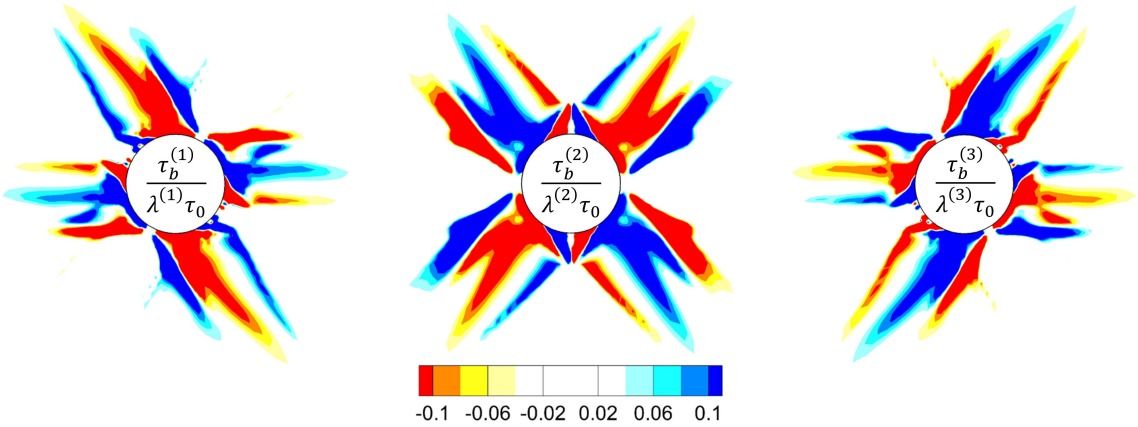

Figure 4.31: Back stress on each of the slip systems for $L/r = 5$, assuming quadratic gradient energy.

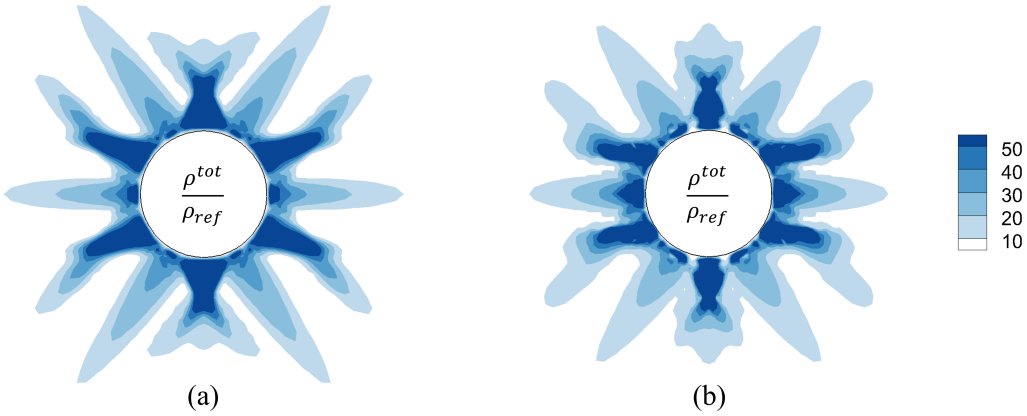

Figure 4.32: Total GND density. (a) Using the thermodynamically consistent back stress (3.23) with $L/r = 25$, $\mu = 0.01$, and $\rho_0 = 10^5$ mm^{-2}, and (b) using the phenomenological back stress (3.24) with $L/r = 5$, $\kappa = 0.1$, and $\tau_T/\tau_0 = 0.2$.

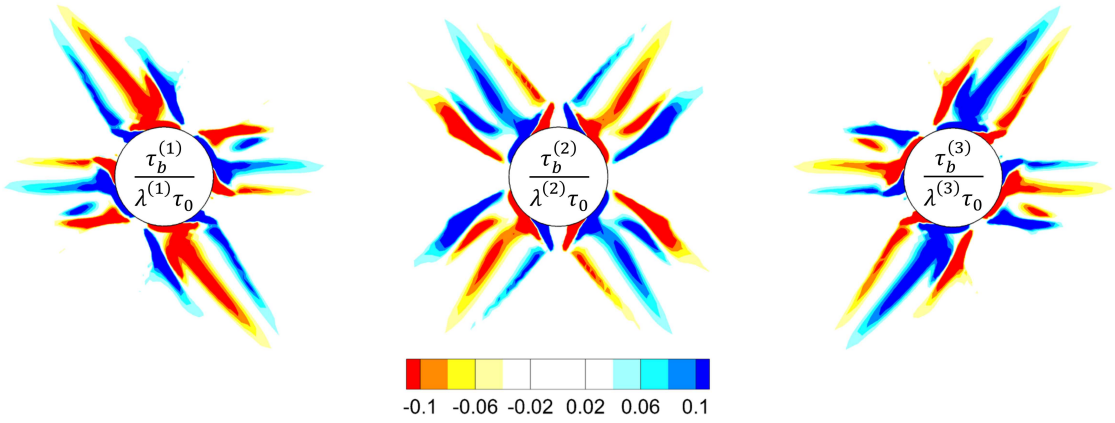

Figure 4.33: Back stress on each of the slip systems using back stress relation (3.23) with $L/r = 25$, $\mu = 0.01$, and $\rho_0 = 10^5$ mm^{-2}.

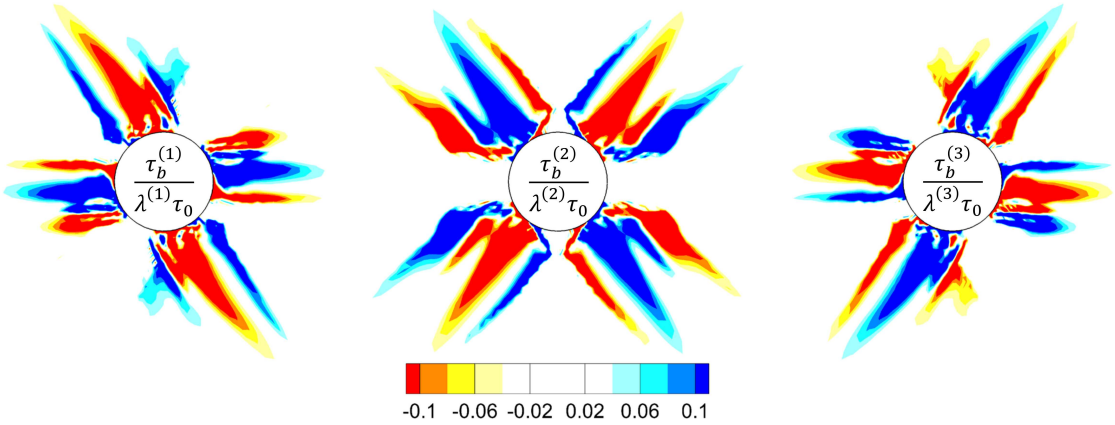

Figure 4.34: Back stress on each of the slip systems using back stress relation (3.24) with $L/r = 5$, $\kappa = 0.1$, and $\tau_T/\tau_0 = 0.2$.

Chapter 5

Experimental considerations

5.1 Experimental design

The purpose of the experimental study is to investigate the interaction of a blunt notch tip, subject to Mode I loading, with a single void in front. Here, the evolution of geometrically necessary dislocation structures is of particular interest. The experimental investigation is expected to supply new insight into the micro-mechanics of ductile fracure. Similar to the studies of e.g. Kysar et al. (2010) and Dahlberg et al. (2014), an FCC single crystal is considered, which shall be oriented and loaded such that a state of plane strain deformation, in the (110) crystallographic plane, prevails in a significant part of the cross-section. This state is facilitated by activity on three effective in-plane slip systems as described in Section 3.3. The plane strain deformation enables the subsequent application HR-EBSD techniques to obtain a detailed measure of the GND density (Öztop, 2011). The general concept for the single crystal experimental set-up is illustrated in Fig. 5.1. The crystal is supported by a rigid base on the $(1\bar{1}1)$ plane, and the notch is loaded by a wedge, driven into a widened part of the notch, forcing the notch faces apart in a mode I loading. The design of the single crystal notch and void specimen (NVS) and some central theory behind the measurement of GNDs are described in the following sections.

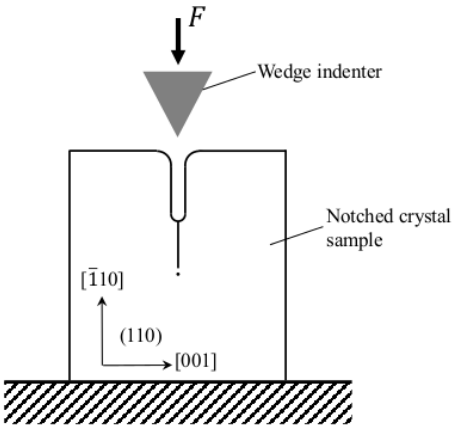

Figure 5.1: Schematic of the experimental setup.

5.2 Preparation and crystallographic orientation of the aluminum crystal

The as-grown six-nine (99.999999% pure) aluminum crystal was oriented using Laue X-ray diffraction. To remove oxide from the surface, the crystal was etched in a 0.1 mol/l water solution of Sodium hydroxide (NaOH) for approximately 15 minutes. The as-grown crystal is shown in Fig. 5.2a mounted in a goniometer. Laue X-ray Diffraction images were captured using a Philips XRG 3100 X-ray Generator with a Polaroid image detector. The misorientation was calculated using OrientExpress 3.4, and the solution obtained prescribed rotations of [-19.62° 2.70° -0.42°] about the x_1, x_2, and x_3 directions, respectively, in order to align the (110) crystallographic plane with the image plane. Figure 5.3 shows Laue X-ray diffraction images with the OrientExpress solutions overlain before and after the prescribed rotations.

After crystallographic orientation the crystal was machined using a Mitsubishi wire type electrical discharge machine (EDM), according to the crystallographic planes (see Fig. 5.2b). The final 25.1x23.25x12.88 mm cuboid crystal sample is shown in Fig. 5.2c.

To obtain an order of magnitude estimate of the yield stress of the aluminum crystal, a Vickers hardness micro-indentation test was performed in the [001]-direction on a sample piece of the aluminum single crystal. The Vickers hardness value, H_v, allegedly relates to the yield stress as $\sigma_y \sim 3.3H_v$ (Tabor, 1948), however, the results obtained for the crystal, $\sigma_y = 62$ MPa, are considered highly overestimated. Based on channel die tests the yield stress, is expected to be about 10 MPa.

The sample piece was subsequently finely sanded and polished, and afterwards, electro-polished according to ASTM Standard Method El-10 (Geels, 2006), however it was noticed that the specified current according to the standard was not reached during the procedure. The electro-polishing is performed in order to remove the mechanically affected layer, to obtain a deformation free surface. Nano-indentation tests were conducted on the polished (001) plane, using a 65° diamond wedge with an 800 micron edge length. The indenter load cell only allowed for indentation depths of about 5 to 6 microns, and no immediate size-effects could be identified. Force vs. indentation depth curves for the single crystal sample, as well as a fully annealed 1050 aluminum poly crystal reference sample, can be found in Appendix B.

5.3 Analyzing the dimensions of the notch and void specimen

The notch and void specimen is intended for studying the interaction of a blunt edge notch with a void. A number of parameters must be considered in the experimental design and design of the test specimen. It is crucial that a two dimensional (2D) plastic strain field is maintained, in order to subsequently be able to measure the geometrically necessary dislocation densities. Furthermore, the void in front of the notch tip is desired to be well inside the K dominated field to achieve a well developed interaction. As a starting point, an analytical parameterization of the specimen shall determine the basic design. The design parameters are the thickness dimension, t, the notch tip radius, R, the void diameter, D, and the distance between the notch tip and the void, l, measured from center

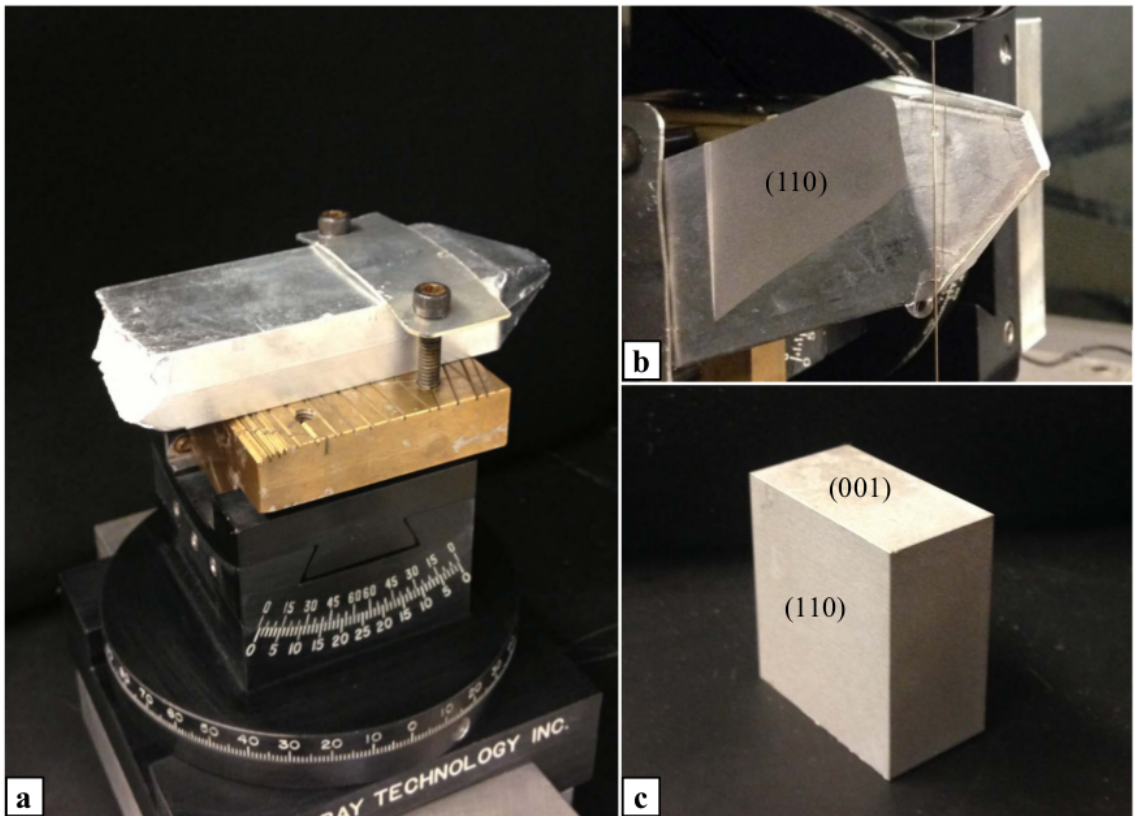

Figure 5.2: (a) The as-grown crystal mounted in the goniometer for orientation. (b) The (110) surface has been exposed by wire electrical discharge machining (EDM). (c) The final resulting cuboid cut according to the crystallographic orientations.

to center. It is decided that the relationship between the notch tip radius and the void diameter are fixed so that $R = D/2$. For a given Mode I stress intensity factor, K_I, the thickness, t, conforming to the standards for plane strain conditions, and the size of the plastic zone, S_{PZ}, can be approximated by the following relations

$$t > 2.5 \left(\frac{K_I}{\sigma_y} \right)^2 \tag{5.1a}$$

$$S_{PZ} \simeq \frac{1}{6\pi} \left(\frac{K_I}{\sigma_y} \right)^2, \tag{5.1b}$$

where σ_y is the initial yield stress. According to the standards a significant portion of the thickness is dominated by a state of approximate plane strain when the inequality of Eq. (5.1a) is fulfilled, whereas a state of plane stress prevails when approaching the free surfaces. Normalizing (5.1b) with (5.1a), the size of the plastic zone relates to the thickness as

$$S_{PZ} \simeq \frac{1}{15\pi} t. \tag{5.2}$$

Imposing that the void shall be situated inside the plastic zone but may not overlap with the notch tip, entails that $S_{PZ} > D$ and thus a lower limit for the specimen thickness to

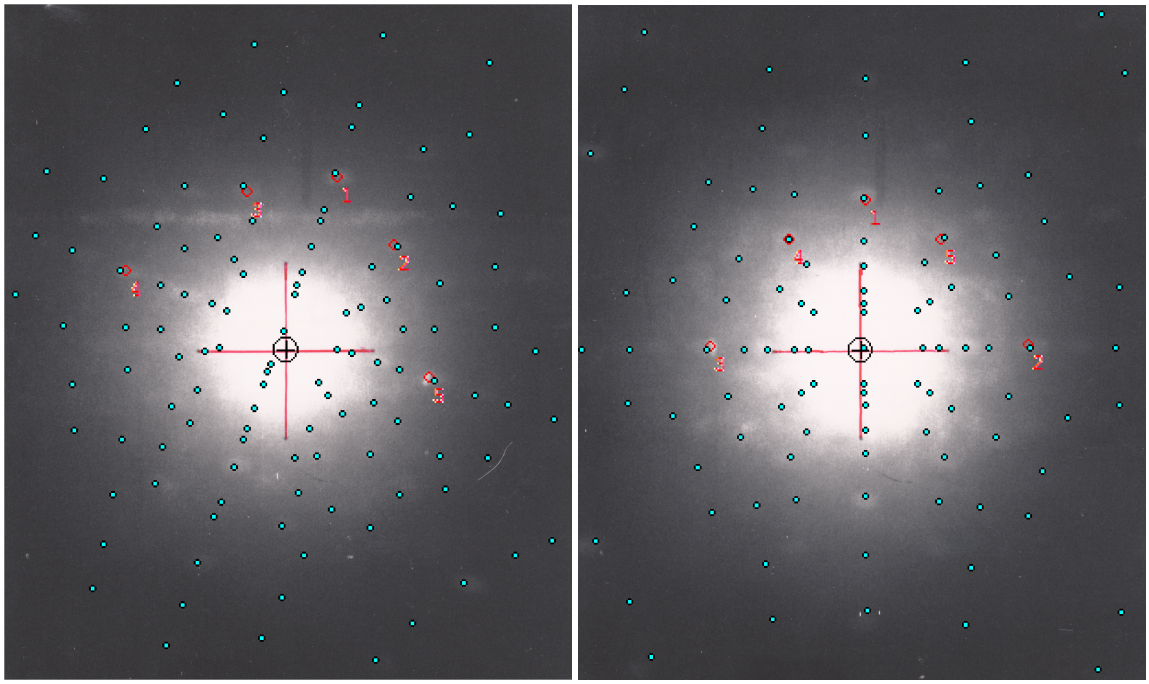

(a) (b)

Figure 5.3: X-rays with OrientExpress solution overlain. (a) Initial orientation. (b) After rotations of [-19.62° 2.70° -0.42°].

maintain plane strain conditions can be expressed in terms of the notch to void distance as

$$t = 15\pi l \quad , \quad l > D. \tag{5.3}$$

Inserting Eq. (5.3) into Eq. (5.1a), the magnitude of K_I necessary in order to maintain plane strain deformation is then given by

$$K_I > \sigma_y \sqrt{6\pi l} \quad , \quad l > D. \tag{5.4}$$

Since the present limitations in machining the notch and void using wire electrical discharge machining (EDM) and plunge EDM dictates that the void diameter be approximately 127 μm and the void is placed so that the edge of the void does not go beyond the extent of the plastic zone, the lower limit for the thickness amounts to approximately 6 mm ($15\pi 127$ μm $\simeq$ 6 mm). It is expected that, in addition to the stress field due to loading of the notch, the stress concentration around the hole it self will extend the size of the plastic zone. A preliminary design of the single crystal specimen based on the dimensions of the machined crystal sample and the analysis above can be found in Appendix C.

For the further analysis, and in order to verify the plane strain assumption of the NVS, an elastic-plastic 3D FEM model was built using 20-node brick elements. Both an isotropic plasticity analysis was carried out with the commercial software ANSYS and a crystal plasticity analysis was carried out in ABAQUS using the crystal plasticity UMAT written by Huang (1991) and Kysar (1997). A power hardening approximation of the plastic

behavior was used for the isotropic model. The analysis showed that the assumption of plane strain is valid for the larger portion of the thickness.

5.4 The Nye tensor

The Nye dislocation density tensor, after Nye (1953), serves as a continuum description of geometrically necessary dislocations and provides a link between the elastic deformation and the plastic deformation within crystals. The presence of dislocations is associated with lattice distortion, and its direction and magnitude is expressed in terms of a Burgers vector (see Fig. 5.4). The lattice distortion is defined as

$$U_{ij} = u_{i,j} = U^e_{ij} + U^p_{ij}, \tag{5.5}$$

and the net Burgers vector is given by

$$\bar{b}_i = \int_{\partial A} U^p_{ij} \mathrm{d}x_j, \quad U^p_{ij} = \sum_\alpha \gamma^{(\alpha)} s^{(\alpha)}_i m^{(\alpha)}_j. \tag{5.6}$$

Applying Stoke's theorem for i = 1,2,3, the net Burgers vector can be written as the integral, over the surface A, of the surface normal projection of the curl of U^p_{ij}. Here, written in tensor form as

$$\bar{b}_i = \int_A e_{jlk} U^p_{ik,l} n_j \mathrm{d}A, \tag{5.7}$$

where e_{ijk} is a third order permutation tensor given by

$$e_{ijk} = \begin{cases} 1 & , \text{ for } ijk \in \mathrm{PG}(123) \\ 0 & , \text{ for } i = j \vee i = k \vee j = k \\ -1 & , \text{ for } ijk \in \mathrm{PG}(132) \end{cases}, \tag{5.8}$$

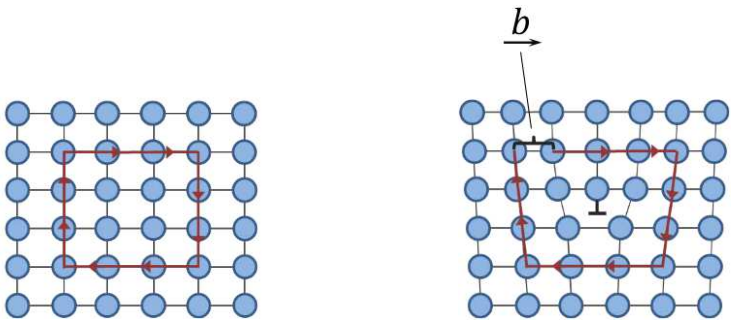

Figure 5.4: Schematic illustration showing the concept of closure failure and definition of Burgers vector. (a) Perfect crystal lattice domain with closed Burgers circuit (Red arrowed line). (b) A crystal lattice domain with a net Burgers vector: A single edge dislocation has entered the domain due to plastic slip causing lattice distortion and closure failure defined by the Right-hand-finish-to-start (RHFS) convention.

and PG(•) denotes permutation group. The integrand of Eq. (5.7) is identified as the net Burgers vector density

$$B_i = e_{jlk} U^p_{ik,l} n_j = \mathscr{G}_{ij} n_j, \tag{5.9}$$

where $\mathscr{G}_{ij}$ is the geometric dislocation tensor often referred to as the Nye tensor. Assuming that we have a continuous material, we can exploit that $e_{ijk}(U^e_{ij} + U^p_{ij})_{,k} = 0$, and thus the Nye tensor can be written

$$\mathscr{G}_{ij} = -e_{jlk} U^e_{ik,l} = e_{jlk} U^p_{ik,l}. \tag{5.10}$$

The elastic part of Eq. (5.10) can be written in terms of the elastic strains and rotations as

$$\mathscr{G}_{ij} = -e_{jlk} \left(\varepsilon^e_{ik} + W^e_{ik}\right)_{,l}, \tag{5.11}$$

with $\varepsilon^e_{ij} = 1/2(U^e_{ij} + U^e_{ji})$ and $W^e_{ij} = 1/2(U^e_{ij} - U^e_{ji})$. Since W^e_{ij} is skew-symmetric with only three different components, one can write a vector ω^e_k such that $W^e_{ij} = e_{ijk}\omega^e_k$, and thus

$$e_{jlk} W^e_{ik,l} = e_{jlk} e_{ikj} \omega^e_{j,l}, \tag{5.12}$$

Exploiting the relationship between Kronecker's delta, δ_{ij}, and the permutation tensor, $e_{ijk}e_{lmk} = \delta_{il}\delta_{jm} - \delta_{im}\delta_{jl}$, Eq. (5.12) can be rewritten as

$$e_{jkl} W^e_{il,k} = \delta_{ij}\omega^e_{k,k} - \omega^e_{i,j}. \tag{5.13}$$

Inserting Eq. (5.13) into Eq. (5.11), and identifying the lattice curvature as $\kappa_{ij} = \omega^e_{i,j}$, we obtain the Nye (1953) tensor given by

$$\mathscr{G}_{ij} = \kappa_{ij} - \delta_{ij}\kappa_{kk} - e_{kil}\varepsilon^e_{lj,k}. \tag{5.14}$$

Using Eq. (5.14) it is possible to determine the Nye tensor based on experimental measurements of the lattice rotations, assuming that the elastic contribution is negligible. However, in general, when using orientation imaging microscopy (OIM), not all components of the curvature tensor are readily available due to the lack of information in the direction perpendicular to the imaging plane. In the literature, this issue has been avoided by exploiting the symmetries in FCC crystals to obtain an approximate two-dimensional deformation state, where only three in-plane effective slip systems are active (e.g. Kysar et al., 2010; Öztop, 2011; Dahlberg et al., 2014).

Now, in order to determine the GND density based on the experimentally determined Nye tensor, one can exploit the plastic part of the relation (5.10), and U^p_{ij} expressed in terms of crystallographic slip (given in Eq. (5.6)). By the product rule, the spatial derivative of U^p_{ij} then reads

$$U^p_{ij,k} = \sum_\alpha \left(\gamma^{(\alpha)} \left(s^{(\alpha)}_{i,k} m^{(\alpha)}_j + s^{(\alpha)}_i m^{(\alpha)}_{j,k}\right) + \gamma^{(\alpha)}_{,k} s^{(\alpha)}_i m^{(\alpha)}_j\right). \tag{5.15}$$

Assuming small deformations, one can neglect the spatial derivatives of the unit vectors ($s^{(\alpha)}_{i,j} \simeq m^{(\alpha)}_{i,j} \simeq 0$), and thus, through Eq. (5.10), the Nye tensor can be written in terms of the spatial gradients of slip as

$$\mathscr{G}_{ij} = \sum_\alpha e_{ikl} \gamma^{(\alpha)}_{,k} s^{(\alpha)}_j m^{(\alpha)}_l. \tag{5.16}$$

The spatial gradients of slip, $\gamma^{(\alpha)}_{,k}$, can be expressed as a set of three orthonormal base vectors as

$$\gamma^{(\alpha)}_{,k} = \gamma^{(\alpha)}_{,i} s^{(\alpha)}_i s^{(\alpha)}_k + \gamma^{(\alpha)}_{,i} m^{(\alpha)}_i m^{(\alpha)}_k + \gamma^{(\alpha)}_{,i} p^{(\alpha)}_i p^{(\alpha)}_k, \tag{5.17}$$

with $p^{(\alpha)} = s^{(\alpha)} \times m^{(\alpha)}$. Inserting Eq. (5.17) into Eq. (5.16) yields

$$\mathscr{G}_{ij} = \sum_\alpha \left(\gamma^{(\alpha)}_{,k} s^{(\alpha)}_k s^{(\alpha)}_i p^{(\alpha)}_j - \gamma^{(\alpha)}_{,k} p^{(\alpha)}_k s^{(\alpha)}_i s^{(\alpha)}_j \right). \tag{5.18}$$

Using relation (2.6), this can be expressed in terms of GNDs as

$$\mathscr{G}_{ij} = b \sum_\alpha \left(\rho^{(\alpha)}_{G(s)} s^{(\alpha)}_i s^{(\alpha)}_j - \rho^{(\alpha)}_{G(e)} s^{(\alpha)}_i p^{(\alpha)}_j \right). \tag{5.19}$$

The total GND density is usually taken to be given by the Euclidean norm of the edge and screw components as

$$\rho^{(\alpha)}_{GND} = \sqrt{\left(\rho^{(\alpha)}_{G(e)}\right)^2 + \left(\rho^{(\alpha)}_{G(s)}\right)^2}. \tag{5.20}$$

Chapter 6

Concluding remarks

A finite element implementation of the non-work conjugate higher order strain gradient crystal plasticity model, proposed by Kuroda and Tvergaard (2006, 2008), has formed the basis in the development of back stress formulations, including considerations of free energy and phenomenological approaches, aimed at improving the ability to predict micro-structural evolution. An extensive numerical investigation was conducted, treating different scenarios for monotonic and cyclic loading of a single slip crystal domain in pure shear and a multi-slip two dimensional analysis of plane strain deformation in FCC crystals. It was shown that novel modeling capabilities are available through the proposed formulations in terms of prediction of micro-structure and capturing complex macroscopic behavior within a continuum framework. Following the theory of Gurtin (2000, 2002) in the derivation of the back stress, ensures thermodynamic consistency in the Kuroda & Tvergaard theory, and led to the formulation of a generalized back stress relation, in the present work, allowing an investigation of the form of the defect energy. Assuming a defect energy close to linear in the GND density gradients, results in a back stress relation much similar to relations obtained via discrete dislocation theory, and is in agreement with the view put forth by Evans and Hutchinson (2009). This back stress, in effect, has a non-constant coefficient, which evolves with the GND density. Here, it was found necessary to introduce a numerical parameter in the back stress, which resembles the presence of statistically stored dislocations in the discrete formulations. The introduction of the new parameter led to the capability of modeling a complex Bauschinger effect reported in the literature, where the hysteresis contains inflection points attributed to long range internal stresses. A more aberrant postulate of cubic defect energy was also studied, which, from a phenomenological point of view, was found to offer interesting capabilities in terms of dislocation wall formations. Apart from the defect energy based formulation, a purely phenomenological back stress formulation, proposed in the present work, was shown to posses capabilities similar to the energy based formulation, offering additional control of the microscopic vs. macroscopic model behavior.

New insight into the modeling of plane strain deformation in FCC crystals was obtained, through the proposed framework, in terms of effective equations and scaling coefficients. It was shown that the effective material length scale quantity is identical to its crystallographic counterpart. When analyzing deformation around a void an FCC crystal, the phenomenological back stress formulation predicted a more localized micro-structure, while the generalized defect energy based back stress formulation agreed with the bench-

mark quadratic defect energy approach.

In the authors opinion, further development of the proposed models should include more considerations of three dimensional crystallographic interaction effects associated with the evolution of micro-structure. To this end, employing quantities, such as the Nye tensor, in the free energy considerations and in the back stress formulation is necessary. Furthermore, future work should include more complex equations for governing the self and latent work hardening contributions to include effects such as dislocation line entanglement.

Future developments within the strain gradient theories may incorporate more physics into the models, or may adopt a more phenomenological approach. It is important to maintain focus on the application of the models. If these shall be applied to real problems, such as micron scale metal forming processes, they must capture the essence of the physics involved while maintaining practicality, not least in terms of computational feasibility. For this purpose, the continuum theories are a powerful tool. However, much valuable insight is gained from the physics based models, which may be useful in the formulation of phenomenological models. It is the authors opinion that research in both areas is highly beneficial.

Appendices

A Generalized back stress model accounting for edge and screw dislocations

Through Eqs. (3.4) and (3.6), the generalized gradient energy potential (Eq. (3.18)) leads to the following back stress

$$\begin{aligned}\tau_b^{(\alpha a)} = \tau_b^{(\alpha a)} = \frac{1}{\lambda^{(\alpha)}}\tau_b^{(\alpha)} = \tau_0 L^{\mu+1}\left\{\sqrt{\left(\gamma_{,m}^{(\alpha a)}s_m^{(\alpha a)}\right)^2+\left(\gamma_{,m}^{(\alpha a)}p_m^{(\alpha a)}\right)^2}\right\}^{\mu-3}\\ \left\{(\mu-1)\gamma_{,k}^{(\alpha a)}s_k^{(\alpha a)}\left(\gamma_{,i}^{(\alpha a)}s_i^{(\alpha a)}s_j^{(\alpha a)}+\gamma_{,i}^{(\alpha a)}p_i^{(\alpha a)}p_j^{(\alpha a)}\right)\gamma_{,jl}^{(\alpha a)}s_l^{(\alpha a)}+\right.\\ (\mu-1)\gamma_{,k}^{(\alpha a)}p_k^{(\alpha a)}\left(\gamma_{,i}^{(\alpha a)}s_i^{(\alpha a)}s_j^{(\alpha a)}+\gamma_{,i}^{(\alpha a)}p_i^{(\alpha a)}p_j^{(\alpha a)}\right)\gamma_{,jl}^{(\alpha a)}p_l^{(\alpha a)}+\\ \left.\left[\left(\gamma_{,k}^{(\alpha a)}s_k^{(\alpha a)}\right)^2+\left(\gamma_{,k}^{(\alpha a)}p_k^{(\alpha a)}\right)^2\right]\left(\gamma_{,ij}^{(\alpha a)}s_j^{(\alpha a)}s_i^{(\alpha a)}+\gamma_{,ij}^{(\alpha a)}p_j^{(\alpha a)}p_i^{(\alpha a)}\right)\right\},\end{aligned} \tag{A.1}$$

$\Updownarrow$

$$\begin{aligned}\tau_b^{(\alpha a)} = \tau_0 L^{\mu+1}\left\{\sqrt{\left(\gamma_{,m}^{(\alpha a)}s_m^{(\alpha a)}\right)^2+\left(\gamma_{,m}^{(\alpha a)}p_m^{(\alpha a)}\right)^2}\right\}^{\mu-3}\left(s_i^{(\alpha a)}s_j^{(\alpha a)}+p_i^{(\alpha a)}p_j^{(\alpha a)}\right)\\ \left\{(\mu-1)\gamma_{,i}^{(\alpha a)}\gamma_{,k}^{(\alpha a)}\left(s_k^{(\alpha a)}s_l^{(\alpha a)}+p_k^{(\alpha a)}p_l^{(\alpha a)}\right)\gamma_{,jl}^{(\alpha a)}+\left[\left(\gamma_{,k}^{(\alpha a)}s_k^{(\alpha a)}\right)^2+\left(\gamma_{,k}^{(\alpha a)}p_k^{(\alpha a)}\right)^2\right]\gamma_{,ij}^{(\alpha a)}\right\},\end{aligned} \tag{A.2}$$

which can be reduced to

$$\tau_b^{(\alpha a)} = \mu\tau_0 L^{\mu+1}\left\{\sqrt{\left(\gamma_{,k}^{(\alpha a)}s_k^{(\alpha a)}\right)^2+\left(\gamma_{,k}^{(\alpha a)}p_k^{(\alpha a)}\right)^2}\right\}^{\mu-1}\gamma_{,ij}^{(\alpha a)}\left(s_i^{(\alpha a)}s_j^{(\alpha a)}+p_i^{(\alpha a)}p_j^{(\alpha a)}\right). \tag{A.3}$$

Written in terms of GND densities, Eq. (A.3) becomes

$$\tau_b^{(\alpha a)} = \mu\tau_0 b^{\mu} L^{\mu+1}\left\{\sqrt{\left(\rho_{G(e)}^{(\alpha a)}\right)^2+\left(\rho_{G(s)}^{(\alpha a)}\right)^2}\right\}^{\mu-1}\left(\rho_{G(e),i}^{(\alpha a)}s_i^{(\alpha a)}+\rho_{G(s),i}^{(\alpha a)}p_i^{(\alpha a)}\right). \tag{A.4}$$

In order for this back stress to be evaluated in the (110) plane strain FCC model, one must introduce the plane strain slip gradients and second order gradients with effective unit vector and associated scaling quantities as described in Section 3.3.

B Nano-indentation curves

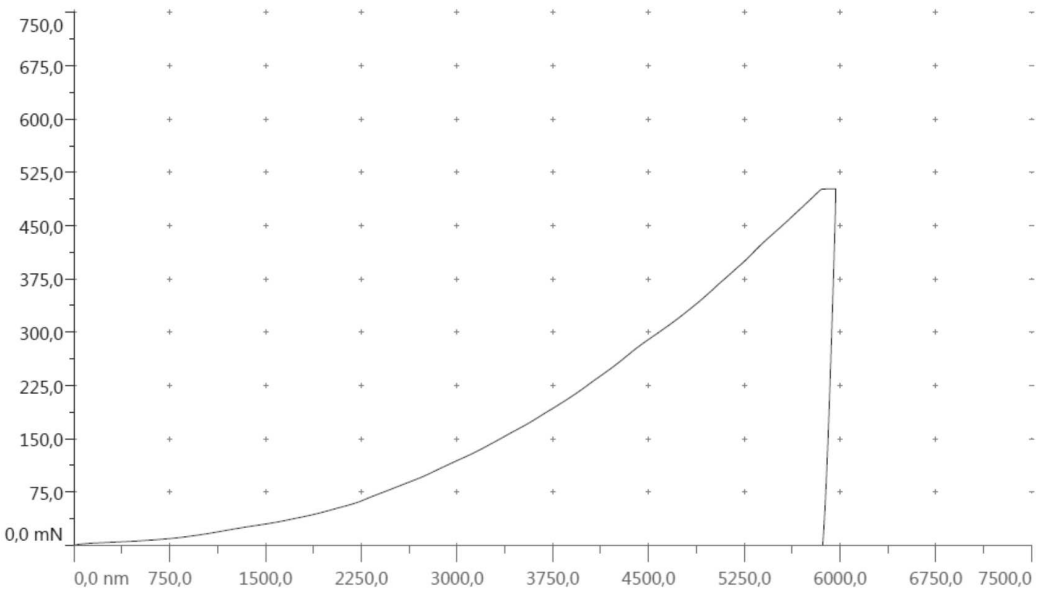

Figure .1: Force vs. indentation depth curve for nano-indentation into the (001) crystallographic plane of a single crystal aluminum sample, using a 65° diamond wedge with an 800 micron edge length.

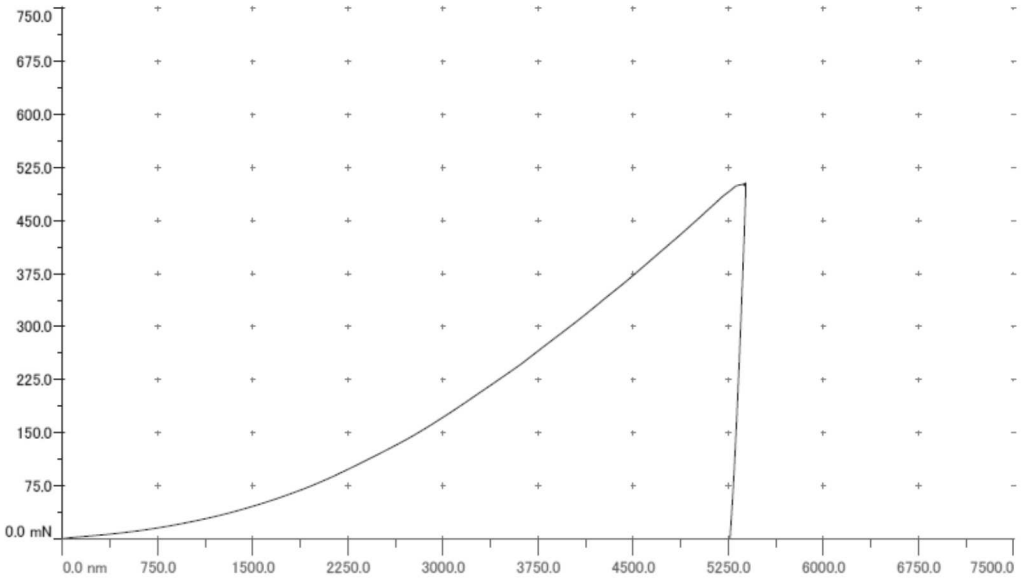

Figure .2: Force vs. indentation depth curve for nano-indentation of a fully annealed 1050 aluminum poly crystal, using a 65° diamond wedge with an 800 micron edge length.

C Engineering drawing of the single crystal specimen

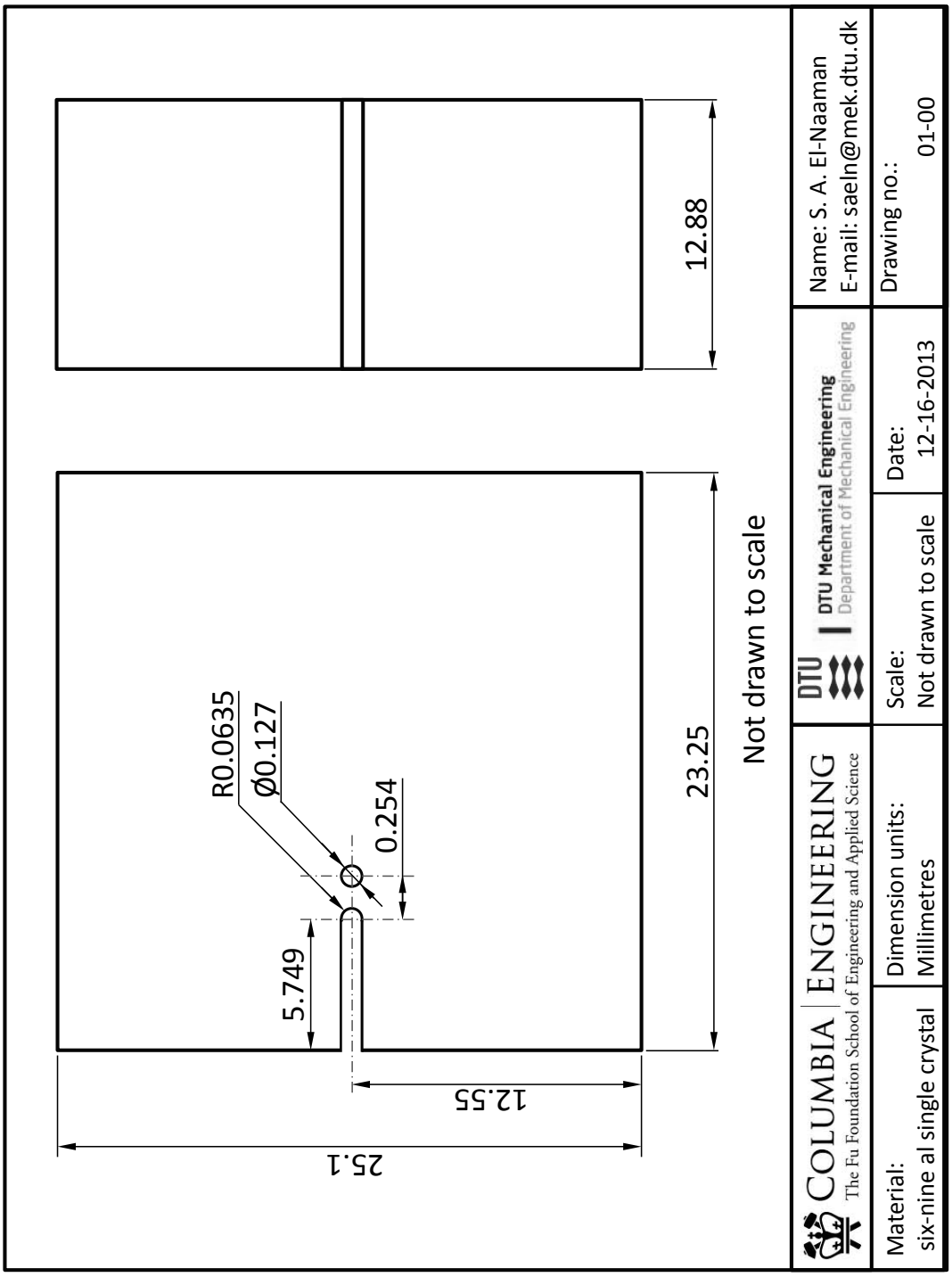

D Errata [P2]

Two minor mistakes have been found in the the publication (El-Naaman et al., 2016c, [P2]). These are accounted for below:

i. Units on numerical quantity ρ_0, were given as m^{-2}, however, the correct unit is mm^{-2}.

ii. In the proposed piece-wise back stress formulation (Eq. 22 in El-Naaman et al., 2016c, [P2]), the conditional statements should be dependent on the absolute value of the back stres, so that the equation reads:

$$\tau_b^{(\alpha)} = \begin{cases} b\tau_0 L^2 \rho_{G(e),i}^{(\alpha)} s_i^{(\alpha)} & , \text{ for } |\tau_b^{(\alpha)}| \leq \tau_T \\ \operatorname{sgn}\left(\rho_{G(e),i}^{(\alpha)} s_i^{(\alpha)}\right) b^{\kappa} \tau_T^{1-\kappa} \tau_0^{\kappa} L^{2\kappa} \left|\rho_{G(e),i}^{(\alpha)} s_i^{(\alpha)}\right|^{\kappa} & , \text{ for } |\tau_b^{(\alpha)}| > \tau_T \end{cases} . \tag{D.5}$$

References

Abbaschian, R., Abbaschian, L., Reed-Hill, R., 2010. Physical Metallurgy Priciples, 4th Edition. Cengaga Learning.

Anand, L., Aslan, O., Chester, S., 2012. A large-deformation gradient theory for elastic-plastic materials: Strain softening and regularization of shear bands. International Journal of Plasticity 30-31, 116–143.

Anand, L., Gurtin, M., Lele, S., Gething, C., 2005. A one-dimensional theory of strain-gradient plasticity: Formulation, analysis, numerical results. Journal of the Mechanics and Physics of Solids 53, 1789–1826.

Ananthan, V., Leffers, T., Hansen, N., 1991. Cell and band structures in cold-rolled polycrystalline copper. Materials Science and Technology 7, 1069–1075.

Asaro, R., 1975. Elastic-plastic memory and kinematic-type hardening. Acta Metallurgica 23, 1255–1265.

Ashby, M., 1970. The deformation of plastically non-homogeneous alloys. Philos. Mag. 21, 399–424.

Atkinson, M., 1995. Further analysis of the size effect in indentation hardness tests of some metals. Journal of Materials Research 10, 2908–2915.

Bardella, L., 2010. Size effects in phenomenological strain gradient plasticity constitutively involving the plastic spin. International Journal of Engineering Science 48, 550–568.

Bardella, L., Panteghini, A., 2015. Modelling the torsion of thin metal wires by distortion gradient plasticity. Journal of the Mechanics and Physics of Solids 78, 467–492.

Bargmann, S., Soyarslan, C., Husser, E., Konchakova, N., 2016. Materials based design of structures: Computational modeling of the mechanical behavior of gold-polymer nanocomposites. Mechanics of Materials 94, 53–65.

Bassani, J., 2001. Incompressibility and a simple gradient theory of plasticity. Journal of the Mechanics and Physics of Solids 49, 1983–1996.

Bayley, C., Brekelmans, W., Geers, M., 2006. A comparison of dislocation induced back stress formulations in strain gradient crystal plasticty. International Journal of Solids and Structures 43, 7268–7286.

Begley, M., Hutchinson, J., 1998. The mechanics of size-dependent indentation. Journal of The Mechanics and Physics of Solids 46, 2049–2068.

Dahlberg, C., Saito, Y., Öztop, M., Kysar, J., 2014. Geometrically necessary dislocation density measurements associated with different angles of indentations. International Journal of Plasticity 54, 81–95.

Deshpande, V., Needleman, A., Van der Giessen, E., 2003. Finite strain discrete dislocation plasticity. Journal of the Mechanics and Physics of Solids 51, 2057–2083.

Deshpande, V., Needleman, A., Van der Giessen, E., 2005. Plasticity size effects in tension and compression of single crystals. Journal of the Mechanics and Physics of Solids 53, 2661–2691.

Doener, M., Nix, W., 1986. A method for interpreting the data from depth-sensing indentation instruments. Journal of Materials Research 1, 601–609.

Ekh, M., Bargmann, S., Grymer, M., 2011. Influence of grain boundary conditions on modeling of size-dependence in polycrystals. Acta Mechanica 218, 103–113.

El-Naaman, S., Nielsen, K., Niordson, C., 2015. Strain gradient crystal plasticity: A continuum mechanics approach to modeling micro-structural evolution. Plastic Behavior of Conventional and Advanced Materials: Theory, Experiment, and Modeling, 7–9.

El-Naaman, S., Nielsen, K., Niordson, C., 2016a. Attaining the rate-independent limit of a rate-dependent strain gradient plasticity theory. Extreme Mechanics Letters, *In Press*.

El-Naaman, S., Nielsen, K., Niordson, C., 2016b. An investigation of back stress formulations under cyclic loading. Submitted.

El-Naaman, S., Nielsen, K., Niordson, C., 2016c. On modeling micro-structural evolution using a higher order strain gradient continuum theory. International Journal of Plasticity 76, 285–298.

El-Naaman, S., Nielsen, K., Niordson, C., Kysar, J., 2016d. Micron scale analysis of deformation around a cylindrical void in a face centered cubic crystal. Extreme Mechanics Letters, *In Preparation*.

Evans, A., Hutchinson, J., 2009. A critical assessment of theories of strain gradient plasticity. Acta Materialia 57, 1675–1688.

Evers, L., Brekelmans, W., Geers, M., 2004. Non-local cystal plasticity model with intrinsic SSD and GND effects. Journal of the Mechanics and Physics of Solids 52, 2379–2401.

Ewing, J., Rosenhain, W., 1900. Bakerian lecture: The crystalline structure of metals. Philosophical Transactions of The Royal Society A 193, 353.

Fleck, N., Hutchinson, J., 2001. A reformulation of strain gradient plasticity. Journal of the Mechanics and Physics of Solids 49, 2245–2271.

Fleck, N., Hutchinson, J., Willis, J., 2015. Guidelines for constructing strain gradient plasticity theories. Journal of Applied Mechanics 82, 1–10.

Fleck, N., Muller, G., Ashby, M., Hutchinson, J., 1994. Strain gradient plasticity: Theory and experiment. Acta Metallurgica et materialia 42 (2), 475–487.

Fleck, N., Willis, J., 2009a. A mathematical basis for strain-gradient plasticity theory. Part I: Scalar plastic multiplier. Journal of the Mechanics and Physics of Solids 57, 161–177.

Fleck, N., Willis, J., 2009b. A mathematical basis for strain-gradient plasticity theory. Part II: Tensorial plastic multiplier. Journal of the Mechanics and Physics of Solids 57, 1045–1057.

Forest, S., Guéninchault, N., 2013. Inspection of free energy functions in gradient crystal plasticity. Acta Mechanica Sinica 29(6), 763–772.

Fredriksson, P., Gudmundson, P., 2007. Modelling of the interface between a thin film and a substrate within a strain gradient plasticity framework. Journal of the Mechanics and Physics of Solids 55 (5), 939 – 955.

Gan, Y., Kysar, J., Morse, T., 2006. Cylindrical void in a rigid-ideally plastic single crystal ii: Experiments and simulations. International Journal of Plasticity 22, 39–72.

Geels, K., 2006. Metallographic and Materialographic Specimen Preparation, Light Microscopy, Image Analysis and Hardness Testing. ASTM International.

Groma, I., Csikor, F., Zaizer, M., 2003. Spatial correlations and higher-order gradient terms in a continuum description of dislocation dynamics. Acta Materialia 51, 1271–1281.

Gurtin, M., 2000. On the plasticity of single crystals: free energy, microforces, plastic-strain gradients. Journal of the Mechanics and Physics of Solids 48 (5), 989–1036.

Gurtin, M., 2002. A gradient theory of single-crystal viscoplasticity that accounts for geometrically necessary dislocations. Journal of the Mechanics and Physics of Solids 50, 5–32.

Gurtin, M., Anand, L., Lele, S., 2007. Gradient single-crystal plasticity with free energy dependent on dislocation densities. Journal of the Mechanics and Physics of Solids 55, 1853–1878.

Harder, J., 1999. A crystallographic model for the study of local deformation processes in polycrystals. International Journal of Plasticity 15, 605–624.

Hong, C., Huang, X., Winter, G., 2013. Dislocation content of geometrically necessary boundaries aligned with slip planes in rolled aluminium. Philosophical Magazine 93 (23), 3118–3141.

Huang, X., Winther, G., 2007. Dislocation structures. Part I. Grain orientation dependence. Philosophical Magazine 87 (33), 5189–5214.

Huang, Y., 1991. A user-material subroutine incorporating single crystal plasticity in the abaqus finite element program: Mech report 178. Tech. rep., Division of Applied Sciences, Harvard University, Cambridge, MA.

Huang, Y., Qu, S., Hwang, K., Li, M., Gao, H., 2004. A conventional theory of mechanism-based strain gradient plasticity. International Journal of Plasticity 20, 753–782.

Hutchinson, J., 1976. Bounds and self-consistent estimates for creep of polycrystalline materials. Proc. R. Soc. Lond. A 348, 101–127.

Hutchinson, J., 2012. Generalized J_2 flow theory: Fundamental issues in strain gradient plasticity. Acta Mechanica Sinica 28(4), 1078–1086.

Kiener, D., Motz, C., Grosinger, W., Weygand, D., Pippan, R., 2010. Cyclic response of copper single crystal micro-beams. Scripta Materialia 63, 500–503.

Klusemann, B., Yalçinkaya, T., 2013. Plastic deformation induced microstructure evolution through gradient enhanced crystal plasticity based on a non-convex Helmholtz energy. International Journal of Plasticity 48, 168–188.

Kraft, O., Hommel, A., Arzt, E., 2000. X-ray diffraction as a tool to study the mechanical behaviour of thin films. Materials Science and Engineering: A 288, 209–216.

Kuroda, M., Tvergaard, V., 2006. Studies of scale dependent crystal viscoplasticity models. Journal of the Mechanics and Physics of Solids 54, 1789–1810.

Kuroda, M., Tvergaard, V., 2008. On the formulation of higher-order strain gradient crystal plasticity models. Journal of the Mechanics and Physics of Solids 56, 1591–1608.

Kysar, J., 1997. Addendum to a user-material subroutine incorporating single crystal plasticity in the abaqus finite element program: Mech report 178. Tech. rep., Division of Applied Sciences, Harvard University, Cambridge, MA.

Kysar, J., Gan, Y., Mendez-Arzuza, G., 2005. Cylindrical void in a rigid-ideally plastic single crystal. part i: Anisotropic slip line theory solution for face-centered cubic crystals. International Journal of Plasticity 21, 1481–1520.

Kysar, J., Gan, Y., Morse, T., Chen, X., Jones, M., 2007. High strain gradient plasticity associated with wedge indentation into face-centered cubic single crystal: Geometrically necessary dislocation densies. Journal of The Mechanics and Physics of Solids 55, 1554–1573.

Kysar, J., Saito, Y., Oztop, M., Lee, D., Huh, W., 2010. Experimental lower bounds on geometrically necessary dislocation density. International Journal of Plasticity 26, 1097–1123.

Martínez-Pañeda, E., Niordson, C., 2015. On fracture in finite strain gradient plasticity. International Journal of Plasticity, *In press*.

Mu, Y., Hutchinson, J., Meng, W., 2014. Micro-pillar measurements of plasticity in confined cu thin films. Extreme Mechanics Letters 1, 62–69.

Nielsen, K., 2015. Rolling induced size effects in elastic-viscoplastic sheet metals. European Journal of Mechanics A/Solids 53, 259–267.

Nielsen, K., Niordson, C., 2012. Rate sensitivity of mixed mode interface toughness of dissimilar meallic materials: Studied at steady state. International Journal of Solids and Structures 49, 576–583.

Nielsen, K., Niordson, C., Hutchinson, J., 2012. Strain gradient effects on steady state crack growth in rate-sensitive materials. Engineering Fracture Mechanics 96, 61–71.

Niordson, C., Hutchinson, J., 2003. On lower order strain gradient plasticity theories. European Journal of Mechanics A/Solids 22, 771–778.

Niordson, C., Kysar, J., 2014. Computational strain gradient crystal plasticity. Journal of the Mechanics and Physics of Solids 62, 31–47.

Nye, J., 1953. Some geometrical relations in dislocated crystals. Acta Metallurgica 1 (2), 153–162.

Ohno, N., Okumara, D., 2007. Higher-order stress and grain size effects due to self-energy of geometrically necessary dislocations. Journal of the Mechanics and Physics of Solids 55, 1879–1898.

Öztop, M., 2011. Multiscale experimental analysis in plasticity: Linking dislocation structures to continuum fields. Ph.D. thesis, Columbia University.

Öztop, M., Niordson, C., Kysar, J., 2012. Length-scale effect due to periodic variation of geometrically nescessary dislocaion densities. International Journal of Plasticity 41, 189–201.

Pantleon, W., 2008. Resolving the geometrically necessary dislocation content by conventional electron backscattering diffraction. Scripta Materialia 58, 994–997.

Peirce, D., Asaro, R., Needleman, A., 1983. Material rate dependence and localized deformation in crystalline solids. Acta Metall. 31, 1951–1976.

Poole, W., Ashby, M., Fleck, N., 1996. Micro-hardness of annealed and work-hardened copper polycrystals. Scripta Materialia 34, 559–564.

Proudhon, H., Poole, W., Wang, X., Bréchet, Y., 2008. The role of internal stresses on the plastic deformation of the Al-Mg-Si-Cu alloy AA611. Philosophical Magazine 88, 621–640.

Read, W., Shockley, W., 1950. Dislocation models of crystal grain boundaries. Physical Review 78, 275–289.

Rice, J., 1987. Tensile crack tip fields in elastic-ideally plastic crystals. Mechanics of Materials 6, 317–335.

Ruggles, T., Fullwood, D., Kysar, J., 2016. Resolving geometrically necessary dislocation density onto individual dislocation types using ebsd-based continuum dislocation microscopy. International Journal of Plasticity 76, 231–243.

Stölken, J., Evans, A., 1998. A microbend test method for measuring the plasticity length scale. Acta Materialia 46, 5109–5115.

Stoltz, R., Pelloux, R., 1976. The Bauschinger effect in precipitation strengthened aluminum alloys. Metallugical Transactions A 7 (8), 1295–1306.

Tabor, D., February 1948. A simple theory of static and dynamic hardness. Proc. R. Soc. Lond. 192, 247–274.

Taillard, R., Pineau, A., 1982. Room temperature tensile properties of Fe-19wt.%Cr alloys precipitation hardened by the intermetallic compound NiAl. Materials Science and Engineering 56, 219–231.

Tarleton, E., Balint, D., Gong, J., Wilkinson, A., 2015. A discrete dislocation plasticity study of the micro-cantilever size effect. Acta Materialia 88, 271–282.

Taylor, G., 1934. The mechanism of plastic deformation of crystals. Part I. Theoretical. Proceeding of The Royal Society A 145, 362–387.

Tresca, H., 1864. Mémoire sur l'écoulement des corps solides soumis à de fortes pressions. Comptes Rendus de l'Académie des Sciences 59, 754.

van Beers, P., McShane, G., Kouznetsova, V., Geers, M., 2013. Grain boundary interface mechanics in strain gradient crystal plasticity. Journal of the Mechanics and Physics of Solids 61, 2659–2679.

Wei, Y., Hutchinson, J., 1997. Steady-State crack growth and work of fracture for solids characterized by strain gradient plasticity. Journal of the Mechanics and Physics of Solids 45, 1253–1273.

Wei, Y., Hutchinson, J., 1999. Models of interface separation accompanied by plastic dissipation at multiple scales. International Journal of Fracture 95, 1–17.

Wulfinghoff, S., Forest, S., Böhlke, 2015. Strain gradient plasticity modeling of the cyclic behavior of laminate microstructures. Journal of the Mechanics and Physics of Solids 79, 1–20.

Xiang, Y., Vlassak, J., 2016. Bauschinger effect in thin metal films. Scripta Materialia 53, 177–182.

Yaghoobi, M., Voyiadjis, G., 2014. Effect of boundary conditions on the MD simulation of nanoindentation. Computational Materials Science 95, 626–636.

Yefimov, S., Groma, I., van der Giessen, E., 2004. A comparison of a statistical-mechanics based plasticity model with descrete dislocation plasticity calculations. Journal of the Mechanics and Physics of Solids 52, 279–300.

Publications

Publication [P1]

Strain gradient crystal plasticity: A continuum mechanics approach to modeling micro-structural evolution

Plastic Behavior of Conventional and Advanced Materials: Theory, Experiment, and Modeling

Proceedings of PLASTICITY ’15:
The Twenty First International Symposium on
Plasticity and its Current Applications

Editor
Akhtar S. Khan

Associate Editor
Hai-Yan Yu

Sponsored by:

International Journal of Plasticity,
University of Maryland Baltimore County,
Deakin University Australia, and
Numerical Engineering Analysis and Testing (NEAT), Inc.

NEAT PRESS

STRAIN GRADIENT CRYSTAL PLASTICITY: A CONTINUUM MECHANICS APPROACH TO MODELING MICRO-STRUCTURAL EVOLUTION

Salim A. El-Naaman*, Kim L. Nielsen, Christian F. Niordson

***saeln@mek.dtu.dk**
Department of Mechanical Engineering, Solid Mechanics
Technical University of Denmark, DK-2800 Kgs. Lyngby, Denmark

ABSTRACT- In agreement with dislocation theory, recent experiments show, both quantitatively and qualitatively, how geometrically necessary dislocations (GNDs) distribute in dislocation wall and cell structures. Hence, GND density fields are highly localized with large gradients and discontinuities occurring between the cells. This behavior is not typical for strain gradient crystal plasticity models. The present study employs a higher order extension of conventional crystal plasticity theory in which the viscous slip rate is influenced by the gradients of GND densities through a back stress. A phenomenological back stress formulation is proposed, through which the effect of the GND gradient exponent can be studied. It is shown that this model can lead to more localized GND distributions.

INTRODUCTION: Published electron backscatter diffraction (EBSD) measurements on a face centered cubic (FCC) nickel single crystal, subject to plane strain wedge indentation, show distinct dislocation patterns (see e.g. Kysar et al. 2010). These patterns represent clear dislocation wall and cell structures, thus highly non-uniform distributions of geometrically necessary dislocations (GNDs) are present, producing discontinuities in the lattice rotations. However, existing continuum models of the micro-structural evolution tend to show a much more smoothened GND field. When the overall dimensions become comparable to the material length scale and deformation gradients become large, so called higher order strain gradient plasticity theories are needed to obtain accurate results. In the present study a non-work conjugate type theory is adopted, which is a higher order extension of conventional crystal plasticity theory. One obvious issue with modeling these experimentally observed physical phenomena, in terms of continuous field quantities, is that the evolution of dislocation structures is inherently a discrete and discontinuous process. This challenge, in particular, motivates the present study, in which the aim is to improve the accuracy of predicting micro-structural evolution using strain gradient crystal plasticity theory in continuum mechanics framework. One key to modeling the GND density distributions observed experimentally is through a back stress formulation, which is related to gradients of GND densities and influences the viscous slip rate in the adopted theory. The work presents an investigation of a phenomenological constitutive equation for the back stress based on experimental observations. Thereby, a new formulation for predicting the micro-structural evolution and plastic material response, of ductile crystalline materials, on the sub-micron level, is proposed. The influence of two key parameters on the GND density distribution is demonstrated through a parametric study.

PROCEDURES, RESULTS AND DISCUSSION: The present study employs a strain gradient plasticity theory within a conventional small strain elasto-viscoplastic framework, proposed by Kuroda and Tvergaard (2008). An additive decomposition of the total strain, $\epsilon_{ij} = \epsilon^e_{ij} + \epsilon^p_{ij}$, into an elastic part, ϵ^e_{ij}, and a plastic part, ϵ^p_{ij}, is used. Plastic strain is due to crystallographic slip rates, $\dot{\gamma}^{(\alpha)}$, on slip planes denoted α

$$\dot{\epsilon}^p_{ij} = \sum_{(\alpha)} \dot{\gamma}^{(\alpha)} P^{(\alpha)}_{ij}, \qquad P^{(\alpha)}_{ij} = \frac{1}{2}(s^{(\alpha)}_i m^{(\alpha)}_j + s^{(\alpha)}_j m^{(\alpha)}_i) \tag{1}$$

with $P^{(\alpha)}_{ij}$ being the Schmid orientation tensor, and $s^{(\alpha)}_i$ and $m^{(\alpha)}_j$ the direction of slip and the slip plane normal, respectively. Apart from the conventional stress equilibrium equation, $\sigma_{ij,j} = 0$, an additional set of differential equations is solved in a staggered solution scheme to obtain the GND density:

$$\frac{1}{b}\gamma^{(\alpha)}_{,i} s^{(\alpha)}_i + \rho^{(\alpha)}_{G(e)} = 0, \qquad \frac{1}{b}\gamma^{(\alpha)}_{,i} p^{(\alpha)}_i + \rho^{(\alpha)}_{G(s)} = 0. \tag{2}$$

Here, $\mathbf{p}^{(\alpha)} = \mathbf{s}^{(\alpha)} \times \mathbf{m}^{(\alpha)}$, b is the magnitude of the Burgers vector, and $\rho^{(\alpha)}_G$ are GND densities on slip system α. The subscripts (e) and (s) denote edge and screw components, respectively. The slip rates are given by a simple extension of the widely used visco-plastic power law slip rate relation

$$\dot{\gamma}^{(\alpha)} = \dot{\gamma}_0 \mathrm{sgn}\left(\tau^{(\alpha)} - \tau^{(\alpha)}_b\right)\left(\frac{|\tau^{(\alpha)} - \tau^{(\alpha)}_b|}{g^{(\alpha)}}\right)^{1/m}, \tag{3}$$

where τ is the Schmid stress taken as the projection of the macroscopic Cauchy stress tensor onto the slip plane, τ_b is a back stress, m is the rate hardening exponent, and g is the slip resistance. The gradient energy is often taken to be of a quadratic nature of the form

$$\psi_G = \frac{1}{2}\tau_0 L^2 \left(s^{(\alpha)}_i \gamma^{(\alpha)}_{,i}\right)^2, \tag{4}$$

where L is a material length scale parameter and τ_0 is the initial critical resolved shear stress. This is, however, mostly for mathematical convenience rather than based on physical arguments. Relating the back stress to the gradient energy as in Kuroda and Tvergaard (2008), Eq. (4) leads to

$$\tau^{(\alpha)}_b = -\tau_0 L^2 s^{(\alpha)}_i s^{(\alpha)}_j \gamma^{(\alpha)}_{,ij} = b\tau_0 L^2 s^{(\alpha)}_i \rho^{(\alpha)}_{G(e),i}. \tag{5}$$

in which case the theory coincides with the work conjugate theory of Gurtin (2002). In order to explore the effect of the relationship between the back stress and the gradients of GND density, we construct a phenomenological back stress power law in the light of the experimental observations. Thus, we introduce a dependence on the gradients of GND density to the power of a parameter μ, taking a value between zero and one:

$$\tau^{(\alpha)}_b = \mathrm{sgn}\left(s^{(\alpha)}_i \rho^{(\alpha)}_{G(e),i}\right) b^\mu \tau_T^{1-\mu} \tau_0^\mu L^{2\mu} \left|s^{(\alpha)}_i \rho^{(\alpha)}_{G(e),i}\right|^\mu, \text{ for } \tau^{(\alpha)}_b > \tau_T, \tag{6}$$

with τ_T being a transition back stress parameter. At the limit of $\mu = 0$, the function initially has an infinite slope. To avoid the difficulties tied to low values of μ, the back stress is assumed to evolve according to Eq. (5) until $\tau_b^{(\alpha)} > \tau_T$. With $\mu = 0$, Eq. (6) corresponds to a blunt cut-off of the back stress at $\tau_b^{(\alpha)} = \tau_T$. For $\mu = 1$, Eq. (5) and (6) are identical, corresponding to a quadratic gradient energy throughout. The theory is applied to a constrained single slip pure shear problem, with height H, Young's modulus $E = 130$ MPa, Poisson's ratio $\nu = 0.3$, $\tau_0 = 50$ MPa, $\tau_T/\tau_0 = 0.12$, and $L/H = 0.3$. The slip system is perpendicular to the shearing direction. Fig. 1 shows the GND density profile for different values of the rate exponent m, with $\mu = 1$ (Fig. 1a) and with $\mu = 0.4$ (Fig. 1b). As μ becomes smaller than unity, the GND density evolves more intensely at the boundaries, resulting in more pronounced dislocation "wall"-structures forming. Particularly for the higher values of m the effect of μ is clear. This micro-structural response bears closer resemblance to what is observed in experimental studies.

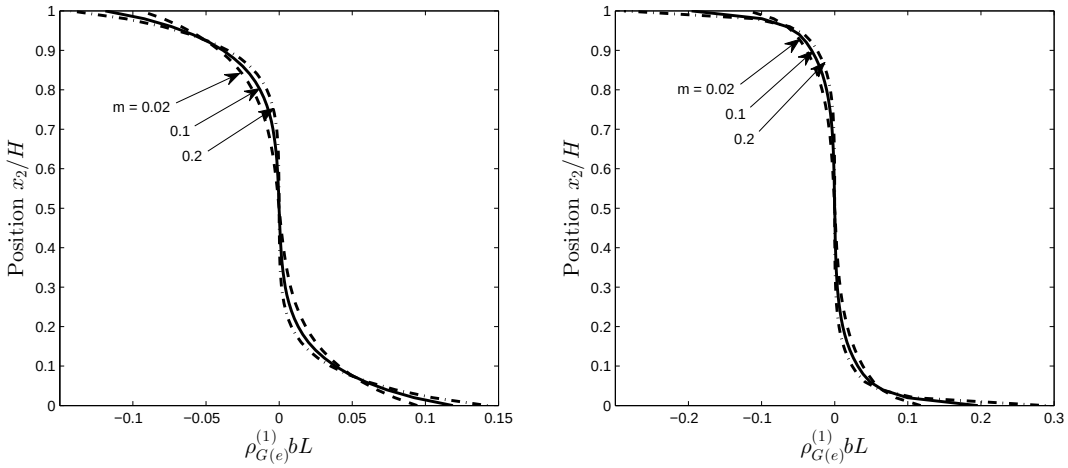

Figure 1: Normalized GND density profile for single slip simple shear of periodic material domain, for different values of the rate exponent m. (a) with $\mu = 1$, and (b) with $\mu = 0.4$.

ACKNOWLEDGMENTS: The work is financially supported by The Danish Council for Independent Research under the research career programme Sapere Aude in the project "Higher Order Theories in Solid Mechanics".

REFERENCES:

Gurtin, M., 2002, "A gradient theory of single-crystal viscoplasticity that accounts for geometrically necessary dislocations", J. Mech. Phys. Solids, **50**, 5-32.

Kuroda, M., Tvergaard, V., 2008, "On the formulation of higher-order strain gradient crystal plasticity models", J. Mech. Phys. Solids, **56**, 1591-1608.

Kysar, J., Saito, Y., Oztop, M., Lee, D., Huh, W., 2010, "Experimental lower bounds on geometrically necessary dislocation density", Int. J. Plasticity, **26**, 1097-1123.

Publication [P2]

On modeling micro-structural evolution using a higher order strain gradient continuum theory

International Journal of Plasticity 76 (2016) 285–298

Contents lists available at ScienceDirect

International Journal of Plasticity

journal homepage: www.elsevier.com/locate/ijplas

On modeling micro-structural evolution using a higher order strain gradient continuum theory

S.A. El-Naaman*, K.L. Nielsen, C.F. Niordson

Department of Mechanical Engineering, Solid Mechanics, Technical University of Denmark, DK-2800 Kgs Lyngby, Denmark

ARTICLE INFO

Article history:
Received 15 May 2015
Received in revised form 24 August 2015
Available online 6 September 2015

Keywords:
Dislocations
Microstructures
Constitutive behavior
Crystal plasticity
Back stress formulations

ABSTRACT

Published experimental measurements on deformed metal crystals show distinct pattern formation, in which dislocations are arranged in wall and cell structures. The distribution of dislocations is highly non-uniform, which produces discontinuities in the lattice rotations. Modeling the experimentally observed micro-structural behavior, within a framework based on continuous field quantities, poses obvious challenges, since the evolution of dislocation structures is inherently a discrete and discontinuous process. This challenge, in particular, motivates the present study, and the aim is to improve the micro-structural response predicted using strain gradient crystal plasticity within a continuum mechanics framework. One approach to modeling the dislocation structures observed is through a back stress formulation, which can be related directly to the strain gradient energy. The present work offers an investigation of constitutive equations for the back stress based on both considerations of the gradient energy, but also includes results obtained from a purely phenomenological starting point. The influence of model parameters is brought out in a parametric study, and it is demonstrated how a proper treatment of the back stress enables dislocation wall and cell structure type response in the adopted framework.

1. Introduction

The ability to accurately predict the response and performance of ductile crystalline materials, on the micron scale and below, is crucial for example when modeling forming processes with thin metal films. In multiscale plasticity problems, it has been established that in the presence of large deformation gradients—invoking a population of geometrically necessary dislocations (GNDs) that becomes significant compared to the statistically stored dislocations—conventional plasticity theory breaks down and so-called higher order strain gradient plasticity theories are needed. While there is an ongoing discussion on whether size-effects result in strain gradient strengthening (delayed yield point) or strain gradient hardening, non-trivial size-effects are well recognized. Since the first gradient dependent theory appeared some 30 years ago, micro-mechanically based crystal plasticity models have been a highly active research subject and recent contributions include Hutchinson (2012), Öztop et al. (2012), van Beers et al. (2013), Klusemann and Yalçinkaya (2013) and Niordson and Kysar (2014). Different families of higher order strain gradient plasticity theories have evolved, but a common feature for all is that they

* Corresponding author. Tel.: +45 4525 4020; fax: +45 4593 1475.
E-mail address: saeln@mek.dtu.dk (S.A. El-Naaman).
URL: http://saeln@mek.dtu.dk

http://dx.doi.org/10.1016/j.ijplas.2015.08.008
0749-6419/

incorporate micro-structural boundary conditions, enabling constraints on plastic flow or associated field quantities, as opposed to the so-called lower order theories (e.g. Bassani, 2001; Huang et al., 2004) for which unexpected strain localization behavior was pointed out by Niordson and Hutchinson (2003).

It is well known that dislocations arrange themselves in wall and cell structures, within grains of crystalline materials, during plastic deformation. Bands of high dislocation density (dislocation walls) typically form webs enclosing regions of relatively low dislocation content (cell interiors). Ananthan et al. (1991) report on clear mesh like dislocation structures in cold rolled polycrystalline copper, while the studies of Huang and Winther (2007) and Hong et al. (2013) reveal details on dislocation structures and geometrically necessary boundaries in aluminum and copper specimens. Recently, Öztop (2011) performed high resolution electron backscatter diffraction (HR-EBSD) measurements on a nickle single crystal, subject to wedge indentation in an approximate two-dimensional plane strain deformation state. These measurements show highly nonuniform and discontinuous lattice rotations, which are linked directly to the existence of geometrically necessary dislocations (GNDs), revealing distinct dislocation wall and cell pattern formation. Details on the experimental methods employed by Öztop (2011) can also be found in Kysar et al. (2010) and Dahlberg et al. (2014), also showing highly localized GND structures.

A vast number of numerical studies on the evolution of dislocation structure exist in the literature, some concerned with discrete dislocations and molecular dynamics (Deshpande et al., 2003, 2005; Yaghoobi and Voyiadjis, 2014; Tarleton et al., 2015; Voyiadjis and Yaghoobi, 2015), while others take a continuum approach (Yefimov et al., 2004; Klusemann and Yalçinkaya, 2013; van Beers et al., 2013). GNDs accommodate the plastic strain gradients and thus, walls of GNDs are associated with high slip gradients occurring in a small region, and therefore also high second gradients of slip. Continuum models of the micro-structural evolution tend to show a much smoother GND field, than observed in reality. Complex physics governs the movement of dislocations at the atomic scale, and linking it to the governing equations of a multi-scale continuum model, poses a considerable challenge. An obvious issue with modeling the evolution of dislocation structures, in terms of continuous field quantities, is that this physical phenomenon is inherently a discrete and discontinuous process. Recently, van Beers et al. (2013) studied the grain boundary interface mechanics using a micro-structurally based formulation within the gradient crystal plasticity framework developed by Evers et al. (2004) and Bayley et al. (2006). Here, wall formation type behavior was predicted at the grain boundaries. However, the micro-structural development was characterized by a rather smooth distribution of GNDs, which clearly demonstrates the challenge of representing the highly nonuniform response associated with dislocation wall and cell structures.

Higher order theories are often categorized into two branches: Work conjugate theories and Non-work conjugate theories. The work conjugate type formulations (e.g. Gurtin, 2002) make use of higher-order stress concepts as work conjugates to the strain/slip gradients, whereas the non-work conjugate type theories do not. The present study employs the non-work conjugate type theory proposed by Kuroda and Tvergaard (2006, 2008), which is a higher order extension of conventional crystal plasticity theory. Nemat-Nasser et al. (1998) suggested a straight forward extension of the widely used visco-plastic power law slip rate relation (Hutchinson, 1976; Peirce et al., 1983), so that the slip rate, $\dot{\gamma}$, on the α'th slip system is given by

$$\dot{\gamma}^{(\alpha)} = \dot{\gamma}_0 \mathrm{sgn}\left(\tau^{(\alpha)} - \tau_b^{(\alpha)}\right)\left(\frac{\left|\tau^{(\alpha)} - \tau_b^{(\alpha)}\right|}{g^{(\alpha)}}\right)^{1/m}, \tag{1}$$

where the superposed dot denotes material time derivative, $\dot{\gamma}_0$ is a reference slip rate, $\tau^{(\alpha)}$ is the Schmid stress (taken as the macroscopic Cauchy stress tensor resolved onto the slip plane), $\tau_b^{(\alpha)}$ is a back stress, m is the rate hardening exponent, and $g^{(\alpha)}$ is the slip resistance. In Eq. (1), the conventional power law slip rate relation is gradient-enhanced by replacing the resolved shear stress, $\tau^{(\alpha)}$, with an effective resolved shear stress taken as the difference between the Schmid stress and a back stress; $\tau^{(\alpha)} - \tau_b^{(\alpha)}$ (Groma, 1997; Evers et al., 2004).[1] The back stress, $\tau_b^{(\alpha)}$, is related directly to the gradients of the GND density (see Section 4), impeding the occurrence of slip at nonuniform pile-ups of GNDs. With this concept, the effective resolved shear stress is perceived as the driving force behind the movement of dislocations (Evers et al., 2004). This type of model can accommodate nonuniform distributions of $\dot{\gamma}^{(\alpha)}$ under a constant stress state, which is needed to give rise to GNDs.

The present study aims to expand the modeling capabilities of predicting micro-structural evolution using strain gradient single crystal plasticity and takes a continuum mechanics approach to the problem. The paper investigates constitutive equations for the back stress and offers a discussion on the underlying physical arguments. Finally, a phenomenological model formulation, for predicting the micro-structural evolution and plastic material response on the sub-micron level, is proposed.

The paper is structured as follows. The strain gradient plasticity model is described in Section 2 and the scope of the paper is outlined in Section 3. Following is the derivation of back stress relations in Section 4, including a series of results presented using a finite element method (FEM) implementation. The final concluding remarks are offered in Section 5.

[1] Note that for $\tau_b^{(\alpha)}$ equal to zero, Eq. (1) reduces to the conventional theory.

2. Strain gradient crystal plasticity model

The non-work conjugate higher order strain gradient plasticity theory formulated by Kuroda and Tvergaard (2006, 2008) is employed in the present study. The theory is of a higher order nature but does not rely on higher order stress concepts. The formulation builds on the framework of conventional crystal visco-plasticity theory, where a second set of differential equations is introduced for the evolution of the GND densities. Here, the GND densities appear directly as free field variables. The present study employs a small strain formulation, so that; $\dot{\varepsilon}_{ij} = (\dot{u}_{i,j} + \dot{u}_{j,i})/2$, and an additive decomposition of the total strain rate is used, so that; $\dot{\varepsilon}_{ij} = \dot{\varepsilon}^e_{ij} + \dot{\varepsilon}^p_{ij}$, where the superscripts '*e*' and '*p*' denote the elastic and plastic parts, respectively. Plastic deformation occurs by the mechanism of crystallographic slip on the individual slip systems denoted α. Thus, the plastic strain rate is given in terms of the sliprate as

$$\dot{\varepsilon}^p_{ij} = \sum_{\alpha} \dot{\gamma}^{(\alpha)} P^{(\alpha)}_{ij}, \quad P^{(\alpha)}_{ij} = \frac{1}{2}\left(s^{(\alpha)}_i m^{(\alpha)}_j + m^{(\alpha)}_i s^{(\alpha)}_j\right), \tag{2}$$

where $s^{(\alpha)}_i$ and $m^{(\alpha)}_i$ are unit vectors specifying the slip direction and slip plane normal, respectively, and $P^{(\alpha)}_{ij}$ is the Schmid orientation tensor (see also Fig. 1b for a schematic definition). The slip rates follow the relation given in Eq. (1), and involves the back stresses, which are the main subject of the present study. The slip resistance $g^{(\alpha)}$ in Eq. (1) is taken to follow the hardening law

$$\dot{g}^{(\alpha)} = \sum_{\beta} h^{(\alpha\beta)} \left|\dot{\gamma}^{(\beta)}\right|, \quad g^{(\alpha)}\big|_{t=0} = \tau_0, \tag{3}$$

where the initial value of $g^{(\alpha)}$ is chosen as the initial critical resolved shear stress τ_0, $h^{(\alpha\beta)}$ are slip hardening moduli, in which the trace accounts for self hardening and the off-diagonal parts for latent hardening, and t is time. The governing equations of the non-work conjugate formulation, are given by the conventional stress equilibrium equation; $\sigma_{ij,j} + f_i = 0$, where f_i are body forces and the Cauchy stress rate is given by the elastic relationship; $\dot{\sigma}_{ij} = \mathscr{L}_{ijkl}(\dot{\varepsilon}_{kl} - \dot{\varepsilon}^p_{kl})$, in which $\mathscr{L}_{ijkl}$ is the fourth order elastic stiffness tensor.

In the framework adopted, the gradients of GND densities influence the viscous slip rate through the back stress, which counteracts the resolved shear stress on the slip systems, and thus the plastic strain rate. This gives rise to a kinematic hardening contribution. In order to determine the distribution of GNDs, an additional set of differential equations is introduced, ensuring that the slip exists in balance with the GND densities:

$$\frac{1}{b}\gamma^{(\alpha)}_{,i} s^{(\alpha)}_i + \rho^{(\alpha)}_{G(e)} = 0 \tag{4a}$$

$$\frac{1}{b}\gamma^{(\alpha)}_{,i} p^{(\alpha)}_i + \rho^{(\alpha)}_{G(s)} = 0. \tag{4b}$$

Here, $\mathbf{p}^{(\alpha)} = \mathbf{s}^{(\alpha)} \times \mathbf{m}^{(\alpha)}$, b is the magnitude of the Burgers vector, and $\rho^{(\alpha)}_G$ are GND densities on slip system α, where the subscripts (e) and (s) denote edge and screw components, respectively (Ashby, 1970). The governing equations for the displacement field and GND density field are evaluated separately, however, the two fields are linked together by the back stress. Hence, it is through the back stress that the gradient effects influence the conventional field equations. Through the principle of virtual work, the weak form of the displacement field equation reads:

$$\int_V \mathscr{L}_{ijkl}\dot{\varepsilon}_{kl}\delta\dot{\varepsilon}_{ij}\mathrm{d}V = \int_V \mathscr{L}_{ijkl}\dot{\varepsilon}^p_{kl}\delta\dot{\varepsilon}_{ij}\mathrm{d}V + \int_V \dot{f}_i\delta\dot{u}_i\mathrm{d}V + \int_S \dot{T}_i\delta\dot{u}_i\mathrm{d}S, \quad \dot{T}_i \equiv \dot{\sigma}_{ij}n_j, \tag{5}$$

where $\dot{T}_i$ are the traction rates, n_i is the outward unit normal field of the surface S bounding the volume V. The weak form of the GND density equations (4) read:

$$\frac{1}{b}\int_V \delta\rho_{,i} s^{(\alpha)}_i \gamma^{(\alpha)}\mathrm{d}V = \frac{1}{b}\int_S \delta\rho\zeta^{(\alpha)}\mathrm{d}S + \int_V \delta\rho\rho^{(\alpha)}_{G(e)}\mathrm{d}V, \quad \zeta^{(\alpha)} \equiv \gamma^{(\alpha)} n_i s^{(\alpha)}_i, \tag{6a}$$

$$\frac{1}{b}\int_V \delta\rho_{,i} p^{(\alpha)}_i \gamma^{(\alpha)}\mathrm{d}V = \frac{1}{b}\int_S \delta\rho\eta^{(\alpha)}\mathrm{d}S + \int_V \delta\rho\rho^{(\alpha)}_{G(s)}\mathrm{d}V, \quad \eta^{(\alpha)} \equiv \gamma^{(\alpha)} n_i p^{(\alpha)}_i, \tag{6b}$$

where $\delta\rho$ is a weighting function or virtual GND density. In the GND density equations, a hard interface impenetrable for dislocations can be enforced as

$$\zeta^{(\alpha)} \equiv \gamma^{(\alpha)} n_i s^{(\alpha)}_i = 0 \tag{7a}$$

$$\eta^{(\alpha)} \equiv \gamma^{(\alpha)} n_i p_i^{(\alpha)} = 0, \tag{7b}$$

whereas a free boundary, where dislocations are free to exit the domain, corresponds to

$$\rho_{G(e)}^{(\alpha)} = \rho_{G(s)}^{(\alpha)} = 0. \tag{8}$$

For a detailed discussion on the micro-structural boundary conditions see Kuroda and Tvergaard (2008).

3. Problem description

In the present study, the focus is on the micro-structural response in strain gradient crystal plasticity and an attempt is made to phenomenologically bridge the gap between the length scales. Traditionally, in strain gradient plasticity models, one can manipulate the material length scale parameter to capture size-effects, however, this does not necessarily lead to a realistic distribution of GNDs. In fact, current theories predict smooth and uniform micro-structures, which is not sufficient for describing the highly non-uniform nature of dislocation patterning. Generally, the clustering of dislocations is characterized by sharp and abrupt transitions between cell walls and cell interiors, which, in a continuum context, translates into high spatial gradients of GND density. As will be demonstrated in the following section, the micro-structural behavior can be tied to the choice of free energy formulation and ultimately to the form of the back stress.

In order to quantify the desired response, in terms of dislocation wall and cell structures, it has been chosen to define a dislocation cell, within a phenomenological continuum mechanics representation, by the following two characteristics:

1 Dislocation wall: The minor portion of the cell structure, dominated by high GND density and high GND density gradients.

2 Cell interior: The major portion of the cell structure, dominated by low (several orders of magnitude lower than the walls) to zero GND density and low (approaching zero) GND density gradients.

The present study is confined to two dimensional space, i.e., all terms associated with screw dislocations vanish and the interaction between slip systems is omitted for clarity of the analysis. Thus, the single slip simple shear problem, illustrated in Fig. 1, is considered in order to demonstrate the influence of back stress formulations. In order to allow comparison with the results of Kuroda and Tvergaard (2008), the following model parameters are used throughout: Slip angle $\theta = 90^\circ$, Young's modulus $E = 130$ GPa, Poisson's ratio $\nu = 0.3$, $\tau_0 = 50$ MPa, $b = 0.286$ nm, $h^{(\alpha\beta)} = h = 250$ MPa, and $m = 0.02$. On the semi-infinite material slab, of height H and width W, the following boundary conditions are imposed on the displacement field

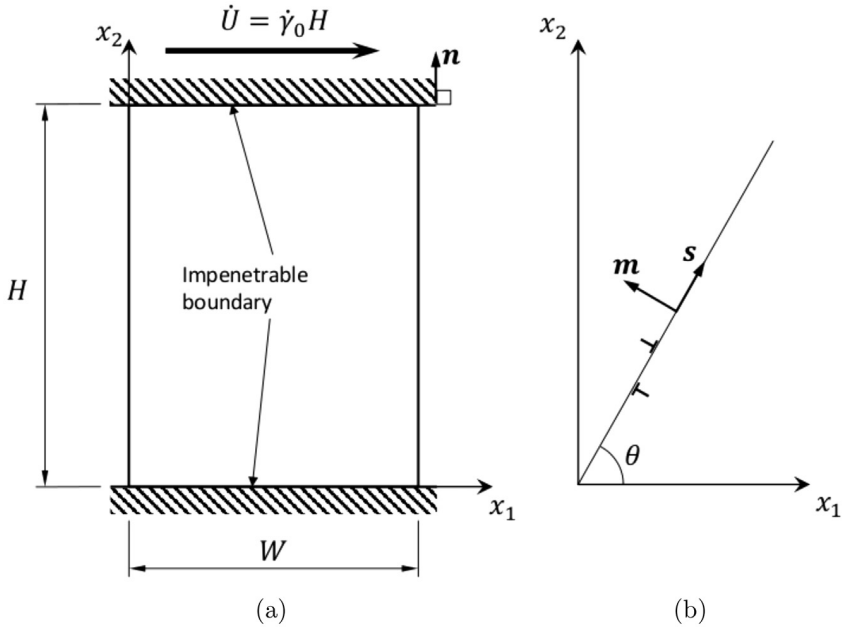

Fig. 1. Schematic of the simple shear problem: (a) a semi-infinite slab of material, constrained by two rigid impenetrable boundaries, subject to a prescribed displacement rate $\dot{\boldsymbol{U}}$. (b) definition of the slip system.

$$u_1 = u_2 = 0 \text{ at } x_2 = 0 \tag{9a}$$

$$u_1 = U(t) = H\dot{\gamma}_0 t \text{ and } u_2 = 0 \text{ at } x_2 = H, \tag{9b}$$

where the overall macroscopic shear strain applied is $\Gamma = 0.03$. Microscopic clamped boundary conditions are imposed on the GND density field as

$$\varsigma^{(\alpha)} \equiv \gamma^{(\alpha)} n_i s_i^{(\alpha)} = 0 \text{ at } x_2 = 0 \text{ and } x_2 = H, \tag{10}$$

and periodicity in the x_1-direction requires that

$$u_i(0, x_2) = u_i(W, x_2) \tag{11a}$$

$$\rho_{G(e)}^{(\alpha)}(0, x_2) = \rho_{G(e)}^{(\alpha)}(W, x_2). \tag{11b}$$

This means that all fields become effectively one dimensional. The results are obtained using the finite element method (FEM), solving the conventional system of equations and the GND system of equations in a staggered scheme. The discretized finite element equations can be found in Kuroda and Tvergaard (2008). Eight-node isoparametric quadrilateral elements with reduced Gauss integration are used for the displacement field analysis, whereas equivalent four-node elements with full Gauss integration are used for the GND density field analysis. Time integration is done by the forward Euler method. Typical finite element meshes consist of 50 elements in the x_2-direction and mesh refinements is used when steep gradients appear in the solution.

4. Back stress formulations and results

In the gradient visco-plasticity theory proposed by Kuroda and Tvergaard (2006, 2008), which is adopted in the present study, the back stress, τ_b, was originally assumed to be proportional to the first gradients of the GND densities. When assuming that the back stress is given by the divergence of a vector-valued quantity higher order stress, $\xi_i^{(\alpha)}$;

$$\tau_b^{(\alpha)} \equiv -\xi_{i,i}^{(\alpha)}, \tag{12}$$

the adopted theory corresponds to the work conjugate theory of Gurtin (2000, 2002) through the micro-force balance equation

$$\xi_{i,i}^{(\alpha)} + \tau^{(\alpha)} - \tau_{eff}^{(\alpha)} = 0, \tag{13}$$

where $\tau_{eff}^{(\alpha)}$ is the effective resolved shear stress (given by $\tau_{eff}^{(\alpha)} = \tau^{(\alpha)} - \tau_b^{(\alpha)}$). The higher order stress, known as the work conjugate to the slip gradients in other theories, is derived from the free energy as

$$\xi_i^{(\alpha)} = \frac{\partial \psi_G^{(\alpha)}}{\partial \gamma_{,i}^{(\alpha)}}, \tag{14}$$

where ψ_G is the plastic part of the free energy, which is associated with slip gradients. Using relation (12), the non-work conjugate theory is rewritten in a work conjugate form. Following this framework in the model development ensures that it automatically comes out in a thermodynamically consistent manner, once a constitutive relation for the gradient energy, ψ_G, has been assumed. The gradient energy is often taken to be of a quadratic nature on the form (see e.g. Kuroda and Tvergaard, 2006, 2008; Anand et al., 2012; Klusemann and Yalçinkaya, 2013; Niordson and Kysar, 2014).

$$\psi_G^{(\alpha)} = \frac{1}{2}\tau_0 L^2 \left(\gamma_{,i}^{(\alpha)} s_i^{(\alpha)}\right)^2, \tag{15}$$

where L is a material length scale parameter, entering for dimensional consistency. This form of the gradient energy, however, is chosen primarily for mathematical convenience rather than based on physical arguments. Assuming the quadratic gradient energy in Eq. (15), the Eqs. (12) and (14) lead to the following back stress relation, depending on the second gradients of slip

$$\tau_b^{(\alpha)} = -\tau_0 L^2 \gamma_{,ij}^{(\alpha)} s_i^{(\alpha)} s_j^{(\alpha)}, \tag{16}$$

which, expressed in terms of GND densities, becomes

$$\tau_b^{(\alpha)} = b\tau_0 L^2 \rho_{G(e),i}^{(\alpha)} s_i^{(\alpha)}. \tag{17}$$

While this theory captures size effects in strain gradient hardening well, it cannot capture, realistically, the highly non-uniform dislocation structures observed in experimental studies of e.g. wedge indentation (Kysar et al., 2010; Öztop, 2011; Dahlberg et al.,

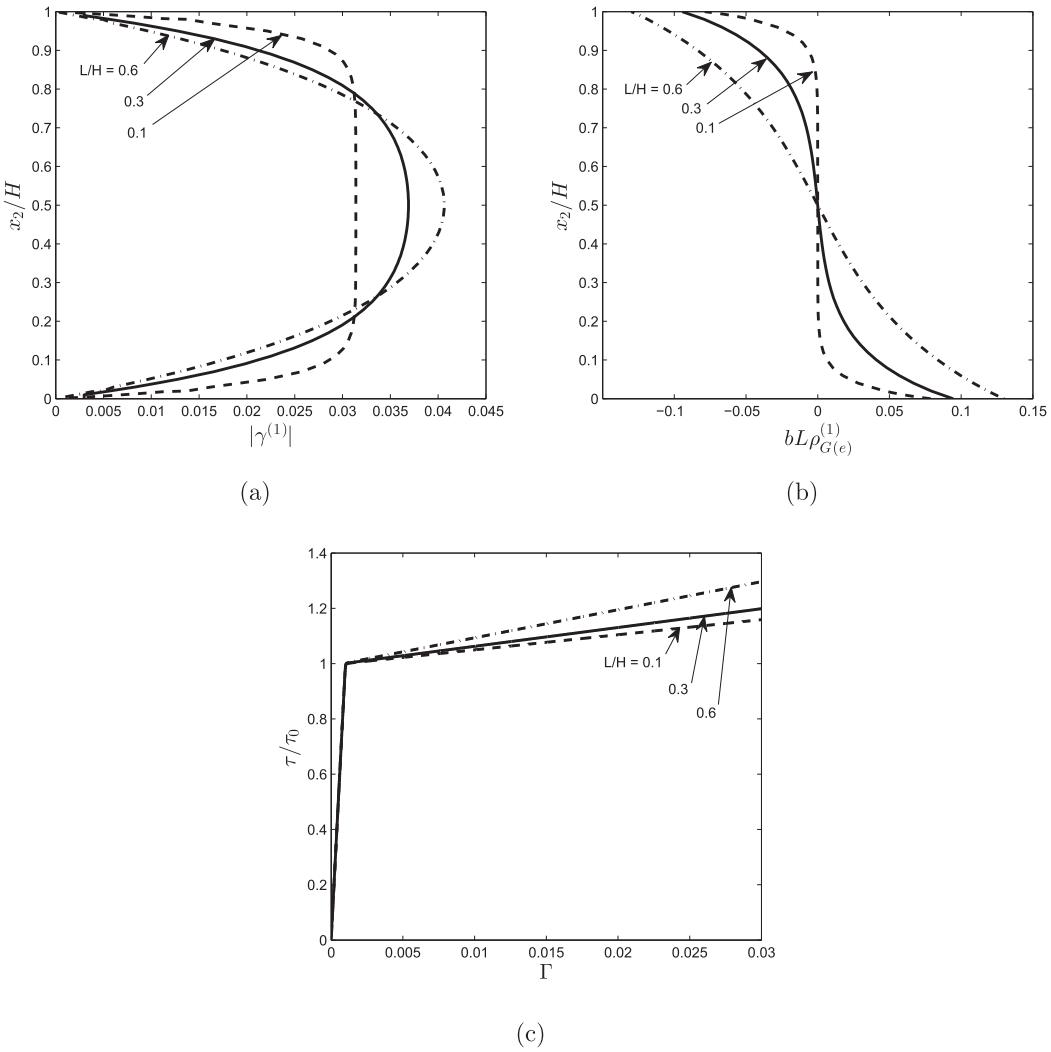

Fig. 2. Numerical results for the single slip simple shear problem (Fig. 1) with $\theta = 90^\circ$, for different values of the material length scale parameter L. The figure shows (a) slip profile, (b) normalized GND density, and (c) shear stress vs. macroscopic shear strain.

2014). The single slip simple shear problem, described in Section 3 and Fig. 1, is solved to demonstrate the behavior of the model assuming the classical perception of the back stress. Results for different values of the material length scale parameter, L, are shown in Fig. 2, assuming a quadratic gradient energy and thus the back stress in Eqs. (16) and (17). The slip profile across the material slab is shown in Fig. 2a and the GND profile is shown in Fig. 2b. The slip profile indicates an increasing flattening of the central part for decreasing L, while a rather smooth distribution of GNDs is obtained. It is noticed, however, that increased localization of GNDs takes place at the boundaries for decreasing values of L. The shear stress vs. macroscopic shear strain response is shown in Fig. 2c. Hardening clearly increases with L, as the back stress effect becomes increasingly significant, whereas for very low values of L, the size-effect diminishes. Similar results can be found in Anand et al. (2005). Although no experimental results exist for direct comparison with the plane strain simple shear case, this boundary value problem outlines the model's ability to represent the highly localized GND structures observed experimentally.[2]

It is possible to achieve increasingly non-uniform GND density distributions, when decreasing the influence of L, however, decreasing L until a satisfactory micro-structure is achieved clearly does not guarantee the proper size-dependence in the hardening behavior. Thus, in general one must assume that more than one constitutive parameter is needed for a model describing both size-effects and evolution of micro-structure.

In the following, alternative options for the back stress formulation will be explored in order to pursue a GND field response closer to experimental observations. There are arguments pointing toward a gradient energy which is closer to

[2] Moreover, in the wedge indentation case studied by Kysar et al. (2010), Öztop (2011), and Dahlberg et al. (2014), there are regions beneath the indentation which are dominated by approximate simple shear, of which Fig. 1 can be considered a simple model.

linear rather than quadratic (Evans and Hutchinson, 2009, see Section 5). A free energy potential linear in the slip gradients was investigated by Ohno and Okumara (2007) and Forest and Guéninchault (2013). Here, a generalization from the quadratic form of the gradient energy in Eq. (15), shall serve as basis for the following analysis. Assuming power law dependence on the slip gradients, one could write the gradient energy as

$$\psi_G^{(\alpha)} = \frac{1}{\mu+1}\tau_0 L^{\mu+1}\left|\gamma_{,i}^{(\alpha)} s_i^{(\alpha)}\right|^{\mu+1}. \tag{18}$$

A similar energy relation was proposed by Fredriksson and Gudmundson (2007) for interface modeling, where a near linear to quadratic dependence on the plastic strain was investigated. For a linear dependence on the plastic strain, their theory conforms with the dislocation based theory of Read and Shockley (1950) for low angle tilt boundaries. Recently, Bardella (2010), Bardella and Panteghini (2015), and Fleck et al. (2015) also proposed expressions for the free energy similar to Eq. (18). The generalized energy expression (Eq. (18)) leads to a back stress which is still a linear function of the second gradients of slip (as Eq. (17)), but in turn reveals a dependence on the first gradients of slip (or the GND densities), to the power of μ-1:

$$\tau_b^{(\alpha)} = -\mu\tau_0 L^{\mu+1}\left|\gamma_{,j}^{(\alpha)} s_j^{(\alpha)}\right|^{\mu-1}\gamma_{,ki}^{(\alpha)} s_i^{(\alpha)} s_k^{(\alpha)}, \tag{19}$$

which, expressed in terms of GND densities, becomes

$$\tau_b^{(\alpha)} = \mu\tau_0 b^{\mu} L^{\mu+1}\left|\rho_{G(e)}^{(\alpha)}\right|^{\mu-1}\rho_{G(e),i}^{(\alpha)} s_i^{(\alpha)}. \tag{20}$$

For $\mu = 1$, Eq. (18) is quadratic and Eqs. (19) and (20) reduce to Eqs. (16) and (17), respectively. The effect of μ is schematically illustrated in Fig. 3. In the studies by Groma et al. (2003) and Yefimov et al. (2004) on a single slip continuum description of dislocation dynamics, a back stress relation similar to Eq. (20) for $\mu \to 0$ was found, based on the shear stress field of a single dislocation. In fact, the functional dependence on dislocation densities in Yefimov et al. (2004) is identical to Eq. (20), if no distinction is made between the so-called total and signed dislocation densities (see Yefimov et al. (2004) Eq. (13)). When the order of the gradient energy is lower than quadratic ($\mu < 1$), numerical solution becomes cumbersome, since the back stress then approaches infinity when the GND density approaches zero. Hence, with a combination of low GND density and relatively high GND density gradients, the numerical solution can become unstable. Therefore, for values of μ below one, an "effective" GND density $\rho_{G(e),eff}^{(\alpha)} = \left|\rho_{G(e)}^{(\alpha)}\right| + \rho_{G(e),0}$ replaces $\left|\rho_{G(e)}^{(\alpha)}\right|$ in Eq. (20), in order to exclude the effect of the singularity in the back stress function. A value of $\rho_{G(e),0} = 10^5$ m^{-2} is used in the present computations and a sensitivity analysis showed $\rho_{G(e),0}$ to have negligible effect on the qualitative results. The effect of $\rho_{G(e),0}$ is demonstrated in Appendix A. The implications of the generalized back stress are demonstrated in Figs. 4 through 6. Figs. 4 and 5 are equivalent but show results for two different regimes of the energy exponent, μ: Quadratic to cubic gradient energy ($1 \le \mu \le 2$) and nearly linear to quadratic gradient energy ($0 < \mu \le 1$), respectively. From a phenomenological point of view, Fig. 4 shows interesting results. The flattening of the slip profile is seen for increasing values of μ in Fig. 4a, associated with an intense build-up of GND density at the boundaries (Fig. 4b). In the case of $\mu = 2$ (cubic energy), the GND density gradients are practically eliminated in the interior region of approximately 70 percent of the slab height, whereas a steep increase takes place at the boundaries. The GND density profile is normalized with its boundary value (the maximum GND density in the material domain, $\rho_{G(e),max}^{(1)}$) in order to qualitatively demonstrate the effect of μ. The normalization value, $\rho_{G(e),max}^{(1)}$, can be seen in Fig. 6 as function of μ. Here, the effect of μ is demonstrated for different values of the material length

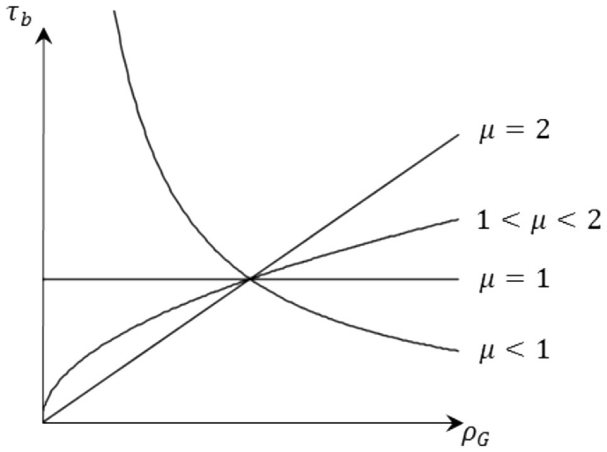

Fig. 3. Schematic illustration of the generalized gradient energy based back stress law (Eq. (20)).

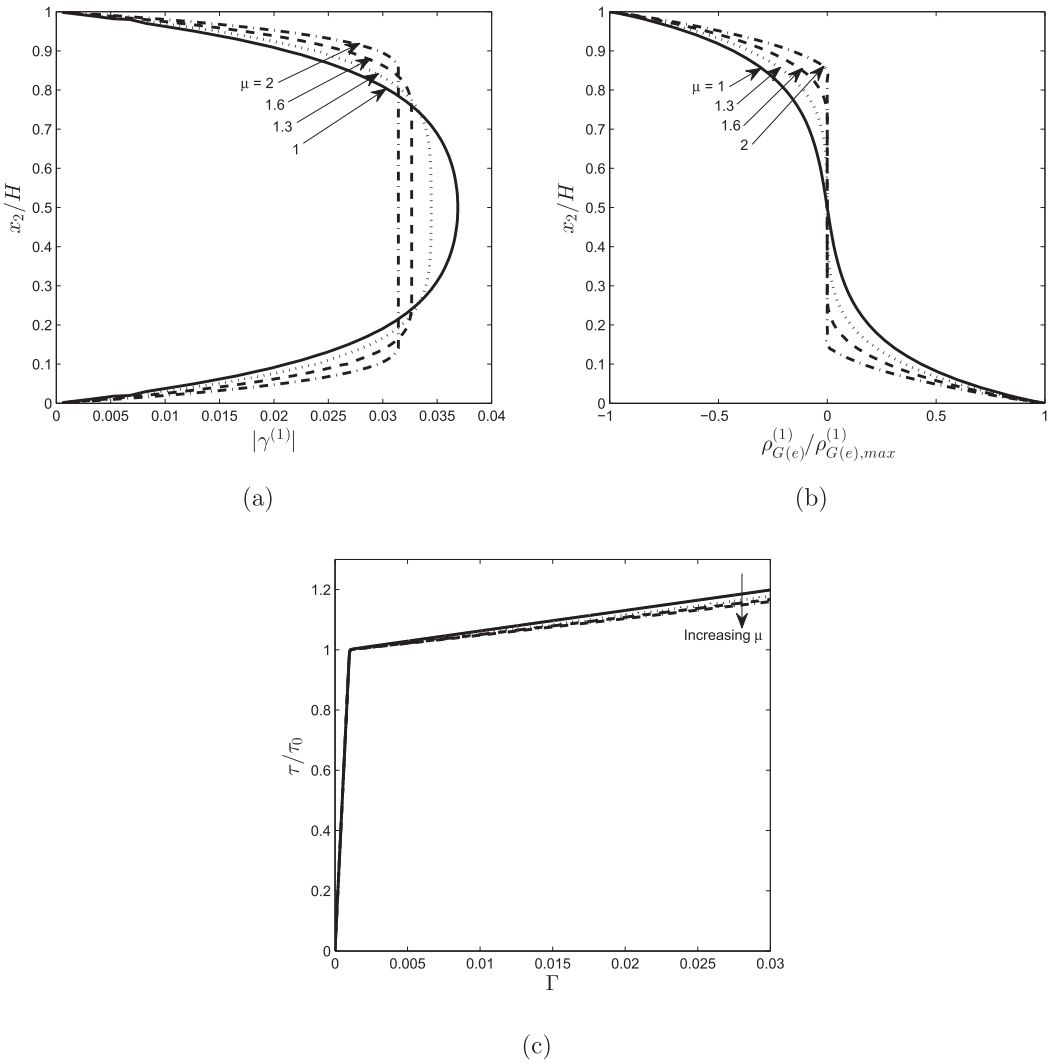

Fig. 4. Numerical results for the single slip simple shear problem (Fig. 1), using the generalized gradient energy based back stress (Eqs. (19) and (20)), with $\theta = 90^\circ$ and $\mathbf{L}/\mathbf{H} = 0.3$, illustrating the effect of the μ parameter in the quadratic to cubic regime ($\mathbf{1} \leq \mu \leq \mathbf{2}$). The figure shows (a) slip profile, (b) normalized GND density, (c) shear stress vs. macroscopic shear strain.

scale parameter, at a macroscopic strain level of $\Gamma = 0.03$. In the shear stress vs. macroscopic shear strain response (Fig. 4c), the linear hardening decreases with increasing μ. This is further demonstrated in Fig. 7 for different values of the material length scale parameter. Fig. 5 shows results in the linear to quadratic regime of the gradient energy, with the flattening of the slip profile evident for low values of μ (Fig. 5a). As μ goes to one, the effect of the back stress singularity moves closer to $\rho_{G(e),0}$ and it starts to have an effect on the hardening behavior. This is seen, in Fig. 5a, as a small notch on the slip profile in the center region of the material domain, that diminishes as μ goes to zero. Fig. 5b shows the GND density profile, where the density is found to intensify at the boundaries for very low values of μ, however, the opposite effect occurs at intermediate values, e.g. at $\mu = 0.4$. The general trend of the dependence on μ has a turning point, which appears as a local minimum in Fig. 6, when plotting $\rho^{(1)}_{G(e),max}$ as function of μ. The local minimum shifts upward for increasing L and is seen, e.g., at approximately $\mu = 0.5$ for $L/H = 0.3$. Fig. 5c shows the shear stress vs. macroscopic shear strain, where a non-linear response is observed for lower values of μ. Here, as well, a non-trivial effect of μ is predicted, which is evident from Fig. 7. It is seen that the flow stress level at $\Gamma = 0.03$ has a local maximum, which shifts upward for increasing L. This maximum is found, e.g., at approximately $\mu = 0.3$ for $L/H = 0.3$ (see Fig. 7).

Evers et al. (2004) argue that the GND density itself does not contribute to the long range internal stresses (i.e. the back stress). However, this is not the case in Eq. (20), where a strong dependence on the GND density is seen. The authors do not attempt to advocate any physical advantages of the dependence on GND density, however, it is noted that a uniform GND field yields zero back stress in accordance with the arguments put forth by Evers et al. (2004).

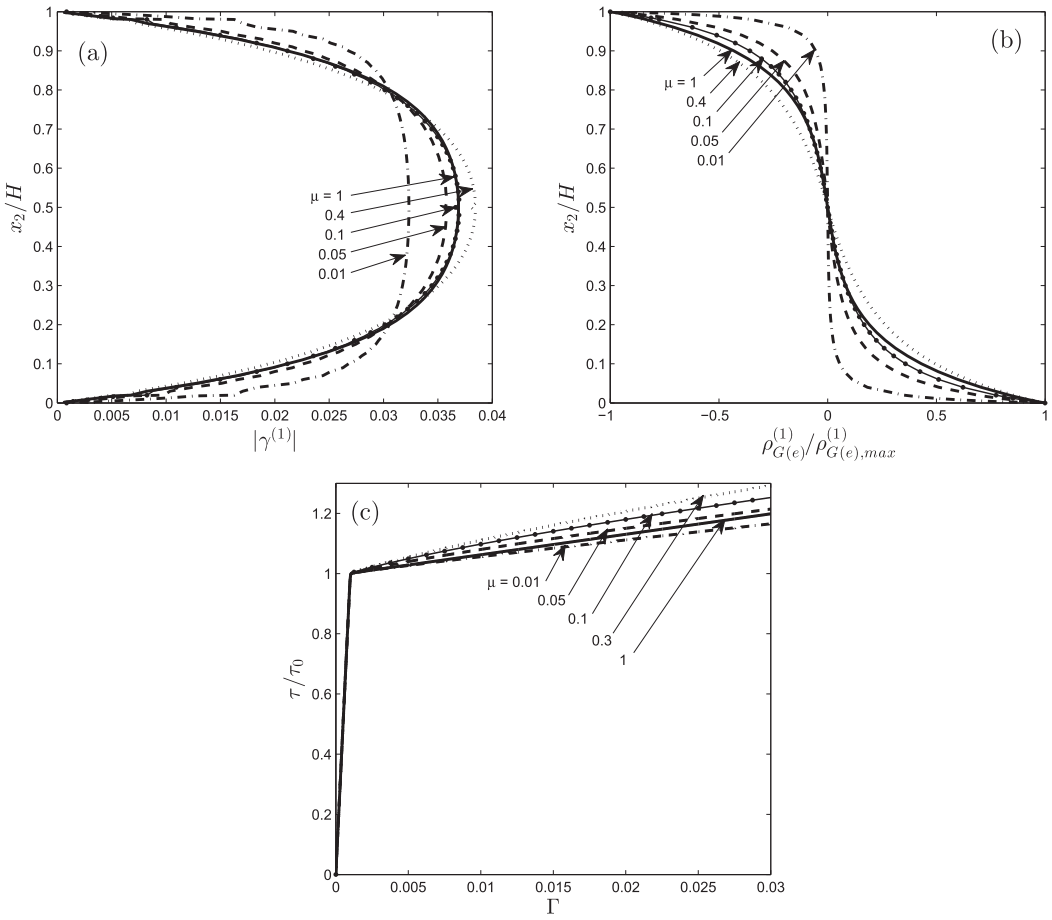

Fig. 5. Numerical results for the single slip simple shear problem (Fig. 1), using the generalized gradient energy based back stress (Eqs. (19) and (20)), with $\theta = 90^{\circ}$, $\mathbf{L}/\mathbf{H} = 0.3$, and $\rho_{\mathbf{G(e)},\mathbf{0}} = 10^5\ \mathrm{m}^{-2}$, illustrating the effect of the μ parameter in the linear to quadratic regime ($\mathbf{0} < \mu \leq \mathbf{1}$). The figure shows (a) Slip profile, (b) normalized GND density, and (c) shear stress vs. macroscopic shear strain.

When $\mu \to 0$ or $\mu \to 2$ in the back stress relation in Eqs. (19) and (20), slip localization is promoted through its relationship with the GND density, enabling GND wall formation at the hard boundaries. This type of behavior can also be imposed through the relationship between the back stress and the GND density gradients, since a GND wall is also tied to high levels of GND density gradients. In the framework proposed by Kuroda and Tvergaard (2006, 2008) any function $\tau_b^{(\alpha)}(\rho^{(\alpha)}_{G(e),i}s_i^{(\alpha)})$ may be considered. Thus, one could assume the following power law proportionality for the back stress relation:

$$\tau_b^{(\alpha)} \propto \left|\rho^{(\alpha)}_{G(e),i}s_i^{(\alpha)}\right|^{\kappa}, \quad 0 \leq \kappa \leq 1. \tag{21}$$

For values of κ below one, this type of relation allows the slip to build up more severely with less restriction imposed by the back stress as the GND density gradients evolve. However, Eq. (21) has an initially infinite slope in the limit of $\kappa = 0$, which would cause numerical difficulties for low values of the quantity $\rho^{(\alpha)}_{G(e),i}s_i^{(\alpha)}$. Thus, in order to investigate the influence of $\left|\rho^{(\alpha)}_{G(e),i}s_i^{(\alpha)}\right|^{\kappa}$ in the back stress formulation, the quadratic gradient energy based back stress is taken as starting point in the back stress power law, so that

$$\tau_b^{(\alpha)} = \begin{cases} b\tau_0 L^2 \rho^{(\alpha)}_{G(e),i}s_i^{(\alpha)} & , \quad \text{for } \tau_b^{(\alpha)} \leq \tau_T \\ \mathrm{sgn}\left(\rho^{(\alpha)}_{G(e),i}s_i^{(\alpha)}\right) b^{\kappa}\tau_T^{1-\kappa}\tau_0^{\kappa}L^{2\kappa}\left|\rho^{(\alpha)}_{G(e),i}s_i^{(\alpha)}\right|^{\kappa} & , \quad \text{for } \tau_b^{(\alpha)} > \tau_T \end{cases}, \tag{22}$$

with τ_T being a transition back stress parameter. When κ is equal to one, Eq. (22) reduces to the expression in Eq. (17), i.e., corresponding to a quadratic gradient energy. With κ equal to zero, Eq. (22) corresponds to a blunt cut-off of the back stress at $\tau_b^{(\alpha)} = \tau_T$. A schematic representation of this back stress relation can be found in Fig. 8. This set-up allows for the back stress to

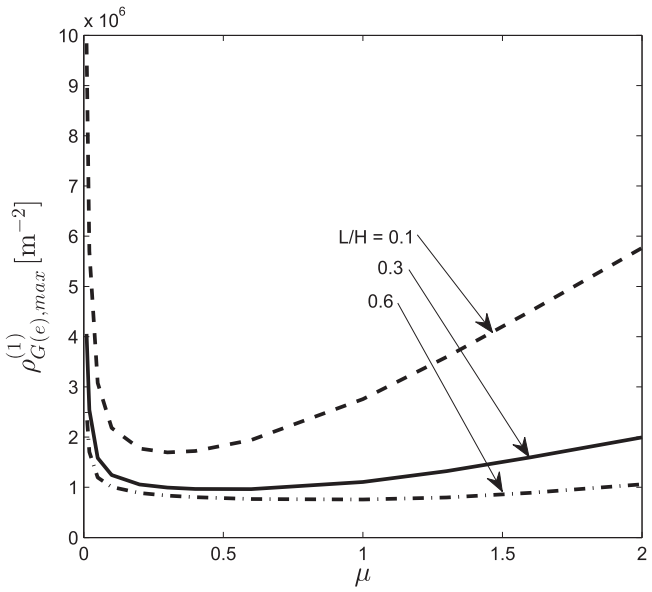

Fig. 6. Magnitude (normalization values in Figs. 7b and 8b) of GND density as function of μ (Eqs. (19) and (20)) at a macroscopic shear strain of $\Gamma = 0.03$. Results are shown for different values of the material length scale parameter L.

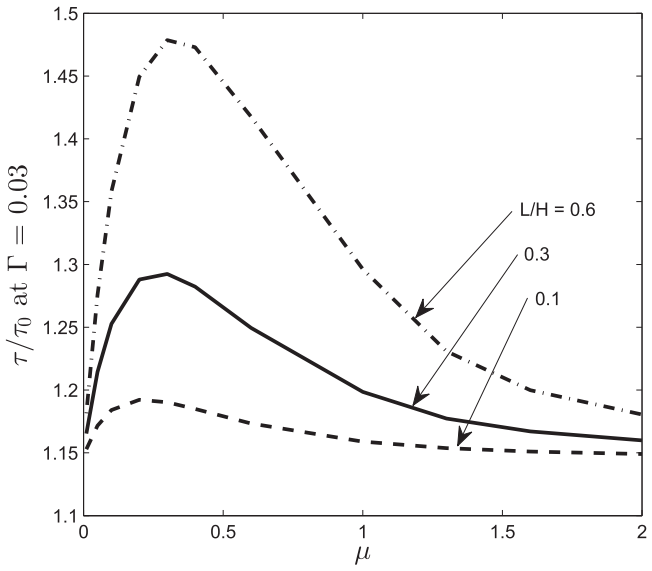

Fig. 7. Shear flow stress at macroscopic shear strain $\Gamma = 0.03$ as function of μ, illustrating the effect of μ (Eqs. (19) and (20)) on the stress/strain response in Figs. 4c and 5c. Results are shown for different values of the material length scale parameter L.

build up linearly, with the gradients of GND density, to a certain level before evolving according to a power law. The two formulations (Eqs. (20) and (22)) coincide for μ and κ equal to one (quadratic gradient energy), for which the back stress in Eq. (22) naturally provides a thermodynamically consistent theory. However, since the full back stress power law in Eq. (22) does not originate from a gradient energy constitutive law, the general form of Eq. (22) must be considered a non-thermodynamically consistent formulation. Fig. 9 shows results using the back stress power law relation in Eq. (22) for different values of κ with $\tau_T/\tau_0 = 0.12$ and $L/H = 0.3$. Fig. 9a shows the slip profile with increased localized slip at the boundaries for decreasing values of κ and Fig. 9b shows the GND density profile normalized with the value at the boundary, $\rho^{(1)}_{G(e),max}$, in order to qualitatively demonstrate the effect of κ. Here, the transition point, $\tau_b = \tau_T$, is marked with a small circle on the individual curves near the lower boundary for the values $0 < \kappa < 1$. This point appears exactly on the boundary for κ equal to zero, since in this case the back stress is forced to not exceed τ_T (hence, not marked on the figure). The normalization value is presented in Fig. 10 as function of κ, showing also the effect of the material length scale parameter L. Here, it is noticed

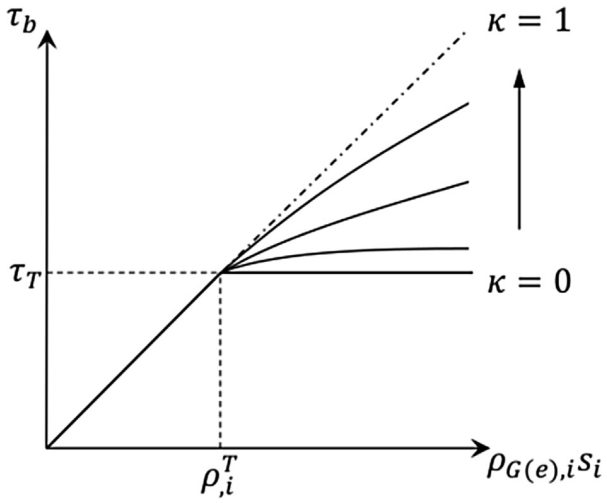

Fig. 8. Schematic illustration of the back stress power law (Eq. (22)).

that the effect of L, on the level of GND density at the boundaries, changes character in the low regime of κ. As κ approaches zero, the GNDs evolve more locally, whereby more pronounced dislocation "walls" form. Thus, for low values of κ, the micro-structural response bears closer resemblance to what is observed in experimental studies. The results demonstrate that a highly non-uniform micro-structure, with high GND density at the boundaries and low GND density and GND density

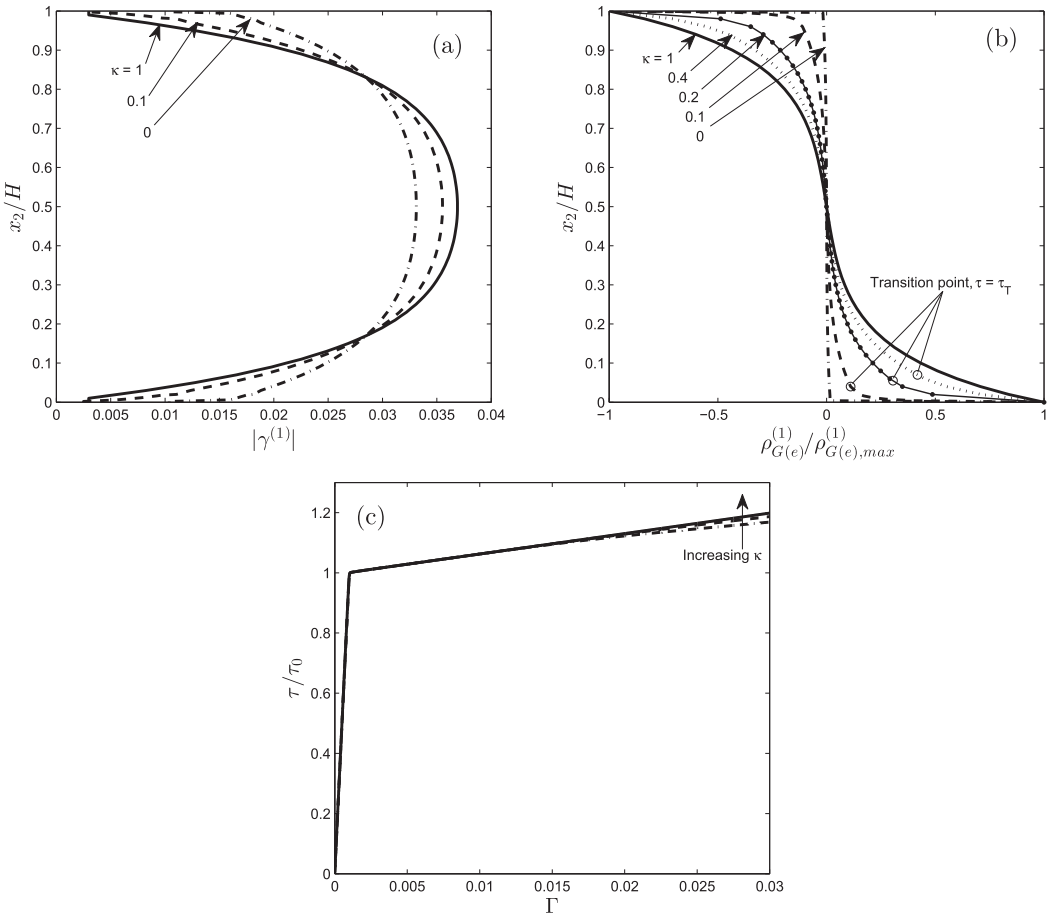

Fig. 9. Numerical results for the single slip simple shear problem (Fig. 1), using the back stress power law (Eq. (22)), with $\theta = 90^\circ$, $\mathbf{L}/\mathbf{H} = 0.3$, and $\tau_{\mathbf{T}}/\tau_{\mathbf{0}} = 0.12$, illustrating the effect of the κ parameter. The figure shows (a) Slip profile, (b) normalized GND density, with circles marking the transition point $\tau_{\mathbf{b}} = \tau_{\mathbf{T}}$, and (c) shear stress vs. macroscopic shear strain.

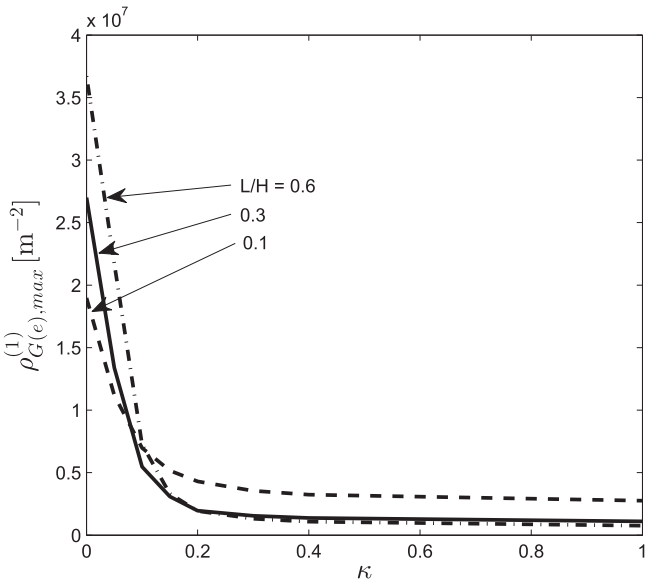

Fig. 10. Magnitude (normalization values in Fig. 4b) of GND density as function of κ (Eq. (22)) at a macroscopic shear strain of $\Gamma = 0.03$. Results are shown for different values of the material length scale parameter L.

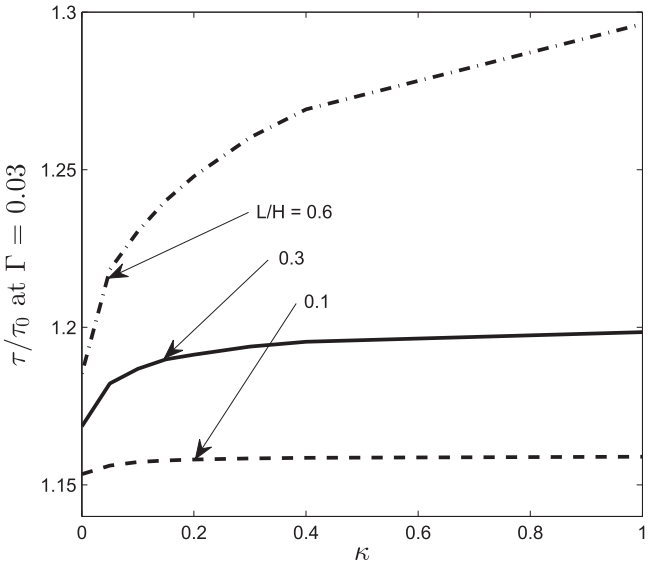

Fig. 11. Shear flow stress at 0.03 macroscopic shear strain as function of κ (Eq. (22)), to illustrate the effect of κ on the stress/strain response in Fig. 9c. Results are shown for different values of the material length scale parameter L.

gradients in the interior region, can be achieved through the dependence of the back stress on the GND density gradient. Fig. 9c shows the shear stress vs. macroscopic shear strain response with little effect of the κ parameter—though with a slight non-linear hardening effect appearing as κ decreases. The effect of κ on the flow stress is further demonstrated in Fig. 11 for different values of the material length scale. The effect of the rate exponent, m, on the GND density distribution, using back stress relation (22), was studied in El-Naaman et al. (2015), where increasing values of m was shown to increase the effect of κ.

5. Concluding remarks

A finite element implementation of the non-work conjugate higher order strain gradient crystal plasticity model, proposed by Kuroda and Tvergaard (2006, 2008), has formed the basis in the development of back stress formulations aimed at improving the ability to predict micro-structural evolution. This paper treats the highly idealized pure shear case, which serves as a benchmark for the performance of the proposed model.

Motivated by experimental observations, two distinct back stress formulations have been proposed in the present study:

i) A back stress based on a general formulation of the strain gradient energy, which provides a thermodynamically consistent theory (Eqs. (19) and (20)). This formulation ensures that the GND density field develops more localized and intensely for a gradient energy in the near linear regime but also in the high quadratic to cubic regime. Thereby, two alternatives are revealed, in terms of the exponential order of the gradient energy, improving the micro-structural response and enabling the representation of a dislocation wall and cell structure. This finding partly supports the argument put forth by Evans and Hutchinson (2009), that the energy associated with GNDs is likely linearly dependent on the plastic strain gradient.
ii) A purely phenomenologically devised back stress power law formulation, taking as starting point the quadratic form of the gradient energy. Here, an exponent κ on the gradients of the GND density, is introduced (see Eq. (22)). This formulation has no direct dependence on the GND density—in line with the quadratic energy based back stress in Eq. (17). Low values of the exponent κ produce a steeper build up of the GND density at the micro-structurally passivated boundaries. Thus, a dislocation wall and cell type response can be achieved through the additional constitutive parameter κ.

With the two different formulations, summarized above, it has been shown that it is possible to achieve a micro-structural response that can represent a dislocation wall and cell structure (as defined in Section 3), while preserving the possibility of capturing size-effects. This feature, which a quadratic gradient energy derived back stress excludes, is offered in the proposed formulations through the introduction of an additional constitutive parameter, dedicated to calibrating the model against experimentally observed micro-structures.

Further research on more complicated boundary value problems, e.g. including multi-slip and latent hardening, as well as an investigation of the proposed models' performance under cyclic loading, is needed in order to fully establish their capabilities.

Acknowledgments

The work is financially supported by The Danish Council for Independent Research under the research career programme Sapere Aude in the project “Higher Order Theories in Solid Mechanics”, grant 11-105098/FTP.

Appendix A. The effect of $\rho_{G(e),0}$

The GND density parameter value $\rho_{G(e),0} = 10^5$ m^{-2} was chosen for the computations in the present study in order to facilitate a solution for all used model parameters. The singularity of the back stress relation in Eq. (20) has an increasing effect as $\rho_{G(e),0}$ is decreased—rendering a solution impossible for very low values of $\rho_{G(e),0}$. Letting $\mu \to 1$ further accentuates this effect, as μ also controls the extent of the singularity effect. In Fig. A.12, the effect of $\rho_{G(e),0}$ is demonstrated through a comparison of GND density at the microscopic hard boundary (See Fig. 1). For a material length scale of $L/H = 0.3$, results obtained with $\rho_{G(e),0} = 10^5$ m^{-2} are compared to results for $\rho_{G(e),0} = 10^4$ m^{-2}. It is seen that the effect of $\rho_{G(e),0}$ is most pronounced for the low intermediate values of μ.

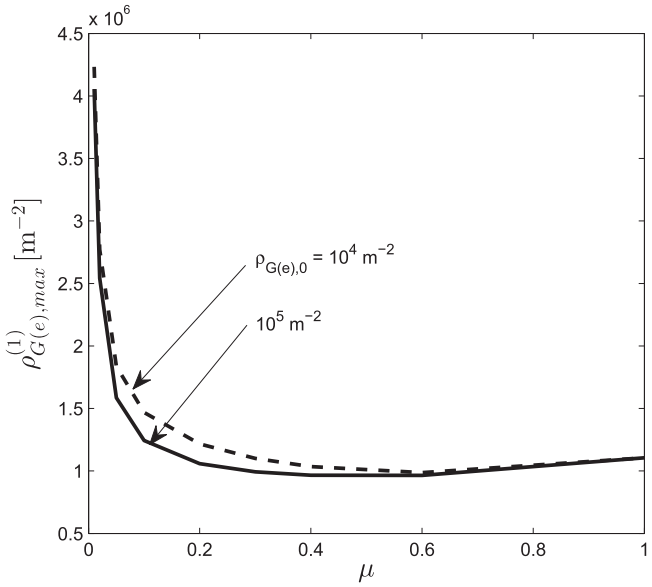

Fig. A.12. Magnitude of GND density as function of μ (Eqs. (19) and (20)) at a macroscopic shear strain of $\Gamma = 0.03$ for $\boldsymbol{L}/\boldsymbol{H} = 0.3$. Results are shown for two different orders of magnitude of $\rho_{\boldsymbol{G(e),0}}$.

References

Anand, L., Aslan, O., Chester, S., 2012. A large-deformation gradient theory for elastic-plastic materials: strain softening and regularization of shear bands. Int. J. Plasticity 30–31, 116–143.

Anand, L., Gurtin, M., Lele, S., Gething, C., 2005. A one-dimensional theory of strain-gradient plasticity: formulation, analysis, numerical results. J. Mech. Phys. Solids 53, 1789–1826.

Ananthan, V., Leffers, T., Hansen, N., 1991. Cell and band structures in cold-rolled polycrystalline copper. Mater. Sci. Technol. 7, 1069–1075.

Ashby, M., 1970. The deformation of plastically non-homogeneous alloys. Philos. Mag. 21, 399–424.

Bardella, L., 2010. Size effects in phenomenological strain gradient plasticity constitutively involving the plastic spin. Int. J. Eng. Sci. 48, 550–568.

Bardella, L., Panteghini, A., 2015. Modelling the torsion of thin metal wires by distortion gradient plasticity. J. Mech. Phys. Solids 78, 467–492.

Bassani, J., 2001. Incompressibility and a simple gradient theory of plasticity. J. Mech. Phys. Solids 49, 1983–1996.

Bayley, C., Brekelmans, W., Geers, M., 2006. A comparison of dislocation induced back stress formulations in strain gradient crystal plasticty. Int. J. Solids Struct. 43, 7268–7286.

Dahlberg, C., Saito, Y., Öztop, M., Kysar, J., 2014. Geometrically necessary dislocation density measurements associated with different angles of indentations. Int. J. Plasticity 54, 81–95.

Deshpande, V., Needleman, A., Van der Giessen, E., 2003. Finite strain discrete dislocation plasticity. J. Mech. Phys. Solids 51, 2057–2083.

Deshpande, V., Needleman, A., Van der Giessen, E., 2005. Plasticity size effects in tension and compression of single crystals. J. Mech. Phys. Solids 53, 2661–2691.

El-Naaman, S., Nielsen, K., Niordson, C., 2015. Strain gradient crystal plasticity: a continuum mechanics approach to modeling micro-structural evolution. Plastic Behav. Conv. Adv. Mater. Theory Exp. Model. 7–9.

Evans, A., Hutchinson, J., 2009. A critical assessment of theories of strain gradient plasticity. Acta Mater. 57, 1675–1688.

Evers, L., Brekelmans, W., Geers, M., 2004. Non-local crystal plasticity model with intrinsic SSD and GND effects. J. Mech. Phys. Solids 52, 2379–2401.

Fleck, N., Hutchinson, J., Willis, J., 2015. Guidelines for constructing strain gradient plasticity theories. J. Appl. Mech. 82, 1–10.

Forest, S., Guéninchault, N., 2013. Inspection of free energy functions in gradient crystal plasticity. Acta Mech. Sin. 29 (6), 763–772.

Fredriksson, P., Gudmundson, P., 2007. Modelling of the interface between a thin film and a substrate within a strain gradient plasticity framework. J. Mech. Phys. Solids 55 (5), 939–955.

Groma, I., 1997. Link between the microscopic and mesoscopic length-scale description of the collective behavior of dislocations. Phys. Rev. B 56 (10).

Groma, I., Csikor, F., Zaizer, M., 2003. Spatial correlations and higher-order gradient terms in a continuum description of dislocation dynamics. Acta Mater. 51, 1271–1281.

Gurtin, M., 2000. On the plasticity of single crystals: free energy, microforces, plastic-strain gradients. J. Mech. Phys. Solids 48 (5), 989–1036.

Gurtin, M., 2002. A gradient theory of single-crystal viscoplasticity that accounts for geometrically necessary dislocations. J. Mech. Phys. Solids 50, 5–32.

Hong, C., Huang, X., Winter, G., 2013. Dislocation content of geometrically necessary boundaries aligned with slip planes in rolled aluminium. Philos. Mag. 93 (23), 3118–3141.

Huang, X., Winther, G., 2007. Dislocation structures. Part I. Grain orientation dependence. Philos. Mag. 87 (33), 5189–5214.

Huang, Y., Qu, S., Hwang, K., Li, M., Gao, H., 2004. A conventional theory of mechanism-based strain gradient plasticity. Int. J. Plasticity 20, 753–782.

Hutchinson, J., 1976. Bounds and self-consistent estimates for creep of polycrystalline materials. Proc. R. Soc. Lond. A 348, 101–127.

Hutchinson, J., 2012. Generalized J_2 flow theory: fundamental issues in strain gradient plasticity. Acta Mech. Sin. 28 (4), 1078–1086.

Klusemann, B., Yalçinkaya, T., 2013. Plastic deformation induced microstructure evolution through gradient enhanced crystal plasticity based on a non-convex Helmholtz energy. Int. J. Plasticity 48, 168–188.

Kuroda, M., Tvergaard, V., 2006. Studies of scale dependent crystal viscoplasticity models. J. Mech. Phys. Solids 54, 1789–1810.

Kuroda, M., Tvergaard, V., 2008. On the formulation of higher-order strain gradient crystal plasticity models. J. Mech. Phys. Solids 56, 1591–1608.

Kysar, J., Saito, Y., Oztop, M., Lee, D., Huh, W., 2010. Experimental lower bounds on geometrically necessary dislocation density. Int. J. Plasticity 26, 1097–1123.

Nemat-Nasser, S., Luqun, N., Okinaka, T., 1998. A constitutive model for fcc crystals with application to polycrystalline OFHC copper. Mech. Mater. 30, 325–341.

Niordson, C., Hutchinson, J., 2003. On lower order strain gradient plasticity theories. Eur. J. Mech. A/Solids 22, 771–778.

Niordson, C., Kysar, J., 2014. Computational strain gradient crystal plasticity. J. Mech. Phys. Solids 62, 31–47.

Ohno, N., Okumara, D., 2007. Higher-order stress and grain size effects due to self-energy of geometrically necessary dislocations. J. Mech. Phys. Solids 55, 1879–1898.

Öztop, M., 2011. Multiscale Experimental Analysis in Plasticity: Linking Dislocation Structures to Continuum Fields. Columbia University (Ph.D. thesis).

Öztop, M., Niordson, C., Kysar, J., 2012. Length-scale effect due to periodic variation of geometrically necessary dislocation densities. Int. J. Plasticity 41, 189–201.

Peirce, D., Asaro, R., Needleman, A., 1983. Material rate dependence and localized deformation in crystalline solids. Acta Metall. 31, 1951–1976.

Read, W., Shockley, W., 1950. Dislocation models of crystal grain boundaries. Phys. Rev. 78, 275–289.

Tarleton, E., Balint, D., Gong, J., Wilkinson, A., 2015. A discrete dislocation plasticity study of the micro-cantilever size effect. Acta Mater. 88, 271–282.

van Beers, P., McShane, G., Kouznetsova, V., Geers, M., 2013. Grain boundary interface mechanics in strain gradient crystal plasticity. J. Mech. Phys. Solids 61, 2659–2679.

Voyiadjis, G., Yaghoobi, M., 2015. Large scale atomistic simulation of size effects during nanoindentation: dislocation length and hardness. Mater. Sci. Eng. A 634, 20–31.

Yaghoobi, M., Voyiadjis, G., 2014. Effect of boundary conditions on the MD simulation of nanoindentation. Comput. Mater. Sci. 95, 626–636.

Yefimov, S., Groma, I., van der Giessen, E., 2004. A comparison of a statistical-mechanics based plasticity model with discrete dislocation plasticity calculations. J. Mech. Phys. Solids 52, 279–300.

Publication [P3]

An investigation of back stress formulations under cyclic loading

An investigation of back stress formulations under cyclic loading

S.A. El-Naaman*, K.L. Nielsen, C.F. Niordson

Department of Mechanical Engineering, Solid Mechanics, Technical University of Denmark, DK-2800 Kgs. Lyngby, Denmark

Abstract

A theory for predicting realistic micro-structural evolution in plastically deformed crystalline materials, suitable for large scale continuum modeling, has yet to be established. In many micro-structurally based continuum theories, a single material length parameter governs both the material size dependence and the micro-structural behavior. In a previous work by the authors, addressing this matter, two new back stress formulations were proposed, which proved to offer novel modeling capabilities in the localization behavior of geometrically necessary dislocation pile-up under monotonic loading. However, the cyclic behavior of these formulations remains to be investigated. The present paper studies the new back stress formulations, within a non-work conjugate type higher order strain gradient crystal plasticity framework, and demonstrates their performance through the idealized single slip simple shear case. At high values of the material length scale parameter, a seemingly anomalous cyclic response is observed when deviating from the conventional type back stress formulation. Similar observations have recently been reported in other numerical studies, and the present work offers a discussion of the physical justification of such material behavior. It is found that the properties of the adopted formulations, in fact, opens the possibility for modeling complex material behavior, tied to the presence of long range internal stresses due to dislocation pile-up. Moreover, the present study extends the discussion on micro-structure predictions as a consequence of the adopted back stress models.

Keywords: Strain gradient plasticity, Size-effects, Bauschinger effect, Geometrically necessary dislocations, Crystal plasticity

1. Introduction

Due to substantial experimental evidence, it is now well established that ductile crystalline materials exhibit size-dependent behavior in the presence of spatial gradients of plastic strain (see e.g. Fleck et al., 1994; Mu et al., 2014). More specifically, an increase in hardening and/or an apparent increase in yield point (also refered to as strengthening) is observed. The phenomena may be explained in terms of the so-called geometrically necessary dislocations (GNDs), and statistically stored dislocations (SSDs), of which the former play a key role in micron and sub-micron scale plasticity problems. One example, often referred to in the literature, is crack tip plasticity and its influence

*Tel: +45 4525-4020, Fax: +45 4593-1475
URL: saeln@mek.dtu.dk (S.A. El-Naaman)

on the fracture toughness (e.g. Wei and Hutchinson, 1997, 1999; Nielsen et al., 2012; Martínez-Pañeda and Niordson, 2015). For several decades gradient effects have been studied and numerous theories have been proposed to model the observed size effects. Within the class of continuum models both so-called lower order theories (e.g Bassani, 2001; Huang et al., 2004) and higher order theories have emerged. It is now generally accepted that higher order theories, which incorporate micro-structural boundary conditions, offer important modeling capabilities. Among the significant contributions are Fleck et al. (1994), Gurtin (2000, 2002), Fleck and Hutchinson (2001),Yefimov et al. (2004), Evers et al. (2004), Bayley et al. (2006), and Fleck and Willis (2009a,b). These theories allow boundary conditions on plastic strain quantities or associated stress quantities, which enter either through an extended virtual work principle or through additional partial differential equations. The continuum theories have, for many cases, been proven to adequately capture the size-dependent macroscopic behavior. However, common for these theories is the tendency to predict a rather smooth micro-structure, which is not consistent with experimental studies of metals (see also the recent discussion in El-Naaman et al., 2016).

It is well known that, during plastic deformation, dislocations tend to arrange in wall and cell structures within grains of crystalline materials, where bands of high dislocation density (dislocation walls) typically enclose regions of relatively low dislocation density (cell interiors) (see e.g. Ananthan et al., 1991; Huang and Winther, 2007; Hong et al., 2013). Öztop (2011) reported the same phenomenon for GNDs, in a nickle single crystal subject to wedge indentation, measured using high resolution electron backscatter diffraction (HR-EBSD) microscopy[1]. Linking the lattice curvature to dislocation density, through the Nye (1953) tensor, revealed distinct and highly localized GND wall and cell structures. A continuum description of this type of micro-structural behavior, suitable for large scale plasticity problems, has not yet been fully established, despite the fact that it has been given significant attention in the recent years (e.g. Klusemann and Yalçinkaya, 2013; van Beers et al., 2013, 2015; El-Naaman et al., 2016).

The micro-structural behavior is of particular interest in the present study, where the non-work conjugate type formulation, treated by Kuroda and Tvergaard (2006, 2008), is adopted. In this type of theory the virtual work principle remains the conventional one, while the evolution of GND densities is accounted for through additional differential equations. In this continuum theory, a back stress, related to the micro-structure, accounts for the gradient effects in the plastic behavior, and the mathematical form of such a back stress is still a rather open matter. However, back stress models can, for the most part, be classified into two types: i) The physically based models, which build on considerations of the stress field of a single dislocation (e.g. Groma et al., 2003; Yefimov et al., 2004), and ii) the phenomenologically based models, which either build on a postulated strain gradient energy relation (e.g. Kuroda and Tvergaard, 2008; Öztop et al., 2012) or may be formulated directly to possess certain constitutive properties as in El-Naaman et al. (2016).

In an attempt to develop suitable back stress formulations, that allow for non-smooth evolution of dislocation micro-structure, two candidates were proposed and

[1]Details on the experimental methods employed by Öztop (2011) can also be found in Kysar et al. (2010) and Dahlberg et al. (2014), also confirming the existence of highly localized GND structures.

studied under monotonic loading in El-Naaman et al. (2016). However, their behavior under cyclic loading remains unexplored despite being highly relevant for this type of model, where the Bauschinger effect is pivotal. In the following study advantages and characteristics of these back stress formulations will be identified and the resulting predictions of micro-structure will be discussed. To this end, attention will be confined to the representation of a single dislocation cell in the idealized simple shear case, which will serve as a lucid benchmark for the performance of the models proposed in El-Naaman et al. (2016).

The paper is structured as follows. The strain gradient plasticity model is described in Section 2, and the two back stress formulations treated are briefly outlined in Section 3 (more details can be found in El-Naaman et al., 2016). The boundary value problem is described in Section 4, after which, a series of results are presented in Section 5, using a finite element method (FEM) implementation. The cyclic response is discussed in Section 6, and the final concluding remarks are given in Section 7.

2. Strain gradient crystal plasticity model

The present study employs a small strain formulation, with the total strain rate given by; $\dot{\varepsilon}_{ij} = \left(\dot{u}_{i,j} + \dot{u}_{j,i}\right)/2$, which decomposes into an elastic part, $\dot{\varepsilon}^e_{ij}$, and a plastic part, $\dot{\varepsilon}^p_{ij}$, so that; $\dot{\varepsilon}_{ij} = \dot{\varepsilon}^e_{ij} + \dot{\varepsilon}^p_{ij}$. The formulation builds on the framework of conventional crystal visco-plasticity theory, where plastic deformation occurs by means of crystallographic slip on the individual slip systems. Thus, the plastic strain rate is given in terms of the slip rate, $\dot{\gamma}$, on the α'th slip system, as

$$\dot{\varepsilon}^p_{ij} = \sum_\alpha \dot{\gamma}^{(\alpha)} P^{(\alpha)}_{ij}, \quad P^{(\alpha)}_{ij} = \frac{1}{2}\left(s^{(\alpha)}_i m^{(\alpha)}_j + m^{(\alpha)}_i s^{(\alpha)}_j\right), \tag{1}$$

where the superposed dot denotes material time derivative, $P^{(\alpha)}_{ij}$ is the Schmid orientation tensor, and $s^{(\alpha)}_i$ and $m^{(\alpha)}_i$ are unit vectors specifying the slip direction and slip plane normal, respectively (see also Fig. 1b for a schematic definition). The slip rate is given by

$$\dot{\gamma}^{(\alpha)} = \dot{\gamma}_0 \mathrm{sgn}\left(\tau^{(\alpha)} - \tau^{(\alpha)}_b\right)\left(\frac{|\tau^{(\alpha)} - \tau^{(\alpha)}_b|}{g^{(\alpha)}}\right)^{1/m}, \tag{2}$$

where $\dot{\gamma}_0$ is a reference slip rate, $\tau^{(\alpha)}$ is the Schmid stress (taken as the macroscopic Cauchy stress tensor resolved onto the slip plane), $\tau^{(\alpha)}_b$ is a back stress, m is the rate sensitivity exponent, and $g^{(\alpha)}$ is the slip resistance, taken to follow the hardening law

$$\dot{g}^{(\alpha)} = \sum_\beta h^{(\alpha\beta)} |\dot{\gamma}^{(\beta)}|, \quad g^{(\alpha)}|_{t=0} = \tau_0, \tag{3}$$

where the initial value of $g^{(\alpha)}$ is chosen as the initial critical resolved shear stress τ_0. Here, t is time and $h^{(\alpha\beta)}$ are slip hardening moduli, in which the trace accounts for self hardening, and the off-diagonal parts for latent hardening. Equation (2) is a gradient-enhanced version of the widely used conventional visco-plastic power law slip rate relation (Hutchinson, 1976; Peirce et al., 1983), in that $\tau^{(\alpha)} - \tau^{(\alpha)}_b$ replaces $\tau^{(\alpha)}$

as an effective resolved shear stress[2]. The back stress, $\tau_b^{(\alpha)}$, is related directly to the gradients of the GND density (see Section 3), and impedes (or aids, depending on load path) slip at nonuniform pile-ups of GNDs. Thereby, the effective resolved shear stress becomes the driving force behind dislocation glide (Harder, 1999; Groma et al., 2003; Yefimov et al., 2004; Evers et al., 2004).

A non-work conjugate type higher order strain gradient plasticity theory is employed in the present study. This theory, formulated by Kuroda and Tvergaard (2006, 2008), is of a higher order nature but does not employ higher order stresses work conjugate to strain gradients or higher order equilibrium equations. Instead, the governing equations of the non-work conjugate formulation, are given by the conventional stress equilibrium equation; $\sigma_{ij,j} + f_i = 0$, where f_i are body forces and the Cauchy stress rate tensor is given by the elastic relationship; $\dot{\sigma}_{ij} = \mathscr{L}_{ijkl}\left(\dot{\varepsilon}_{kl} - \dot{\varepsilon}^p_{kl}\right)$, in which $\mathscr{L}_{ijkl}$ is the fourth order elastic stiffness tensor. Thereby, the conventional rate-dependent incremental principle of virtual work yields the weak form of the velocity field equation:

$$\int_V \mathscr{L}_{ijkl}\dot{\varepsilon}_{kl}\delta\dot{\varepsilon}_{ij}\mathrm{d}V = \int_V \mathscr{L}_{ijkl}\dot{\varepsilon}^p_{kl}\delta\dot{\varepsilon}_{ij}\mathrm{d}V + \int_V \dot{f}_i\delta\dot{u}_i\mathrm{d}V + \int_S \dot{T}_i\delta\dot{u}_i\mathrm{d}S, \quad \dot{T}_i \equiv \dot{\sigma}_{ij}n_j, \quad (4)$$

where $\dot{T}_i$ is the traction rate, n_i is the outward unit normal to the surface S bounding the volume V. The evolution of GND density, in balance with the slip gradients, is accounted for by an additional set of partial differential equations:

$$\frac{1}{b}\gamma^{(\alpha)}_{,i}s^{(\alpha)}_i + \rho^{(\alpha)}_{G(e)} = 0 \quad (5a)$$

$$\frac{1}{b}\gamma^{(\alpha)}_{,i}p^{(\alpha)}_i + \rho^{(\alpha)}_{G(s)} = 0, \quad (5b)$$

where $\mathbf{p}^{(\alpha)} = \mathbf{s}^{(\alpha)} \times \mathbf{m}^{(\alpha)}$, b is the magnitude of the Burgers vector, and $\rho^{(\alpha)}_G$ are GND densities on slip system α (Ashby, 1970). Subscripts (e) and (s) denote edge and screw components, respectively. The GND densities appear directly as free field variables in Eqs. (5a) and (5b), and their weak form reads:

$$\frac{1}{b}\int_V \delta\rho_{,i}s^{(\alpha)}_i\gamma^{(\alpha)}\mathrm{d}V = \frac{1}{b}\int_S \delta\rho\zeta^{(\alpha)}\mathrm{d}S + \int_V \delta\rho\rho^{(\alpha)}_{G(e)}\mathrm{d}V, \qquad \zeta^{(\alpha)} \equiv \gamma^{(\alpha)}n_i s^{(\alpha)}_i, \quad (6a)$$

$$\frac{1}{b}\int_V \delta\rho_{,i}p^{(\alpha)}_i\gamma^{(\alpha)}\mathrm{d}V = \frac{1}{b}\int_S \delta\rho\eta^{(\alpha)}\mathrm{d}S + \int_V \delta\rho\rho^{(\alpha)}_{G(s)}\mathrm{d}V, \qquad \eta^{(\alpha)} \equiv \gamma^{(\alpha)}n_i p^{(\alpha)}_i, \quad (6b)$$

where $\delta\rho$ is a weighting function (or virtual GND density). In the GND density equations, a hard interface impenetrable for dislocations is enforced by

$$\zeta^{(\alpha)} \equiv \gamma^{(\alpha)}n_i s^{(\alpha)}_i = 0 \quad (7a)$$

$$\eta^{(\alpha)} \equiv \gamma^{(\alpha)}n_i p^{(\alpha)}_i = 0, \quad (7b)$$

whereas a free boundary, where dislocations can exit the body, corresponds to

$$\rho^{(\alpha)}_{G(e)} = \rho^{(\alpha)}_{G(s)} = 0. \quad (8)$$

[2]Note that for $\tau_b^{(\alpha)}$ equal to zero, Eq. (2) reduces to the conventional theory.

For a detailed discussion on the micro-structural boundary conditions see Kuroda and Tvergaard (2008), where also the discretized finite element equations can be found.

The governing equations for the displacement field and GND density fields are evaluated separately, but the separate fields are linked together by the back stresses, according to Eq. (2). Hence, it is the back stress that introduces the gradient effects into the material response of the adopted strain gradient plasticity model.

3. Back stress formulations

In a non-uniform field of GNDs, arising due to a spatial variation of plastic strain gradients in ductile crystalline materials, a long range internal stress field emerges. This can be represented as a back stress in continuum models. In the framework adopted, the back stress influences the viscous slip rates, together with the resolved shear stresses on the slip systems. This gives rise to a kinematic hardening contribution, which accounts for the micro-structural effects on plastic flow. Here, the two back stress formulations proposed in El-Naaman et al. (2016) will be investigated under cyclic loading. These are; (i) a thermodynamically consistent formulation based on a generalized gradient energy potential, and (ii) a straightforward purely phenomenological formulation.

The present study is confined to plane strain deformation, and thus, all terms associated with screw dislocations vanish. The interaction between slip systems (such as general latent hardening) is omitted for clarity of the analysis.

3.1. Thermodynamically consistent back stress formulation

By assuming that the back stress is given by the divergence of a higher order stress, $\xi_i^{(\alpha)}$, as

$$\tau_b^{(\alpha)} \equiv -\xi_{i,i}^{(\alpha)}, \tag{9}$$

the adopted theory is equivalent to the work conjugate theory of Gurtin (2000, 2002), as was shown by Kuroda and Tvergaard (2006)[3]. This immediately follows from the micro-force balance equation, $\xi_{i,i}^{(\alpha)} + \tau^{(\alpha)} - \tau_{eff}^{(\alpha)} = 0$, where the effective resolved shear stress is given by $\tau_{eff}^{(\alpha)} = \tau^{(\alpha)} - \tau_b^{(\alpha)}$. The higher order stress is derived from the plastic part of the free energy, ψ_G, as

$$\xi_i^{(\alpha)} = \frac{\partial \psi_G^{(\alpha)}}{\partial \gamma_{,i}^{(\alpha)}}. \tag{10}$$

Note that, by adopting relation (9), the non-work conjugate theory takes a work conjugate form within a thermodynamically consistent framework, once a continuous differentiable constitutive relation for the gradient energy, ψ_G, has been defined. Here, the following generalized gradient energy potential will be assumed:

$$\psi_G^{(\alpha)} = \frac{1}{\mu+1} \tau_0 L^{\mu+1} \left| \gamma_{,i}^{(\alpha)} s_i^{(\alpha)} \right|^{\mu+1}, \tag{11}$$

where L is a material length scale parameter, that enters for dimensional consistency (see also Bardella, 2010; Bardella and Panteghini, 2015; Fleck et al., 2015; El-Naaman et al., 2016).

[3]Note that the term 'higher order stress' refers to the stress quantity which is work conjugate to strain gradients or slip gradients in other theories.

The generalized energy expression in Eq. (11) leads to a back stress which is linear in the second order gradient of slip, but when $\mu \neq 1$, includes a dependence on the first order gradient of slip (or the GND densities), to the power of $\mu - 1$ (El-Naaman et al., 2016):

$$\tau_b^{(\alpha)} = -\mu\tau_0 L^{\mu+1} \left|\gamma^{(\alpha)}_{,j} s_j^{(\alpha)}\right|^{\mu-1} \gamma^{(\alpha)}_{,ki} s_i^{(\alpha)} s_k^{(\alpha)}. \tag{12}$$

Expressed in terms of GND densities, this relation becomes

$$\tau_b^{(\alpha)} = \mu\tau_0 b^{\mu} L^{\mu+1} \left|\rho^{(\alpha)}_{G(e)}\right|^{\mu-1} \rho^{(\alpha)}_{G(e),i} s_i^{(\alpha)}. \tag{13}$$

For $\mu = 1$, Eq. (11) is quadratic and Eqs. (12) and (13) reduce to the more commonly used form of the back stress (e.g. Kuroda and Tvergaard, 2008).

Note that, due to the linear dependence on GND density gradients, the back stress in Eq. (13) does not give rise to long range internal stresses in a uniform field of GNDs. Equations (12) and (13) maintain thermodynamic consistency through Eq. (9), while, in the wording of Kuroda and Tvergaard (2006), they have a non-constant back stress coefficient, which evolves with the GND density for $\mu \neq 1$.

For $\mu < 1$, the back stress in Eq. (13) is singular when the GND density goes to zero, and thus, an "effective" GND density is employed, such that $\rho^{(\alpha)}_{G(e),eff} = |\rho^{(\alpha)}_{G(e)}| + \rho_0$ replaces $|\rho^{(\alpha)}_{G(e)}|$ in Eq. (13), for values of μ below one. This is a numerical trick which is necessary, in order to facilitate a numerical solution at low GND densities, but it resembles the presence of SSDs in the back stress relations of e.g. Groma et al. (2003) and Yefimov et al. (2004). A value of $\rho_{G(e),0} = 10^5$ mm^{-2} is used in the present computations, unless otherwise stated, and a sensitivity analysis, performed in El-Naaman et al. (2016), showed ρ_0 to have relatively little influence on the model behavior[4]. Although this is true for low values of the material length scale (as studied in El-Naaman et al., 2016), the influence becomes significant when going to extreme values of L, as will be demonstrated in the present study.

For the evaluation of Eq. (13), it was chosen to use an element value of $\rho^{(\alpha)}_{G(e)}$, taken as an average of the nodal values, in order to increase numerical stability.

3.2. Phenomenologically constructed back stress formulation

As was shown in El-Naaman et al. (2016), slip localization is promoted through the relationship of the back stress with GND density, when $\mu \longrightarrow 0$ as well as for $\mu \geq 1$, when adopting Eqs. (12) and (13). This property can be attractive when modeling the highly non-uniform distribution of GNDs observed in experimental studies. In the framework proposed by Kuroda and Tvergaard (2006, 2008) any function $\tau_b^{(\alpha)}(\rho^{(\alpha)}_{G(e),i} s_i^{(\alpha)})$ can, however, be considered, and the same type of localization behavior was also achieved for a back stress formulated as a function exclusively dependent on the GND density gradients (El-Naaman et al., 2015, 2016). This back stress is given by a piece-wise function, in which the first part follows from a quadratic free energy (through Eqs. (9) - (10)), and a parameter τ_T defines a transition point into a power law dependence on

[4]Note that in the paper El-Naaman et al. (2016), the unit measure for dislocation density was, by mistake, specified as [m^{-2}] throughout but was in fact [mm^{-2}].

the GND density gradients:

$$\tau_b^{(\alpha)} = \begin{cases} b\tau_0 L^2 \rho_{G(e),i}^{(\alpha)} s_i^{(\alpha)} & , \text{ for } |\tau_b^{(\alpha)}| \leq \tau_T \\ \operatorname{sgn}\left(\rho_{G(e),i}^{(\alpha)} s_i^{(\alpha)}\right) b^{\kappa} \tau_T^{1-\kappa} \tau_0^{\kappa} L^{2\kappa} \left|\rho_{G(e),i}^{(\alpha)} s_i^{(\alpha)}\right|^{\kappa} & , \text{ for } |\tau_b^{(\alpha)}| > \tau_T \end{cases} . \tag{14}$$

The first part of the piece-wise function excludes the initial infinite slope of the power law relation in Eq. (14), and it implies that the back stress evolves corresponding to a quadratic free energy until a preassigned level ($|\tau_b^{(\alpha)}| = \tau_T$), whereafter it subsides according to the power law (for $0 \leq \kappa \leq 1$). Since a gradient energy relation that leads to Eq. (14) is not readily available, this back stress formulation must be considered a non-thermodynamically consistent formulation except for the case of $\kappa = 1$, where a quadratic gradient energy prevails throughout. However, all numerical solutions presented here, were found to satisfy positive dissipation throughout the load history, such that

$$\sigma_{ij}\dot{\varepsilon}_{ij}^{p} = \sum_{\alpha} \tau^{(\alpha)}\dot{\gamma}^{(\alpha)} \geq 0. \tag{15}$$

4. Boundary value problem

The single slip simple shear problem, illustrated in Fig. 1, is considered in order to demonstrate the behavior of the back stress formulations under cyclic loading. To compare results to those found for monotonic loading in Kuroda and Tvergaard (2008) and El-Naaman et al. (2016), the following model parameters are used throughout: Slip angle $\theta = 90^{\circ}$, Young's modulus $E = 130$ GPa, Poisson's ratio $\nu = 0.3$, $\tau_0 = 50$ MPa, and $b = 0.286$ nm. The material slab, of height H and width W, is modeled as infinite in the x_1-direction by imposing the following periodic boundary conditions:

$$u_i(0, x_2) \quad = u_i(W, x_2) \tag{16a}$$

$$\rho_{G(e)}^{(\alpha)}(0, x_2) = \rho_{G(e)}^{(\alpha)}(W, x_2). \tag{16b}$$

The additional boundary conditions imposed on the displacement field are

$$u_1 = u_2 = 0 \;\text{ at }\; x_2 = 0 \tag{17a}$$

$$u_1 = U(t) \;\text{ and }\; u_2 = 0 \;\text{ at }\; x_2 = H, \tag{17b}$$

while the top and bottom boundaries of the material domain are microscopically passivated by the following higher order boundary conditions on the GND density field equations:

$$\zeta^{(\alpha)} \equiv \gamma^{(\alpha)} n_i s_i^{(\alpha)} = 0 \;\text{ at }\; x_2 = 0 \;\text{ and }\; x_2 = H. \tag{18}$$

The above listed boundary conditions imply that all fields become one dimensional. The results are obtained using the finite element method (FEM), solving the conventional and micro-structural equilibrium equations in a staggered scheme. Eight-node isoparametric quadrilateral elements with reduced Gauss integration are used for the displacement field analysis, whereas equivalent four-node elements with full Gauss integration are used for the GND density field analysis. Time integration is carried out by the forward Euler method. The finite element mesh used consists of 58 elements in the x_2-direction including a refined mesh at the microscopically passivated boundaries to resolve the steep gradients.

5. Results

The following numerical study focuses on the macroscopic response under cyclic loading, when employing the two different back stress formulations given by Eq. (13) and Eq. (14). Moreover, the predicted evolution in micro-structure is discussed in relation to the macroscopic behavior.

5.1. Macroscopic response under cyclic loading

At first, the boundary value problem described in Section 4 is solved with conventional hardening ($h^{(\alpha\beta)} = h = 250$ MPa), at a rate sensitivity $m = 0.02$. With $\dot{U} = H\dot{\gamma}_0$, the material domain is sheared to a macroscopic shear strain $\Gamma = 0.03$, after which, one complete load cycle is performed, such that the macroscopic shear strain goes once to -0.03 and back to 0.03. Figure 2 shows results obtained when adopting the thermodynamically consistent back stress formulation in Eq. (13) for different values of μ. The complete shear stress vs. macroscopic shear strain curve is shown in Fig. 2a. For the final load step, the slip profile can be seen in Fig. 2b and the distribution of GNDs can be seen in Fig. 2c. The GND density distributions in Fig. 2c are normalized with the values found at the boundary, denoted $\rho^{(1)}_{G(e),B}$, to enable qualitative comparison. Going from $\mu = 1$ (quadratic free energy) to $\mu = 0.4$ the spatial gradient of slip decreases, corresponding to a smoother distribution of GNDs (Fig. 2c), while a low value of μ (close to linear free energy) results in a steep gradient in slip, and thereby more localized pile-up of GNDs.

Along the same line, using the purely phenomenological back stress formulation in Eq. (14), similar localized GND structures are predicted. For different values of κ and with $\tau_T/\tau_0 = 0.12$, Fig. 3a shows the shear stress vs. macroscopic shear strain over the entire modeling history. Figures 3b and 3c show the slip profile and the GND density, respectively, after the final load step. When letting κ go to zero, large slip gradients occur locally at the hard boundaries (Fig. 3b), resulting in increasingly localized GND structures (Fig. 3c), in contrast to the more smooth development seen for $\kappa = 1$ (quadratic gradient energy). It is noticed that an additional wave appears in the central part of the slip profile for the low values of κ (Fig. 3b).

In the following, a parametric study, for the case of zero conventional hardening ($h^{(\alpha\beta)} = h = 0$), is performed in order to bring out additional details on how the micro-structural predictions relate to the macroscopic response, considering the two different back stress formulations. In these computations it was checked that a steady state cyclic response was achieved by running multiple load cycles about the zero strain axis. Figure 4 shows the shear stress vs. macroscopic shear strain using the thermodynamically consistent back stress formulation (13). Results are shown for different values of the back stress exponent, μ (Fig. 4a), for different values of the material length parameter, L (Fig. 4b), and for different values of the additional micro-structural parameter, ρ_0 (Fig. 4c). For the low material length parameter value ($L/H = 0.3$) there is no considerable difference in the macroscopic response for $\mu = 0.01$, 1.0, and 2.0 (the significance of this observation will be elaborated on in Section 5.2). However, when going to higher values of the material length parameter, a seemingly anomalous local change in slope on the response curves is predicted during plastic flow, so that these exhibit an inflection point close to zero strain (Fig. 4b). For the intermediate material

length scale ($L/H = 5$), Fig. 4c clearly shows that this behavior is largely controlled by the micro-structural parameter, ρ_0 (see discussion in Section 6).

Figure 5 shows the shear stress vs. macroscopic shear strain using the purely phenomenologically constructed back stress formulation (13). Results are shown for different values of the back stress exponent, κ (Fig. 5a), for different material length scales, L (Fig. 5b), and for different values of the transition parameter, τ_T (Fig. 5c). Similarly, Fig. 5a shows no significant difference in the macroscopic response, for the low value of the material length parameter ($L/H = 0.3$), when varying the value of κ (see also Section 5.2). Again, similar to the predictions resulting from the former back stress formulation, when going to higher material length scales, an anomalous local change in slope on the response curves is seen during plastic flow, with an inflection point close to zero strain (Fig. 5b). Figure 5c shows that this behavior is largely controlled by the transition parameter, τ_T. For the thermodynamically consistent formulation this local slope change takes place rather smoothly, whereas the purely phenomenological formulation displays a much more rapid change in slope. This is due to the particular choice of constitutive parameters, which will be elaborated in the following (see also Section 6).

To understand what controls this seemingly anomalous cyclic behavior observed for both back stress formulations, the plastic slip and back stress distribution are plotted across the material slab height at different stages of the load cycle (Figs. 6 through 10). The different load stages are marked and numbered on one representative curve in each of Figs. 4b and 5b. Figure 6 shows results for a back stress based on quadratic free energy ($\mu = \kappa = 1$), while Figs. 7 and 8 show results using back stress relation (13) with $\mu = 0.01$ and back stress relation (14) with $\kappa = 0.1$, respectively. In these computations a low value of the material length parameter ($L/H = 0.3$) is used. For the phenomenological back stress formulation (Eq. (14)), the value $\tau_T/\tau_0 = 0.06$ will be used henceforth. It is generally observed that, when the load is reversed, the back stress changes direction over a gradually increasing domain (illustrated by stages 1 through 6), and that the change initiates locally at the micro-structurally passivated boundaries. A large central portion of the slab height experiences relatively little change in back stress (see Figs. 6-8). This is especially true when assuming a cubic energy potential ($\mu = 2.0$), where the central part remains basically unchanged with zero back stress throughout the deformation (Fig. 7d)[5]. Furthermore, it is noticed that for the purely phenomenological formulation, the majority of the material is dominated by a quadratic free energy, which is illustrated by the $|\tau_b^{(1)}| = \tau_T$ lines plotted in Fig. 8b. Thus, the power law part of Eq. (14) controls only the outermost regions of the material domain close to the passivated boundaries.

In Figs. 9 and 10, where a high material length scale is employed ($L = 10$), it is observed that a high level of back stress develops in the entire material domain (see Figs. 9b and 10b). Thus, the behavior of the back stress controls, quite directly, the macroscopic response throughout, resulting in the pronounced unconventional Bauschinger effect, in terms of inflection points. The change in back stress initiates at the boundaries here as well, but subsequently the shift from aiding slip to impeding slip, takes

[5]It is noted that some asymmetries appear for $\mu = 2$, which is especially clear when comparing stage 1 and stage 6 in Fig. 7c.

place in the entire domain upon reversed loading. Moreover, it is noticed in Fig. 10b, that the power law part of Eq. (14) dominates the material completely in stages 1, 2, 5, and 6.

The macroscopic behavior of the models is further discussed in Section 6.

5.2. Micro-structure evolution predictions

In general, dislocations tend to form cell structures in metals under plastic deformation and the same behavior has been reported for the evolution of GNDs. The following results confirm the fact that the approaches in El-Naaman et al. (2016) to a back stress formulation offer additional control of the micro-structural predictions mainly through one additional model parameter (μ or κ in the two models). As will become evident, this additional modeling capability is useful when seeking realistic micro-structures, and cannot be achieved in the classical type of back stress formulation (corresponding to $\mu = \kappa = 1$), where the material length scale parameter, L, alone governs the micro-structural behavior.

Figures 11 and 12 show that there is a significant difference in the micro-structure predicted when deviating from the classical back stress formulation based on quadratic free energy ($\mu = \kappa = 1$). The figures show the GND density normalized with the value at the boundary, $\rho^{(1)}_{G(e),B}$, at $\Gamma = 0.03$ after the final load step. Results are shown for different values of μ and κ, respectively. Figure 11 shows that, compared to a quadratic free energy, a more localized pile up of GNDs is predicted near the micro-structurally passivated boundaries, when approaching a linear gradient energy ($\mu = 0.01,\ 0.03$). Similarly, when assuming a cubic free energy ($\mu = 2$), localization of GNDs is achieved at the boundaries. However, clear qualitative differences are observed here, in that dislocations of opposite sign appear to pile up adjacent to the dislocation walls at the passivated boundaries. For the purely phenomenological formulation a clearly localized micro-structure is achieved with a low power law dependence ($\kappa = 0.1$) compared to the traditional quadratic free energy assumption.

The results outlined above should be seen in contrast to the fact that the shear stress vs. macroscopic shear strain curves in Fig. 4a, representing the assumption of quadratic free energy ($\mu = 1$), near linear free energy ($\mu = 0.01,\ 0.03$), and cubic free energy ($\mu = 2$), can be considered as macroscopically equivalent, as is the case for the response curves in Fig. 5a, for the two choices of exponent ($\kappa = 0.1$ and 0.4) of the purely phenomenological back stress, including the assumption of quadratic free energy throughout ($\kappa = 1.0$).

6. Discussion of the predicted Bauschinger effect

Cyclic plastic deformation of ductile crystalline materials gives rise to the Bauschinger effect, which reflects micro-structural mechanisms related to the pile up of dislocations. Compared to the findings in the present study, however, the Bauschinger effect is usually taken to proceed more smoothly or gradually, and not cause inflection points such as those seen in Figs. 4 and 5. The inflection points on the flow curves express a sudden increase and subsequent decrease in growth rate of the back stress close to the zero strain point. This causes a shift in the flow stress level and, in some cases, gives the impression of two stages of plastic deformation. In terms of the thermodynamically consistent formulation (Eqs. (12) and (13)), the inflection points are essentially caused

by the back stress approaching its singularity as the GND density goes to zero (in competition with the GND density gradient going to zero). How close the back stress can come to singular behavior is controlled by ρ_0, and thus, also the characteristics of the flow curve surrounding the inflection point is controlled by ρ_0 (see Fig. 4c). When the macroscopic shear strain changes sign, the growth rate of the back stress starts to decrease as it moves away from the singularity.

Interestingly, the very differently devised purely phenomenological back stress formulaion (Eq. (14)) exhibits a behavior similar to that of the thermodynamically consistent back stress. Here, also showing a temporary change in slope of the flow curve, which initiates immediately after stage 4 (see Fig. 5) and persists approximately until stage 5. Approximately at stage 4, the back stress in the majority of the material domain has changed sign and is now impeding slip. Moreover, at this point and until stage 5, the quadratic free energy dominates (see Fig. 10b), and the slope of the inflection tangent is approximately that corresponding to quadratic free energy. Thus, for $\kappa = 1$ (quadratic gradient energy throughout), the inflection tangent slope will persist throughout the plastic deformation. The appearance of the jump in the flow curve, in terms of strain interval and slope of the inflection tangent, is controlled by an interplay between τ_T and L (see Figs. 5b and 5c). The rather pronounced inflection point, resulting from the present particular combination of κ, τ_T, and L, may not be physically accurate, but emphasizes how this back stress relation works in practice.

Not only has the inflected type of Bauschinger effect been reported recently in other numerical strain gradient plasticity studies (Bardella and Panteghini, 2015; Wulfinghoff et al., 2015), but also experimental evidence of such cyclic behavior exists in the literature: Taillard and Pineau (1982) observed unusual inflected hysteresis curves in an overaged large grained alloy during the initial 20 cycles, which they attributed to long range internal stresses due to dislocation loops deposited around precipitates—in line with the preceding findings of Stoltz and Pelloux (1975), where the inflected Bauschinger effect was found to diminish or vanish with annealing treatments in alloys containing non-shearable precipitates. The governing mechanisms involved in these experimental studies, are analogous to the pile-up of dislocations at the passivated boundaries imposed in the present computations. Asaro (1975) also observed hysteresis curves with inflection points in the dispersion hardened super alloy In-753, which exhibits what they refer to as type III kinematic hardening, and it was stated that this type of hardening was also observed in a material that did not contain any substantial substructure aside from grain boundaries. Moreover, they showed that this behavior is a natural outcome of theories that incorporate hardening due to long range internal stresses. More recently, Proudhon et al. (2008) reported anomalous changes in slope upon reentry into plastic deformation in aluminum alloys.

At present, due to the lack of experimental data, it is unknown whether this type of macroscopic behavior is acceptable, from a physical point of view, in a single crystal theory. However, since the inflected hysteretic behavior is believed to be tied to the influence of long range internal stresses due to pile-up of dislocations, which plays a significant role in micron-scale plasticity within the grains of metals, it is not reasonable to brush this type of behavior aside as nonphysical.

7. Concluding remarks

A finite element implementation of the non-work conjugate higher order strain gradient crystal plasticity model, proposed by Kuroda and Tvergaard (2006, 2008), has formed the basis of an investigation of back stress formulations under cyclic loading. The back stress formulations used were proposed in El-Naaman et al. (2015, 2016) with the objective of improving the ability to predict micro-structural evolution. This paper treats the highly idealized pure shear case, which serves as a benchmark for the performance of the proposed model.

The key findings of the present study can be summarized as follows:

i) Both employed back stress models perform well under cyclic loading, however, it is predicted that the hysteresis curves, in some cases, have inflection points, at around zero macroscopic shear strain, when deviating from the quadratic form of the free energy. This type of hysteretic behavior has substantial experimental backing, and is believed to be tied to the long range internal stresses due to dislocation pile-up and the reversibility of these during backward straining (Asaro, 1975). The characteristics of the inflected Bauschinger effect, is controlled by the parameters L, μ, ρ_0, κ, and τ_T, in the two models respectively, and thus, the additional model parameters offer the possibility to model this particular material behavior reported in the literature. Moreover, the authors believe that it is these properties that may be utilized in an attempt to capture the micro-structural heterogeneity and discontinuities of real ductile crystalline materials.

ii) It is demonstrated that with both back stress formulations it is possible to exert some level of control of the micro-structural predictions of the model, and to some extend, independently of the macroscopic response. This is achieved mainly through the additional model parameter denoted μ or κ in the two models, respectively.

With the present cyclic investigation, the performance of the two adopted back stress formulations is further established, both in terms of the macroscopic response but also in relation to the predicted dislocation micro-structure. However, it must be emphasized that further research on more complicated boundary value problems, e.g. including multi-slip and latent hardening, is needed in order to fully establish the applicability of the back stress formulations proposed in El-Naaman et al. (2016).

8. Acknowledgments

The work is financially supported by The Danish Council for Independent Research under the research career programme Sapere Aude as part of the project “Higher Order Theories in Solid Mechanics”, grant 11-105098/FTP.

References

Ananthan, V., Leffers, T., Hansen, N., 1991. Cell and band structures in cold-rolled polycrystalline copper. Materials Science and Technology 7, 1069–1075.

Asaro, R., 1975. Elastic-plastic memory and kinematic-type hardening. Acta Metallurgica 23, 1255–1265.

Ashby, M., 1970. The deformation of plastically non-homogeneous alloys. Philos. Mag. 21, 399–424.

Bardella, L., 2010. Size effects in phenomenological strain gradient plasticity constitutively involving the plastic spin. International Journal of Engineering Science 48, 550–568.

Bardella, L., Panteghini, A., 2015. Modelling the torsion of thin metal wires by distortion gradient plasticity. Journal of the Mechanics and Physics of Solids 78, 467–492.

Bassani, J., 2001. Incompressibility and a simple gradient theory of plasticity. Journal of the Mechanics and Physics of Solids 49, 1983–1996.

Bayley, C., Brekelmans, W., Geers, M., 2006. A comparison of dislocation induced back stress formulations in strain gradient crystal plasticty. International Journal of Solids and Structures 43, 7268–7286.

Dahlberg, C., Saito, Y., Öztop, M., Kysar, J., 2014. Geometrically necessary dislocation density measurements associated with different angles of indentations. International Journal of Plasticity 54, 81–95.

El-Naaman, S., Nielsen, K., Niordson, C., 2015. Strain gradient crystal plasticity: A continuum mechanics approach to modeling micro-structural evolution. Plastic Behavior of Conventional and Advanced Materials: Theory, Experiment, and Modeling, 7–9.

El-Naaman, S., Nielsen, K., Niordson, C., 2016. On modeling micro-structural evolution using a higher order strain gradient continuum theory. International Journal of Plasticity 76, 285–298.

Evers, L., Brekelmans, W., Geers, M., 2004. Non-local cystal plasticity model with intrinsic SSD and GND effects. Journal of the Mechanics and Physics of Solids 52, 2379–2401.

Fleck, N., Hutchinson, J., 2001. A reformulation of strain gradient plasticity. Journal of the Mechanics and Physics of Solids 49, 2245–2271.

Fleck, N., Hutchinson, J., Willis, J., 2015. Guidelines for constructing strain gradient plasticity theories. Journal of Applied Mechanics 82, 1–10.

Fleck, N., Muller, G., Ashby, M., Hutchinson, J., 1994. Strain gradient plasticity: Theory and experiment. Acta Metallurgica et materialia 42 (2), 475–487.

Fleck, N., Willis, J., 2009a. A mathematical basis for strain-gradient plasticity theory. Part I: Scalar plastic multiplier. Journal of the Mechanics and Physics of Solids 57, 161–177.

Fleck, N., Willis, J., 2009b. A mathematical basis for strain-gradient plasticity theory. Part II: Tensorial plastic multiplier. Journal of the Mechanics and Physics of Solids 57, 1045–1057.

Groma, I., Csikor, F., Zaizer, M., 2003. Spatial correlations and higher-order gradient terms in a continuum description of dislocation dynamics. Acta Materialia 51, 1271–1281.

Gurtin, M., 2000. On the plasticity of single crystals: free energy, microforces, plastic-strain gradients. Journal of the Mechanics and Physics of Solids 48 (5), 989–1036.

Gurtin, M., 2002. A gradient theory of single-crystal viscoplasticity that accounts for geometrically necessary dislocations. Journal of the Mechanics and Physics of Solids 50, 5–32.

Harder, J., 1999. A crystallographic model for the study of local deformation processes in polycrystals. International Journal of Plasticity 15, 605–624.

Hong, C., Huang, X., Winter, G., 2013. Dislocation content of geometrically necessary boundaries aligned with slip planes in rolled aluminium. Philosophical Magazine 93 (23), 3118–3141.

Huang, X., Winther, G., 2007. Dislocation structures. Part I. Grain orientation dependence. Philosophical Magazine 87 (33), 5189–5214.

Huang, Y., Qu, S., Hwang, K., Li, M., Gao, H., 2004. A conventional theory of mechanism-based strain gradient plasticity. International Journal of Plasticity 20, 753–782.

Hutchinson, J., 1976. Bounds and self-consistent estimates for creep of polycrystalline materials. Proc. R. Soc. Lond. A 348, 101–127.

Klusemann, B., Yalçinkaya, T., 2013. Plastic deformation induced microstructure evolution through gradient enhanced crystal plasticity based on a non-convex Helmholtz energy. International Journal of Plasticity 48, 168–188.

Kuroda, M., Tvergaard, V., 2006. Studies of scale dependent crystal viscoplasticity models. Journal of the Mechanics and Physics of Solids 54, 1789–1810.

Kuroda, M., Tvergaard, V., 2008. On the formulation of higher-order strain gradient crystal plasticity models. Journal of the Mechanics and Physics of Solids 56, 1591–1608.

Kysar, J., Saito, Y., Oztop, M., Lee, D., Huh, W., 2010. Experimental lower bounds on geometrically necessary dislocation density. International Journal of Plasticity 26, 1097–1123.

Martínez-Pañeda, E., Niordson, C., 2015. On fracture in finite strain gradient plasticity. International Journal of Plasticity, *In press*.

Mu, Y., Hutchinson, J., Meng, W., 2014. Micro-pillar measurements of plasticity in confined cu thin films. Extreme Mechanics Letters 1, 62–69.

Nielsen, K., Niordson, C., Hutchinson, J., 2012. Strain gradient effects on steady state crack growth in rate-sensitive materials. Engineering Fracture Mechanics 96, 61–71.

Nye, J., 1953. Some geometrical relations in dislocated crystals. Acta Metallurgica 1 (2), 153–162.

Öztop, M., 2011. Multiscale experimental analysis in plasticity: Linking dislocation structures to continuum fields. Ph.D. thesis, Columbia University.

Öztop, M., Niordson, C., Kysar, J., 2012. Length-scale effect due to periodic variation of geometrically nescessary dislocaion densities. International Journal of Plasticity 41, 189–201.

Peirce, D., Asaro, R., Needleman, A., 1983. Material rate dependence and localized deformation in crystalline solids. Acta Metall. 31, 1951–1976.

Proudhon, H., Poole, W., Wang, X., Bréchet, Y., 2008. The role of internal stresses on the plastic deformation of the Al-Mg-Si-Cu alloy AA611. Philosophical Magazine 88, 621–640.

Stoltz, R., Pelloux, R., 1975. The Bauschinger effect in precipitation strengthened aluminum alloys. Metallugical Transactions A 7 (8), 1295–1306.

Taillard, R., Pineau, A., 1982. Room temperature tensile properties of Fe-19wt.%Cr alloys precipitation hardened by the intermetallic compound NiAl. Materials Science and Engineering 56, 219–231.

van Beers, P., McShane, G., Kouznetsova, V., Geers, M., 2013. Grain boundary interface mechanics in strain gradient crystal plasticity. Journal of the Mechanics and Physics of Solids 61, 2659–2679.

van Beers, R., Kouznetsova, V., Geers, M., 2015. Defect redistribution within a continuum grain boundary plasticity model. Journal of the Mechanics and Physics of Solids 83, 243–262.

Wei, Y., Hutchinson, J., 1997. Steady-State crack growth and work of fracture for solids characterized by strain gradient plasticity. Journal of the Mechanics and Physics of Solids 45, 1253–1273.

Wei, Y., Hutchinson, J., 1999. Models of interface separation accompanied by plastic dissipation at multiple scales. International Journal of Fracture 95, 1–17.

Wulfinghoff, S., Forest, S., Böhlke, 2015. Strain gradient plasticity modeling of the cyclic behavior of laminate microstructures. Journal of the Mechanics and Physics of Solids 79, 1–20.

Yefimov, S., Groma, I., van der Giessen, E., 2004. A comparison of a statistical-mechanics based plasticity model with descrete dislocation plasticity calculations. Journal of the Mechanics and Physics of Solids 52, 279–300.

Figures

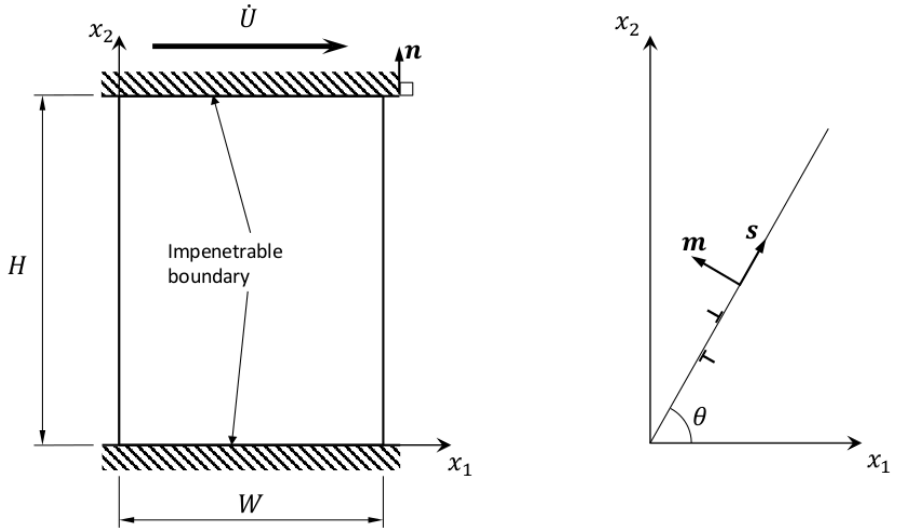

Figure 1: Schematic of the simple shear problem: (a) the material domain, which is modeled as infinite in the x_2-direction, is constrained by two rigid impenetrable boundaries and subject to a prescribed displacement rate $\dot{U}$. (b) definition of the slip system.

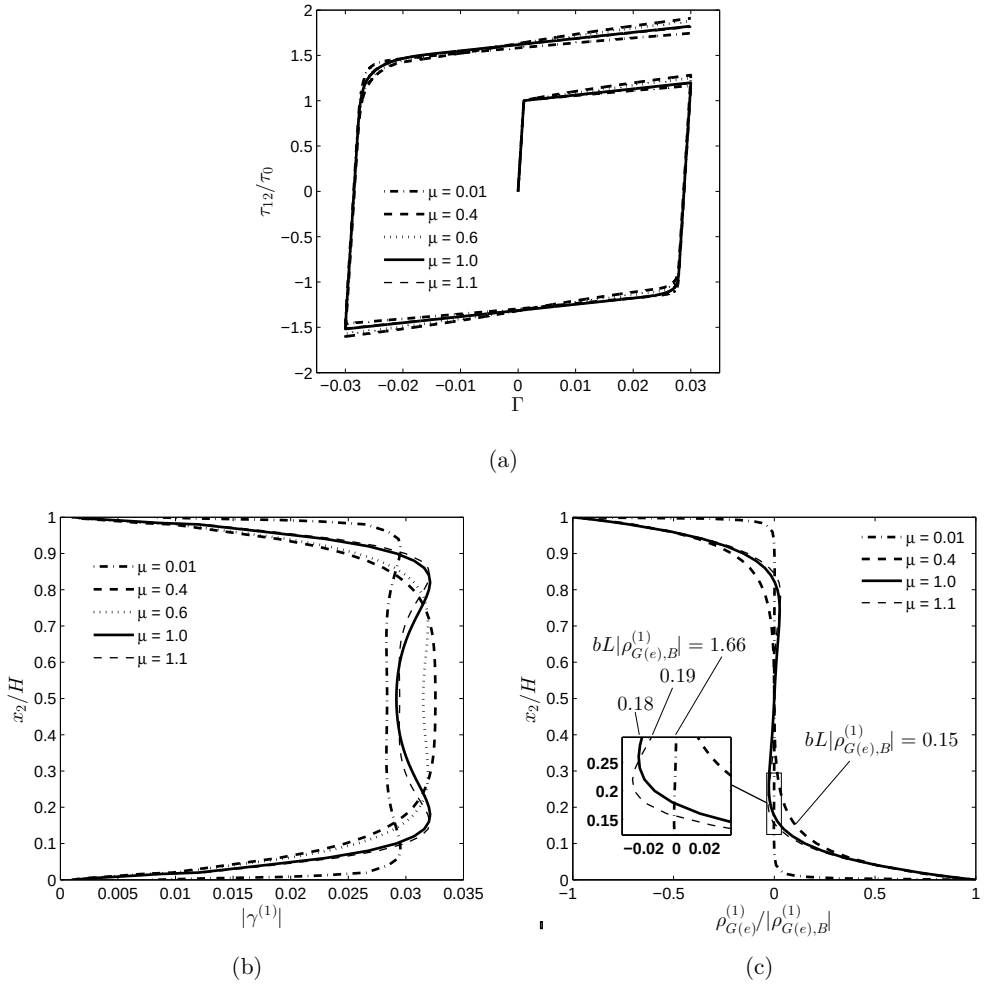

(a)

(b)

(c)

Figure 2: Numerical results for the single slip simple shear problem (Fig. 1) subject to one load cycle, using the generalized gradient energy based back stress (Eqs. (12) and (13)), with $\theta = 90°$, $h^{(\alpha\beta)} = h = 250$ MPa, $L/H = 0.3$, $m = 0.02$, $\rho_0 = 10^5$ mm^{-2}, and $\dot{U} = H\dot{\gamma}_0$, illustrating the effect of the μ parameter, on the cyclic behavior, in the linear to quadratic regime ($0 < \mu \leq 1$). The figure shows (a) shear stress vs. macroscopic shear strain, (b) slip profile, and (c) normalized GND density. Slip profile (b) and GND density (c) are shown for $\Gamma = 0.03$ after the final load step.

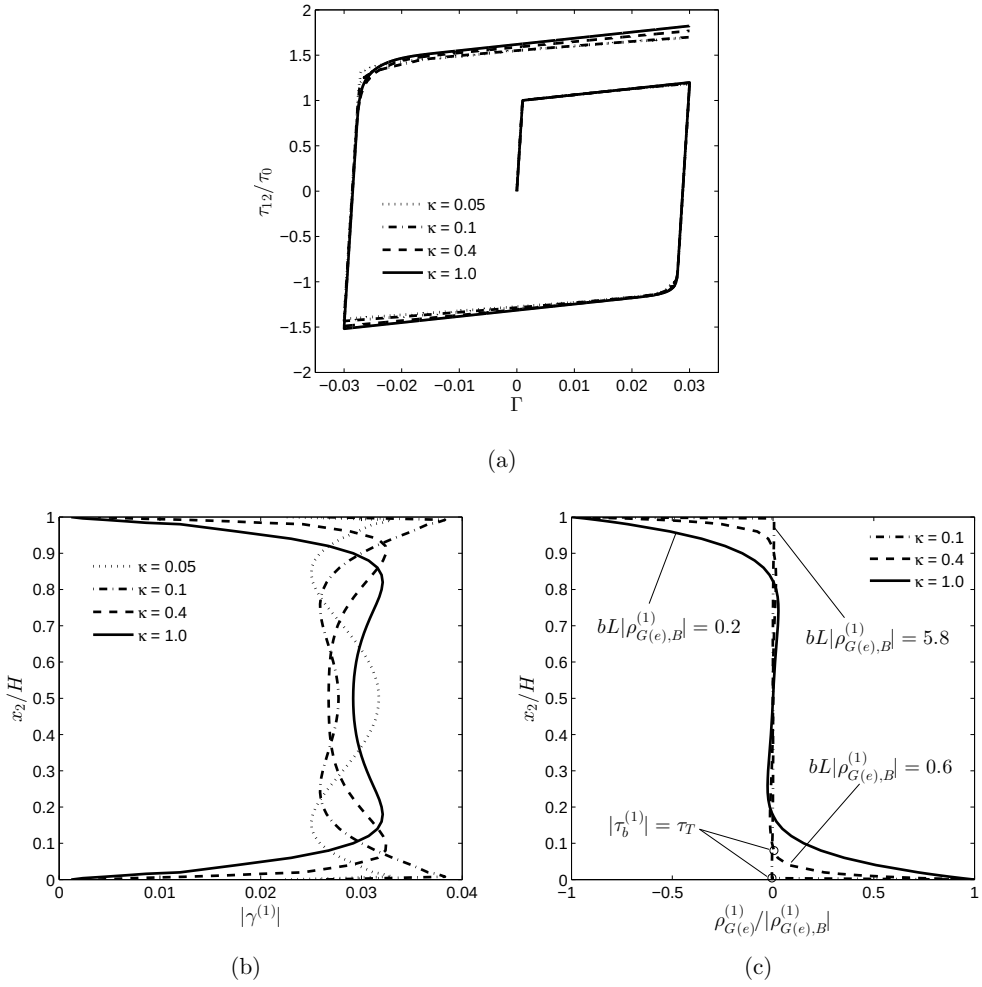

Figure 3: Shear stress vs. macroscopic shear strain for the single slip simple shear problem (Fig. 1) subject to one load cycle, using the back stress power law (Eq. (14)), with $\theta = 90°$, $h^{(\alpha\beta)} = h = 250$ MPa, $L/H = 0.3$, $m = 0.02$, $\tau_T/\tau_0 = 0.12$, and $\dot{U} = H\dot{\gamma}_0$, illustrating the effect of the κ parameter on the cyclic behavior. The figure shows (a) shear stress vs. macroscopic shear strain, (b) Slip profile, and (c) normalized GND density, with circles marking the back stress transition point ($|\tau_b^{(1)}| = \tau_T$) near the lower horizontal boundary. Slip profile (b) and GND density (c) are shown for $\Gamma = 0.03$ after the final load step.

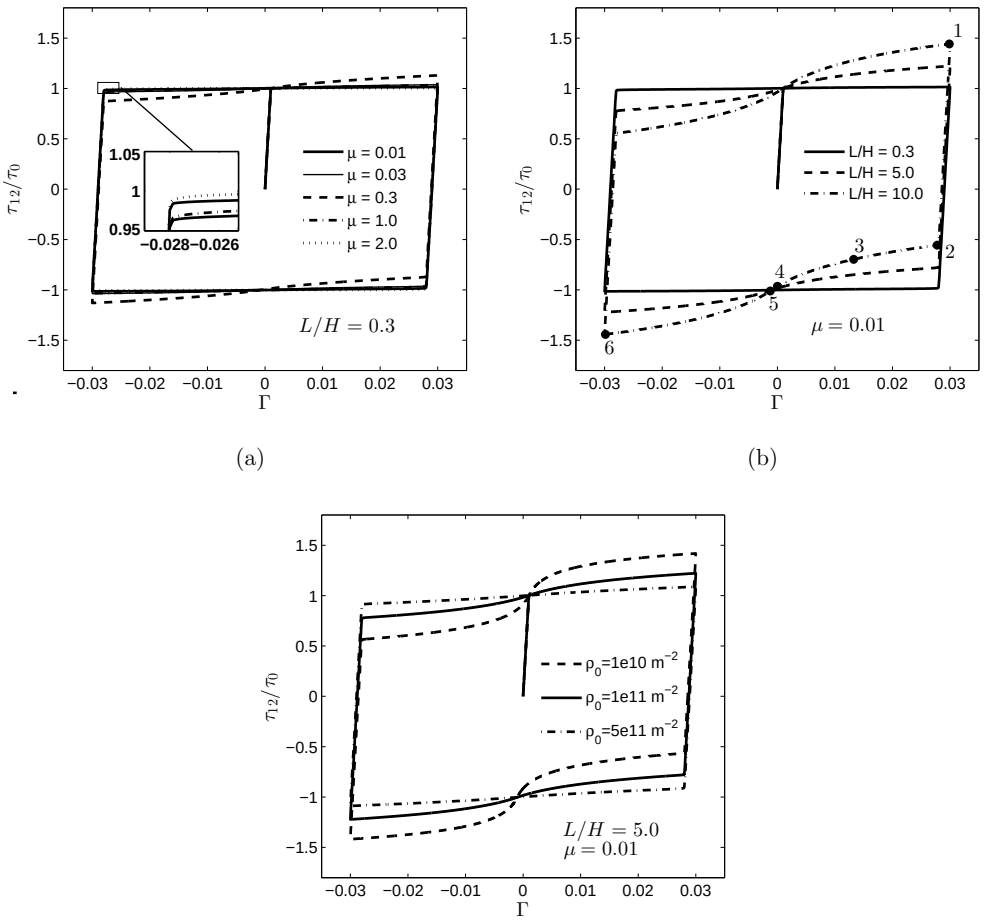

Figure 4: Numerical results for the single slip simple shear problem (Fig. 1), using the generalized gradient energy based back stress (Eqs. (12) and (13)), with $\theta = 90°$, $h^{(\alpha\beta)} = h = 0$, $m = 0.02$, and $\dot{U} = H\dot{\gamma}_0$. The figure shows normalized shear stress vs. macroscopic shear strain: (a) for different values of μ, (b) for different values of L, and (c) for different values of ρ_0. In (a) and (b), $\rho_0 = 1.0\text{e}11$ m^{-2} for $\mu < 1$, and otherwise zero. In (b) the numbered dots mark the load stages at which the slip and back stress are plotted in the subsequent figures.

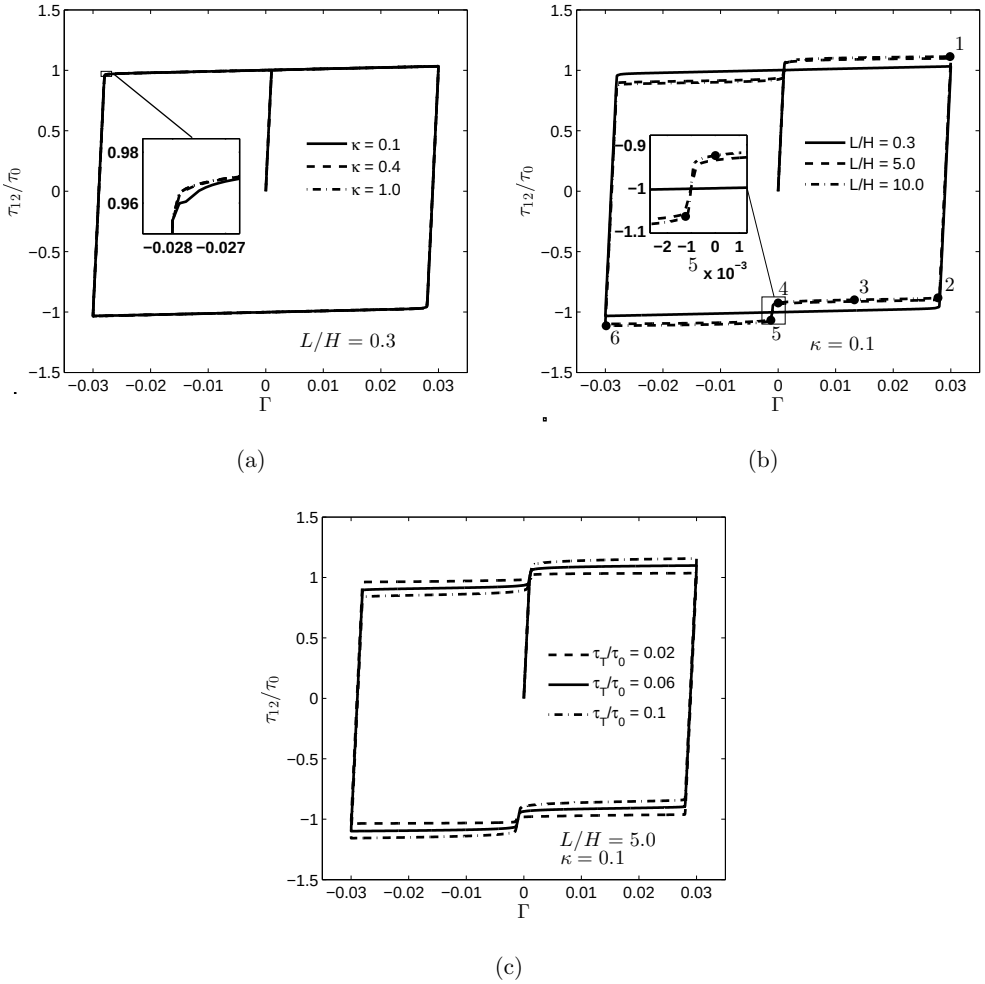

Figure 5: Numerical results for the single slip simple shear problem (Fig. 1), using the purely phenomenological back stress formulation (Eq. (14)), with $\theta = 90°$, $h^{(\alpha\beta)} = h = 0$, $m = 0.02$, and $\dot{U} = H\dot{\gamma}_0$. The figure shows normalized shear stress vs. macroscopic shear strain: (a) for different values of κ, (b) for different values of L, and (c) for different values of τ_T. In (a) and (b), $\tau_T/\tau_0 = 0.06$. In (b) the numbered dots mark the load stages at which the slip and back stress are plotted in the subsequent figures.

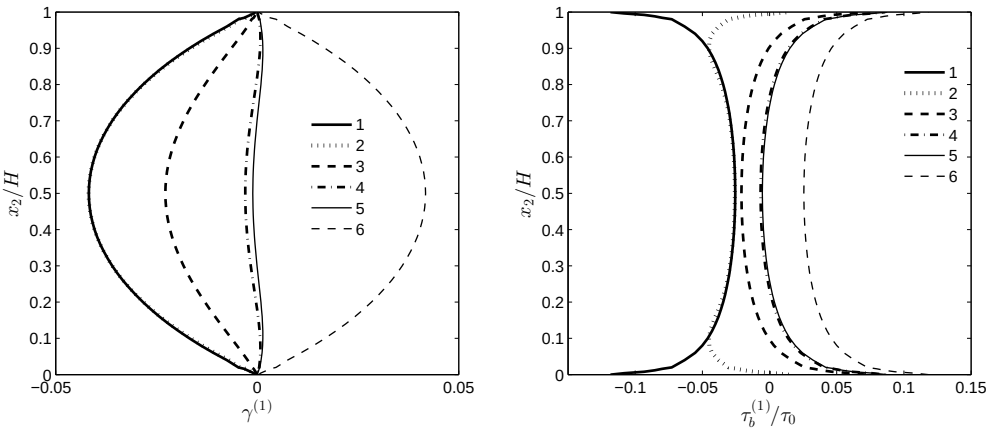

(a) (b)

Figure 6: Numerical results for the single slip simple shear problem (Fig. 1), using the classical quadratic gradient energy based back stress (corresponding to $\mu = \kappa = 1$), with $\theta = 90^\circ$, $h^{(\alpha\beta)} = h = 0$, $m = 0.02$, and $\dot{U} = H\dot{\gamma}_0$, The figure shows (a) slip profiles and (b) back stress distribution at six different stages during cyclic loading corresponding to the points marked on the curve in Fig. 4.

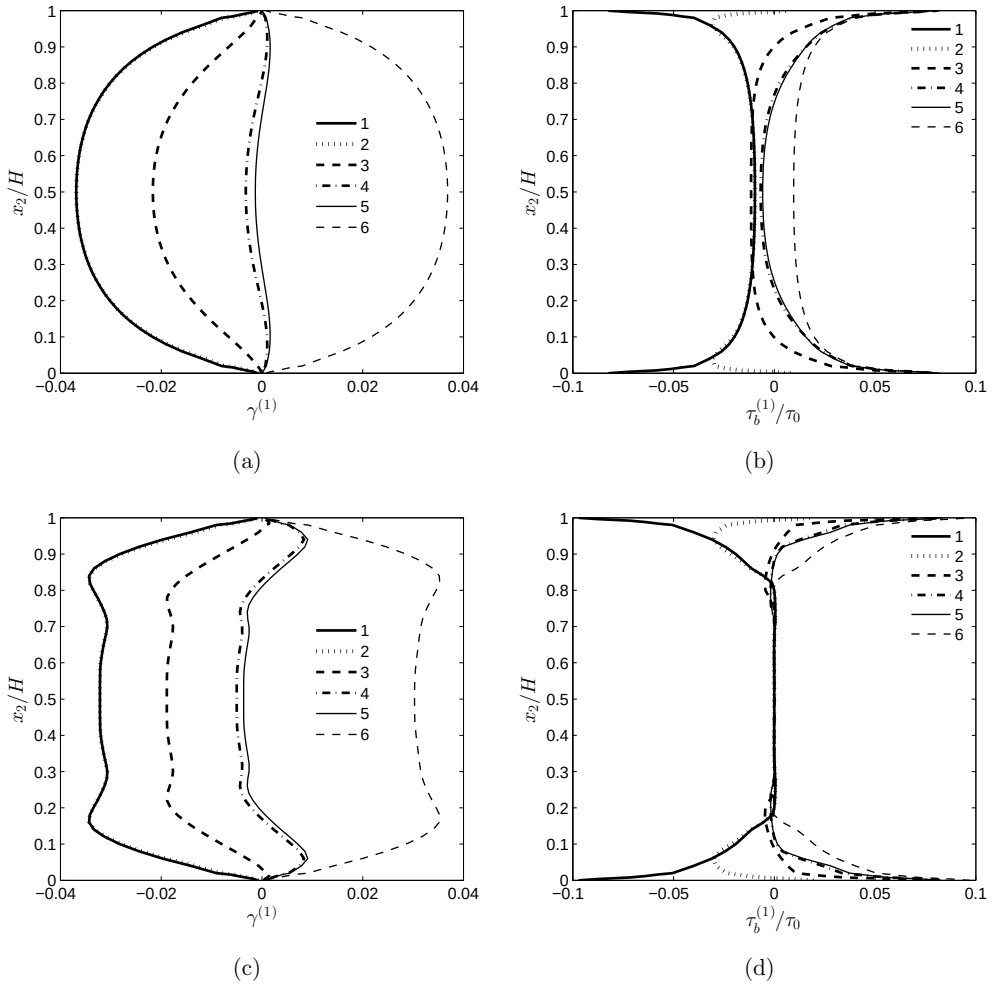

Figure 7: Numerical results for the single slip simple shear problem (Fig. 1), assuming a nearly linear gradient energy based back stress ($\mu = 0.01$ in (a) and (b)) and cubic gradient energy ($\mu = 2.0$ in (c) and (d)) (Eqs. (12) and (13)), with $\theta = 90°$, $h^{(\alpha\beta)} = h = 0$, $m = 0.02$, $L/H = 0.3$, and $\dot{U} = H\dot{\gamma}_0$. The figure shows slip profiles ((a) and (c)) and back stress distribution ((b) and (d)) at six different stages during cyclic loading corresponding to the points marked on the curve in Fig. 4.

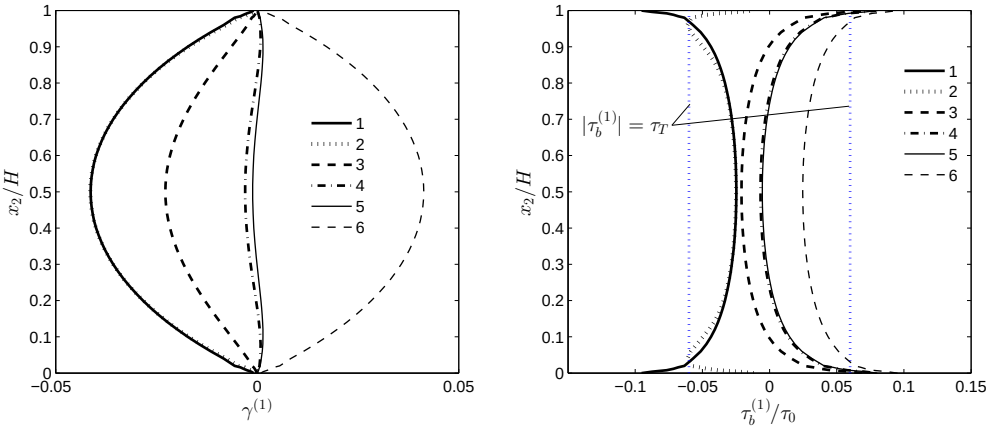

(a) (b)

Figure 8: Numerical results for the single slip simple shear problem (Fig. 1), using the back stress power law (Eq. (14)), with $\theta = 90°$, $h^{(\alpha\beta)} = h = 0$, $L/H = 0.3$, $m = 0.02$, $L/H = 0.3$, $\kappa = 0.1$, $\tau_T/\tau_0 = 0.06$, and $\dot{U} = H\dot{\gamma}_0$. The figure shows (a) slip profiles and (b) back stress distribution at six different stages during cyclic loading corresponding to the points marked on the curve in Fig. 5.

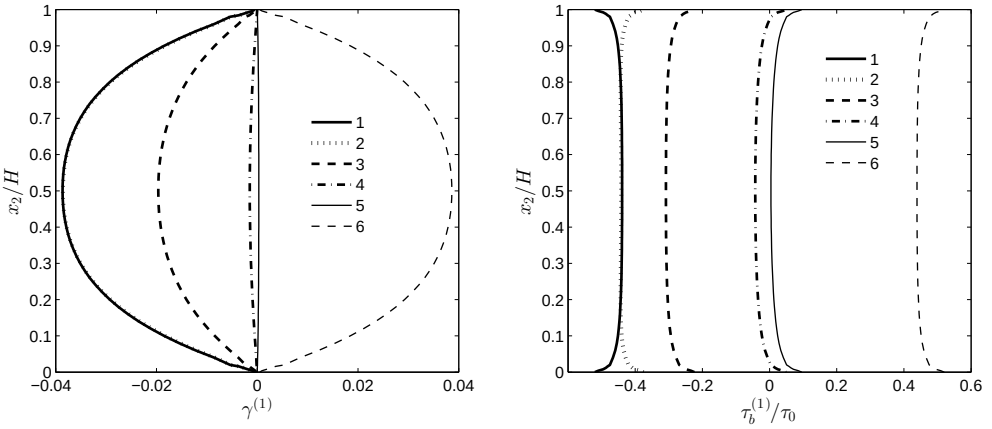

(a) (b)

Figure 9: Numerical results for the single slip simple shear problem (Fig. 1), assuming a nearly linear gradient energy based back stress (Eqs. (12) and (13)), with $\theta = 90°$, $h^{(\alpha\beta)} = h = 0$, $m = 0.02$, $L/H = 10.0$, $\mu = 0.01$, and $\dot{U} = H\dot{\gamma}_0$. The figure shows (a) slip profiles and (b) back stress distribution at six different stages during cyclic loading corresponding to the points marked on the curve in Fig. 4.

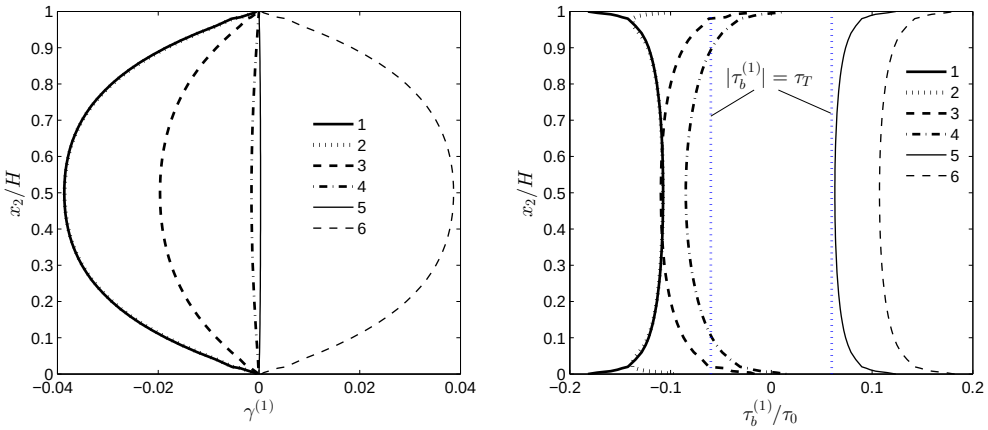

(a) (b)

Figure 10: Numerical results for the single slip simple shear problem (Fig. 1), using the back stress power law (Eq. (14)), with $\theta = 90°$, $h^{(\alpha\beta)} = h = 0$, $m = 0.02$, $L/H = 10.0$, $\kappa = 0.1$, $\tau_T/\tau_0 = 0.06$, and $\dot{U} = H\dot{\gamma}_0$. The figure shows (a) slip profiles and (b) back stress distribution at six different stages during cyclic loading corresponding to the points marked on the curve in Fig. 5.

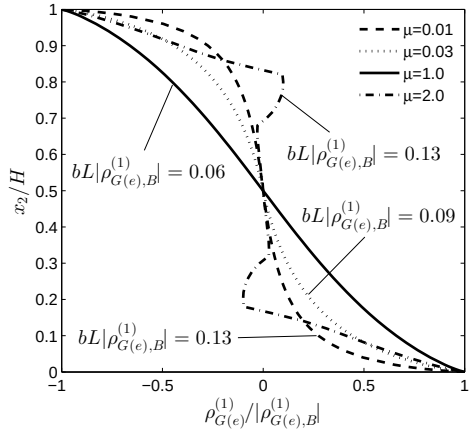

Figure 11: Predicted GND micro-structure, at $\Gamma = 0.03$ after two load cycles, assuming a nearly linear (dashed line, $\mu = 0.01$ and dotted line, $\mu = 0.03$), quadratic (solid line, $\mu = 1.0$), and cubic (dashed-dotted line, $\mu = 2.0$) gradient energy based back stress (Eqs. (12) and (13)), with $\theta = 90°$, $h^{(\alpha\beta)} = h = 0$, $m = 0.02$, $L/H = 0.3$, and $\dot{U} = H\dot{\gamma}_0$.

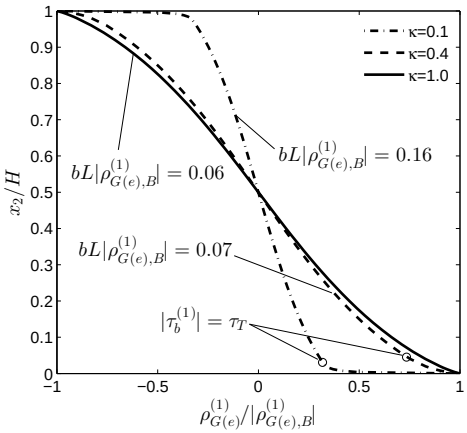

Figure 12: Predicted GND micro-structure, at $\Gamma = 0.03$ after two load cycles, using the back stress power law (Eq. (14)) with $\kappa = 0.1$ and $\kappa = 0.4$, and $\tau_T/\tau_0 = 0.06$, compared with the the classical quadratic gradient energy based back stress formulation ($\kappa = 1.0$), with $\theta = 90^\circ$, $h^{(\alpha\beta)} = h = 0$, $m = 0.02$, $L/H = 0.3$, and $\dot{U} = H\dot{\gamma}_0$. Circles mark the back stress transition point ($|\tau_b^{(1)}| = \tau_T$) near the lower horizontal boundary.

Publication [P4]

Attaining the rate-independent limit of a rate-dependent strain gradient plasticity theory

ARTICLE IN PRESS

Extreme Mechanics Letters ▮ (▮▮▮▮) ▮▮▮–▮▮▮

Contents lists available at ScienceDirect

Extreme Mechanics Letters

journal homepage: www.elsevier.com/locate/eml

Attaining the rate-independent limit of a rate-dependent strain gradient plasticity theory

S.A. El-Naaman *, K.L. Nielsen, C.F. Niordson

Department of Mechanical Engineering, Solid Mechanics, Technical University of Denmark, DK-2800 Kgs. Lyngby, Denmark

ARTICLE INFO

Article history:
Received 1 April 2016
Received in revised form 29 April 2016
Accepted 29 April 2016
Available online xxxx

Keywords:
Strain gradient plasticity
Size-effects
Rate-dependent theory
Crystal plasticity
Back stress formulation

ABSTRACT

The existence of characteristic strain rates in rate-dependent material models, corresponding to rate-independent model behavior, is studied within a back stress based rate-dependent higher order strain gradient crystal plasticity model. Such characteristic rates have recently been observed for steady-state processes, and the present study aims to demonstrate that the observations in fact unearth a more widespread phenomenon. In this work, two newly proposed back stress formulations are adopted to account for the strain gradient effects in the single slip simple shear case, and characteristic rates for a selected quantity are identified through numerical analysis. Evidently, the concept of a characteristic rate, within the rate-dependent material models, may help unlock an otherwise inaccessible parameter space.

1. Introduction

Strain gradient plasticity theories have become an established part of contemporary solid mechanics due to the increasing interest in micron and nano scale plasticity. Experiments have demonstrated that size-dependent behavior, in terms of increased hardening and/or strengthening, is associated with spatial gradients of plastic strain in ductile crystalline materials (see e.g. [1,2]). The plastic strain gradients are accommodated by a portion of lattice defects, often referred to as geometrically necessary dislocations (GNDs), which leads to a long range internal stress field. Many gradient theories of plasticity have been proposed to capture size-effects, and although so-called lower order theories have been explored (e.g. [3–5]), the common approach involves theories of a higher order nature, which enable micro-structural boundary conditions (e.g. [1,6–13]). The present study employs the rate-dependent non-work conjugate type (or back stress based) higher order theory formulated by Kuroda and Tvergaard [14,15]. In this type of theory the virtual work principle remains the conventional one, while the evolution of GND densities is accounted for through additional differential equations. Here, a back stress, representing the long range internal stresses due to pile-up of GNDs, affects the plastic slip rate as kinematic hardening.

In the following study the existence of a characteristic slip rate, at which a specific macroscopic quantity becomes independent of the rate sensitivity exponent, will be demonstrated through numerical analysis of the idealized simple shear case for a single crystal. The adopted methodology represents a promising tool for obtaining rate-independent results using rate-dependent frameworks, and the extent of the matter remains to be explored. The idea of a characteristic rate was first discussed in detail by Nielsen and Niordson [16] in relation to conventional rate-dependent steady-state modeling and later exploited in [17] to extract rate-independent results from a scale-dependent steady-state framework. Nielsen [18] also found similar results for steady-state sheet rolling. Characteristic rates may exist for a wide range of other structural problems, and a broader sense of the phenomenon is demonstrated through the results of the present study.

* Corresponding author. Tel.: +45 4525 4020; fax: +45 4593 1475.
E-mail address: saeln@mek.dtu.dk (S.A. El-Naaman).

http://dx.doi.org/10.1016/j.eml.2016.04.012
2352-4316/

The paper is structured as follows. The strain gradient plasticity model and adopted back stress formulations are briefly outlined in Section 2, (details can be found in [14,15, 19,20]). The boundary value problem treated is described in Section 3, after which, a series of numerical results are presented in Section 4. The study is concluded in Section 5.

2. Strain gradient crystal plasticity model

The present study employs the strain gradient crystal plasticity theory proposed by Kuroda and Tvergaard [14,15] within a conventional rate-dependent small strain elasto-viscoplastic framework. Hence, the total strain rate is given by; $\dot{\varepsilon}_{ij} = \left(\dot{u}_{i,j} + \dot{u}_{j,i}\right)/2$, which is additively decomposed into an elastic part, $\dot{\varepsilon}^e_{ij}$, and a plastic part, $\dot{\varepsilon}^p_{ij}$, so that $\dot{\varepsilon}_{ij} = \dot{\varepsilon}^e_{ij} + \dot{\varepsilon}^p_{ij}$. Plastic deformation occurs as a result of crystallographic slip on the individual slip systems, and thus, the Cartesian components of the plastic strain rate is given in terms of the slip rate, $\dot{\gamma}$, on the α'th slip system, as

$$\dot{\varepsilon}^p_{ij} = \sum_\alpha \dot{\gamma}^{(\alpha)} P^{(\alpha)}_{ij}, \qquad P^{(\alpha)}_{ij} = \frac{1}{2}\left(s^{(\alpha)}_i m^{(\alpha)}_j + m^{(\alpha)}_i s^{(\alpha)}_j\right). \tag{1}$$

The superposed dots denote material time derivative, $P^{(\alpha)}_{ij}$ is the Schmid orientation tensor, and unit vectors $s^{(\alpha)}_i$ and $m^{(\alpha)}_i$ specify the slip direction and the slip plane normal, respectively (see Fig. 1). The equilibrium equations for the non-work conjugate formulation are given by conventional stress equilibrium in absence of body forces; $\sigma_{ij,j} = 0$, where the Cauchy stress rate tensor is given by; $\dot{\sigma}_{ij} = \mathscr{L}_{ijkl}\left(\dot{\varepsilon}_{kl} - \dot{\varepsilon}^p_{kl}\right)$, in which $\mathscr{L}_{ijkl}$ is the fourth order elastic stiffness tensor. Thereby, the conventional incremental principle of virtual work reads

$$\int_V \mathscr{L}_{ijkl}\dot{\varepsilon}_{kl}\delta\dot{\varepsilon}_{ij}\mathrm{d}V = \int_V \mathscr{L}_{ijkl}\dot{\varepsilon}^p_{kl}\delta\dot{\varepsilon}_{ij}\mathrm{d}V + \int_S \dot{T}_i\delta\dot{u}_i\mathrm{d}S, \qquad \dot{T}_i \equiv \dot{\sigma}_{ij}n_j, \tag{2}$$

where $\dot{T}_i$ are the traction rates, n_i is the outward unit normal to the surface S bounding the volume V. In a two dimensional setting, an additional partial differential equation accounts for the evolution of GND density; $1/b\gamma^{(\alpha)}_{,i}s^{(\alpha)}_i + \rho^{(\alpha)}_G = 0$, where b is the magnitude of the Burgers vector, and $\rho^{(\alpha)}_G$ is the GND density of edge type on slip system α [21]. The GND density balance equation is expressed on weak form as

$$\frac{1}{b}\int_V \delta\rho_{,i}s^{(\alpha)}_i\gamma^{(\alpha)}\mathrm{d}V = \frac{1}{b}\int_S \delta\rho\zeta^{(\alpha)}\mathrm{d}S + \int_V \delta\rho\rho^{(\alpha)}_G\mathrm{d}V, \qquad \zeta^{(\alpha)} \equiv \gamma^{(\alpha)}n_i s^{(\alpha)}_i, \tag{3}$$

where $\delta\rho$ is a weighting function (or virtual GND density).[1]

A perfectly plastic, gradient-enhanced version of the widely used conventional power law slip rate relation [22,23] is employed, so that

$$\dot{\gamma}^{(\alpha)} = \dot{\gamma}_0 \mathrm{sgn}\left(\tau^{(\alpha)} - \tau^{(\alpha)}_b\right)\left(\frac{|\tau^{(\alpha)} - \tau^{(\alpha)}_b|}{\tau_0}\right)^{1/m}, \tag{4}$$

where $\dot{\gamma}_0$ is a reference slip rate, $\tau^{(\alpha)}$ is the Schmid stress ($\tau^{(\alpha)} = \sigma_{ij}P^{(\alpha)}_{ij}$), $\tau^{(\alpha)}_b$ is a back stress, m is the rate sensitivity exponent, and τ_0 is the critical resolved shear stress.[2] The back stress, $\tau^{(\alpha)}_b$, is phenomenologically related to the distribution of the GND density, and accounts for the long range internal stresses due to dislocation pile-up. In the present study, two back stress formulations, proposed in [19], are adopted. One is a thermodynamically consistent formulation derived from a free energy potential

$$\tau^{(\alpha)}_b = \mu\tau_0 b^\mu L^{\mu+1}\left(\left|\rho^{(\alpha)}_G\right| + \rho_0\right)^{\mu-1}\rho^{(\alpha)}_{G,i}s^{(\alpha)}_i, \qquad 0 < \mu \le 1, \tag{5}$$

where ρ_0 is a non-zero numerical parameter, which resembles the presence of statistically stored dislocations (see e.g. [24,9]). Note that Eq. (5) corresponds to a quadratic free energy for $\mu = 1$.

The second back stress relation employed in the present study is given by the piece-wise function,

$$\tau^{(\alpha)}_b = \begin{cases} b\tau_0 L^2\rho^{(\alpha)}_{G,i}s^{(\alpha)}_i & \text{, for } |\tau^{(\alpha)}_b| \le \tau_T \\ \mathrm{sgn}\left(\rho^{(\alpha)}_{G,i}s^{(\alpha)}_i\right) & \\ \quad b^\kappa\tau_T^{1-\kappa}\tau_0^\kappa L^{2\kappa}\left|\rho^{(\alpha)}_{G,i}s^{(\alpha)}_i\right|^\kappa & \text{, for } |\tau^{(\alpha)}_b| > \tau_T \end{cases}, \tag{6}$$

where $0 \le \kappa \le 1$ is assumed and τ_T defines a transition point, from a quadratic free energy based back stress, into a power law dependence on the GND density gradients. Note that Eq. (6) corresponds to a quadratic free energy for $\kappa = 1$, but thermodynamical consistency is not guaranteed for other values of κ. However, the numerical solutions presented, have been found to satisfy positive dissipation throughout the loading history, such that; $\sigma_{ij}\dot{\varepsilon}^p_{ij} = \sum_\alpha \tau^{(\alpha)}\dot{\gamma}^{(\alpha)} \ge 0$.

For a detailed description of the adopted back stress formulations and choice of model parameters see [20,19].

3. Boundary value problem

The single slip simple shear problem, with positive slip in the x_2-direction, is considered in order to demonstrate the rate-dependent behavior of the adopted back stress based strain gradient plasticity model (see Fig. 1 for a schematic illustration and definition of the slip system). The following model parameters are used throughout: Young's modulus $E = 130$ GPa, Poisson's ratio $\nu = 0.3$, $\tau_0 = 50$ MPa, and $b = 0.286$ nm. The following two back stress model parameters are used: $\rho_{G,0} = 10^5$ mm^{-2} and

[1] For a detailed discussion on the micro-structural boundary conditions see [15].

[2] Note that for $\tau^{(\alpha)}_b$ equal to zero, Eq. (4) reduces to the conventional theory.

Please cite this article in press as: S.A. El-Naaman, et al., Attaining the rate-independent limit of a rate-dependent strain gradient plasticity theory, Extreme Mechanics Letters (2016), http://dx.doi.org/10.1016/j.eml.2016.04.012

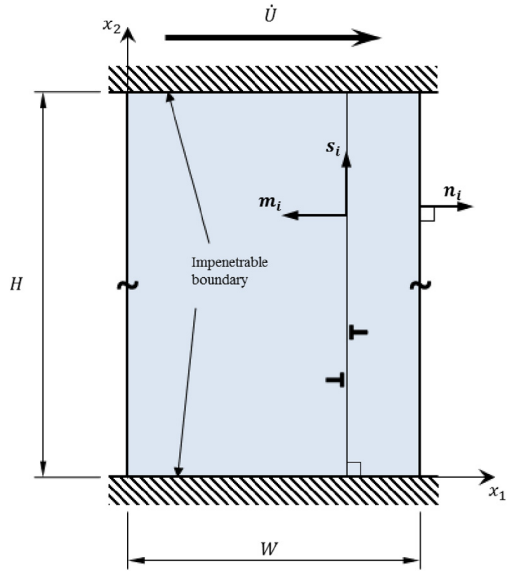

Fig. 1. Schematic of the simple shear problem showing a thin film of height H between rigid platens, modeled as infinite in the x_1-direction with model domain width W. The film has a single vertical slip system, which is passivated at the top and bottom horizontal boundaries. The domain is subject to a prescribed displacement rate $\dot{U}$.

$\tau_T/\tau_0 = 0.06$ in Eqs. (5) and (6), respectively. Periodicity in the x_1-direction is imposed for the material domain of height H and width W, such that

$$u_i(0, x_2) = u_i(W, x_2) \tag{7a}$$

$$\rho_G^{(\alpha)}(0, x_2) = \rho_G^{(\alpha)}(W, x_2). \tag{7b}$$

The following additional boundary conditions are imposed on the displacement field:

$$u_1 = u_2 = 0 \quad \text{at } x_2 = 0 \tag{8a}$$

$$u_1 = U(t) \quad \text{and} \quad u_2 = 0 \quad \text{at } x_2 = H. \tag{8b}$$

The top and bottom boundaries of the material domain are microscopically passivated by the following higher order boundary conditions imposed on the GND density field equation:

$$\zeta^{(\alpha)} \equiv \gamma^{(\alpha)} n_i s_i^{(\alpha)} = 0 \quad \text{at } x_2 = 0 \quad \text{and} \quad x_2 = H. \tag{9}$$

This models that dislocations are unable to exit through these boundaries.

The conventional and micro-structural equilibrium equations are solved in a staggered scheme, using the finite element method (FEM), with time integration carried out by the forward Euler method. Eight-node isoparametric quadrilateral elements, with reduced Gauss integration, are used for the displacement field analysis, and equivalent four-node elements, with full Gauss integration, are used for the GND density field analysis. The employed finite element mesh consists of 58 elements in the x_2-direction and includes a refined mesh at the microscopically passivated boundaries to resolve the possibly steep gradients.

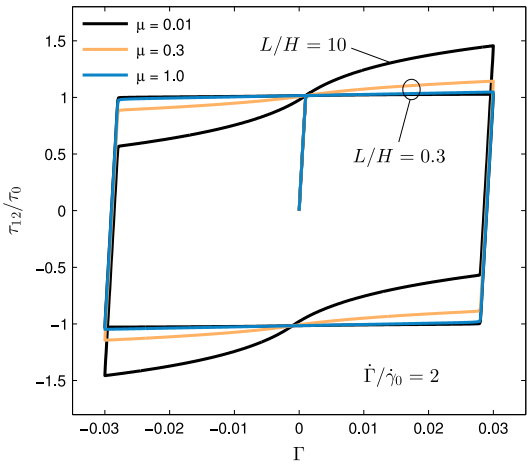

Fig. 2. Numerical results for the single slip simple shear problem (Fig. 1) subject to one hysteretic cycle at a macroscopic shear rate of $\dot{\Gamma} = 2\dot{\gamma}_0$, using the thermodynamically consistent back stress (Eq. (5)). Results are shown for different values of μ and L, with $m = 0.02$ and $\rho_0 = 10^5$ mm^{-2}.

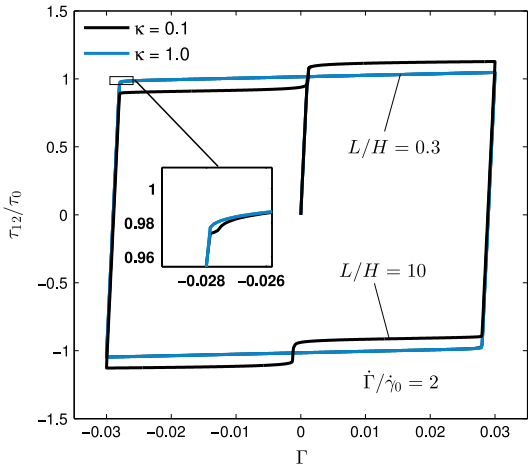

Fig. 3. Numerical results for the single slip simple shear problem (Fig. 1) subject to one hysteretic cycle at a macroscopic shear rate of $\dot{\Gamma} = 2\dot{\gamma}_0$, using the purely phenomenologically devised back stress (Eq. (6)). Results are shown for different values of κ and L, with $m = 0.02$ and $\tau_T/\tau_0 = 0.06$.

4. Methods, results, and discussion

The present numerical study focuses on the macroscopic response of the adopted gradient crystal plasticity model, where the model rate sensitivity is investigated, and a problem dependent characteristic rate is identified for the constrained simple shear problem. The material domain is sheared to a macroscopic shear strain $\Gamma = 0.03$, after which, one complete load cycle is performed, so that the macroscopic shear strain goes once to -0.03 and back to 0.03. Care was taken to ensure that a steady state cyclic response is obtained by running multiple load cycles about the zero strain axis.

Figs. 2 and 3 show the shear stress vs. macroscopic shear strain using the thermodynamically consistent back stress

Please cite this article in press as: S.A. El-Naaman, et al., Attaining the rate-independent limit of a rate-dependent strain gradient plasticity theory, Extreme Mechanics Letters (2016), http://dx.doi.org/10.1016/j.eml.2016.04.012

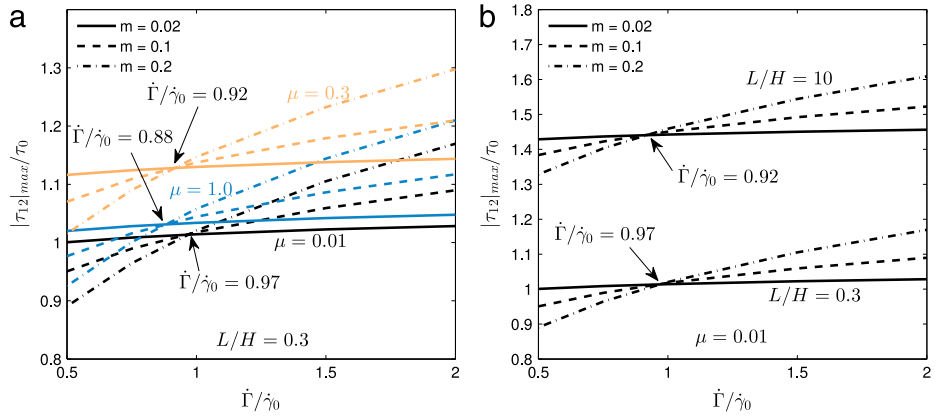

Fig. 4. Maximum shear stress vs. macroscopic shear strain rate for three different values of the rate sensitivity exponent m. The figure shows (a) results for three different values of μ with $L/H = 0.3$, and (b) results for two different values of L with $\mu = 0.01$. The characteristic rates corresponding to the intersections are given in the figures.

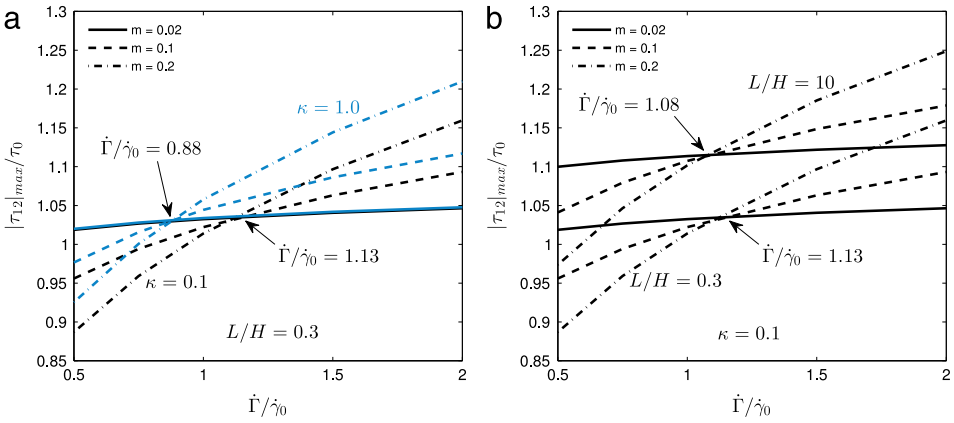

Fig. 5. Maximum shear stress vs. macroscopic shear strain rate using the back stress power law (Eq. (6)) for three different values of the rate sensitivity exponent m. The figure shows (a) results with $\kappa = 0.1$ and $\tau_T/\tau_0 = 0.06$, compared with the classical quadratic gradient energy based back stress, both with $L/H = 0.3$, and (b) shows results for two different values of L with $\kappa = 0.1$. The characteristic rates corresponding to the intersections are given in the figures.

formulation (Eq. (5)) and the purely phenomenological back stress (Eq. (6)), respectively. Results are shown for a macroscopic shear rate of $\dot{\Gamma} = 2\dot{\gamma}_0$, for different values of the material length parameter, L, and for different values of the back stress exponents μ and κ, respectively. In both cases, the response curves for $L/H = 10$ show a seemingly anomalous change in slope during plastic flow with inflection points close to zero strain. This phenomenon is discussed in detail in [20] and will not be elaborated in the present paper.

In order to identify the characteristic rate for a given specific quantity, a simple procedure is carried out. This procedure implies running a series of calculations for different values of the rate exponent, m, so that the quantity of interest can be plotted as function of the applied rate for each value of m. The convergent intersection between the curves then reveals the quantity specific rate-independent point. The existence of a well defined intersection is contingent upon the quantity investigated being monotonically increasing or decreasing with the rate sensitivity in an interval above and below the characteristic rate, respectively. Note that in order to identify the rate-independent point it is not necessary to employ low values of m, since the intersection may be obtained for curves at any given rate sensitivity. Indirectly introduced through the reference slip rate, $\dot{\gamma}_0$, in Eq. (4), the rate-independent point, tied to the characteristic rate, may open the door for a parameter space, which is otherwise inaccessible due to the numerical difficulties associated with the limit $m \longrightarrow 0$ (see also [17]).

The [14,15] theory is not formulated in a rate-independent framework, however, rate-independent results may readily be extracted by identifying the characteristic rate through the aforementioned procedure. In the following, this will be demonstrated for the maximum attained shear stress on the hysteresis curve, $|\tau_{12}|_{\max}$.

Figs. 4 and 5 show $|\tau_{12}|_{\max}$ as function of the applied shear rate. Fig. 4 shows results obtained using the thermodynamically consistent back stress formulation (Eq. (5))

Please cite this article in press as: S.A. El-Naaman, et al., Attaining the rate-independent limit of a rate-dependent strain gradient plasticity theory, Extreme Mechanics Letters (2016), http://dx.doi.org/10.1016/j.eml.2016.04.012

for different values of μ and L, and Fig. 5 shows results obtained using the purely phenomenological back stress formulation (Eq. (6)) for different values of κ and L. Clearly convergent intersections are observed for both back stress models. In both formulations, the intersections occur at a higher shear stress when L is increased, due to the increased strain gradient hardening. Furthermore, the intersection translates slightly toward lower rates for increasing L.[3]

Analogous to the results obtained for the maximum shear stress, $|\tau_{12}|_{\max}$, rate-independent points also exist for the dissipated hysteresis energy, which is defined as the area inside the hysteresis loop. However, these results are omitted in the present paper, since a high level of coincidence between the curves impair a graphical representation. This is due to the fact that, while the shape of the hysteresis loop changes significantly, the area remains approximately the same for all computations, as one may perceive from Figs. 2 and 3. The uncertainty in the intersections for the hysteresis energy were found to be on the order of 0.5% (or below).

5. Conclusion

The existence of a characteristic rate at which specific macroscopic quantities reveal their rate-independent value has been demonstrated for the pure shear case of an infinite slab between rigid platens. Here, considering the visco-plastic higher order strain gradient crystal plasticity model proposed by Kuroda and Tvergaard [14,15]. Both when assuming a quadratic free energy, but also when adopting the newly proposed back stress formulations [19,20], clear and unambiguous intersections (defining the characteristic rate) are found when plotting the quantities vs. deformation rate for various rate sensitivity exponents. Specific to the purely phenomenological back stress formulation (Eq. (6)), the transition parameter τ_T is significant for the quality of the intersection and should be chosen carefully. Choosing τ_T too high can result in a response dominated by quadratic free energy. In general, the choice of back stress models was found to have a slight influence on the resulting characteristic rate as well as the corresponding rate-independent value of the objective quantity.

The characteristic rate is strongly tied to the characteristic time introduced into the material model by the reference strain rate, $\dot{\gamma}_0$, and is fundamental to the power law type strain rate hardening relations used in the visco-plastic theories. The presented results and observations establish the findings reported in [16–18] as a widespread phenomenon, and show that by exploiting it, results at the rate-independent limit may, in fact, be reached for the present model, which only exists in a rate-dependent framework. It should be made clear, however, that the phenomenon is a purely theoretical concept and, to the best of the authors knowledge, remains to be observed in experiments. Regardless of this, the concept is highly significant in modeling contexts, since it does in fact exist within widely used visco-plastic theories. Bearing this in mind, the authors encourage experimental investigations to clarify the matter.

[3] The peak in strain gradient hardening at intermediate values of μ (also reported in [19]) is evident in Figs. 2 and 4(a) for $\mu = 0.3$.

Acknowledgment

The work is financially supported by The Danish Council for Independent Research under the research career programme Sapere Aude as part of the project "Higher Order Theories in Solid Mechanics", grant 11-105098/FTP.

References

[1] N. Fleck, G. Muller, M. Ashby, J. Hutchinson, Strain gradient plasticity: Theory and experiment, Acta Metall. Mater. 42 (2) (1994) 475–487.
[2] Y. Mu, J. Hutchinson, W. Meng, Micro-pillar measurements of plasticity in confined Cu thin films, Extreme Mech. Lett. 1 (2014) 62–69.
[3] J. Bassani, Incompressibility and a simple gradient theory of plasticity, J. Mech. Phys. Solids 49 (2001) 1983–1996.
[4] Y. Huang, S. Qu, K. Hwang, M. Li, H. Gao, A conventional theory of mechanism-based strain gradient plasticity, Int. J. Plast. 20 (2004) 753–782.
[5] C. Niordson, J. Hutchinson, On lower order strain gradient plasticity theories, Eur. J. Mech. A Solids 22 (2003) 771–778.
[6] M. Gurtin, On the plasticity of single crystals: free energy, microforces, plastic-strain gradients, J. Mech. Phys. Solids 48 (5) (2000) 989–1036.
[7] M. Gurtin, A gradient theory of single-crystal viscoplasticity that accounts for geometrically necessary dislocations, J. Mech. Phys. Solids 50 (2002) 5–32.
[8] N. Fleck, J. Hutchinson, A reformulation of strain gradient plasticity, J. Mech. Phys. Solids 49 (2001) 2245–2271.
[9] S. Yefimov, I. Groma, E. van der Giessen, A comparison of a statistical-mechanics based plasticity model with descrete dislocation plasticity calculations, J. Mech. Phys. Solids 52 (2004) 279–300.
[10] L. Evers, W. Brekelmans, M. Geers, Non-local cystal plasticity model with intrinsic SSD and GND effects, J. Mech. Phys. Solids 52 (2004) 2379–2401.
[11] C. Bayley, W. Brekelmans, M. Geers, A comparison of dislocation induced back stress formulations in strain gradient crystal plasticty, Internat. J. Solids Structures 43 (2006) 7268–7286.
[12] N. Fleck, J. Willis, A mathematical basis for strain-gradient plasticity theory. Part I: Scalar plastic multiplier, J. Mech. Phys. Solids 57 (2009) 161–177.
[13] N. Fleck, J. Willis, A mathematical basis for strain-gradient plasticity theory. Part II: Tensorial plastic multiplier, J. Mech. Phys. Solids 57 (2009) 1045–1057.
[14] M. Kuroda, V. Tvergaard, Studies of scale dependent crystal viscoplasticity models, J. Mech. Phys. Solids 54 (2006) 1789–1810.
[15] M. Kuroda, V. Tvergaard, On the formulation of higher-order strain gradient crystal plasticity models, J. Mech. Phys. Solids 56 (2008) 1591–1608.
[16] K. Nielsen, C. Niordson, Rate sensitivity of mixed mode interface toughness of dissimilar meallic materials: Studied at steady state, Internat. J. Solids Structures 49 (2012) 576–583.
[17] K. Nielsen, C. Niordson, J. Hutchinson, Strain gradient effects on steady state crack growth in rate-sensitive materials, Eng. Fract. Mech. 96 (2012) 61–71.
[18] K. Nielsen, Rolling induced size effects in elastic–viscoplastic sheet metals, Eur. J. Mech. A Solids 53 (2015) 259–267.
[19] S. El-Naaman, K. Nielsen, C. Niordson, On modeling micro-structural evolution using a higher order strain gradient continuum theory, Int. J. Plast. 76 (2016) 285–298.
[20] S. El-Naaman, K. Nielsen, C. Niordson, An investigation of back stress formulations under cyclic loading, 2016, submitted for publication.
[21] M. Ashby, The deformation of plastically non-homogeneous alloys, Phil. Mag. 21 (1970) 399–424.
[22] J. Hutchinson, Bounds and self-consistent estimates for creep of polycrystalline materials, Proc. R. Soc. Lond. Ser. A Math. Phys. Eng. Sci. 348 (1976) 101–127.
[23] D. Peirce, R. Asaro, A. Needleman, Material rate dependence and localized deformation in crystalline solids, Acta Metall. 31 (1983) 1951–1976.
[24] I. Groma, F. Csikor, M. Zaizer, Spatial correlations and higher-order gradient terms in a continuum description of dislocation dynamics, Acta Mater. 51 (2003) 1271–1281.

Please cite this article in press as: S.A. El-Naaman, et al., Attaining the rate-independent limit of a rate-dependent strain gradient plasticity theory, Extreme Mechanics Letters (2016), http://dx.doi.org/10.1016/j.eml.2016.04.012

Publication [P5]

Micron scale analysis of deformation around a cylindrical void in a face centered cubic crystal

Micron scale analysis of deformation around a cylindrical void in a face centered cubic crystal

S.A. El-Naaman*, K.L. Nielsen, C.F. Niordson

Department of Mechanical Engineering, Solid Mechanics, Technical University of Denmark, DK-2800 Kgs. Lyngby, Denmark

J.W. Kysar

Department of Mechanical Engineering, Columbia University, NewYork, NY 10027, United States

Abstract

Plastic deformation around a cylindrical void in a face centered cubic crystal is studied within the framework of a back stress based higher order crystal plasticity theory. New insight into the modeling of plane strain deformation in the (110) crystallographic plane in face centered cubic crystals is obtained, where the effect of both edge and screw dislocation densities is accounted for. To account for the gradient effects in the numerical model, two novel back stress formulations, proposed in a previous work, are employed and studied for the first time in a two dimensional multi-slip setting. The back stress formulations are extended to incorporate the screw contributions and their influence on microscopic and macroscopic predictions are discussed.

Keywords: Strain gradient plasticity, Back stress, Size-effects, Geometrically necessary dislocations, Crystal plasticity

1. Introduction

Nowadays it is well-known that ductile crystalline materials exhibit size-dependent behavior due to the presence of geometrically necessary dislocations (GNDs), introduced by spatial gradients of plastic strain (see e.g. Fleck et al., 1994; Atkinson, 1995; Stölken and Evans, 1998; Mu et al., 2014). More specifically, the phenomenon entails an increase in hardening and/or an apparent increase in yield point (also refered to as strengthening) or a combination of the two. A vast experimental record of the phenomenon has accumulated during the past few decades. One example, often referred to in the literature, is crack tip plasticity and its influence on the fracture toughness (e.g. Wei and Hutchinson, 1997, 1999; Nielsen et al., 2012; Martínez-Pañeda and Niordson, 2015). Fracture in metals usually occurs by void growth to coalescence, and the size of initial voids may on the order of microns and below. Such void may exist in grain boundaries or within single grains, and the orientation of the crystal structure has a significant influence on the void growth behavior (Borg and Kysar, 2007). Apart

*Tel: +45 4525-4020, Fax: +45 4593-1475
URL: saeln@mek.dtu.dk (S.A. El-Naaman)

from the work of Borg and Kysar (2007), Niordson and Kysar (2014) also studied the deformation around micron scale voids in single crystals both within work-conjugate strain gradient crystal plasticity frameworks and Kysar et al. (2005) and Gan and Kysar (2016) derived analytical solutions using an-isotropic slip line theory. The observed gradient effects have been studied extensively over the years and many theories have been proposed to model the underlying physical phenomena and observations. Within the class of continuum models both so-called lower order theories (e.g Bassani, 2001; Huang et al., 2004) and higher order theories have emerged. It is now generally accepted that higher order theories, which incorporate micro-structural boundary conditions, offer important modeling capabilities. Among significant contributions to the higher order theories are Fleck et al. (1994), Gurtin (2000, 2002), Fleck and Hutchinson (2001),Yefimov et al. (2004), Evers et al. (2004), Bayley et al. (2006), and Fleck and Willis (2009a,b). These theories allow boundary conditions on plastic strain quantities or associated stress quantities, which enter either through an extended virtual work principle or through additional partial differential equations. The importance of this capability was illustrated experimentally by Kraft et al. (2000) in uniaxial testing of polycrystalline copper films (0.4 μm to 1.5 μm thickness) deposited onto polymer substrates. The substrates functioned as micro-structural passivation layers, obstructing the dislocations from exiting the material, which in turn results in dislocation pile up at the boundary causing long range internal stresses. The samples with passivation layers were significantly stronger than regular free-standing samples. Similar results were found by Xiang and Vlassak (2016) and Mu et al. (2014). The continuum theories have, for many cases, been proven to adequately capture the size-dependent macroscopic behavior. However, common for these theories is the tendency to predict a rather smooth micro-structure, which is not consistent with experimental studies of metals (see also the recent discussion in El-Naaman et al., 2016c).

In general, dislocations tend to form cellular structures in plastically deformed metals, and most likely the same general tendency applies to the particular densities of signed dislocations referred to as GNDs. In fact, Öztop (2011) measured complicated GND cell structures in a plastically deformed nickel crystal, using high resolution electron backscatter diffraction (HR-EBSD) microscopy[1], by linking the lattice curvature to dislocation density through the Nye (1953) tensor. Since the strain gradient effects are attributed the development of micro-structure, it is a natural step, in the further development of gradient theories, to focus on their ability to capture realistic micro-structural evolution, and it has been given significant attention in the recent years (e.g. Klusemann and Yalçinkaya, 2013; van Beers et al., 2013, 2015; El-Naaman et al., 2016c,b).

In the present study the non-work conjugate type formulation, proposed by Kuroda and Tvergaard (2006, 2008), is employed. In this type of theory the conventional crystal visco plasticity framework is extended through additional differential equations, which account for the evolution of GND densities. The microscopic and macroscopic equations are linked by a back stress, which accounts for the long range internal stresses that arise due to dislocation pile-up and affects the evolution of slip as kinematic hardening.

[1]Details on the experimental methods employed by Öztop (2011) can also be found in Kysar et al. (2010) and Dahlberg et al. (2014), also confirming the existence of highly localized GND structures.

Two back stress formulations, proposed in El-Naaman et al. (2016c), are adopted in the present study. These were found to add an additional degree of freedom to the model enabling a better representation of highly localized micro-structures. The present paper adds new insight into the two dimensional modeling of face centered cubic (FCC) single crystals with associated effective quantities and derives more general extensions of the adopted back stress formulations. The micro-structural predictions are studied along with the associated size-effects on void growth in a single crystal.

The paper is structured as follows. The strain gradient plasticity model is described in Section 2, and the two back stress formulations treated are briefly outlined in Section 3 (more details can be found in El-Naaman et al., 2016c). The effective framework for plane strain modeling of FCC crystals is derived in Section 4, which includes a description of the boundary value problem studied. A series of results are presented in Section 5, using a finite element method (FEM) implementation, after which, the final concluding remarks are given in Section 6.

2. Strain gradient crystal plasticity model

The present study employs a small strain formulation, with the total strain rate given by; $\dot{\varepsilon}_{ij} = (\dot{u}_{i,j} + \dot{u}_{j,i})/2$, which decomposes into an elastic part, $\dot{\varepsilon}^e_{ij}$, and a plastic part, $\dot{\varepsilon}^p_{ij}$, so that; $\dot{\varepsilon}_{ij} = \dot{\varepsilon}^e_{ij} + \dot{\varepsilon}^p_{ij}$. The formulation builds on the framework of conventional crystal visco-plasticity theory, where plastic deformation occurs by means of crystallographic slip on the individual slip systems. Thus, the plastic strain rate is given in terms of the slip rate, $\dot{\gamma}$, on the (α)'th slip system, as

$$\dot{\varepsilon}^p_{ij} = \sum_\alpha \dot{\gamma}^{(\alpha)} P^{(\alpha)}_{ij}, \quad P^{(\alpha)}_{ij} = \frac{1}{2}\left(s^{(\alpha)}_i m^{(\alpha)}_j + m^{(\alpha)}_i s^{(\alpha)}_j\right), \tag{1}$$

where the superposed dot denotes material time derivative, $P^{(\alpha)}_{ij}$ is the Schmid orientation tensor, and $s^{(\alpha)}_i$ and $m^{(\alpha)}_i$ are unit vectors specifying the slip direction and slip plane normal, respectively. The slip rate is given by

$$\dot{\gamma}^{(\alpha)} = \dot{\gamma}_0 \mathrm{sgn}\left(\tau^{(\alpha)} - \tau^{(\alpha)}_b\right)\left(\frac{|\tau^{(\alpha)} - \tau^{(\alpha)}_b|}{g^{(\alpha)}}\right)^{1/m}, \tag{2}$$

where $\dot{\gamma}_0$ is a reference slip rate, $\tau^{(\alpha)}$ is the Schmid stress (taken as the macroscopic Cauchy stress tensor resolved onto the slip plane), $\tau^{(\alpha)}_b$ is a back stress, m is the rate sensitivity exponent, and $g^{(\alpha)}$ is the slip resistance, taken to follow the hardening law

$$\dot{g}^{(\alpha)} = \sum_\beta h^{(\alpha\beta)} |\dot{\gamma}^{(\beta)}|, \quad g^{(\alpha)}|_{t=0} = \tau_0, \tag{3}$$

where the initial value of $g^{(\alpha)}$ is chosen as the initial critical resolved shear stress τ_0. Here, t is time and $h^{(\alpha\beta)}$ are slip hardening moduli, in which the trace accounts for self hardening, and the off-diagonal parts for latent hardening. Equation (2) is a gradient-enhanced version of the widely used conventional visco-plastic power law slip rate relation (Hutchinson, 1976; Peirce et al., 1983), in that $\tau^{(\alpha)} - \tau^{(\alpha)}_b$ replaces $\tau^{(\alpha)}$ as an effective resolved shear stress[2]. The back stress, $\tau^{(\alpha)}_b$, is related directly to the

[2]Note that for $\tau^{(\alpha)}_b$ equal to zero, Eq. (2) reduces to the conventional theory.

gradients of the GND density (see Section 3), and impedes (or aids, depending on load path) slip at nonuniform pile-ups of GNDs. Thereby, the effective resolved shear stress becomes the driving force behind dislocation glide (Harder, 1999; Groma et al., 2003; Yefimov et al., 2004; Evers et al., 2004).

A non-work conjugate type higher order strain gradient plasticity theory is employed in the present study. This theory, formulated by Kuroda and Tvergaard (2006, 2008), is of a higher order nature but does not employ higher order stresses work conjugate to strain gradients or higher order equilibrium equations. Instead, the governing equations of the non-work conjugate formulation, are given by the conventional stress equilibrium equation,

$$\sigma_{ij,j} + f_i = 0, \tag{4}$$

where f_i are body forces and the Cauchy stress rate tensor is given by the elastic relationship; $\dot{\sigma}_{ij} = \mathscr{L}_{ijkl}\,(\dot{\varepsilon}_{kl} - \dot{\varepsilon}^p_{kl})$, in which $\mathscr{L}_{ijkl}$ is the fourth order elastic stiffness tensor. Thereby, the conventional rate-dependent incremental principle of virtual work yields the weak form of the velocity field equation:

$$\int_V \mathscr{L}_{ijkl}\dot{\varepsilon}_{kl}\delta\dot{\varepsilon}_{ij}\mathrm{d}V = \int_V \mathscr{L}_{ijkl}\dot{\varepsilon}^p_{kl}\delta\dot{\varepsilon}_{ij}\mathrm{d}V + \int_V \dot{f}_i\delta\dot{u}_i\mathrm{d}V + \int_S \dot{T}_i\delta\dot{u}_i\mathrm{d}S, \quad \dot{T}_i \equiv \dot{\sigma}_{ij}n_j, \tag{5}$$

where $\dot{T}_i$ is the traction rate, n_i is the outward unit normal to the surface S bounding the volume V. The evolution of GND density, in balance with the slip gradients, is accounted for by an additional set of partial differential equations:

$$\frac{1}{b}\gamma^{(\alpha)}_{,i}s^{(\alpha)}_i + \rho^{(\alpha)}_{G(e)} = 0 \tag{6a}$$

$$\frac{1}{b}\gamma^{(\alpha)}_{,i}p^{(\alpha)}_i + \rho^{(\alpha)}_{G(s)} = 0, \tag{6b}$$

where $\mathbf{p}^{(\alpha)} = \mathbf{s}^{(\alpha)} \times \mathbf{m}^{(\alpha)}$, b is the magnitude of the Burgers vector, and $\rho^{(\alpha)}_G$ are GND densities on slip system α (Ashby, 1970). Subscripts (e) and (s) denote edge and screw components, respectively. The GND densities appear directly as free field variables in Eqs. (6a) and (6b), and their weak form reads:

$$\frac{1}{b}\int_V \delta\rho_{,i}s^{(\alpha)}_i\gamma^{(\alpha)}\mathrm{d}V = \frac{1}{b}\int_S \delta\rho\zeta^{(\alpha)}\mathrm{d}S + \int_V \delta\rho\rho^{(\alpha)}_{G(e)}\mathrm{d}V, \qquad \zeta^{(\alpha)} \equiv \gamma^{(\alpha)}n_is^{(\alpha)}_i, \tag{7a}$$

$$\frac{1}{b}\int_V \delta\rho_{,i}p^{(\alpha)}_i\gamma^{(\alpha)}\mathrm{d}V = \frac{1}{b}\int_S \delta\rho\eta^{(\alpha)}\mathrm{d}S + \int_V \delta\rho\rho^{(\alpha)}_{G(s)}\mathrm{d}V, \qquad \eta^{(\alpha)} \equiv \gamma^{(\alpha)}n_ip^{(\alpha)}_i, \tag{7b}$$

where $\delta\rho$ is a weighting function (or virtual GND density). In the GND density equations, a hard interface impenetrable for dislocations is enforced by

$$\zeta^{(\alpha)} \equiv \gamma^{(\alpha)}n_is^{(\alpha)}_i = 0 \tag{8a}$$

$$\eta^{(\alpha)} \equiv \gamma^{(\alpha)}n_ip^{(\alpha)}_i = 0, \tag{8b}$$

whereas a free boundary, where dislocations can exit the body, corresponds to

$$\rho^{(\alpha)}_{G(e)} = \rho^{(\alpha)}_{G(s)} = 0. \tag{9}$$

For a detailed discussion on the micro-structural boundary conditions see Kuroda and Tvergaard (2008), where also the discretized finite element equations can be found.

The governing equations for the displacement field and GND density fields are evaluated separately, but the separate fields are linked together by the back stresses, according to Eq. (2). Hence, it is the back stress that introduces the gradient effects into the material response of the adopted strain gradient plasticity model.

3. Back stress formulations

In a non-uniform field of GNDs, arising due to a spatial variation of plastic strain gradients in ductile crystalline materials, a long range internal stress field emerges. This can be represented as a back stress in continuum models. In the framework adopted, the back stress influences the slip rates, by lowering or enhancing the effective resolved shear stresses on the slip systems. This gives rise to a kinematic hardening contribution, which accounts for the micro-structural effects on plastic flow. Back stress models can, for the most part, be classified into two types: i) The physically based models, which build on considerations of the stress field of a single dislocation (e.g. Groma et al., 2003; Yefimov et al., 2004), and ii) the more phenomenologically based models, which either build on a postulated strain gradient energy relation (e.g. Kuroda and Tvergaard, 2008; Öztop et al., 2012) or may be formulated directly to possess certain constitutive properties as in El-Naaman et al. (2016c). In the present work, the two back stress formulations proposed in El-Naaman et al. (2016c) are adopted. In summary, these are

i. A thermodynamically consistent formulation based on a generalized gradient energy potential.

ii. A straightforward purely phenomenological formulation, constructed to possess certain properties.

The performance of these back stress formulations was demonstrated for pure shear monotonic and cyclic loading in El-Naaman et al. (2016c,b), respectively and rate-independent results were obtained in El-Naaman et al. (2016a). Each formulation is described briefly below.

3.1. Thermodynamically consistent back stress formulation

It was shown by Kuroda and Tvergaard (2006), that by defining the back stress as the divergence of a higher order stress, $\xi_i^{(\alpha)}$, so that

$$\tau_b^{(\alpha)} \equiv -\xi_{i,i}^{(\alpha)}, \tag{10}$$

the adopted theory is equivalent to the work conjugate theory of Gurtin (2000, 2002)[3]. This relation is obtained from the micro-force balance equation,

$$\xi_{i,i}^{(\alpha)} + \tau^{(\alpha)} - \tau_{eff}^{(\alpha)} = 0, \tag{11}$$

[3]Note that the term 'higher order stress' refers to the stress quantity which is work conjugate to strain gradients or slip gradients in other theories.

where the effective resolved shear stress is given by $\tau_{eff}^{(\alpha)} = \tau^{(\alpha)} - \tau_b^{(\alpha)}$. The higher order stress is derived from the plastic part of the free energy, ψ_G, as

$$\xi_i^{(\alpha)} = \frac{\partial \psi_G^{(\alpha)}}{\partial \gamma_{,i}^{(\alpha)}}. \tag{12}$$

Note that, by adopting relation (10), the non-work conjugate theory takes a work conjugate form within a thermodynamically consistent framework, once a continuous differentiable constitutive relation for the defect energy, ψ_G, has been defined. In El-Naaman et al. (2016c), the following generalized gradient energy potential was proposed:

$$\psi_G^{(\alpha)} = \frac{1}{\mu+1}\tau_0 L^{\mu+1}\left|\gamma_{,i}^{(\alpha)} s_i^{(\alpha)}\right|^{\mu+1}, \tag{13}$$

where L is an intrinsic material length scale parameter, that enters for dimensional consistency but has no direct simple physical interpretation(similar choices for the defect energy can be found in Bardella, 2010; Bardella and Panteghini, 2015; Fleck et al., 2015; El-Naaman et al., 2016c).

The generalized energy expression in Eq. (13) leads to a back stress which is linear in the second order gradient of slip, but reveals a dependence on the first order gradient of slip (or the GND densities) when $\mu \neq 1$. This back stress relation is given by

$$\tau_b^{(\alpha)} = -\mu\tau_0 L^{\mu+1}\left|\gamma_{,j}^{(\alpha)} s_j^{(\alpha)}\right|^{\mu-1}\gamma_{,ki}^{(\alpha)} s_i^{(\alpha)} s_k^{(\alpha)}, \tag{14}$$

which is expressed in terms of GND densities as

$$\tau_b^{(\alpha)} = \mu\tau_0 b^{\mu} L^{\mu+1}\left|\rho_{G(e)}^{(\alpha)}\right|^{\mu-1}\rho_{G(e),i}^{(\alpha)} s_i^{(\alpha)}. \tag{15}$$

For $\mu = 1$, Eq. (13) is quadratic and Eqs. (14) and (15) reduce to the more simple form used in e.g. Kuroda and Tvergaard (2008).

Equations (14) and (15) maintain thermodynamic consistency through Eq. (10), while, in the wording of Kuroda and Tvergaard (2006), they have a non-constant back stress coefficient, which evolves with the GND density for $\mu \neq 1$. Moreover, for $\mu \to 0$, Eqs. (14) and (15) resemble the back stress relation obtained in Groma et al. (2003) and Yefimov et al. (2004) for a single slip continuum description of dislocation dynamics based on the shear stress field of a single dislocation. Note that, due to the linear dependence on GND density gradients, the back stress in Eq. (15) does not give rise to long range internal stresses in a uniform field of GNDs.

For $\mu < 1$, the back stress in Eq. (15) has a singularity at zero GND density, and thus, an "effective" GND density is employed, such that $\rho_{G(e),eff}^{(\alpha)} = |\rho_{G(e)}^{(\alpha)}| + \rho_0$ replaces $|\rho_{G(e)}^{(\alpha)}|$ in Eq. (15), for values of μ below one. This is a numerical necessity, but nevertheless it may physically be interpreted as a presence of SSDs, such as in the back stress relations proposed by Groma et al. (2003) and Yefimov et al. (2004). A value of $\rho_{G(e),0} = 10^5$ mm^{-2} is used in all computations in the present work (for more details on this parameter see El-Naaman et al., 2016c,b).

3.2. Phenomenologically constructed back stress formulation

In El-Naaman et al. (2016c) it was shown that addition control of the micro-structural behavior and associated macroscopic response was obtained by introducing a transition from linear to power law dependence on the GND density gradients in the back stress. This approach showed promising capabilities which will be investigated further in the present study. The versatile framework proposed by Kuroda and Tvergaard (2006, 2008) allows any function $\tau_b^{(\alpha)}(\rho_{G(e),i}^{(\alpha)} s_i^{(\alpha)})$ to be considered, which was exploited in (El-Naaman et al., 2015, 2016c) to construct the following piece-wise back stress function:

$$\tau_b^{(\alpha)} = \begin{cases} b\tau_0 L^2 \rho_{G(e),i}^{(\alpha)} s_i^{(\alpha)} & , \text{ for } |\tau_b^{(\alpha)}| \leq \tau_T \\ \text{sgn}\left(\rho_{G(e),i}^{(\alpha)} s_i^{(\alpha)}\right) b^{\kappa} \tau_T^{1-\kappa} \tau_0^{\kappa} L^{2\kappa} \left|\rho_{G(e),i}^{(\alpha)} s_i^{(\alpha)}\right|^{\kappa} & , \text{ for } |\tau_b^{(\alpha)}| > \tau_T \end{cases}, \tag{16}$$

where the first part follows from a quadratic free energy (through Eqs. (10) - (12)), and the parameter τ_T defines a transition point into a power law dependence on the GND density gradients. The initial infinite slope of the power law relation in Eq. (16) precludes the choice $\tau_T \to 0$. Since a gradient energy relation that leads to Eq. (16) is not readily available, this back stress formulation must be considered a non-thermodynamically consistent formulation except for the case of $\kappa = 1$, where a quadratic gradient energy prevails throughout. However, all numerical solutions presented here, were found to satisfy positive dissipation throughout the load history, such that

$$\sigma_{ij}\dot{\varepsilon}_{ij}^{p} = \sum_{\alpha} \tau^{(\alpha)}\dot{\gamma}^{(\alpha)} \geq 0. \tag{17}$$

4. Effective framework for plane strain deformation in FCC crystals

In the following a two dimensional multi-slip numerical analysis is carried out. Here, plane strain deformation in the (110) plane of an FCC single crystal is considered. In FCC crystals a total of twelve individual slip systems exist and plastic deformation occurs by slip on a combination of these slip systems. In the present study an FCC crystal, which is assumed infinite in the [110] direction, is loaded in far-field equi-biaxial tension, so that plane strain deformation occurs in the (110) plane. The boundary value problem considered in the present study is illustrated in Fig. 1a, with the definition of slip systems shown in Fig. 1b. In the 2D representation of the FCC crystal given in Fig. 1, this deformation state implies that equal amounts of slip occurs on three pairs of slip systems which are symmetric about the (110) plane and that together each pair wise combine to form one effective in-plane slip system (Rice, 1987; Kysar et al., 2005). In Fig. 2 (from Kysar et al. (2005)) the family of (111) planes can be seen shaded in gray, and the wire frame can be viewed as a representation of the considered crystal which is rotated 45° about the [001] axis relative to the FCC unit cell. Here it is seen that the in-plane slip system (1) is formed by pairing slip systems $(1\bar{1}1)[\bar{1}01]$ and $(1\bar{1}1)[011]$, resulting in the effective slip system $(1\bar{1}1)[\bar{1}12]$, in-plane slip system (3) is formed by pairing slip systems $(\bar{1}11)[101]$ and $(\bar{1}11)[0\bar{1}1]$, resulting in the effective slip system $(\bar{1}11)[1\bar{1}2]$, and in-plane slip system (2) is formed by pairing slip systems $(111)[\bar{1}10]$ and $(11\bar{1})[\bar{1}10]$, resulting in the effective slip system $(001)[\bar{1}10]$. In order for the effective 2D FCC crystal to correspond to plane strain deformation in the true

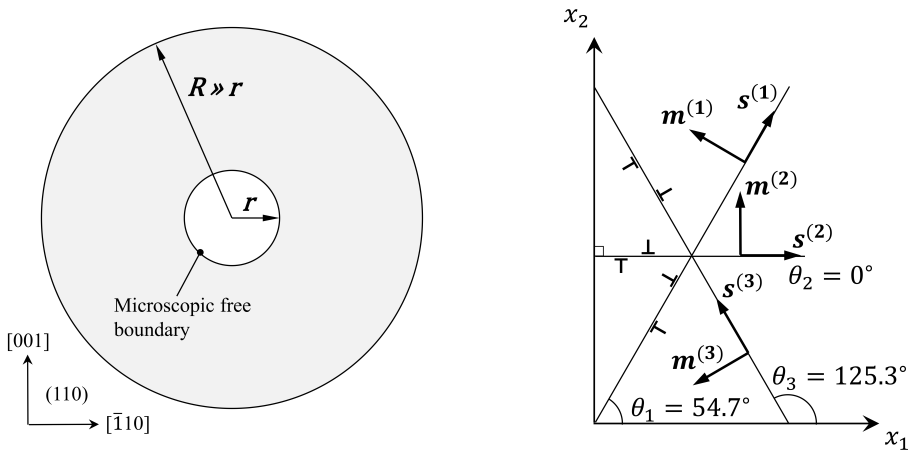

(a) (b)

Figure 1: Illustraion of the boundary value problem: (a) the (110) crystallographic plane material domain with a cylindrical void, which is modeled with a microscopic free boundary along the inner perimeter and subject to equi-biaxial tension in the (110) plane. (b) definition of the effective in-plane slip systems for the FCC crystal.

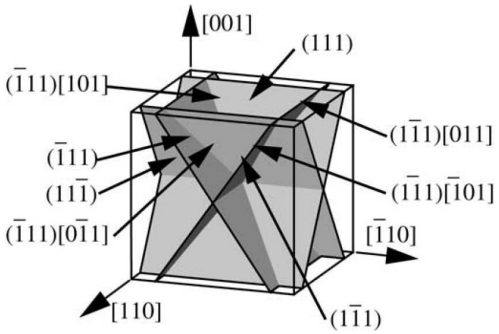

Figure 2: The {111} crystallographic planes in a FCC crystal. The wire frame illustrates the outer surface of the crystal which is rotated 45° about the [001] direction relative to the FCC unit cell. The figure is copied from Kysar et al. (2005).

FCC crystal structure, the plastic properties which enter into the slip rate relation (Eq. (2)) and back stress relations (Eqs. (15) and (16)), must be scaled in an appropriate manner, assuming that these quantities refer to the true FCC crystal. This is done by the following relations for the reference slip rate and critical resolved shear stress (Niordson and Kysar, 2014; Rice, 1987):

$$\dot{\gamma}_0^{(\alpha)} = \beta^{(\alpha)}\dot{\gamma}_0, \tag{18}$$

$$\tau_0^{(\alpha)} = \lambda^{(\alpha)}\tau_0, \tag{19}$$

with $\lambda^{(\alpha)} = 2/\beta^{(\alpha)}$. Since dislocations of both edge and screw type may exist on the three dimensional crystallographic slip systems, they can both contribute to the

gradient energy. Thus, assuming a unified material length scale parameter, L, for both edge and screw components, we rewrite Eq. (13) as a function of the Euclidean norm of the edge and screw densities (e.g. Gurtin et al., 2007) so that

$$\psi_G^{(\alpha a)} = \frac{1}{\mu+1}\tau_0 L^{\mu+1}\left\{\sqrt{\left(\gamma_{,i}^{(\alpha a)}s_i^{(\alpha a)}\right)^2+\left(\gamma_{,i}^{(\alpha a)}p_i^{(\alpha a)}\right)^2}\right\}^{\mu+1}. \tag{20}$$

The back stress relation that results from this choice of gradient energy reads

$$\tau_b^{(\alpha a)} = \mu\tau_0 L^{\mu+1}\left\{\sqrt{\left(\gamma_{,k}^{(\alpha a)}s_k^{(\alpha a)}\right)^2+\left(\gamma_{,k}^{(\alpha a)}p_k^{(\alpha a)}\right)^2}\right\}^{\mu-1}\gamma_{,ij}^{(\alpha a)}\left(s_i^{(\alpha a)}s_j^{(\alpha a)}+p_i^{(\alpha a)}p_j^{(\alpha a)}\right). \tag{21}$$

For simplicity, Eq. (20) is not based on an invariant of the Nye tensor, and thus, the interaction between slip systems is omitted, except for screw dislocations on the pair of slip systems that constitute the second effective slip system, as will be discussed in the following. Equation (20) can be written in terms of effective quantities as

$$\psi_G^{(\alpha a)} = \frac{1}{\mu+1}\tau_0 L^{\mu+1}\frac{1}{(\beta^{(\alpha)})^{\mu+1}}\left\{\sqrt{\left(\omega^{(\alpha)}\gamma_{,i}^{(\alpha)}s_i^{(\alpha)}\right)^2+\left(\chi^{(\alpha)}\gamma_{,i}^{(\alpha)}\mathscr{P}_i^{(\alpha)}\right)^2}\right\}^{\mu+1}, \tag{22}$$

with

$$\mathscr{P}_i^{(\alpha)} = \begin{cases} s_i^{(\alpha)} & , \text{ for } \alpha = 1 \text{ or } 3 \\ m_i^{(\alpha)} & , \text{ for } \alpha = 2 \end{cases}, \tag{23}$$

given that $\gamma_{,3}^{(\alpha)} = 0$. $\mathscr{P}_i^{(\alpha)}$ is the unit vector that represents the direction of $p_i^{(\alpha a)}$ and $p_i^{(\alpha b)}$ projected onto the (110) plane. The scaling coefficients, $\omega^{(\alpha)}$ and $\chi^{(\alpha)}$, are the lengths of the projections of the vectors $s_i^{(\alpha a)}$ and $p_i^{(\alpha a)}$, respectively, onto the plane (110). Their values can be found in Table 1. However, for plane strain deformation of FCC crystals in the (110) plane, the symmetric activity of screw dislocations on each of the crystallographic slip systems of the pair that forms effective slip system 2, cancel each other out or annihilate (the projections of $p_i^{(\alpha a)}$ and $p_i^{(\alpha b)}$ are opposite). These can therefore be considered as effective SSDs, which do not contribute to the long range internal stresses. This can be seen through the Nye (1953) tensor, which can be written in terms of slip gradients as

$$\mathscr{G}_{ij} = \sum_\alpha e_{jkl}\gamma_{,k}^{(\alpha)}m_l^{(\alpha)}s_i^{(\alpha)}. \tag{24}$$

Expressing the slip gradients by an orthonormal basis $(s_i^{(\alpha)}, m_i^{(\alpha)}, p_i^{(\alpha)})$,

$$\gamma_{,k} = \gamma_{,l}^{(\alpha)}s_l^{(\alpha)}s_k^{(\alpha)}+\gamma_{,l}^{(\alpha)}m_l^{(\alpha)}m_k^{(\alpha)}+\gamma_{,l}^{(\alpha)}p_l^{(\alpha)}p_k^{(\alpha)}, \tag{25}$$

and using relation (6), the Nye tensor can be written as

$$\mathscr{G}_{ij} = b\sum_\alpha\left(\rho_{G(s)}^{(\alpha)}s_i^{(\alpha)}s_j^{(\alpha)}-\rho_{G(e)}^{(\alpha)}s_i^{(\alpha)}p_j^{(\alpha)}\right). \tag{26}$$

The only nonzero components of the Nye tensor for plane strain deformation in this crystal configuration are $\mathscr{G}_{12}$ and $\mathscr{G}_{13}$ (Kysar et al., 2007), which do not include contributions from screw density. From a physical point of view, this "annihilation" can be facilitated by cross-slip of the screw dislocations. For this reason $\chi^{(2)} = 0$ is chosen. Moreover, since $\omega^{(2)} = 1$ and $\sqrt{(\omega^{(1)})^2 + (\chi^{(1)})^2} = \sqrt{(\omega^{(3)})^2 + (\chi^{(3)})^2} = 1$, Eq. (22), written in terms of GND density, reduces to

$$\psi_G^{(\alpha a)} = \frac{1}{\mu+1}\tau_0 L^{\mu+1}\frac{1}{(\beta^{(\alpha)})^{\mu+1}}\left|\rho_{G(e),i}^{(\alpha)}\right|^{\mu+1}, \tag{27}$$

which gives the following back stress on the (αa)'th crystallographic slip system:

$$\tau_b^{(\alpha a)} = \mu\tau_0 b^\mu L^{\mu+1}\frac{1}{(\beta^{(\alpha)})^{\mu+1}}\left|\rho_{G(e)}^{(\alpha)}\right|^{\mu-1}\rho_{G(e),i}^{(\alpha)}s_i^{(\alpha)}. \tag{28}$$

The total back stress on the (α)'th effective slip system is then given by

$$\tau_b^{(\alpha)} = \lambda^{(\alpha)}\tau_b^{(\alpha a)} = \lambda^{(\alpha)}\tau_b^{(\alpha b)} = \mu\tau_0 b^\mu L^{\mu+1}\frac{\lambda^{(\alpha)}}{(\beta^{(\alpha)})^{\mu+1}}\left|\rho_{G(e)}^{(\alpha)}\right|^{\mu-1}\rho_{G(e),i}^{(\alpha)}s_i^{(\alpha)}. \tag{29}$$

Similarly, we can write Eq. (16) for the effective FCC crystal as

$$\tau_b^{(\alpha)} = \begin{cases} \tau_0 b L^2\dfrac{\lambda^{(\alpha)}}{(\beta^{(\alpha)})^2}\rho_{G(e),i}^{(\alpha)}s_i^{(\alpha)} & , \text{ for } |\tau_b^{(\alpha)}| \le \tau_T^{(\alpha)} \\ \operatorname{sgn}\left(\rho_{G(e),i}^{(\alpha)}s_i^{(\alpha)}\right)\tau_0^\kappa b^\kappa\left(\tau_T^{(\alpha)}\right)^{1-\kappa}L^{2\kappa}\dfrac{(\lambda^{(\alpha)})^\kappa}{(\beta^{(\alpha)})^{2\kappa}}\left|\rho_{G(e),i}^{(\alpha)}s_i^{(\alpha)}\right|^\kappa & , \text{ for } |\tau_b^{(\alpha)}| > \tau_T^{(\alpha)} \end{cases}, \tag{30}$$

where $\tau_T^{(\alpha)} = \lambda^{(\alpha)}\tau_T$. Thus, in the present case, the material length parameter for the effective slip systems corresponds exactly to the crystallographic length parameter. This result differs from the findings of Niordson and Kysar (2014), where the contribution from screw dislocations was neglected leading to a scaling of the material length parameters.

5. Results

Throughout the subsequent numerical analysis, the following model parameters are used: Young's modulus $E = 63{,}9$ GPa, Poisson's ratio $\nu = 0.36$, $\tau_0 = 10$ MPa, $\dot{\gamma}_0 = 10^{-3}$, $b = 0.286$ nm, and $m = 0.02$. Zero conventional hardening is assumed, so that , $h^{(\alpha\beta)} = h = 0$. The crystal is subjected to the equi-biaxial macroscopic strain $\Gamma_{biaxial} = \delta_{biaxial}/R = 3.75\text{x}10^{-4}$. Figure 3 shows the finite element mesh used for the numerical analysis.

Figure 4 shows the void area as function of the macroscopic biaxial strain for different values of L and the exponents μ and κ. The void area is numerically integrated by the trapezoid rule.

Figure 5 shows the slip on each of the effective slip systems for zero material length scale parameter ($L = 0$) normalized with a reference slip, while Fig. 6 shows the total slip, defined as the sum of the absolute value of slip on each effective slip system. The reference slip is defined as $\gamma_{ref} = \tau_0/G$, where G is the shear modulus. Figure 7 shows the GND density on each of the effective slip systems for zero material length

Table 1: Scaling coefficients between crystallographic and effective quantities

Effective slip system no., α	(1)	(2)	(3)
Angle to $[\bar{1}10]$ in (110) plane, θ	54.7°	0°	125.3°
$\beta^{(\alpha)} = \dfrac{\dot{\gamma}_0^{(\alpha)}}{\dot{\gamma}_0} = \dfrac{s_i^{(\alpha a)} m_j^{(\alpha a)} + s_i^{(\alpha b)} m_j^{(\alpha b)}}{s_i^{(\alpha)} m_j^{(\alpha)}}$	$\sqrt{3}$	$\dfrac{2}{\sqrt{3}}$	$\sqrt{3}$
$\lambda^{(\alpha)} = \dfrac{\tau_0^{(\alpha)}}{\tau_0} = \dfrac{2}{\beta^{(\alpha)}}$	$\dfrac{2}{\sqrt{3}}$	$\sqrt{3}$	$\dfrac{2}{\sqrt{3}}$
$\omega^{(\alpha)} = s_i^{(\alpha)} s_i^{(\alpha a)} = s_i^{(\alpha)} s_i^{(\alpha b)}$	$\dfrac{\sqrt{3}}{2}$	1	$\dfrac{\sqrt{3}}{2}$
$\chi^{(\alpha)} = \begin{cases} s_i^{(\alpha)} p_i^{(\alpha a)} = s_i^{(\alpha)} p_i^{(\alpha b)} & \text{, for } \alpha = 1 \text{ or } 3 \\ m_i^{(\alpha)} p_i^{(\alpha a)} = m_i^{(\alpha)} p_i^{(\alpha b)} & \text{, for } \alpha = 2 \end{cases}$	$\dfrac{1}{2}$	$\dfrac{\sqrt{3}}{\sqrt{2}}$	$\dfrac{1}{2}$

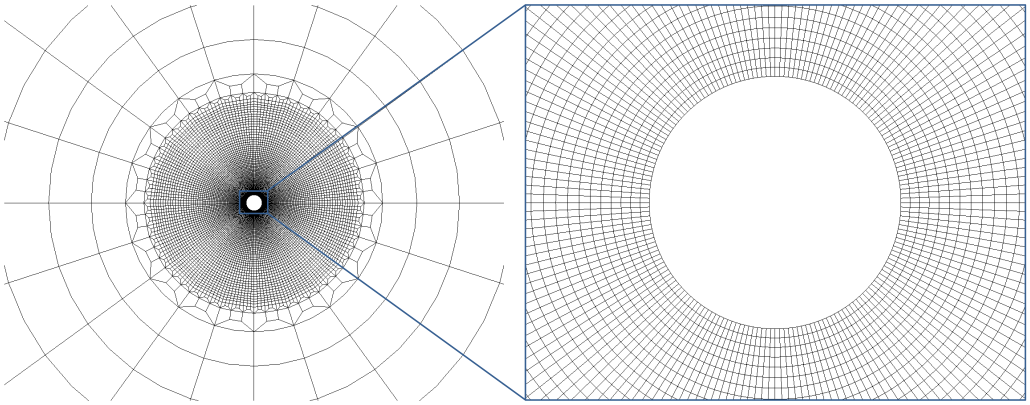

Figure 3: The finite element mesh employed for the analysis on the left with a zoom of the void region on the right.

scale parameter ($L = 0$) normalized with a reference density, while Fig. 8 shows the total GND density, defined as the sum of the absolute value of GND density on each effective slip system. The reference GND density is defined as $\rho_{ref} = \gamma_{ref}/(br)$. The scaling provided through $\beta^{(\alpha)}$ and $\lambda^{(\alpha)}$ results in more curved slip lines and GND density contours. The results show consistency with the lattice rotation measurements performed on a compression tested single crystal with a cylindrical void by Gan et al. (2006). In these measurements the curved lines, seen in the slip and GND contours predicted with the numerical model, are visible. The density on slip systems (1) and (3), may be considered as a combination of edge and screw density, while the density on slip system (2) is of pure edge character. Neglecting the cancellation of the screw density on slip system (2) in the analysis, and evaluating the screw density based on the slip gradient in the direction of $\mathscr{P}_i^{(2)} = m_i^{(2)}$, would be equivalent to the edge density

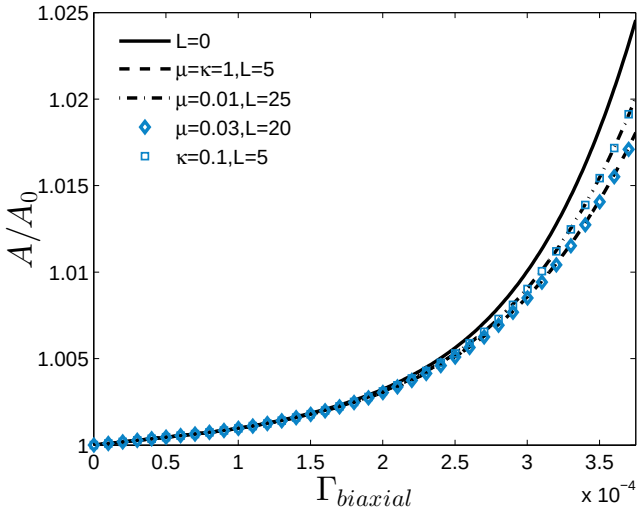

Figure 4: Predicted macroscopic response for different material parameters showing void area as function of macroscopic biaxial straining.

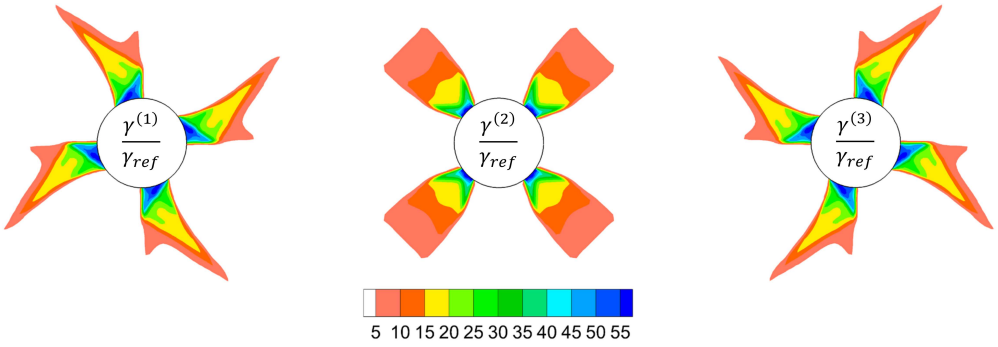

Figure 5: Predicted crystallographic slip on each of the slip systems for $L = 0$.

shown in Fig. 7, however, it would be rotated 90° clockwise about the void axis ([110] direction).

The size-effects on void growth and micro-structure in now analyzed by employing a material length scale parameter of $L/r = 5$ and assuming a quadratic gradient energy based back stress. This corresponds to having $\mu = \kappa = 1$ in Eqs. (29) and (30). Figure 9 shows the slip on each effective slip system and Fig. 10 shows the total slip. The effect of strain gradients serves to suppress slip. Moreover, the slip is more widely spread, creating more overlap between the single slip sectors compared to the conventional solution. Figure 11 shows the evolved GND micro-structure on each effective slip system, which reflects the smaller size of the plastically deforming region by less localized GND structures. Figure 12 shows the total predicted GND density, where structures along the effective slip planes appear together with secondary orthogonal structures. The length scale effect is based on the internal back stress field, $\tau_b^{(\alpha)}$, which is shown

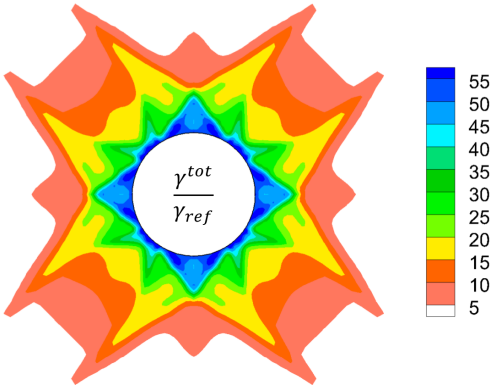

Figure 6: Total slip for $L = 0$.

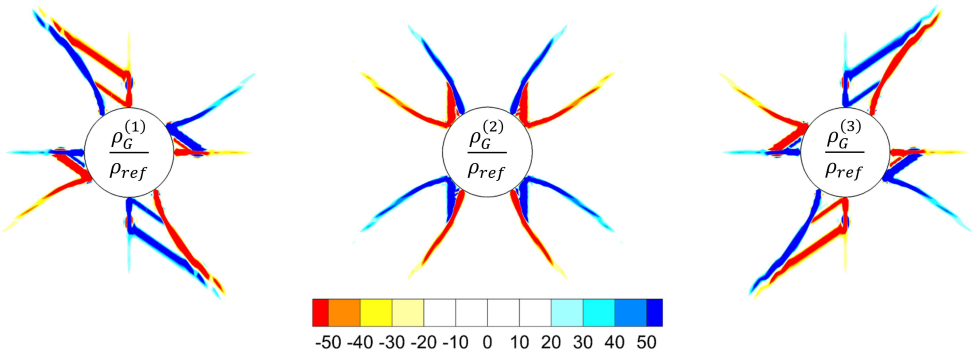

Figure 7: GND density on each of the slip systems for $L = 0$.

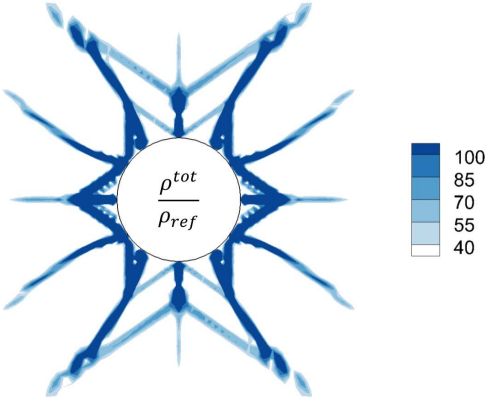

Figure 8: Total GND density for $L = 0$.

for each effective slip system in Fig. 13 normalized with the effective critical resolved shear stress. The back stress on each slip system develops in directions perpendicular to the slip planes, with features that run along the slip directions of the two other effective slip systems. Furthermore, it is observed that a spatially larger stress field

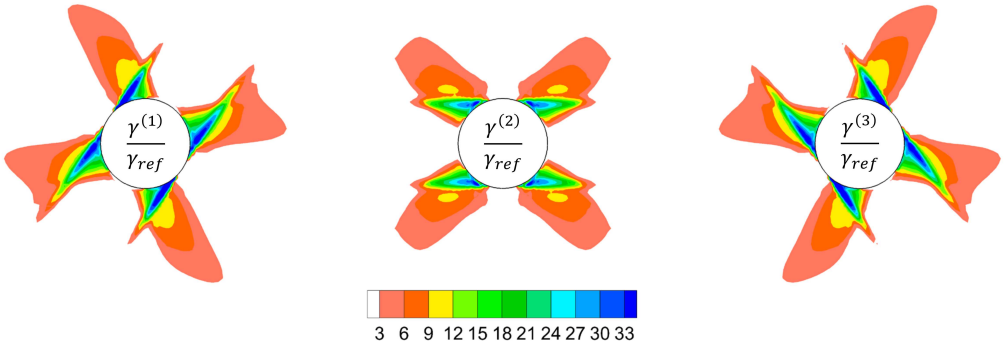

Figure 9: Predicted crystallographic slip on each of the slip systems for $L/r = 5$ assuming quadratic gradient energy.

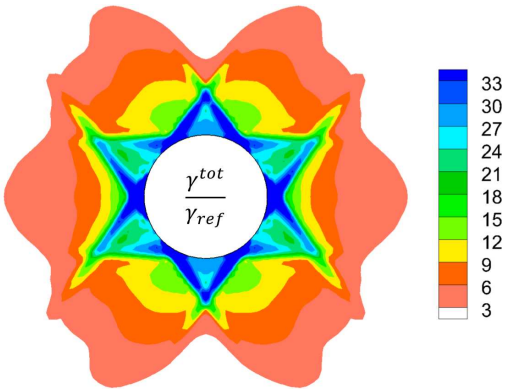

Figure 10: Total slip for $L/r = 5$ assuming quadratic gradient energy.

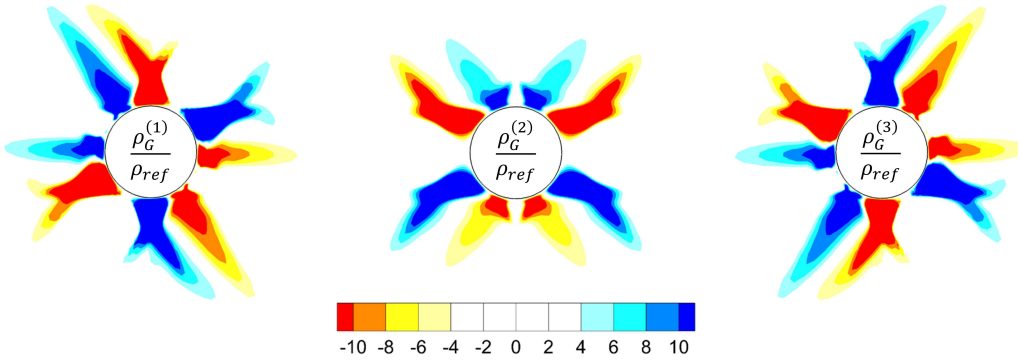

Figure 11: GND density on each of the slip systems for $L/r = 5$ assuming quadratic gradient energy.

develops on slip system (2) compared to systems (1) and (3). In comparison to the assumption of quadratic gradient energy, no immediate effect of the parameters μ and

Figure 12: Total GND density for $L/r = 5$ assuming quadratic gradient energy.

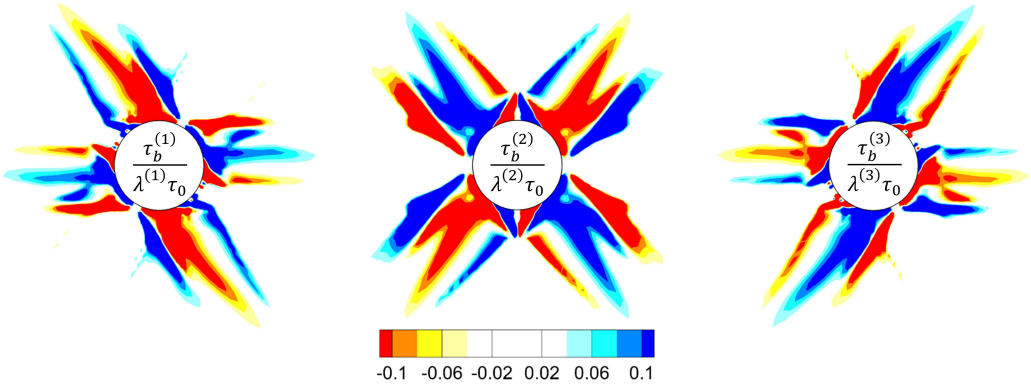

Figure 13: Back stress on each of the slip systems for $L/r = 5$, assuming quadratic gradient energy.

ρ_0 were found independent of L, when employing the back stress (29) resulting from the generalized gradient energy potential (27). This contradicts the findings in El-Naaman et al. (2016c) and (El-Naaman et al., 2016b). However, a more elaborate parametric study for the current type of boundary value problem may reveal other capabilities. As an example of the findings of the present study, the computation for $\mu = 0.03$ with $L = 20$ has a macroscopic response very close to the one for quadratic gradient energy with $L = 5$. Despite the different setup of the back stress in the two computations, there is no significant difference in the predicted micro-structure. On the other hand, when comparing the micro-structures predicted using back stress (29) with $L/r = 25$, $\mu = 0.01$, and $\rho_0 = 10^5$ mm^{-2} (Fig. 14a), with those obtained using back stress (30) with $L/r = 5$, $\kappa = 0.1$, and $\tau_T/\tau_0 = 0.2$ (Fig. 14b), these show significant differences despite the fact that the void growth vs. biaxial straining curves are virtually identical (see Fig. 4). The GND density in Fig. 14a extends farther out from the void, while a tendency toward developing structures parallel to effective slip system (2) is observed in Fig. 14b. The different behaviors resulting from the two different back stress formulations is clearly reflected in their very different stress fields shown in Figs. 15 and 16. The field obtained for effective slip system (2) using the phenomenological back

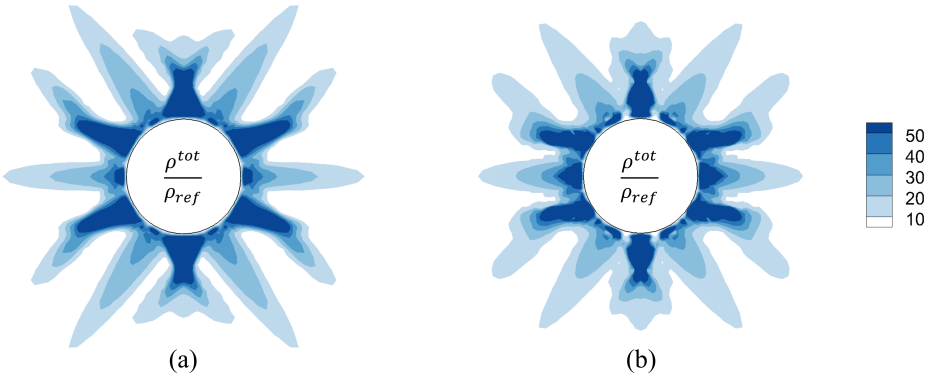

Figure 14: Total GND density. (a) Using the thermodynamically consistent back stress (29) with $L/r = 25$, $\mu = 0.01$, and $\rho_0 = 10^5$ mm^{-2}, and (b) using the phenomenological back stress (30) with $L/r = 5$, $\kappa = 0.1$, and $\tau_T/\tau_0 = 0.2$.

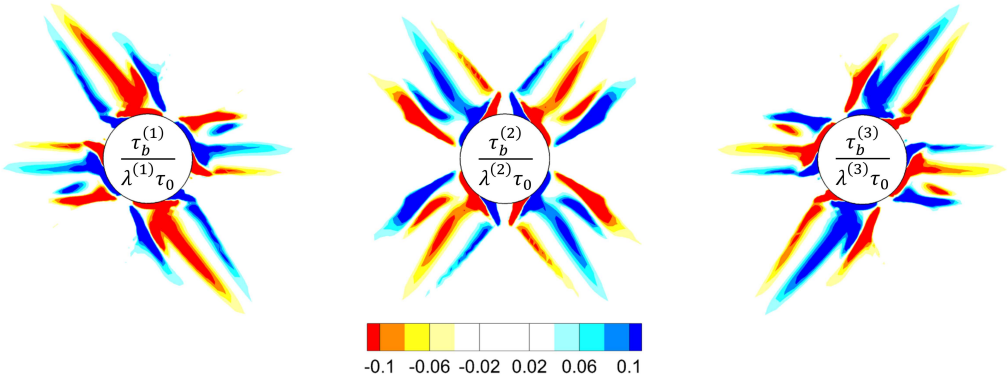

Figure 15: Back stress on each of the slip systems using back stress relation (29) with $L/r = 25$, $\mu = 0.01$, and $\rho_0 = 10^5$ mm^{-2}.

stress (30) develops more contour lines parallel to the slip system, which also extend farther out from the void. For all three slip systems in Fig. 16, additional features are developed compared to Fig. 15. The power law part of the piece-wise back stress function (30) governs only a very minor part of the back stress field shown in Fig. 16. The power law governed regions are shown in Fig. 17.

6. Concluding remarks

A finite element implementation of the non-work conjugate higher order strain gradient crystal plasticity model, proposed by Kuroda and Tvergaard (2006, 2008), has been employed for analyzing deformation around a cylindrical void in an FCC single crystal at small scales. Two novel back stress formulations, proposed in El-Naaman et al. (2015, 2016c), were employed, and, in the present study, the performance of these has been investigated within a two dimensional multi-slip setting. Moreover, additions

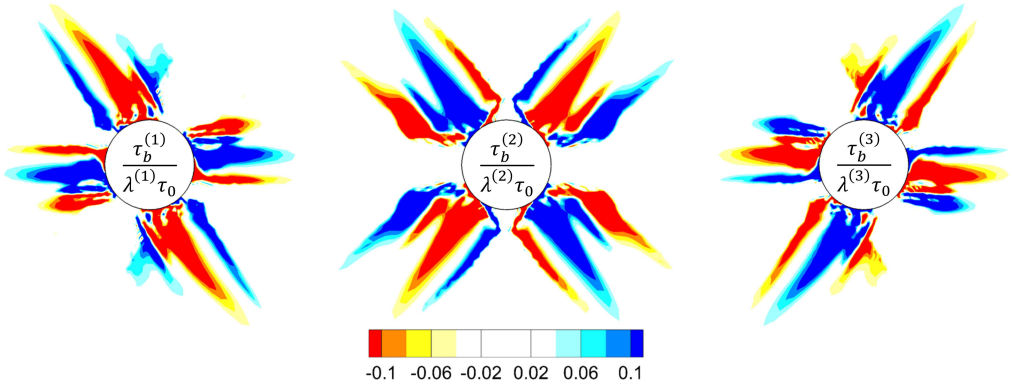

Figure 16: Back stress on each of the slip systems using back stress relation (30) with $L/r = 5$, $\kappa = 0.1$, and $\tau_T/\tau_0 = 0.2$.

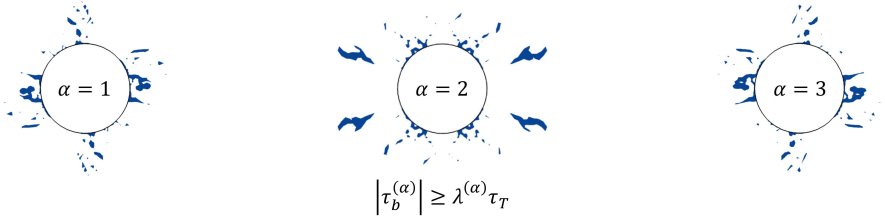

Figure 17: The regions governed by the power law part of back stress relation (30) with $L/r = 5$, $\kappa = 0.1$, and $\tau_T/\tau_0 = 0.2$.

to the framework for modeling (110) plane strain deformation of FCC crystals within strain gradient continuum theories has been made. This framework includes the proper account for the contribution arising from GND density of screw character into the constitutive equations. The promising capabilities of the thermodynamically consistent formulation (Eq. (15)), in terms of additional control of the micro-structural evolution found in El-Naaman et al. (2016c) and El-Naaman et al. (2016b), were not evident for the problem studied in the present work. However, the phenomenologically constructed back stress formulation (Eq. (16)) clearly leads to a different development of micro-structure independent of the macroscopic behavior for the present boundary value problem.

7. Acknowledgments

The work is financially supported by The Danish Council for Independent Research under the research career programme Sapere Aude as part of the project "Higher Order Theories in Solid Mechanics", grant 11-105098/FTP. The work of SAE is moreover supported by The Denmark-America Foundation and The FLSmidth Group.

References

Ashby, M., 1970. The deformation of plastically non-homogeneous alloys. Philos. Mag. 21, 399–424.

Atkinson, M., 1995. Further analysis of the size effect in indentation hardness tests of some metals. Journal of Materials Research 10, 2908–2915.

Bardella, L., 2010. Size effects in phenomenological strain gradient plasticity constitutively involving the plastic spin. International Journal of Engineering Science 48, 550–568.

Bardella, L., Panteghini, A., 2015. Modelling the torsion of thin metal wires by distortion gradient plasticity. Journal of the Mechanics and Physics of Solids 78, 467–492.

Bassani, J., 2001. Incompressibility and a simple gradient theory of plasticity. Journal of the Mechanics and Physics of Solids 49, 1983–1996.

Bayley, C., Brekelmans, W., Geers, M., 2006. A comparison of dislocation induced back stress formulations in strain gradient crystal plasticty. International Journal of Solids and Structures 43, 7268–7286.

Borg, U., Kysar, J., 2007. Strain gradient crystal plasticity analysis of a single crystal containing a cylindrical void. International Journal of Solids and Structures 44, 6382–6397.

Dahlberg, C., Saito, Y., Öztop, M., Kysar, J., 2014. Geometrically necessary dislocation density measurements associated with different angles of indentations. International Journal of Plasticity 54, 81–95.

El-Naaman, S., Nielsen, K., Niordson, C., 2015. Strain gradient crystal plasticity: A continuum mechanics approach to modeling micro-structural evolution. Plastic Behavior of Conventional and Advanced Materials: Theory, Experiment, and Modeling, 7–9.

El-Naaman, S., Nielsen, K., Niordson, C., 2016a. Attaining the rate-independent limit of a rate-dependent strain gradient plasticity theory. Extreme Mechanics Letters, *In Press*.

El-Naaman, S., Nielsen, K., Niordson, C., 2016b. An investigation of back stress formulations under cyclic loading. Submitted.

El-Naaman, S., Nielsen, K., Niordson, C., 2016c. On modeling micro-structural evolution using a higher order strain gradient continuum theory. International Journal of Plasticity 76, 285–298.

Evers, L., Brekelmans, W., Geers, M., 2004. Non-local cystal plasticity model with intrinsic SSD and GND effects. Journal of the Mechanics and Physics of Solids 52, 2379–2401.

Fleck, N., Hutchinson, J., 2001. A reformulation of strain gradient plasticity. Journal of the Mechanics and Physics of Solids 49, 2245–2271.

Fleck, N., Hutchinson, J., Willis, J., 2015. Guidelines for constructing strain gradient plasticity theories. Journal of Applied Mechanics 82, 1–10.

Fleck, N., Muller, G., Ashby, M., Hutchinson, J., 1994. Strain gradient plasticity: Theory and experiment. Acta Metallurgica et materialia 42 (2), 475–487.

Fleck, N., Willis, J., 2009a. A mathematical basis for strain-gradient plasticity theory. Part I: Scalar plastic multiplier. Journal of the Mechanics and Physics of Solids 57, 161–177.

Fleck, N., Willis, J., 2009b. A mathematical basis for strain-gradient plasticity theory. Part II: Tensorial plastic multiplier. Journal of the Mechanics and Physics of Solids 57, 1045–1057.

Gan, Y., Kysar, J., 2016. Cylindrical void in a rigid-ideally plastic single crystal iii: Hexagonal close-packed crystal. International Journal of Plasticity 23, 592–619.

Gan, Y., Kysar, J., Morse, T., 2006. Cylindrical void in a rigid-ideally plastic single crystal ii: Experiments and simulations. International Journal of Plasticity 22, 39–72.

Groma, I., Csikor, F., Zaizer, M., 2003. Spatial correlations and higher-order gradient terms in a continuum description of dislocation dynamics. Acta Materialia 51, 1271–1281.

Gurtin, M., 2000. On the plasticity of single crystals: free energy, microforces, plastic-strain gradients. Journal of the Mechanics and Physics of Solids 48 (5), 989–1036.

Gurtin, M., 2002. A gradient theory of single-crystal viscoplasticity that accounts for geometrically necessary dislocations. Journal of the Mechanics and Physics of Solids 50, 5–32.

Gurtin, M., Anand, L., Lele, S., 2007. Gradient single-crystal plasticity with free energy dependent on dislocation densities. Journal of the Mechanics and Physics of Solids 55, 1853–1878.

Harder, J., 1999. A crystallographic model for the study of local deformation processes in polycrystals. International Journal of Plasticity 15, 605–624.

Huang, Y., Qu, S., Hwang, K., Li, M., Gao, H., 2004. A conventional theory of mechanism-based strain gradient plasticity. International Journal of Plasticity 20, 753–782.

Hutchinson, J., 1976. Bounds and self-consistent estimates for creep of polycrystalline materials. Proc. R. Soc. Lond. A 348, 101–127.

Klusemann, B., Yalçinkaya, T., 2013. Plastic deformation induced microstructure evolution through gradient enhanced crystal plasticity based on a non-convex Helmholtz energy. International Journal of Plasticity 48, 168–188.

Kraft, O., Hommel, A., Arzt, E., 2000. X-ray diffraction as a tool to study the mechanical behaviour of thin films. Materials Science and Engineering: A 288, 209–216.

Kuroda, M., Tvergaard, V., 2006. Studies of scale dependent crystal viscoplasticity models. Journal of the Mechanics and Physics of Solids 54, 1789–1810.

Kuroda, M., Tvergaard, V., 2008. On the formulation of higher-order strain gradient crystal plasticity models. Journal of the Mechanics and Physics of Solids 56, 1591–1608.

Kysar, J., Gan, Y., Mendez-Arzuza, G., 2005. Cylindrical void in a rigid-ideally plastic single crystal. part i: Anisotropic slip line theory solution for face-centered cubic crystals. International Journal of Plasticity 21, 1481–1520.

Kysar, J., Gan, Y., Morse, T., Chen, X., Jones, M., 2007. High strain gradient plasticity associated with wedge indentation into face-centered cubic single crystal: Geometrically necessary dislocation densies. Journal of The Mechanics and Physics of Solids 55, 1554–1573.

Kysar, J., Saito, Y., Oztop, M., Lee, D., Huh, W., 2010. Experimental lower bounds on geometrically necessary dislocation density. International Journal of Plasticity 26, 1097–1123.

Martínez-Pañeda, E., Niordson, C., 2015. On fracture in finite strain gradient plasticity. International Journal of Plasticity, *In press*.

Mu, Y., Hutchinson, J., Meng, W., 2014. Micro-pillar measurements of plasticity in confined cu thin films. Extreme Mechanics Letters 1, 62–69.

Nielsen, K., Niordson, C., Hutchinson, J., 2012. Strain gradient effects on steady state crack growth in rate-sensitive materials. Engineering Fracture Mechanics 96, 61–71.

Niordson, C., Kysar, J., 2014. Computational strain gradient crystal plasticity. Journal of the Mechanics and Physics of Solids 62, 31–47.

Nye, J., 1953. Some geometrical relations in dislocated crystals. Acta Metallurgica 1 (2), 153–162.

Öztop, M., 2011. Multiscale experimental analysis in plasticity: Linking dislocation structures to continuum fields. Ph.D. thesis, Columbia University.

Öztop, M., Niordson, C., Kysar, J., 2012. Length-scale effect due to periodic variation of geometrically nescessary dislocaion densities. International Journal of Plasticity 41, 189–201.

Peirce, D., Asaro, R., Needleman, A., 1983. Material rate dependence and localized deformation in crystalline solids. Acta Metall. 31, 1951–1976.

Rice, J., 1987. Tensile crack tip fields in elastic-ideally plastic crystals. Mechanics of Materials 6, 317–335.

Stölken, J., Evans, A., 1998. A microbend test method for measuring the plasticity length scale. Acta Materialia 46, 5109–5115.

van Beers, P., McShane, G., Kouznetsova, V., Geers, M., 2013. Grain boundary interface mechanics in strain gradient crystal plasticity. Journal of the Mechanics and Physics of Solids 61, 2659–2679.

van Beers, R., Kouznetsova, V., Geers, M., 2015. Defect redistribution within a continuum grain boundary plasticity model. Journal of the Mechanics and Physics of Solids 83, 243–262.

Wei, Y., Hutchinson, J., 1997. Steady-State crack growth and work of fracture for solids characterized by strain gradient plasticity. Journal of the Mechanics and Physics of Solids 45, 1253–1273.

Wei, Y., Hutchinson, J., 1999. Models of interface separation accompanied by plastic dissipation at multiple scales. International Journal of Fracture 95, 1–17.

Xiang, Y., Vlassak, J., 2016. Bauschinger effect in thin metal films. Scripta Materialia 53, 177–182.

Yefimov, S., Groma, I., van der Giessen, E., 2004. A comparison of a statistical-mechanics based plasticity model with descrete dislocation plasticity calculations. Journal of the Mechanics and Physics of Solids 52, 279–300.

DTU Mechanical Engineering
Section of Solid Mechanics
Technical University of Denmark

Nils Koppels Allé, Bld. 404
DK-2800 Kgs. Lyngby
Denmark
Phone (+45) 4525 4250
Fax (+45) 4593 1475
www.mek.dtu.dk
ISBN: 978-87-7475-465-7

DCAMM
Danish Center for Applied Mathematics and Mechanics

Nils Koppels Allé, Bld. 404
DK-2800 Kgs. Lyngby
Denmark
Phone (+45) 4525 4250
Fax (+45) 4593 1475
www.dcamm.dk
ISSN: 0903-1685